Debris flows on Earth and Mars

Thesis

Debris flows on Earth and Mars

Susan Jane Conway

BA, MSci, MA cantab

12th February 2010

A thesis submitted to the Open University in the subject of Earth and Environmental Sciences for the degree of Doctor of Philosophy.

Earth and Environmental Sciences

Open University

Abstract

This thesis explores the morphology of debris flows and their role in shaping planetary surfaces. The primary objective is to assess the scale of the present martian near-surface water budget by studying recent gullies visually similar to water-carved gullies on Earth. The potential involvement of debris flow in forming these gullies is important, because it implies the action of liquid water. To assess the role of debris flow in forming martian gullies requires a better understanding of debris flows on Earth.

I first performed a detailed study of unconfined debris flows in NW Iceland and developed a model to predict their path and deposition thickness using only the morphology of the previous deposits. I used this model to define areas at risk from debris flow inundation. Secondly I have used quantitive geomorphological methods to study long profiles and digital elevation models and have successfully ascertained the geomorphic "fingerprint" of mass wasting, debris flow and pure water flow on Earth. Using these methods, I then confirmed that gullies on Mars contain the signature of debris flow. In addition, these investigations revealed a strong climatic signal in gully development.

Laboratory simulation experiments showed that under present martian climate liquid water can not only survive for appreciable time-scales, but can perform significant geomorphic work. Freezing at the base of the flow not only decreases infiltration, but increases the runout of the flow.

These results indicate that gullies are a product of the recent action of thaw of ice on Mars. I suggest that moderate orbital spin obliquity is required to form gullies (rather than high obliquity suggested previously), because this is consistent with their distribution,

the time needed for their development, and their relative youth. Thus the surface of Mars has been wetter, more recently than previously thought.

Acknowledgements

I don't want to gush and spout
or make a fuss about
those that helped me on my way
so let's hope this ain't cliché…

Many people gave support,
kind advice and helpful thought,
even contributed pieces,
to this academic thesis.

When I first embarked upon,
this great thesis, It was John,
Martin Towner, Matt as well,
got this thesis going well.

The support from all these three,
Was of course exemplary;
and you'll never guess,
how I loved John's GPS!
Which was useful, heaven knows,
measuring those debris flows!

And I thanked my lucky stars,
when Martin Towner made the Mars-
Chamber, which was near as dammit,
like the surface of that planet!

Can a thesis come to harm
supervised by dear Matt Balme?
Need a student ever worry ,
supervised by good John Murray?

Someone who gave me help as well
was the wonderful Armelle -
Decaulne; she who really knows
everything of debris flows.
In Icelandic countryside
she was my unfailing guide.

Now I have to mention Mum,
Who'd expect one's mum to come,
on the top of debris flows,
where one's nose and fingers froze,
what more useful to me than,
Mum and motorcaravan!

Most of all I really am
grateful for the help of Sam -
Hammond; when I hurt my ankle she,
was as helpful as can be,
walking where the fieldwork led
Silly hat upon her head!

Mischa Kreslavsky, oh he,
was as useful as can be,
with the code he gave to me
measuring gullies was easy!

Alvaro and Tatiana
in La Gomera they made calmer,
surveying with the GPS
hot and sweaty, what a mess!

Saskia, Guillermo, Anne,
Marc, Mel, Wesley and Sam,
in the office they did roam
supporting me with this tome!

The NASA RPIF data-
Centre, whose DTM creator
drives Pete G up the wall,
but the results do enthral!

Nina said, go summon Chris!
and it is because of this
he gave me elevation,
data, a total revelation!

Someone once said that Lionel,
smelt like a urin-el!
but I think that he is great
and his odor is first rate!
and that person who called him such
for his help thanks very much!

Now it is time to stop the rhyme
and carry on with my usual crime
to the language of these isles
hope this ditty brought you smiles!

This work would not have been possible without a postgraduate studentship grant from the U.K. Natural Environment Research Council (NERC): NER/S/A/2006/14026. I thank the NERC Airborne Research and Survey Facility for obtaining the air photography and LiDAR data essential to the work in NW Iceland. Additional funding was awarded by Earth and Space Awards, the Geological Society's W.G. Fearnsides Award, The Dudley Stamp Fund, and the British Society for Geomorphology's postgraduate funds. I gratefully acknowledge the support of the staff at the Open University's Research Design and Engineering Facility and technical staff at Earth and Environmental Sciences and Planetary and Space Science Research Institute. I thank Luther Beegle for sharing his raw data on grainsize analysis of JSC-1 and MMS Mars simulants and Karl Atkinson for allowing me to use his grainsize analyses results. I thank the staff at Soil Property Testing Ltd., Huntingdon, UK for performing the permeability testing and grainsize analysis. I am grateful to Helen Townsend for her assistance in the laboratory.

Table of Contents

List of Figures

List of Tables

Chapter 1. Introduction

1.1. Aims and objectives

The objective of this work is to use studies of debris flows to help understand the distribution in time and space of water at the martian surface. This in turn ties into questions of biological habitability of the planet and the potential for future human exploration. Knowledge of the water budget also affects our understanding of the modern climate and that of the recent past.

1.2. Methodology

Geomorphology is the study of how different processes interact to create the shape of the landscape. This thesis uses a geomorphological approach to study debris flow landforms on Earth and Mars. The debris flow process is a type of mass movement composed of a poorly sorted mixture of water and sediment. The debris flow process is both hazardous and distinctive, creating landforms that can be easily recognised in terms of morphology. For brevity, throughout the rest of this thesis, the process of debris flow will be referred to simply as "debris flow" and debris flow landforms as "a/the debris flow" or "(the) debris flows".

Gullies on Mars provide the most convincing evidence for the action of liquid water on the surface in the recent martian past (Malin and Edgett, 2000; Figure 1-1). However, their formation mechanisms, and hence the amounts of mobile water they represent, are poorly understood. Therefore this study aims to test models of gully formation and to assess the impact of these landforms on the martian water budget.

The progression of this project is as follows:

(1) to characterise and better understand the morphology of debris flows on Earth at the scale of the individual flow and at a landscape scale;

(2) to determine if the morphological signature of debris flow can be detected on Mars;

(3) if so, determine if liquid water can mobilise sufficient sediment to create gullies on the *present* surface of Mars.

Figure 1-1. Examples of gullies on Mars. Scalebar is 100 m and the triangle points north. The image is from colour High Resolution Imaging Science Experiment (HiRISE) data, credit NASA/JPL/UofA.

To achieve these aims I employed three approaches: fieldwork, remote sensing and laboratory simulations. The fieldwork comprised field observations and measurements using high accuracy differential Global Positioning System (GPS) and Total Station

surveying techniques. Remote sensing data for Earth were in the form of airborne laser altimetry and aerial photography. The fieldwork and remotely sensed data on Earth allowed the accurate and detailed quantification of debris flows on Earth. On Mars, the remotely sensed data were collected by orbiting satellites providing image and elevation data. These data were at an equivalent resolution to those collected on Earth and allowed comparison between the two planets to determine if the debris flow signature could be detected on Mars. The laboratory simulation experiments were performed to ascertain whether water is able to transport sediment despite the freezing conditions and thin atmosphere on the present-day surface of Mars.

1.3. Thesis structure

Chapter 2 presents a review of the current literature on gullies on Mars and places them in the broader martian geological and climatic context. In Chapter 3 I present a review of the terrestrial debris flow literature and provide a preliminary assessment of debris flow as a potential mechanism for the formation of martian gullies. Chapter 4 presents a quantitative geomorphological study of unconfined debris flows in NW Iceland based on high resolution (1 m/pixel) airborne laser altimeter data and differential GPS, and a qualitative study of other debris flows around Iceland. This study leads on to the development of a new hazard analysis technique for debris flows in Iceland, as well as a providing further clues as to whether debris flow is a suitable mechanism for forming martian gullies.

Chapter 5 forms an introduction to Chapters 6 and 7, describing the data and methods used in those chapters. Chapters 6 and 7 present morphometric comparisons between alluvial and debris flow gullies on Earth and gullies on Mars. Chapter 6 presents the analysis of the properties of topographic long profiles on Earth and Mars. Analysis of terrestrial long profiles is undertaken to characterise the different properties that are indicative of (1) debris flow and (2) alluvial gullies. This analysis is then applied in turn to Mars to ascertain the active processes in forming gullies there. Chapter 7 describes the

analysis of high resolution (1 m/pixel) elevation models of gullies on Earth and Mars. These elevation models are used to derive three-dimensional morphometric properties of slopes containing gullies on both planets. Process domains based on these properties, developed from studies of fluvial landscapes on Earth, are applied to gullies on Earth to test their suitability for differentiating debris flow and alluvial processes. These analyses are then applied to Mars to determine the surface processes that formed the martian gullies.

Chapter 8 describes laboratory work to simulate water flow over sediment on Mars. A summary of the experimental procedure is given, in which water is introduced to a tilted sediment-filled tray within a hypobaric chamber under realistic martian surface conditions. This chapter reports the observations made during the experiments, calculations of erosion rates, and the changes in surface topography of the sediments.

The thesis ends with a synthesis of the conclusions that can be drawn from the interlinked studies that make up the chapters. Finally the appendices include detailed calculations that support the main text.

1.4. Published or submitted work

Parts of this thesis have been published, are in review, or have been submitted for publication in the peer-reviewed literature. Table 1-1 shows the chapters for which this is the case and the contribution of the co-authors to the work. The co-authors listed in the table are in addition to my supervisors, Matthew Balme, John Murray and Martin Towner. The content of the manuscripts remains essentially unchanged from the published or submitted versions, except where noted otherwise in the text. Slight alterations have been made for consistency within the thesis, for example figure and table numbers have been changed so as to run consecutively and the first person plural in the manuscripts has been changed to the first person singular, where appropriate.

Table 1-1. Summary of published material and contribution of co-authors.

Title	Co-authors	Contribution %, substance		Journal	Status	Chapter(s)
A new Approach to Estimating Hazard posed by Debris Flows in the Westfjords of Iceland	Armelle Decaulne	10	Knowledge of the recent history of the Westfjords and in depth knowledge of the geomorphology of the debris flows in the area.	Geomorphology, 114(4), 556-572 (2010)	Published	4
The determination of martian gully formation processes by slope-area analysis.	Peter Grindrod	5	Use of the UCL RPIF Facility	"Planetary Geomorphology", a Geological Society Special Publication.	In review	5, 7
	Chris Okubo	5	Data, two HiRISE DEMs of gullies.			
Experimental study of sediment transport by water flowing under martian conditions: application to gullies on Mars.	-	-	-	Icarus	In review	8

Chapter 2. Recent Water Flows on Mars

2.1. Water on Mars through time

Unlike the Earth, the surface of Mars provides a continuous record of almost all of its long geological history. The lack of tectonic recycling of Mars' crust over the last 3 Ga (e.g. Nimmo and Stevenson, 2000) means that the surface bears all the scars of the changing climate and resulting surface processes. Hence, the study of Mars' landscape, or the geomorphology of Mars has a much longer timespan than comparable studies of Earth. This means the exposure time of a martian surface feature can be ascertained by determining the size-frequency distribution of its impact craters. This distribution can then be compared to a chronology based on the expected impact size-frequency for surfaces of a certain age (e.g. Hartmann et al., 2008). Geological time on Mars is split into three periods. In chronological order these are: the Noachian, the Hesperian and the Amazonian (Figure 2-1). These terms are derived from the surface units (respectively: Noachis Terra, Hesperia Planum, Amazonia Planitia) which host the impact crater distribution characteristic for each of the time periods.

From this dating we know that early in Mars' history water was abundant, or at least episodically abundant on its surface (e.g. Sharp and Malin, 1975). Outflow channels and/or channel networks have been dated as active from the Noachian (e.g. Hauber et al., 2009a) up to as recently as the Amazonian (e.g. Warner et al., 2009), although most of the activity of these channels was focussed around the Hesperian (Coleman et al., 2007; Leverington, 2009). There are many theories for the origins of the various and numerous large channels on Mars, for example, dewatering of hydrous rocks by volcanic heating

(Montgomery and Gillespie, 2005), or localised precipitation (Burr et al., 2009), or even purely volcanic origin (Leverington, 2009). However, most commonly these channels are attributed to groundwater sources (e.g. Carr, 1979; Coleman et al., 2009; Warner et al., 2009). On the whole these channels debouched into the northern lowlands and it is commonly hypothesised that a standing body of water was formed, often cited as the "northern ocean" (Clifford and Parker, 2001; Ivanov and Head, 2001). The large amounts of water involved in forming these channels is not only implicated by their dimensions, but by the large areal extent of the channel networks and their density, which is only 2.5 times lower than Earth (Luo and Stepinski, 2009).

The presence of features reminiscent of alluvial fans on Earth near the dichotomy boundary on Mars also argue for widespread liquid water, or even rainfall early in Mars' history (e.g. Moore and Howard, 2005), with some isolated examples possibly as young as early Hesperian in age (e.g. Williams and Malin, 2008).

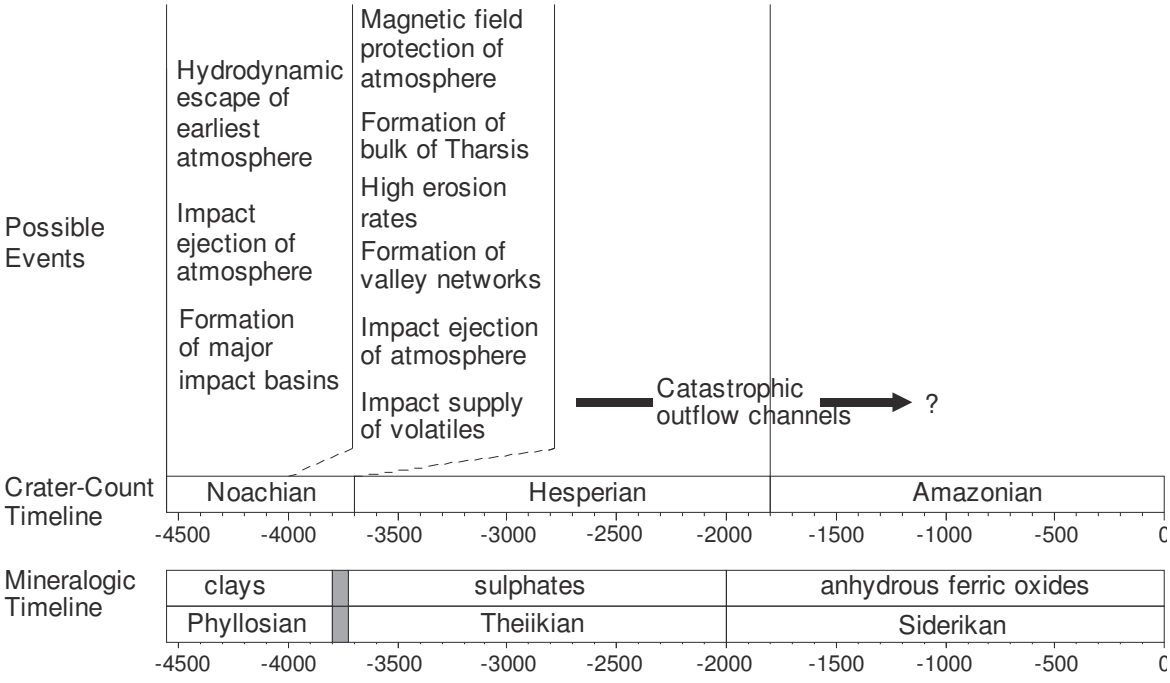

Figure 2-1. Mars Timeline. All numerals given in thousands of years before present. Possible past events and crater-count timeline from Jakosky and Philips (2001) and mineralogic timeline from Bibring et al. (2005).

The fate of this large amount of water that was present on the surface of Mars up until the early Amazonian is vigorously debated. There are two potential scenarios: (1) the water is locked up in a deep cryosphere or (2) the majority of the water was lost to space and little remains today. These scenarios have profoundly different implications on the possibility of finding extant life on Mars. A long-lived martian hydrosphere would be the most favourable environment in which life could survive beneath the surface, away from the high radiation, large temperature gradients and dry, low density atmosphere. The absence of such a large hydrosphere would make the persistence of life much more unlikely.

Clues to the fate of the water on Mars are locked up in the present surface. There is much evidence to support the presence of long lived surface ice in the mid and high latitudes: e.g., the hydrogen ion signature found by the Gamma Ray and Neutron Spectrometers (e.g. Tokar et al., 2002; Jakosky et al., 2005), the ice found by the Phoenix lander (Mellon et al., 2008), spectral data from OMEGA (Bibring et al., 2005) and CRISM and the presence of so called “fluidised” craters (e.g. Barlow and Perez, 2003) and rampart craters (Carr et al., 1977). The polar caps are known to “lock away” water ice, and are thought to provide the seasonal variation in water vapour in the atmosphere (e.g. Pankine et al., 2009). However, the precise quantity of water ice locked away in the caps is not known.

The possibility of recent geological activity involving liquid water on the surface is still controversial. There are only four examples of regional-scale features being formed by liquid water in geologically recent timescales. Firstly, the “Elysium sea”, sourced from the Cereberus Fossae outpoured water less than 10 Ma ago (Murray et al., 2005). However, modelling indicates that it is doubtful that much water is still preserved there today (Kossacki et al., 2006). There are still arguments that the landforms seen there could be volcanic (Jaeger et al., 2007b), however many investigators agree that this volcanic activity

could have interacted strongly with water (Keszthelyi et al., 2010). In this same region Balme and Gallagher (2009) and Page (2007) find additional evidence for the activity of very recent liquid water, but on a smaller scale, in the form of pingoes, pingo scars, evaporated thermokarst lakes and ice-wedge polygons. A second example is presented by Dickson et al. (2009) who find evidence for local melting forming a large channel network around the Lyot crater during the late Amazonian. Thirdly, Athabasca Vallis located near the equator of Mars is the youngest confirmed outflow channel, with crater counting giving the age for the most recent event as a few million years ago (Burr et al., 2004). A fourth example is the north polar cap, hypothesised to be a source of outflow generated from recent sub-cap volcanic activity (Hovius et al., 2008), although the observed features can also be attributed to wind (Warner and Farmer, 2008).

There are several lines of evidence for the recent activity of liquid water on a smaller-scale but with a very large regional extent. Firstly from global topographic data, pole-facing slopes in mid-latitudes are observed to be subdued, attributed to freeze-thaw assisted creep (Squyres and Carr, 1986; Kreslavsky and Head, 2003). Secondly the discovery of periglacial landform assemblages at low latitudes (Page, 2007; Banks et al., 2008; Balme and Gallagher, 2009; Balme et al., 2009; Page et al., 2009), including pingoes, retrogressive thaw and sorted stone circles. Thirdly, “wet” glacial landforms assemblages have been observed, such as lobate debris aprons, ring-mold craters and linear valley fill (Carr et al., 1977; Kress and Head, 2008), which still contain ice (Plaut et al., 2009). Finally, the observation of widespread mid-latitude gullies (Malin and Edgett, 2000) that resemble water-carved or fluvial features on Earth provides a persuasive line of evidence for the recent activity of liquid water on the surface. However, their formation mechanism is still under debate, and the possible mechanisms affect whether such gullies support, or contradict the evidence for recent surface water on Mars. These gullies are the focus of the following review and form the central theme of this thesis.

2.2. Gullies on Mars

Gullies on Mars were first studied in detail by Malin and Edgett (2000) with data from the Mars Global Surveyor (MGS) Mars Orbiter Camera (MOC). They defined gullies on Mars as features that have an alcove, a channel and a debris apron. They observed that these gullies are visually similar to features carved by liquid water on Earth (Figure 2-2). They suggested that the water that formed the gullies must have been sourced from an underground aquifer, as the current surface temperature and pressure on Mars means liquid water is not stable (Figure 2-3). This apparent paradox between the present instability of water and the presence of recent features carved by water has caused intense debate. Dating from crater counting has confirmed the youthful nature of these gullies and suggests the age of most gullies is < 1.4 Ma (Reiss et al., 2004; Schon et al., 2009).

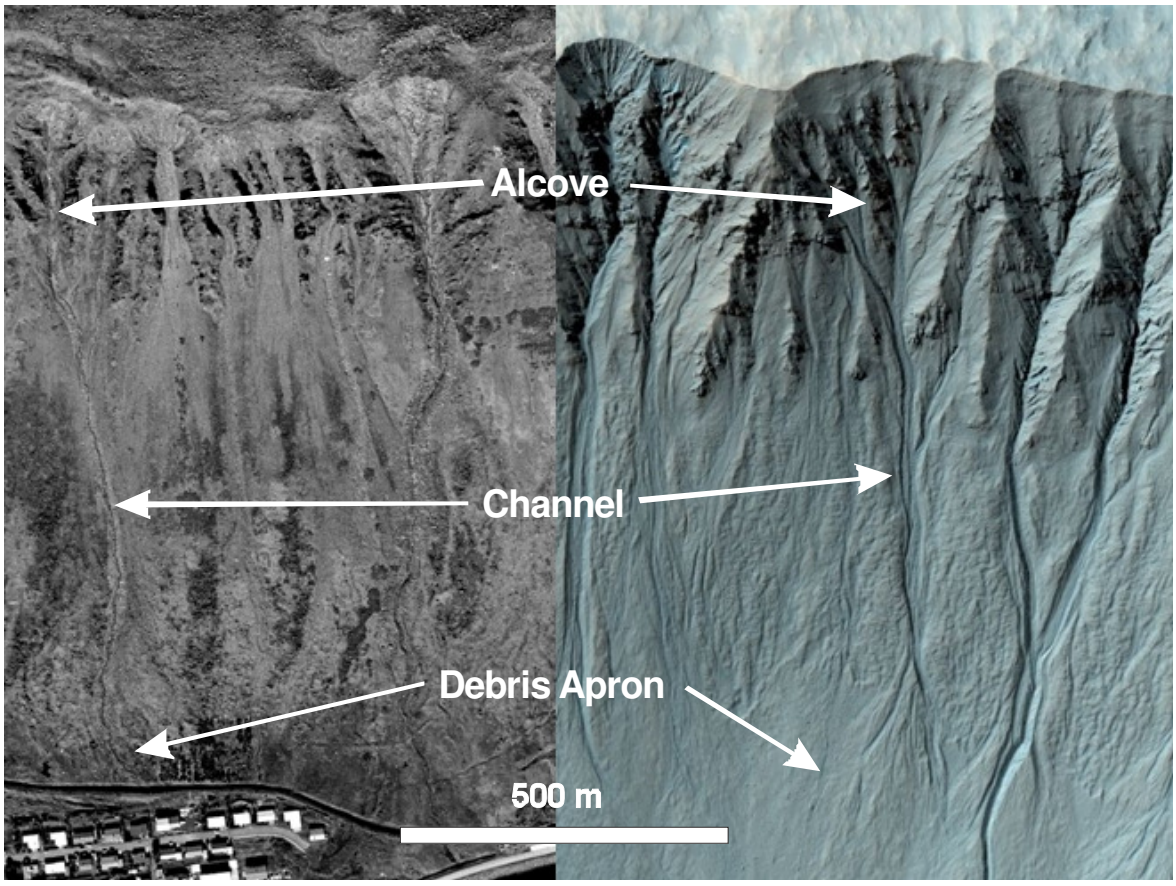

Figure 2-2. Structure of gullies on Earth and Mars. The images are at the same scale as shown by the shared scale bar at the bottom of the figure. Image to the left is of debris flows above the town of Ísafjörður in NW Iceland, courtesy of NERC ARSF. Image to the right is of gullies on Mars taken by the HiRISE camera, image number: PSP_005985_1455 credit: NASA/JPL/UofA.

In the following sections I provide an overview of the main hypotheses within the context of the potential mechanisms for forming gullies, dry genesis (Section 2.3) and wet genesis (Section 2.4). I then detail the insights gained from a variety of different study types (Section 2.5): remote sensing, modelling, Earth analogues and experimental work.

2.3. Gully formation by dry flow or CO_2

Dry granular flow is the simplest explanation for the origin of gullies, because it does not require the problematic inclusion of liquid water. Treiman (2003) suggested a type of flow analogous to a powder snow avalanche on Earth to explain the morphological features of gullies on Mars. These avalanches have wide straight central channels and lateral levees. These flows would also be analogous to flows down slip-faces of sand dunes on Earth. Gullies formed by this mechanism would need steep slopes and a supply of unstable material.

Another variation of this theory is the gas-supported density flow, analogous to pyroclastic flows on Earth, in which the gas would be carbon dioxide. Hoffman (2000) and Musselwhite et al. (2001) suggested that gullies could be formed by a mechanism driven by explosive expansion of CO_2 gas from either solid or liquid CO_2. Hoffman (2002) suggested that this mechanism was more likely for gullies near the south pole, where seasonal build-up of significant quantities of CO_2 frost is more likely. This model relies on sufficient accumulation of CO_2 and sudden insolation to trigger the explosive gas release.

2.4. Gully formation by water or brine

Pure liquid water is thermodynamically unstable on the surface of present day Mars (Figure 2-3). Temperatures vary from 130 K to 250 K and the surface pressure is around 7 mB, which is not within the stability field for liquid water. Therefore, special conditions must be invoked to enable water to be a source of fluid to form gullies. The atmosphere is ~ 95 % carbon dioxide and only ~ 0.03 % water vapour.

All of the water-based models of gully formation rely on the action of liquid water at the surface. This water either flows down the gully in its pure form, or forms a debris flow: a hyperconcentrated mix of sediment and water. For liquid water to be stable on the surface of Mars, either (1) the pressure-temperature stability field of water needs to change, by the addition of salts, for example, or (2) the pressure-temperature conditions need to have been different from present day, allowing water to be stable. The aquifer models and surface melting model, described in further detail in Sections 2.4.1 and 2.4.2 respectively, both take the approach of changing the pressure-temperature conditions to allow water to be stable. Section 2.4.3 addresses the potential role of brines and other more exotic fluids in the formation of gullies on Mars.

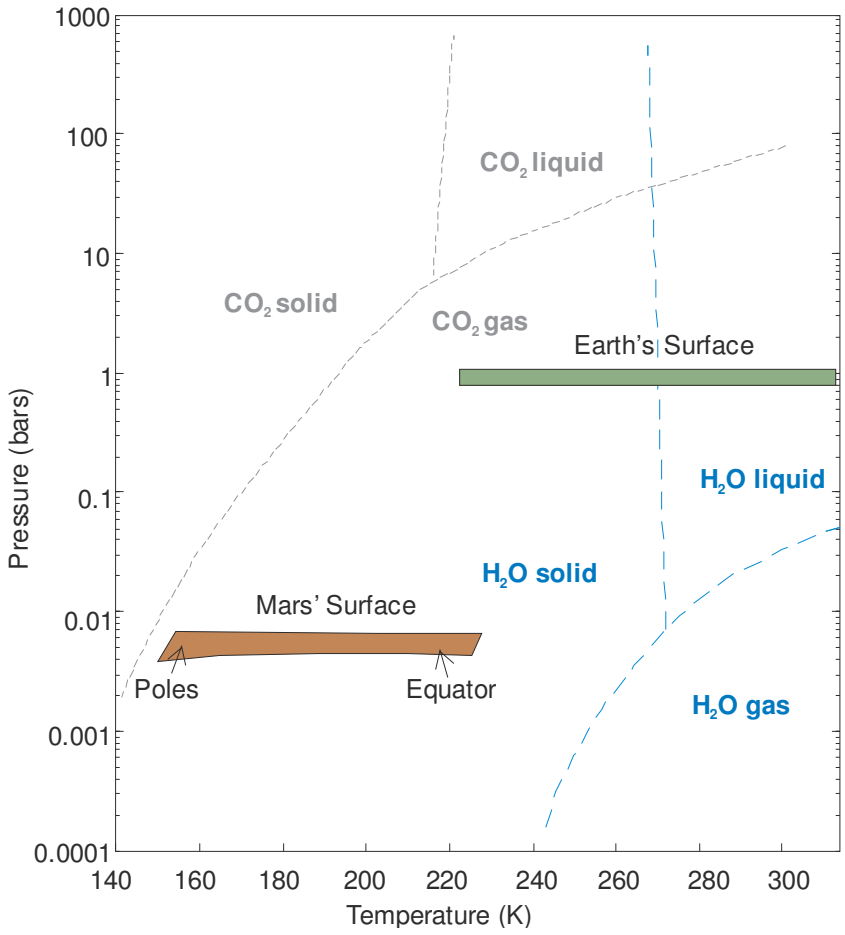

Figure 2-3. Pressure-temperature stability of the phases of water and carbon dioxide. The surface conditions for Earth and Mars are indicated on the plot. For Mars the surface pressure and temperature (averaged according to latitude) is from Kieffer (1992). Adapted from Longhi (2006).

2.4.1. Surface melting model

There are two principal climate-related hypotheses that invoke melting of surface ice directly supplying water to form gullies. The first, in which accumulation occurs in the past and melting occurs at the present day (Christensen, 2003) and the second in which both accumulation and melting occur in the past (Costard et al., 2002). However, both models invoke obliquity changes to explain the distribution of the surface ice (Figure 2-4). There is a third model (Hecht, 2002), which does not depend on climate. Hecht (2002) suggests that both accumulation and melting of surface ice can occur at the present day.

In models of martian climate (e.g. Mellon and Jakosky, 1995), the polar regions receive more insolation at high obliquities (Figure 2-4). Hence water locked up in the polar caps is destabilised and sublimes, making the atmosphere more humid. This water is re-deposited in the winter hemisphere at mid to high latitudes as surface ice. Over time there is a net deposition at mid and high latitudes at the expense of the poles, which effectively creates a thinner polar cap, but with a larger spatial extent. Water accumulated on pole-facing slopes maintains a protective coating of CO_2 frost, which prevents sublimation of the water. The CO_2 on the other slopes is lost due to insolation and hence the water is lost back to the atmosphere too.

In the model of Christensen (2003), the ice is preserved on these slopes until the obliquity swings to lower values and the ice then melts. This model relies on the assumption that ice can be preserved on timescales of 10,000 to 100,000 years. However, in the model of Costard et al. (2002) the melting occurs seasonally under high obliquity conditions, as a result of greater seasonal accumulation on pole-facing slopes and annual removal of the CO_2 layer at springtime. The model of Costard et al. (2002) needs sufficient accumulation to occur to produce enough meltwater to form gullies.

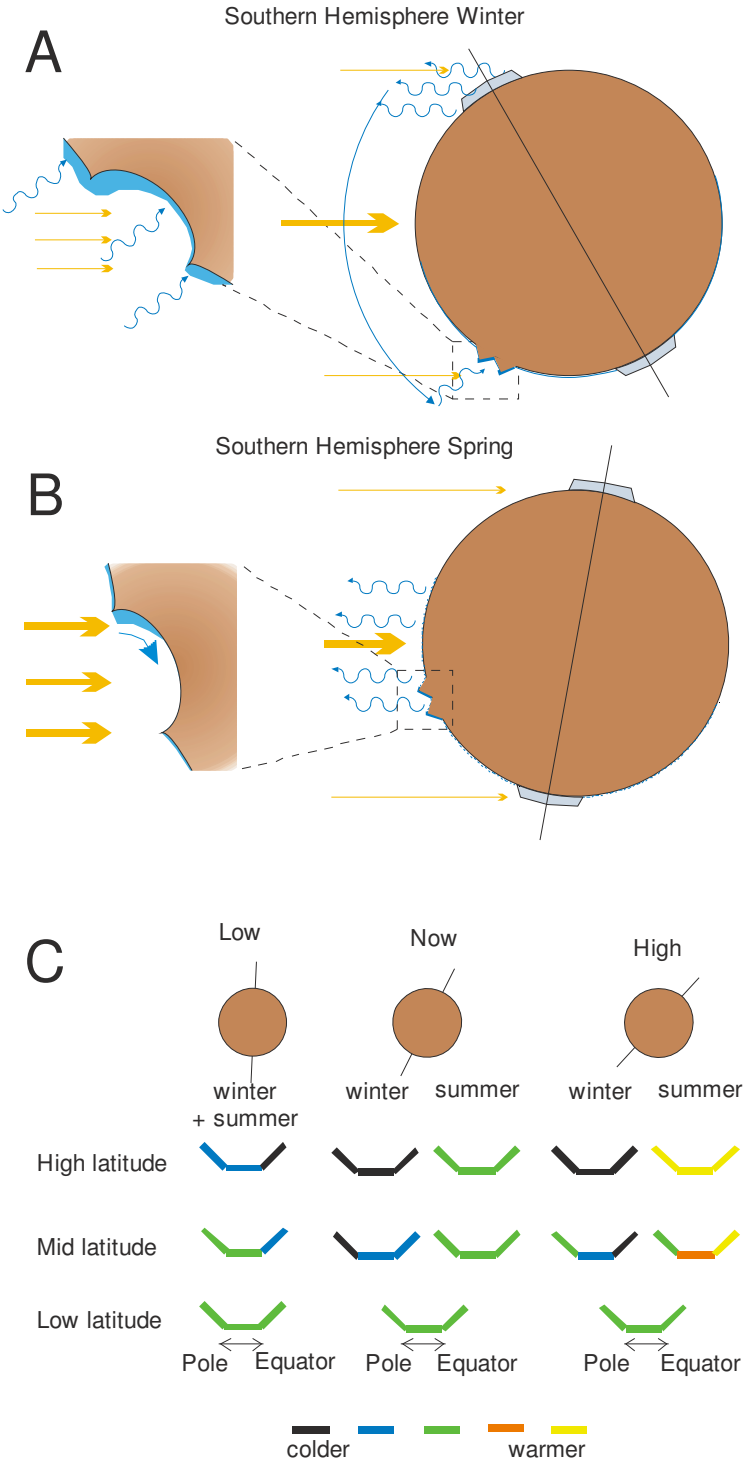

Figure 2-4. Effect of different obliquity on volatiles within craters at different latitudes. (A) and (B) at 30° obliquity, there is a greater column of precipitable water, sourced from the seasonal sublimation of the polar caps and the ice-rich subsurface. (A) Winter solstice in the southern hemisphere - water is sublimating from the north polar cap and diffusing out from pores in the subsurface in the northern hemisphere. This builds up the atmospheric water column. Water and CO_2 ice accumulate in both the southern mid-latitudes and the south cap, which are shaded and cold. Pole-facing slopes are coldest, so more water ice accumulates. (B) In late southern spring, the ground in the southern hemisphere warms up and water diffuses/sublimates into the atmosphere. Pole-facing slopes maintain a CO_2 frost that maintains a low temperature, preventing the water sublimating. Sudden, intense insolation removes this frost, the slope warms suddenly and water may be released. (C) Schematic diagram taken from Kreslavsky at al. (2008) showing the temperatures of slopes in summer and winter with three different obliquities. The coldest winters and warmest summers are experienced by pole-facing slopes in the mid-latitudes at high obliquities, and are ideal conditions for water generation from melt.

2.4.2. Aquifer Model

2.4.2.1. Deep Aquifer Mechanism

The cryosphere model of gully formation (Gaidos, 2001) is based on a global cryosphere model (Clifford and Parker, 2001) and invokes a deep (several kilometres) source for the water. The water is ponded in confined aquifers at intermediate or deep levels within the cryosphere. Changes in the geothermal structure mean that a freezing front impinges on these liquid aquifers, over-pressuring them and forming liquid water "dikes". These dikes can spread laterally as sills on reaching an impediment and eventually will reach the surface. The surface conditions then determine where the liquid water will be able to flow. On equator-facing slopes the top of the regolith will be desiccated and the water will evaporate, however shaded pole-facing slopes allow the water to flow.

2.4.2.2. Shallow Confined Aquifer Mechanism

A shallow aquifer model (Figure 2-5) was initially suggested when the gullies were first discovered (Malin and Edgett, 2000) and has been expanded since (Hartmann, 2001; Mellon and Phillips, 2001). In this model a subsurface aquifer is confined by either ice, or impermeable rock strata. The aquifer body intersects with the surface on slopes, and an ice-plug is formed. On cold (pole-facing) slopes the plug freezes back into the aquifer causing overpressure. On equator-facing slopes the water evaporates and a large plug cannot be built up. The plug is important because as it grows it overpressures the aquifer, causing ice in the plug to fail and release water onto the surface to form a gully. Hartmann (2001) suggests that the aquifers originate from sub-surface ice being melted by geothermal fluctuations and Mellon and Phillips (2001) suggest water is able to persist in these aquifers due to the natural geothermal gradient. These models rely on assumptions about the subsurface structure and composition of not only the first few hundreds of metres of the martian crust, but also the deep structure responsible for the planet's heat flow, or

geothermal gradient. All of these are very poorly constrained and are unlikely to be better understood in the near future.

Another shallow aquifer model invokes stratification caused by a regolith saturated by a eutectic brine (Knauth and Burt, 2002). A eutectic brine is one in which two salts are mixed in proportions such that the freezing point depression is maximised. In this case a eutectic brine "aquifer" is confined between frozen ice on top and salts beneath, both sourced from the brine body.

These models all require significant quantities of long-lived liquid water or to be present in the near subsurface. Mellon and Phillips (2001) suggest that water evaporated from a deep cryosphere migrates upwards through the porous regolith and is re-condensed near the surface. They also suggest the water could come from ground-ice or permafrost situated at latitudes higher than 30°.

2.4.2.3. Shallow Unconfined Aquifer Mechanism

In this model, near-surface ground-ice melts and percolates downwards through the regolith to form an unconfined aquifer on top of an impermeable or semi-permeable layer (Gilmore and Phillips, 2002). If these layers dip towards and intersect a pole-facing slope then the water exits, producing gullies.

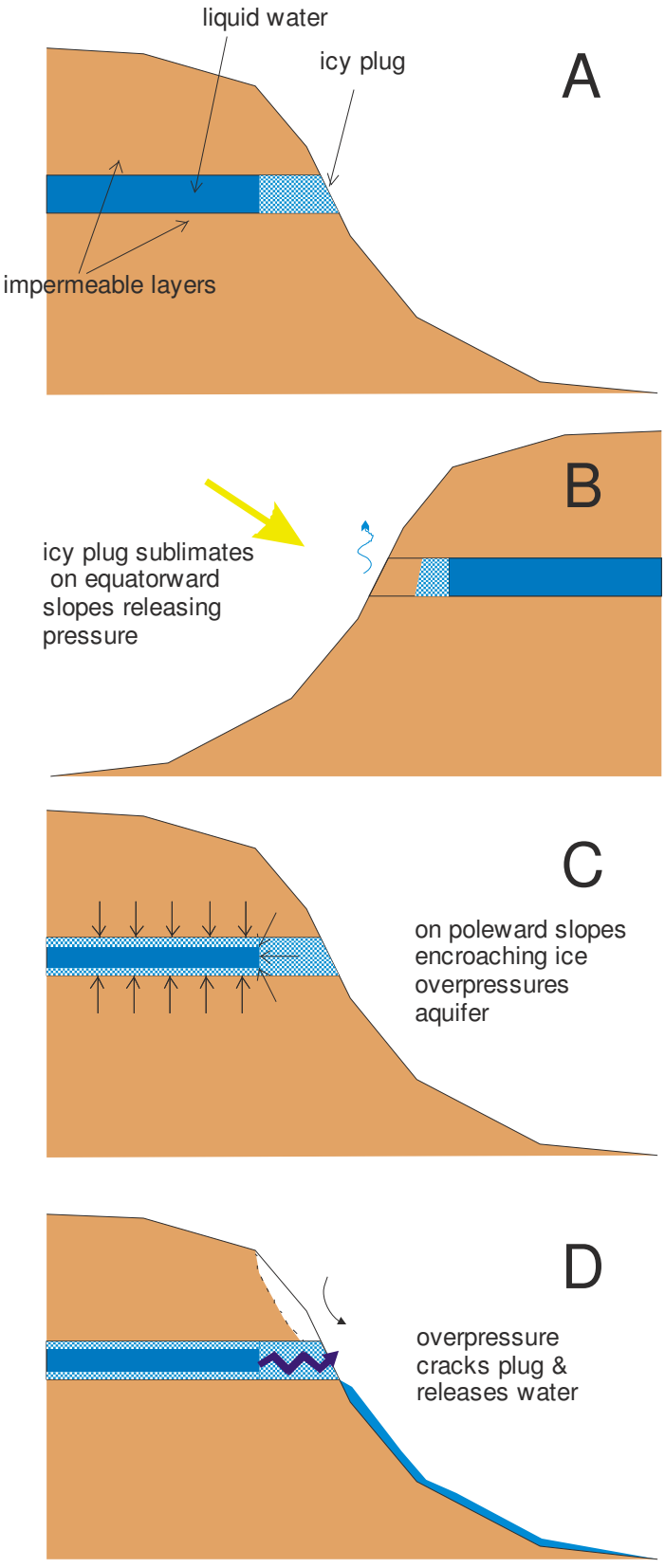

Figure 2-5. Aquifer model of gully formation. (A) An aquifer is formed between impermeable layers of rock/ice and a plug forms where the aquifer intersects the surface, e.g. in an impact crater. (B) On equator-facing slopes the icy plug sublimates and the water does not get released. (C) On pole-facing slopes the advancing freezing front overpressures the aquifer. (D) The internal pressure cracks the ice and releases water onto the surface; this causes the material above to collapse and forms a gully. Note: this model can be applicable to all of the aquifer models.

2.4.3. The role of brines, or other dissolved compounds

Based on the assumption that stable water is required to form gullies, several authors have suggested the presence of brines to stabilise water at the surface (e.g. Wynn-Williams et al., 2001; Knauth and Burt, 2002; Marchant and Head, 2007). Although no specific model is associated with the formation of brines (or other dissolved phases), their production is more likely in an aquifer setting. This is because more time is allowed for the phase to dissolve. Water ice accumulated from the atmosphere would be free of any salts. However, this does not preclude the formation of brines, or other more exotic fluids by water running over the surface once melted. Surface dissolution is particularly relevant for perchlorate salts, that have recently been discovered at the Phoenix landing site (Catling et al., 2009; Hecht et al., 2009). Chlorine signatures at other landing sites in the southern hemisphere have also been linked to perchlorates hinting at a more global distribution (Zorzano et al., 2009).

The availability of these compounds on Mars, and more specifically at all the sites of gully formation, is the major limiting factor in the viability of these compounds as candidates for depressing the freezing temperature of water. Suggested compounds in addition to perchlorates have included: Calcium Chloride (Knauth and Burt, 2002), Sodium Chloride (Sears et al., 2002), and Ferric Sulphate (Chevrier and Altheide, 2008) brines; organics (Jean et al., 2008) and acids (Benison et al., 2008).

2.5. Remote sensing observations of gullies

The majority of the studies relating to gullies on Mars include remotely sensed data, usually but not exclusively, in the form of image data. Table 2-1 summarises the instruments, resolution and data-types used in the studies described in this section. Figure 2-6 shows the locations of primarily remote sensing studies that have been published to date and are detailed further below. Any model of gully formation must provide a

satisfactory explanation for all the observations and here I critically compare the results of these studies with the models described above in Sections 2.3 and 2.4.

Table 2-1. Summary of instruments used in published studies of gullies on Mars.

Spacecraft	Instrument	Abbreviation	Horizontal Resolution (m/pix)	Datatypes	Dates of Operation
Viking Orbiters (1&2)			8-300	Visual monochrome	1976-1980
Mars Global Surveyor (MGS)	Mars Orbiter Camera Wide Angle	MOC-NA	1.4-12	Visual monochrome	1997-2005
	Mars Orbiter Camera Narrow Angle	MOC-WA	240-7500	Visual 3 band	1997-2005
	Mars Orbiter Laser Altimeter	MOLA	500-1000 (interpolated)	Elevation	1997-2001
Mars Odyssey	Thermal Emission Imaging System	THEMIS	100 (IR), 19 (VIS)	5 visible, 10 IR	2002-
Mars Express (MEX)	Observatoire pour la Mineralogie, l'Eau, les Glaces, et l'Activite	OMEGA	300-4000	Spectrometer (IR)	2003-
	High Resolution Stereo Camera	HRSC	2-12	Visual 3 bands	2003-
Mars Reconnaissance Orbiter (MRO)	High Resolution Science Imaging Experiment	HiRISE	0.25-0.50	Visual 3 bands	2006-
	Context Camera	CTX	6	Visual monochrome	2006-
	Compact Reconnaissance Imaging Spectrometer for Mars	CRISM	100-200	Spectrometer (IR)	2006-
	Shallow Radar	ShaRAD	100m depth (10m resolution vertically), track width 3-7km, along track 300-1000m	Radar	2006-

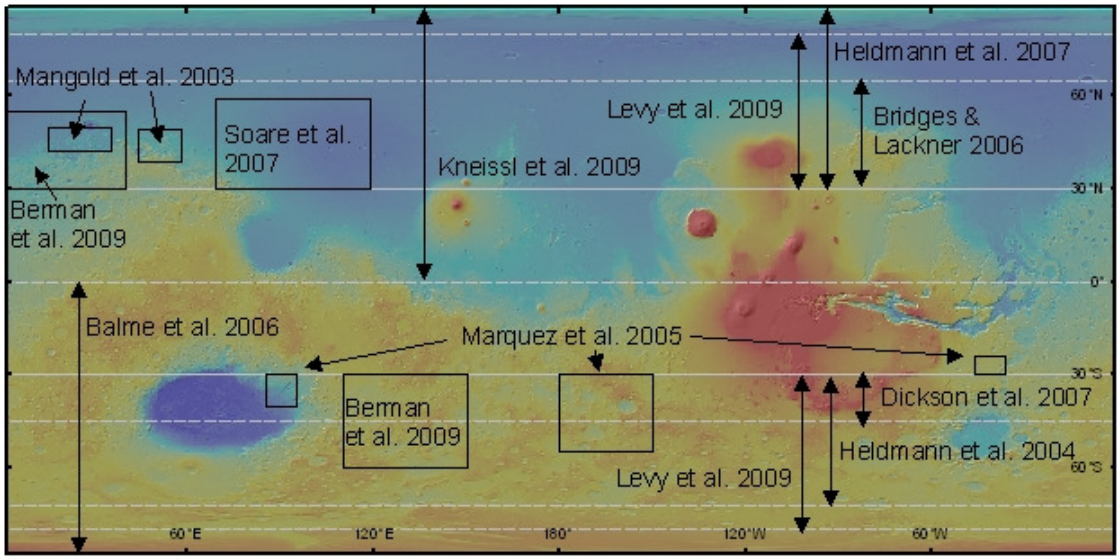

Figure 2-6. Geographical extent of remote sensing studies of gullies on Mars. Vertical double-ended arrows indicate that a study was carried out with latitudinal extents.

2.5.1. Distribution, orientation and co-location

Numerous studies have shown that gullies are much more common in the southern hemisphere than in the northern hemisphere of Mars (e.g. Malin and Edgett, 2000; Heldmann and Mellon, 2004; Heldmann et al., 2007). It is generally agreed that the reason for this is the lack of steep slopes in the northern hemisphere (Kreslavsky and Head, 2000), which are thought to be necessary to form gullies. Gullies are generally located between 30° and 40° in both hemispheres, the primary exception being those located in the south polar pits (~70°S).

Regional scale studies conclude that gullies generally have a pole-facing preference in both hemispheres, independent of the datasets used (Balme et al., 2006; Dickson et al., 2007; Kneissl et al., 2009). If broken down by latitude, this preference is more marked at lower latitudes (30-40°) and vanishes almost entirely at higher latitude, where gullies show either no preference, or equatorward preference depending on the study (Heldmann and Mellon, 2004; Berman et al., 2005; Balme et al., 2006). The polar pits have a pole-facing preference (Heldmann and Mellon, 2004). This general pattern was not observed in the northern hemisphere by Bridges and Lackner (2006), nor Heldmann et al. (2007). However, a more recent survey by Kneissl et al. (2009) including more gullies and HRSC as well as MOC images, concluded the distribution of aspect with latitude was the same as found for the southern hemisphere (with a definite equator-facing preference at higher latitudes).

A regional study of the height of alcoves by Marquez et al. (2005) showed that gullies were oriented in the same direction as the down-dip direction of the regional slope. They linked this to a groundwater source for these gullies. However, this pattern could equally have been generated by insolation-driven melting.

It has been recognised that gullies often co-occur with other features associated with glacial (Berman et al., 2009), or periglacial activity (Levy et al., 2009b), or with

mantle terrain (Christensen, 2003; Bridges and Lackner, 2006). Landform assemblages such as these hint at a possible genetic relationship between gullies and these water/ice related features.

The location of gullies on steep slopes is consistent with formation by dry mass wasting; however orientation and latitude observations are not. On Earth the rate of debris production is controlled by the intensity of the diurnal thermal cycling, which then controls mass wasting (Matsuoka and Sakai, 1999; McFadden et al., 2005; Sumner et al., 2007; Regmi and Watanabe, 2009). Most slopes on Mars experience, or have experienced in the recent past, this intense cycling and hence dry mass wasting should occur on most steep slopes practically independently of latitude and orientation. The gullies' latitude and orientation patterns and their co-location with periglacial and glacial landforms strongly suggest a climatic influence. Both the dry CO_2 model and the surface melting model require the atmospheric accumulation and then sublimation, or melting of a volatile compound. The aquifer model requires intense cooling to pressurise the aquifer causing fracturing to release water. In some versions of the aquifer model the accumulation is controlled in the subsurface, so is not climate dependent. However, in other aquifer models (e.g. Mellon and Phillips, 2001) it is controlled by the distribution of ground ice, and thus the accumulation relies on climate as well. The requirement for accumulation-then-melting results in different latitude and orientation patterns to the intense-cooling-only requirement (Figure 2-4).

The observations support the surface melting model and the dry CO_2 model, whereby it is only those slopes that receive cold winters and then very warm summers that host gullies. Although the ground-ice sourced aquifer model has similar constraints there is one major difference: gullies located at high latitude should have no orientation preference, as ground ice is located everywhere at that latitude. Most studies find that the orientation of gullies at high latitudes is biased, rather than neutral. The aquifer models where the water

has a deep source are not supported by the observations, because gullies do not occur at low latitudes.

The latitude-dependence of the gully-aspect distribution is strong evidence for a climatic influence on gullies, where insolation is one of the main controls. As discussed above this does not provide good discrimination between some of the proposed models, as the accumulation and subsequent melting, or sublimation of icy-plugs/surface ice/CO_2 are all dependent on climatic cycles.

2.5.2. Setting and Morphology

It has been noted that gullies occur in many geological settings: south polar pits, hills, crater inner walls, crater outer walls, central peaks, dunes and valleys (e.g. Malin and Edgett, 2000; Balme et al., 2006). Although the morphology varies widely (Figure 2-7), there is no distinct difference between different settings with respect to their aspect and latitude distribution (Balme et al., 2006). Gullies are found across all elevations on Mars, but are notably absent within their general latitudinal distribution from the Tharsis bulge and the Hellas basin (Heldmann and Mellon, 2004; Dickson et al., 2007; Heldmann et al., 2007). Gilmore and Phillips (2002) initially reported the co-location of gully alcoves with outcropping bedrock layers. However, this observation has not been supported by later studies and in cases where it was first reported higher resolution images highlights in many cases that the water flows originate above the bedrock layer and flow over it (Dickson and Head, 2009). Treiman (2005) and others have noted that the geological structure of impact craters, which host the majority of gullies, is not a logical location for an aquiclude, because: (1) bedrock layers after impact tend to dip away from the crater, and (2) bedrock becomes shattered after impact (although there is the possibility of melt lenses).

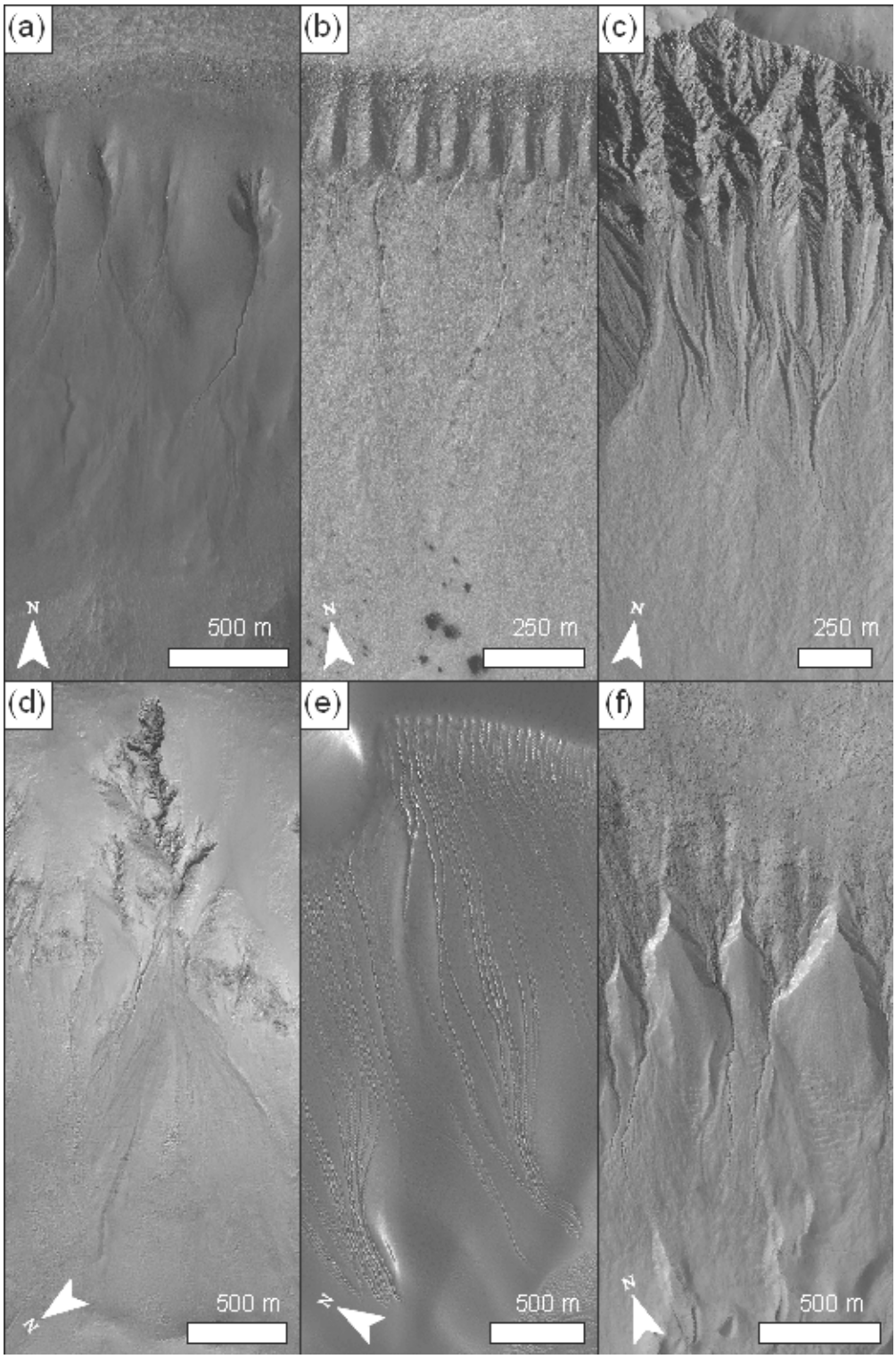

Figure 2-7. Example of gully morphologies on Mars in HiRISE data. Image credits: NASA/JPL/UofA. (a) Gullies on the wall of a small impact crater within Kaiser crater, site H in this study, image number: PSP_003418_1335. (b) gullies within a polar pit, image number: PSP_003498_1090. (c) Gullies on the wall of an Galap crater, near Sirenum Fossae, image number: PSP_003939_1420 (d) Gullies on the wall of Wirtz crater, a large impact crater to the east of Argyre basin, image number: PSP_002457_1310 (e) Gullies on the slip face of dunes in Russell Crater, located in Noachis Terra, image number: PSP_001440_1255 (f) Gullies on the wall of an impact crater to the west of Newton Crater in Terra Sirenum, image number: PSP_005930_1395.

The neighbouring Hale and Bond craters were studied by Reiss et al. (2009) because the presence of gullies in Hale but not Bond was used as evidence against a surface melting source. However, important differences exist between the craters that counteract this argument, namely that Hale possesses steeper slopes, and thermal inertia data suggest a greater abundance of fine grained material in Hale, but more consolidated material in Bond.

The lengths, volumes and depths of alcoves found by various workers is summarised in Table 2-2. There is generally agreement between different surveys on the various spatial dimensions of gullies on Mars. Slopes have been measured from MOLA spot heights, so are likely to be much higher, as noted by Dickson and Head (2009).

Table 2-2. Summary of published morphological measurements of gullies on Mars. Many of the values are estimated from figures. * indicates that the aggregate values in the table were calculated from average values.

	Bridges, et al. (2006)			**Heldmann and Mellon (2004)**			**Heldmann et al. (2007)**			**Soare, et al. (2007)***			**Dickson et al. (2007)**		
	min.	mean	max.	min.	mean	max.	min.	mean	max.	min.	mean	max.	min.	mean	max.
Number of gullies.	249			~ 202			~ 182			164			3154		
stream order	1	3	6												
elevation above Mars datum (m)				-5000		2000	-5400		800				-5177		3089
depth to top of alcove (m)				0	150	990									
depth to alcove base (m)				0	600	990	100	350	550						
alcove length (m)				50	500	2300	100	500	1600	63	366	690			
channel length (m)	50	700	2900	20	500	3200	200	700	2700	106	591	1723			
debris apron length (m)				20	600	1600	100	400	950	141	388	735			
position in slope (1-bottom, 0-top)				0.1	0.2	0.85									
alcove slope (m/m)				0.5	0.3	0.9	0.25	0.5	0.85				0.16	0.5	0.87
debris apron width (m)										50	230	787			
channel width (m)										8	67	184			
alcove width (m)										28	240	574			
total length (m)										381	134	2952			

The following attributes have been commonly observed in association with gullies: channels that narrow downslope (Hartmann et al., 2003), v-shaped channels, digitate deposits (Dickson and Head, 2009), sometimes high sinuosity (Arfstrom and Hartmann, 2005), tributary systems (Malin and Edgett, 2000), terraced cutbacks and longitudinal bars (Schon and Head, 2009), levees (Hugenholtz, 2008; Lanza et al., 2010), and distributary and braided systems (McEwen et al., 2007). It is not uncommon that all or a large proportion of these features are observed in the same well developed gully systems. Bridges and Lackner (2006) and Heldmann et al. (2007) noted that gullies in the northern hemisphere are more degraded-looking than those in the south.

Early work concluded that the debris aprons of gullies are free from boulders (Treiman, 2003), however although this is often the case, recent work has disproved this as a universal property of gullies (McEwen et al., 2007).

Grainflow (either dry, or CO_2 mediated) is inconsistent with many of the morphological observations, including v-shaped channels, terraces, sinuous channels, tributary systems and divergent flow sections. Grainflow normally results in a straight broad central channel and flanking levees (e.g. Shinbrot et al., 2004).

The geological setting of gullies is consistent with formation by surface melting and by dry failure. However, gullies found on isolated hills, dunes and mesas, and gullies where the flow starts at the crest of the slope, are inconsistent with the aquifer model. Nor are gullies systematically observed in conjunction with aquicludes or competent rock layers, as predicted by the aquifer model.

The observed morphological attributes of gullies cannot differentiate between aquifer and surface models. However, morphology provides clues as to process, and both debris flow and water flow are consistent with the observations. The availability of plenty of unconsolidated material at the surface of Mars has lead many workers to cite debris flow

as the most likely process. Dry mass wasting is consistent with some, but not all, of the observed attributes of gullies and can be implicated in some, but not all, cases.

2.5.3. Composition Observations

There have been limited composition observations to date on gullies due to the poor resolution of OMEGA data and the "noisy" nature of CRISM data. Fan et al. (2009) investigated the relative water content of four gully sites compared to their surrounding areas and found that the gully sites had elevated water contents by using statistical analysis of OMEGA data. Dickson and Head (2009) used colour HiRISE to identify the seasonal accumulation of frost in the alcoves and channels of two gully systems and in one case they used CRISM to confirm its composition as water ice. Initial results using CRISM to examine the composition of the materials in and around gullies (Barnouin-Jha et al., 2008) has suggested that: (1) gullies are hosted on a wide range of geological materials, (2) in some cases gullies expose underlying rock and move it downslope, (3) many other gullies show no spectral difference from their surroundings and (4) there is no evidence for hydrated minerals even in the new light-toned deposits near gullies. Heldmann et al. (2009) used CRISM data and also confirmed that recent light-toned deposits in Penticton Crater have no spectral differences to surrounding material.

Carrozzo et al. (2009) observe from OMEGA data that low latitude ice condensation occurs preferentially on shadowed (i.e. pole-facing at the present day) slopes between 30°S and 30°N. Kuzmin et al. (2009) used TES thermal inertia data to map water ice at the surface and report widespread water ice condensation on the surface occurring in winter between 50°S and 50°N, with the greatest concentration of water ice being above 30°, especially in the northern hemisphere.

The lack of systematic observations of hydrated or brine spectral signals in gullies does not mean these materials are absent. A surface coating of millimetres of dust can easily obscure a spectral signal and such dust is pervasive on Mars. The observed seasonal

accumulation of water ice, and its preferential accumulation inside alcoves and channels shows that these environments form suitable cold traps. This provides credibility to the surface melting model as it shows accumulation is possible, even under present climate. However, just because it is possible does not mean that the process has in fact occurred. Therefore these observations do not completely rule out any of the models.

2.5.4. Recent Activity

Recent activity has been detected in some of the gullies on Mars in the form of the appearance of "light-toned" deposits between subsequent MOC and/or the High Resolution Science Imaging Experiment (HiRISE) images (Malin et al., 2006). However, not only is the formation process for these new deposits under debate, but also whether these deposits are primary or secondary to the gully forming process. They have persisted over several martian seasons and form digitate deposits in the distal half of some gully systems. There is no central channel defined by these deposits and they seem to overtop some obstacles and divert around others. The persistent visibility of these deposits argues against the high albedo being a result of volatile content, but suggests that it could either be an influence of salts, or simply an exposure of fresh material to the martian atmosphere.

2.6. Numerical modelling studies relevant to gullies

Numerical models have helped to build and limit ideas on gully formation. However, all numerical models must have well-observed parameters as constraints to make them useful. In the following sections I split the numerical models into broad categories and assess their assumptions. In Section 2.6.6 I summarise the combined implications of the numerical modelling on proposed gully formation mechanisms.

2.6.1. Global Circulation Models (GCMs)

Global Circulation Models (GCMs) of Mars can be used to predict, amongst other things, the surface temperature and pressure, precipitable water and CO_2 concentration of the

atmosphere. They have been widely used to simulate present as well as past climate conditions on Mars. These models are well constrained for present climate, as they can be validated extensively using satellite and ground based observations. However, when considering past climate these models are poorly constrained, as detailed further below. In the study of gullies GCMs have been used to determine where ice, water and CO_2 can be stable, and where such accumulations can melt, as discussed further below.

When considering present day climate, GCMs predict favourable zones for the production of liquid water which do not correlate well with the distribution of martian gullies (Haberle et al., 2001). However as noted by these authors, freezing point depression (for example by brines) would significantly expand these favourable regions to overlap with the observed distribution. Haberle et al. (2001) also noted that the surface pressures today are very low almost everywhere, which means that water should evaporate and sublimate very quickly if near the surface.

The surface melting model of Costard et al (2002) is based on results from incorporating slope into a one dimensional GCM and predicts melting (>0°C temperatures) on pole-facing slopes at ~ 40° latitudes and melting on any orientation of slopes at ~70° latitudes, but only at high obliquity. High obliquity results in a higher average amount of precipitable water, with estimates as large as ~1000 precipitable micrometers (Mellon and Jakosky, 1995), and 20-80 precipitable micrometers (Mischna and Richardson, 2005). Mellon and Jakosky (1995) suggested that as a result, water ice would accumulate in the top metres of regolith, but the results of Mischna and Richardson (2005) suggest this accumulation is more limited. Haberle et al. (2003) found that at high obliquity, despite the favourable thermal conditions, the surface pressures are lower than today, which means water would evaporate or sublimate quickly. These apparently conflicting findings can be explained by the inherent uncertainties in projecting GCMs into the past where the constraints are poorly known. Kreslavsky et al. (2008) identified the two most important

unknowns: (1) there are no good constraints on how much additional CO_2 would be available at high obliquity and (2) it is not known if increased CO_2 would lead to run-away greenhouse or icehouse planet conditions. These uncertainties are due to the fact that the amount of CO_2 in the present-day polar caps is also not known and neither is its potential for redistribution (i.e. how easily it can be released and by what processes).

Kreslavsky et al. (2008) took the approach of considering insolation only, with the justification that at low atmospheric pressure insolation is the main driver of surface temperature. Insolation alone can be more readily calculated than a full GCM. They found that, with increasing obliquity, the insolation maximum moves towards the poles and gets larger in amplitude (with the equatorial regions reasonably steady). In addition they found that seasonal and slope orientation differences are minor unless the obliquity is very high (>35°), under which circumstances pole-facing slopes in the mid-latitudes and all slopes at high latitudes receive the greatest insolation (Figure 2-4). The greatest omission from this model is surface albedo, which the authors estimated could have ± 20 °C influence on the day-average temperatures by using the GCM of Forget et al. (1999).

The models considered so far have been concerned only with producing conditions favourable for melting of surface ice, rather than its accumulation. Mischna et al. (2003) considered the accumulation of water ice under different obliquities. Their results show that, with increasing obliquity, surface ice accumulation moves from the poles towards the low latitudes. Under extreme obliquity ice is stable at the mid-latitudes only, particularly in those areas with elevated topography and/or high thermal inertia. They predict maximum surface ice thicknesses of ~ 5 cm. Their predicted spatial distribution of surface ice and its changes with obliquity are in general agreement with those predicted for ground ice by Mellon and Jakosky (1995). However the results of Mischna et al. (2003) suggest that a thin layer of ice is condensed at the surface rather than very thick ice (metres) at 5-10 cm depth as predicted by Mellon and Jakosky (1995).

There is one final assumption that all these models make: they all assume predictable variations in Mars' past orbital spin parameters. There are three interacting orbital parameters: eccentricity, obliquity and position of the perihelion (precession). Together with latitude, slope orientation and season, these three parameters control the insolation received at given point on the surface of a planet, and hence control the global climate. Each has a quasi-periodic oscillation. However, due to the difficulties in calculating the solar system dynamics the variations in these parameters on Mars cannot reliably be extended further back than 10-20 Ma if a single solution is needed or 250 Ma if multiple solutions are acceptable (Laskar and Robutel, 1993; Laskar et al., 2004). Calculations by Laskar et al. (2004) suggest that present obliquity is lower than average and that Mars obliquity has ranged from 0° to 65° and in the past 20 Ma.

Results from GCMs suggest that the accumulation and melting of water required to form gullies by the surface melting model is not occurring at the present day. This modelling suggests that if gullies are forming contemporaneously, then an underground source would be more likely. However, GCMs highlight particular past climate conditions that would be favourable for the formation of gullies via the surface melting model.

2.6.2. Longevity of ice and water

Williams et al. (2008) and Williams et al. (2009) modelled the longevity of a snowpack on the surface of Mars. Their model includes heat, radiation and mass transfer equations. The surface ice parameters used in their model area are summarised in Figure 2-8. Williams et al. (2008) used the model to perform the following experiments: (1) testing the long-term longevity of a snowpack and (2) testing the potential for generating meltwater. They calculated that the longest lifetime of a snowpack under optimal conditions at high obliquity is 9 seasons, which could only be exceeded if the precipitable water was much higher than the predicted values of Mischna and Richardson (2005), or even Mellon and Jakosky (1995). They find melting, rather than sublimation, occurs only when the

snowpack is less than 10 cm thick, and the maximum meltwater generated is about 1.4 l/m^2. Williams et al. (2009) used the same model to: (1) assess the potential for seasonal melting of a thin snowpack as predicted by the GCM of Mischna et al. (2003) at high obliquity, and (2) to determine the distribution and thickness of warm soils at high obliquity. They found that the regions expected from their modelling to have snowmelt runoff match the observed distribution of gullies. In these areas they estimate melting to penetrate > 1 mm in depth (equivalent to 0.25 mm/h of rainfall) and these areas have > 1 cm depth of warm soil. Williams et al. (2007) used the same model to estimate the lifetime of the new light-toned deposits, supposing they were composed of water ice. They found that the maximum lifetime would be 1-2 years if they contained moderate amounts of dust. This model relies on the accurate parameterisation of the radiative balance and inherently on the accuracy of the GCMs for predicting the input parameters, which possess significant uncertainties for past epochs.

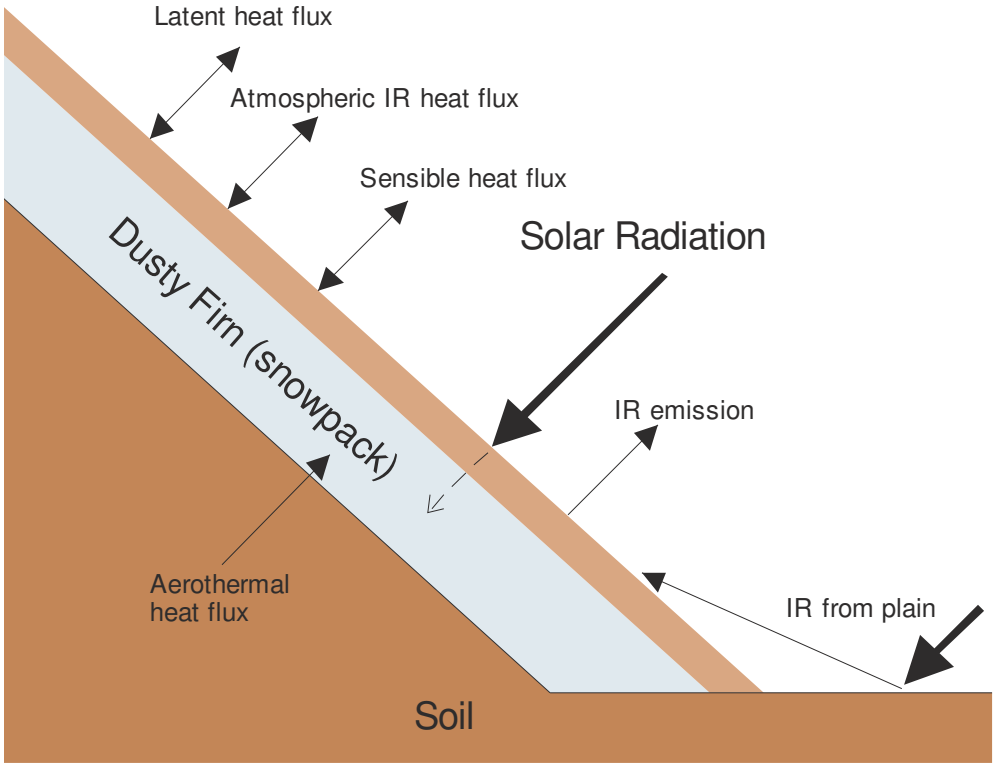

Figure 2-8. Radiation balance model of Williams et al. (2008).

Hecht (2002) modelled the stability of water on present day Mars by considering a simple heat balance model, where inputs from insolation and geothermal heat are balanced by conduction, convection, radiation and evaporation within the water body. Within this context Hecht (2002) found that the geometry of the slope has a very important effect on the results. He found that melting is promoted where the water is subject to normal incident insolation, the albedo is low, and the geometry of the slope protects the water from radiation to the cold sky. These conditions can be met on a large majority of slopes on present-day Mars. Hence, accumulation of ice is the limiting factor and Hecht (2002) suggests accumulation could occur within cold-traps in sheltered locations at high latitudes. The water once generated would not be thermodynamically stable, and has been termed "metastable" by Hecht (2002). Kossacki and Markiewicz (2004) also considered the stability of water on the surface of present day Mars, but they looked at a full seasonal cycle of both water and CO_2, rather than selecting optimal conditions for water ice (Hecht, 2002). They also used a radiative balance model, but considered radiation within a 10 m wide trough (to represent an alcove, or channel). They included seasonal windspeed, atmospheric pressure, and water content from the GCM of Forget et al. (1999). They found that small amounts of melt can be produced once the protective sheath of CO_2 ice has been sublimated. They estimate a maximum accumulation of ~ 0.6 l/m^2 can be achieved and a maximum of ~ 0.2 l/m^2 meltwater can be generated from it. However, they predicted that larger values of precipitable water (> 10 μm) and higher windspeeds (> 5 m/s) than used in this model would result in more accumulation and thus more meltwater. This is because in their equations the condensation rate of water onto a surface is directly proportional to the windspeed and is strongly dependent on the value of precipitable water.

Aharonson and Schorghofer (2006) used MOLA data to extrapolate global roughness down to the metre-scale and combined this with a thermal model defining how subsurface ice depends on slope to produce a predictive map of location of ground ice at

the present day. Their results indicate ground ice can be stable to latitudes as low as 25º, but never at the equator, which significantly expands the zone of stability from that predicted by the GCMs.

Mellon and Phillips (2001) also examined the possibility of melting water under present and past conditions on Mars, and their focus was ground ice or permafrost. They considered two scenarios: (1) potential for melting ground ice by solar heating and (2) the melting and freeing of water at shallow depths by geothermal heating. Using their radiative balance model they found that ground ice sublimates rather than melts for a comprehensive range of obliquities, latitudes, surface slopes, and soil properties. This is due to the dry atmosphere, but can be counteracted by the lowering of the freezing point of water (e.g. by brines). However, their radiative balance model did not include the influence of the geometry of the local topography, unlike Hecht (2002) and Kossacki and Markiewicz (2004).

Considering subsurface water and ice, Mellon and Phillips (2001) find that water can be stable within the first few hundred metres beneath the surface with a normal geothermal gradient, but only if low thermal conductivity regolith lies above. They hypothesise that an advancing freezing front from the surface causes over-pressurisation of this shallow aquifer which then cracks the confining ice, releasing the water. They estimate that the pressure induced by approximately two million years of obliquity cycles is sufficient to produce periodic breaching. They surmise that an aquifer with an areal extent of < 1 km^2 would produce sufficient flow to form gullies (~ 2500 m^3 of water flow). There are a large number of assumptions about the subsurface in this model: the presence of suitable aquicludes at the correct depth, the presence of a thick layer of unsaturated unconsolidated soil in the top hundred metres of the surface and the assumption of the geothermal gradient, which depends on the heat flux, crustal thickness, composition and structure. These are all poorly constrained and not easy to test.

Gaidos (2001) used several numerical models to complete his theory of cryovolcanism as a formation mechanism for gullies. He hypothesised that the cryosphere has an impermeable basement with the geothermal heat flow determining the level of stability. Aquifers will freeze from the top down and create confining pressure. These calculations have many uncertainties including the structure and thickness of the crust, which affects heat flow and the potential to form an aquifer. The resulting eruption is completed in an analogous way to dike propagation on Earth, with crack propagation followed by flow due to buoyancy. Surface expression will depend on surface properties: for example, on a sunny slope the water would evaporate, whereas on a shaded slope the water may form a gully. Gaidos (2001) performs these calculations with realistic values for rock strength, porosity, geothermal flux, etc, but there is no sensitivity analysis on these values that would make his model more applicable.

This modelling suggests that both the aquifer model and surface melting models are plausible mechanisms. However the aquifer model does require more assumptions, especially about the subsurface, which are poorly constrained. Although this does not rule out this model it means that more observations are required to validate it. Models also indicate that the quantities of meltwater produced by surface melting could be low, and that it is unlikely that a surface ice body (even covered with dust) could survive between obliquity cycles. Modelling of local conditions also highlights that regions of accumulation and potential melting predicted by GCMs can be extended, both at the present day and in the past. A climatic origin for gullies, in which seasonal meltwater is produced, seems to be the primary candidate from the suite of surface melting models.

2.6.3. Longevity of CO_2

Stewart and Nimmo (2002) examined the possibility of generating liquid CO_2 on the martian surface and found that it is even less plausible than producing liquid water. The production of CO_2 liquid requires pressures exceeding 5 bar and temperatures exceeding

220 K (Figure 2-3). Liquid reservoirs could be maintained at depth, where the pressure and temperature are higher. However, this depends upon the accumulation of either solid or liquid CO_2 at depth. Through thermodynamic stability considerations Stewart and Nimmo (2002) and Heldmann and Mellon (2004) found that it was not possible to deposit a large thickness of CO_2 at depth. Solid CO_2 can only accumulate under high atmospheric pressure. Using the balance of the geothermal and insolation fluxes Stewart and Nimmo (2002) calculate that once atmospheric pressure drops, the CO_2 would sublimate rapidly, as quickly as 7 m/yr. They also calculate that the diffusion rate of CO_2 gas (which is temperature dependent) would be too slow to locally increase pore pressures and trigger a density flow. In summary, flow generation by a CO_2 mediated mechanism seems an unlikely formation mechanism for gullies.

2.6.4. Modelling the dynamics of gullies

Heldmann et al. (2005) used the geometry of gullies on Mars to estimate likely flow rates. They assumed turbulent, clear water flow with flow depths of 0.15-1.0 m, channel roughness on the order of a metre and an assumed average channel gradient of 18°. This modelling gave flow rates in the order of 30 m^3/s, assuming a channel width of 10 m. Without considering fluid loss the authors obtained flow runout distances of the order of tens of kilometres. To make their results more consistent with the observed channel geometry Heldmann et al. (2005) included a fluid loss parameter. This included terms for evaporation rate and freezing rate, but not infiltration. They found that the flow speed was reduced by including this fluid loss parameter and surmised that the water that forms gullies must be unstable, otherwise gully channels would be longer.

Hart et al. (2009) also used gully channel geometry to calculate discharge from gullies at Lyot crater. They used two methods: the first was based on width-averaged flow velocity, including flow depth, local slope, and an empirical friction factor (calculated from mean grainsize); the second was based on the use of an empirical relationship relating

wave-number of channel meanders to alluvial discharge. They found discharges ranging from 0.75-83 m^3/s. Parsons and Nimmo (2009) used the same two equations on gullies on interior crater slopes between Pickering and Newton Craters in Terra Sirenum, and calculated discharges from 0.5-10.6 m^3/s. They also estimated the erosion and deposition of these flows using a 1D model and concluded that the entire morphology of gullies could be formed on very short timescales. They concluded that the discharge required could be accommodated easily by an aquifer and would be consistent with the gully spacing.

These works (Heldmann et al., 2005; Hart et al., 2009; Parsons and Nimmo, 2009) have assumed that the gullies form via bankfull discharge. However, this is not a necessary condition, for bankfull discharge is rarely achieved in river systems on Earth, nor in mature gully systems (Torri et al., 2006). The equations they used to determine the flow regime are also more appropriate to lowland rivers rather than upland streams (potentially more analogous to gullies on Mars). These calculations certainly do not apply if the gullies are dominantly formed by debris flow, rather than pure water flow.

Miyamoto et al. (2004) performed modelling focused on the genesis of the unusual gullies located on dunes in Russell Crater (Figure 2-7e). They modelled the formation of these gullies as a Bingham plastic fluid (i.e. debris flow) over a range of parameters. The parameters that produced the best fit to the observed lengths and widths of the gullies are: viscosity 10^2 Pas, yield strength 10^2 Pa, and a flow rate of 0.5 m^3/s with a flow duration in the order of minutes (total discharge hundreds of cubic metres). They surmised that sufficient water can be supplied by melting a surface layer of ~ 50 % interstitial ice to centimetres depth.

Chevrier et al. (2009b) used a Bernoulli fluid mechanics model to estimate the flow speed of viscous ferric sulphates on Mars. This model uses an open v-shaped channel of hydraulic radius 4 (flow depth 2.0 m), roughness of 0.1 m and slope 20º. They simulated expected viscosities over the temperature range 200-280 K. Above 242 K the flow is fully

turbulent and the resulting flow speed, 8.1-8.7 m/s (9.3-10 m^3/s), varies little with composition or temperature. Below 242 K the flow passes through a transition zone with maximum flow rate of 14 m/s (16 m^3/s) before reaching the laminar regime of where the flow rate falls off to almost zero at 200 K. They use these flow speeds and viscosities to calculate the maximum boulder size that could be displaced, which is 4 m in the transition regime, 3 m in the turbulent regime, down to 0.5 m in the laminar regime. They conclude that the viscosity required to transport many small (0.5 m) boulders is more likely to be formed by inclusion of sediment rather than hyperconcentrated salts.

Pelletier et al. (2008) used a Bingham model to simulate both dry flow and debris flow. They used a 1 m/pixel resolution digital elevation model from HiRISE stereo (Kirk et al., 2008) and used a commercial flow modelling package FLO-2D to reproduce the new light-toned deposits in Penticton Crater in Eastern Hellas reported by Malin et al. (2006). In the debris flow case they adjusted the fluid loss parameter (implicitly including infiltration, freezing and evaporative losses) until the correct runout was achieved. Their fluid loss parameter was seven times smaller than that used by Heldmann et al. (2005) and they used an initial volume of water of 2500 m^3. In the dry case they considered a uniform grainsize ranging from fine to coarse sand, a variable source size and flow initiation point to generate the required runout. The morphology of the deposit produced in the dry case was more similar to the observed deposit than for the debris flow case. They hypothesised that a dry formation process would be the best explanation for this deposit although the debris flow case was also convincing. There is still intense debate about whether these new deposits are primary or secondary to gully formation. In addition, the gullies on this slope do not have the classic morphology of gullies: they have poorly defined, discontinuous channels and poorly defined source areas (alcoves).

In all these models of gully dynamics the major uncertainties are: the type of flow occurring, the liquid loss parameter, the grainsize of the material involved, and the 3D

surface with which it is interacting. Successful modelling depends on knowing the flow type of the material and having good geometrical constraints.

2.6.5. Geochemical modelling

Geochemical modelling uses thermodynamic considerations to estimate and predict the pressure-temperature stability field of water with various dissolved phases. The principal aim of this type of modelling is to predict the maximum freezing point depression of water given the addition of certain concentrations of other compounds. This then allows extension of the stability field of liquid water into the current temperatures on Mars. Table 2-3 summarises the results of some published models. Geochemical modelling has also been used to trace the evolution of fluids and to make a prediction of the expected mineral precipitates – for example Marion et al. (2008) used the starting point of acid weathering of basalt to predict the observed surface mineralogical assemblages on Mars.

Table 2-3. Summary of published geochemical modelling results.

Author	Compound	Solubility	Resulting freezing point (K)	Viscosity	Viscosity units
Jean et al. (2008)*	Ethylene glycol	infinite	260.5	16.1	cp at 298.15K
	1,3-propylene glycol	infinite	245.4	40.4	cp at 298.15K
	Diethylene glycol	infinite	264.8	30.2	cp at 298.15K
	Triethylene glycol	infinite	266.1	48.5	cp at 298.15K
Marion et al. (2008)	Fe_3Cl	molar concentration 2.5	238		
Chevrier and Altheide (2008)	$Fe_2(SO_4)_3$	48wt%	205		
Chevrier et al (2009b)(experiment)	$Fe_2(SO_4)_3$	38.8-58.2wt%		7.0x10-3 TO 4.6	Pa s at 285.15-260.15K
Chevrier et al (2009a)	Sodium perchlorate $NaClO_4$	52wt%	236		
	Magnesium perchlorate $Mg(ClO_4)_2$	44wt%	206		
Burt and Knauth (2003)	$CaCl_2$		220		

Many compounds cause freezing point depression in water, and an important constraint for the applicability of these models is an assessment of the availability of the

proposed dissolved mineral/compound on Mars. Jean et al. (2008) do not consider this and the exotic compounds that they suggest have not yet been found by any remote or direct sensing instrument. Ferric sulphates were modelled by Chevrier and Altheide (2008) as potential candidates for freezing point depression because they have been found by the both MER landers (Klingelhöfer et al., 2004; Johnson et al., 2007; Lane et al., 2008) and in spectral data OMEGA (Bibring et al., 2006). The inspiration for the modelling of perchlorates by Chevrier et al. (2009a) was the discovery of these compounds by the Phoenix lander (Hecht et al., 2009; Kounaves et al., 2009). Compounds containing chlorine have been detected on Mars, but remain localised to Noachian deposits in the southern hemisphere (Osterloo et al., 2008), so in light of these recent results chlorine-bearing salts seem like a less favourable candidate.

Using kinetic and thermodynamic arguments Oyarzun et al. (2003) noted that water can become supercooled in confined spaces, such as porous media. They suggested that this may become important during mudflows, especially considering that a mudflow exerts a confining pressure on the water – its metastability would not be broken because of the higher viscosity within the pores. Hence, mudflow could be a viable way of creating gullies without salts, or with low concentrations of salts.

Lu and Kieffer (2009) and Longhi (2006) both predicted that any ice deposited on slopes on Mars at the present day is likely to be a combination of water ice and water-CO_2 clathrate, not pure CO_2 ice. This raises the possibility that any fluid produced might have high dissolved levels of CO_2 and the dynamics of such a system under martian ambient conditions should be explored as they are currently not well constrained.

2.6.6. Combined implications of modelling results on gully formation

Considering these modelling results, it seems likely that CO_2 does not play a significant role in forming gullies. Current modelling suggests that long-lived bodies of ice or snow could not have survived since the last obliquity cycle, which would rule out the surface

melting model of Christensen (2003). However, survivability is poorly understood (e.g. Smoluchowski, 1968). There is considerable uncertainty about the recent past climate on Mars, and it certainly seems plausible that seasonal melting could have taken place under past climate regimes. The arguments put forward by Hecht (2002) for seasonal melting of ice to form metastable water at the present day are convincing. They also highlight the strong effect of local conditions on the accumulation and melting of water on Mars. However, modelling also suggests that only small amounts of water can be produced by surface melting either now or in the past. Geochemical modelling has shown that brines could play a very important role in increasing the stability field of water, and could widen the scope of climatic conditions under which gullies can form. However, universal stability of brines alone cannot explain the observed distribution of gullies, and there needs to be careful consideration of the availability of the proposed compound(s). Dynamical modelling has served to highlight the number of unconstrained parameters when modelling flow on the surface of Mars. Determination of the flow-type (dry, debris flow, pure water, turbulent, laminar, etc) and good geometric constrains are major omissions. Current estimates of flow rates and required volumes of water are useful starting points, but this area needs significant development to make it useful.

2.7. Earth analogues for gullies

Earth analogues have been used by many researchers to help explain and constrain their ideas about gully formation on Mars. Table 2-4 is a summary of the analogues that have been published. The geology of the analogue sites is very varied; from volcanic (e.g. Hartmann et al., 2003) to sedimentary bedrock types (e.g. Costard et al., 2007). There are two main processes that have been used as analogues, overland water flow and debris flow.

Overland flow of water sourced from meltwater in the dry valleys of Antarctica produces many of the features associated with gullies on Mars: sinuosity, v-shaped channels, lateral levees (although their topographic expression is small) and fan-shaped

deposits. The cold dry climate of the Antarctic dry valleys makes them a particularly suitable analogue for Mars, which very few other terrestrial analogues can match. In this area, as in many studies, gully alcoves are observed to form traps for windblown snow and ice, otherwise known as nivation hollows (e.g. Lee et al., 2004; Dickson et al., 2007). Because of the aridity of the dry valleys there are usually high concentrations of salt at the surface, which cause any water flow to be salty (Marchant and Head, 2007). However, the seeps that contain the highest concentrations of salts are sourced from groundwater and do not have morphological similarity to martian gullies. They form channels that are often paved with stones, have high albedo and there is no mention in the literature of sinuosity, digitate deposits, or levees (Lyons et al., 2005; Harris et al., 2007). The same morphology of brine seeps are observed on Axel Heiberg Island, Arctic Canada (Andersen et al., 2002), but again have no strong morphological resemblance to gullies on Mars.

Debris flow analogue sites are dominantly located in periglacial, or glacial climates. Many authors have noted the key characteristics: (1) lateral levees (2) lobate or digitate deposits and (3) poorly-sorted gravel or coarser sized sediments as deposits (Hartmann et al., 2003; Costard et al., 2007; Kochel and Trop, 2008; Reiss et al., 2009).

Heldmann et al. (2009) compared mudflows in Atacama to the new light-toned deposits on Mars. They found the higher albedo mudflow was a smooth deposit, with 90% fines compared to 78% fines in the surrounding material. However, the deposit and surrounding material were spectrally indistinguishable. The mudflows described by Heldmann et al. (2009) are different to the ones described nearby by Oyarzun et al. (2003) in that the deposits have no channel, nor discernable topographic effect – they are a surface coating. The mudflows of Oyarzun et al. (2003), however, have very marked topographic effects and form an elevated digitate fan deposit and a channel with lateral levees.

Another planetary analogue is the Moon, which is dry and airless. Bart (2007) observed gully-like features on the lunar surface, which she concluded must be formed by

dry granular flow, because there is no water on the Moon. She used this analogue to suggest that gullies on Mars are also formed without water. However, the observations made by Bart (2007) are from very noisy images and would be better re-examined with better data before any comparison can be made.

Yet another new formation mechanism has been suggested for gullies on Mars, based on the study of frosted granular flows in Quebec (Hugenholtz, 2008). This mechanism involves the coating of grains in a scree slope with water, either by condensation, or rain. When the temperature is elevated above freezing this water lubricates the grain contacts and causes failure. The deposits produced have a runout greater than expected for dry mass wasting only and form deposits that are very similar to debris flow, with lateral levees, digitate or lobate deposits and a central channel. The authors note two attributes that are not commonly observed in debris flows on Earth: the channels develop sinuosity at lower slope gradients ($< 27°$) and sorting of the grains occurs, with larger clasts at the surface and the margins of the flow deposit.

Snow avalanche has been one of the suggested mechanisms for forming gullies. However observations of many snow avalanches by Kochel and Trop (2008) in the Wrangell Mountains in Alaska point to some obvious differences: avalanches have very straight, wide channels, with broad levees, the terminal deposit is square-lobate and shows no digitate break-offs. These landforms are similar in morphology to those produced by dry granular flow in experiments (see Section 2.8) and modelling (see Section 2.6.4).

From the literature, frosted granular flow, debris flow and overland water flow all exhibit many of the attributes shown by gullies on Mars. From general and sporadic observations of length-scales, slope and setting it is difficult to distinguish between these processes. A thorough quantitive comparison is required to allow Earth analogue sites to be of any further use.

Table 2-4. Summary of published analogue sites used for gullies on Mars. Starred entries are estimates from the figures in the paper.

Authors	Location	climate	Average temperature	precipitation	ground conditions	process	trigger	channel length (m)	channel width (m)	channel depth (m)	alcove length (m)	alcove width (m)	levee height (m)	gully slope (degrees)	fan deposit	sinuosity	levees	digitate deposits, or lobes
Bart (2007)	The Moon	dry, airless						125-500*										
Costard et al. (2007)	Jameson Land, E Greenland	dry periglacial	-6.7 to -8	428 mm/yr snow	thick permafrost, active layer 1m	debris flows	melting permafrost	300-500			15-60	50-100	0.1-0.5	25-30	x		x	
Heldmann et al. (2009)	Atacama desert	arid desert		mm in decades	dry	debris flows	rare rain event		1.2									x
Oyarzun et al. (2003)	Atacama, Chile, Road from Copiapo´ to Maricunga					mudflow		500-600*	10*						x		x	x
Pacifici (2009)	Santa Cruz region, Argentinean Patagonia	arid steppe highlands	7.7 (low -25)	150-200 mm/yr	pro-glacial deposit, unknown if ice	?unknown	?unknown											
Hugenholtz (2008)	St. Pierre valley, Gaspé region, Quebec					frosted granular flow	temperature oscillations around freezing	500	1-3				0.2-0.75	31		x	x	x
Lee et al. (2002; 2004; 2006)	Devon Island, High Arctic; valleys and Haughton impact	polar desert climate			talus	debris flows	all Temperature triggered (very transient)	1-50	0.1-5								x	x
					talus	snow gullies	snow gullies, surface snowmelt	10	1									

Authors	Location	climate	Average temperature	precipitation	ground conditions	process	trigger	channel length (m)	channel width (m)	channel depth (m)	alcove length (m)	alcove width (m)	levee height (m)	gully slope (degrees)	fan deposit	sinuosity	levees	digitate deposits, or lobes
Marchant and Head (2007)	McMurdo Dry Valleys, Antarctica	hyper-arid cold polar desert	-40 to -58	10-100mm/yr	permafrost		insolation			3-5								
Dickson and Head (2009)								1000-2000						30	x			
Levy et al. (2007; 2009b)																		
Morgan et al. (2007)						pure water flow									x		x	
Harris et al. (2007)	McMurdo Dry Valleys, Antarctica					groundwater and surface flow of brines	meltwater	2							x			
Lyons et al. (2005)					permafrost at 35-45 cm	groundwater seep	melting of subsurface ice	1200*										
Marquez et al. (2005)	La Gomera, Canary Islands				no ice, but wet	aquifer outflow	aquifer outflow											
Hartmann et al. (2003)	Iceland	periglacial	5	1500-3000 mm/yr ~50 % as snow	ground sometimes frozen	debris flow	snowmelt, connected to drainage,	100-500*	4				1		x		x	
Whalley and Azizi (2003)	Mynydd Ddu, Wales	temperate													x		x	x

Authors	Location	climate	Average temperature	precipitation	ground conditions	process	trigger	channel length (m)	channel width (m)	channel depth (m)	alcove length (m)	alcove width (m)	levee height (m)	gully slope (degrees)	fan deposit	sinuosity	levees	digitate deposits, or lobes
Kochel et al. (2008)	Wrangell Mountains Alaska	supraglacial			substantial snow and ground ice on debris fans	icy debris flow snow avalanche	rainfall solar heating	100-500	10-50					>25			x	x
Soare et al. (2007)	Tuktoyaktuk, NWP	thermokarst - degraded permafrost areas	1.3		permafrost and substantial segregated ice lenses	long term temperature increase and thaw	insolation triggered snowmelt, or permafrost	10-15										
Hugenholtz and Tseung (2007)	-Escuer fan in central Spanish Pyrenees, -intense thawing of frozen sand Canada, -New Zealand, beach sand fans triggered by groundwater, -Spain base of cliffs with ephemeral groundwater.					debris flow dominated alluvial fans									x	x	x	x
Mangold et al. (2003)	Southern Alps,				talus	debris flows		100-500	3-10				1	10-30			x	
Andersen at al. (2002)	Axel Heiberg Island, Canada	polar desert climate	-15	low	permafrost 600 m thick	brine flow from groundwater												
Heldmann et al. (2005)						brine flow from groundwater		600-625	0.2									
Reiss et al. (2009); Hauber et al. (2009b)	Svalbard, Norway	arctic desert	Low	Low (snow)	permafrost	debris flow		1400*	0-12*	0-2.5*	600*	300*		29	x	x	x	x

2.8. Experimental work

There have been several recent numerical and experimental studies that have investigated the sublimation and freezing of stationary bodies of ice, water and brines with application to gullies on Mars. For evaporation experiments it is found that brines have much lower evaporation rates than pure water (Table 2-5), however temperature seems to be the most important factor. Sublimation experiments have shown that temperature, followed by windspeed, is the strongest factor at low humidity (Chittenden et al., 2008). Humidity nearer the vapour saturation point retards sublimation, a finding also made by Schorghofer (2005) on Earth when ground-ice in Antarctica was found to be 8 Ma old, despite a dry atmosphere. Bryson et al. (2008) studied the sublimation rate of ice under very fine to fine sand-sized basaltic regolith and found that at 224 K, thin ice deposits at 10 mm depth would sublimate in less than ten hours, but 1 m ice layers beneath 1 m of regolith could last 600-1300 years. They suggest deeper ice deposits could last even longer.

Table 2-5. Summary of published experimental evaporation and sublimation results.

Authors	Fluid/material	Temperature (K)	Pressure (mbar)	Atmosphere	evaporation or sublimation rate with g correction (mm/ h)	additional parameters
Sears and Moore (2005)	water	273	7	CO_2	0.73+/- 0.14	
Sears and Chittenden (2005)	brine (eutectic NaCl and $CaCl_2$)	247	7	CO_2	0.04	
	brine (eutectic NaCl and $CaCl_2$)	273	7	CO_2	0.88	
Chittenden et al. (2008)	water ice	258	6.5-7.5	CO_2, 1% humidity	0.70-0.97	wind 0.7-11.4 m/s
	water ice	258	6.5-7.5	CO_2, 30-35% humidity	0.33+/- 0.04	wind 0.7-11.4 m/s
Chevrier and Altheide (2008)	brine (58.2wt% $Fe_2(SO_4)_3$)	263	7	CO_2	0.03	
	brine (29.1wt% $Fe_2(SO_4)_3$)	266	7	CO_2	0.42	
Chevrier et al. (2009a)	brine (52wt% sodium perchlorate)	255-275	7	CO_2	0.07-0.49	
	brine (44wt% magnesium perchlorate)	255-275	7	CO_2	0.06-0.29	

Hudson and Aharonson (2008) performed experiments to assess the degree of protection afforded to ice against sublimation/evaporation by (1) a salt crust, (2) tightly packed dust and (3) particle mixtures. They found that these mechanisms produced very minor reductions in the diffusion coefficient.

Although the experiments described above give important constraints on the behaviour of water on the surface of Mars, their results cannot be extrapolated to flowing water. Only a few studies have specifically tried to replicate the form of gullies on Mars: Benison et al. (2008) investigated the formation of gullies by solutions of sulphuric acid under Earth temperature and pressure; Védie et al. (2008) performed experiments designed to simulate the formation of Russell Crater's dune gullies under ambient Earth pressure and low temperature; and Coleman et al. (2009) simulated gullies formed by emergence of water from an underground aquifer under Earth temperature and pressure. All these experiments produced gully-like forms, but, none of them attempted to produce flows under the low temperature and pressure experienced on the present day martian surface. Attempts have also been made to simulate gully-forming processes under low gravity, notably Shinbrot (2004; 2007), through the use of a spinning disc to simulate the lower cohesion induced by lower gravity. This set of experiments was focussed on dry granular flow and was performed under Earth temperature and pressure. The authors generated gullies with wide, shallow channels and gentle lateral levees. This is in agreement with numerical models that have confirmed that pyroclastic flows on Earth behave like dense granular flows and do produce a central linear channel with lateral levees and terminal lobes (Félix and Thomas, 2004; Mangeney et al., 2007).

The experiments confirm the results of numerical models that suggest that surface ice cannot persist at the surface of Mars for long periods of time, however they indicate that burial could prolong its life. These results confirm that seasonal surface melting is a realistic proposal, but not long-term preservation of surface ice. Evaporation rates on

stationary bodies of water are < 1 mm/h and significantly less when considering brines, but these rates would change when the water flows. However, as all models of gully formation suggest episodic events (hours up to days, rather than months, or years) these evaporation rates would not account for significant attenuation of the flow. Experiments have been successful at producing gully-like forms at the centimetre to metre scale, but realistic martian ground conditions were not used and there are problems with scaling-up these experiments.

2.9. Conclusions

The combination of the observations, modelling and experimental work suggests that a climatic origin for gullies is more likely than a dry or aquifer origin. However, it is likely that when considered globally, gullies can form by several different processes (both regionally and locally) and better constraints are needed before the surface melting origin of gullies can be confirmed.

To ascertain the availability of water at the martian surface my literature search has identified three key areas where further research is required: (1) systematic quantitative geomorphology measurements of gullies on Mars, (2) quantitative Earth analogue comparisons and (3) experimental work on flowing water performed under low temperature and pressure conditions. These will all provide important constraints to models both at the global and local scale and will help to determine the active processes forming gullies. This is central to determining how much water is needed to form them and thus, to placing gullies in the global hydrological and climatic context of the recent evolution of the surface of Mars.

Chapter 3. Debris Flows

3.1. Introduction

The commonly quoted definition of a debris flow from Iverson (1997) is "a mix of poorly sorted sediment and water that surges downhill under the force of gravity". However, many different types of flows fall within this broad definition, for example, earthflows, lahars, and debris slides. I will be considering only those flows which produce the classic landforms indicative of debris flow: lateral levees and depositional lobes. The detailed physics of debris flows is poorly understood, which makes dynamic modelling of debris flows very challenging. Their rheology is spatially and temporally extremely variable, because it is controlled by the interplay of granular interactions and fluid dynamics on multiple scales (Iverson, 1997). However, the landforms and sedimentology associated with debris flow have been well characterised.

Debris flows produce landforms which show visual similarities with gullies on Mars (compare Figure 3-1 and Figure 2-7). If gullies on Mars are indeed formed by liquid water then debris flow seems a likely mechanism: it protects water from evaporation and freezing and allows greater geomorphic work with less water than overland flow. Their distinctive morphology, as described in detail in this chapter, means that they are particularly suitable for the method of comparative geomorphology, which is employed in Chapters 6 and 7.

A review of the current state of knowledge is included below; encompassing behaviour and morphology (Section 3.2), triggering and composition (Section 3.3) setting

and landscape evolution (Section 3.5) and a brief summary of debris flows and hazard assessment (Section 3.6).

3.2. Behaviour and Morphology

Debris flows fall into two broad categories: confined and unconfined. Confined flows are those restricted to a pre-existing valley and unconfined flows are those that occur on an open slope; the latter are thus often termed "hillslope" debris flows. Confined flows have been studied in greater detail: for example in-situ measurements on velocity, viscosity, basal shear and normal stresses have been made, since it is easy to predict their path, or simulate them in a flume. Hence, much of our understanding of debris flows comes from studies of confined debris flows. The difference in behaviour between confined and unconfined debris flows has not been widely acknowledged in the literature. There are two exceptions: (1) confined and unconfined sections of debris flows were given different empirical relationships for erosion and deposition in the probability model of Fannin and Wise (2001), and (2) the difference in behaviour was one of the motivations behind the study of Lorente et al. (2003), because empirical relationships established for confined debris flows (e.g. Rickenmann, 1999) did not predict the behaviour of unconfined debris flows in their study area in the Spanish Pyrenees.

Figure 3-1. Examples of debris flows on Earth. (A) Debris flows on a talus slope in Glacier National Park, Montana, "fire hose" (see text for detail) triggered (Wilkerson and Schmid, 2003), (B) hillslope debris flows and debris flows originating from alcoves in Longyear Valley, Spitsbergen, Norway (Larsson, 1982), (C) hillslope debris flow originating from a landslip in a topographic hollow, Colorado Front Range (Coe et al., 2002), (D) mobilisation of sediments from pre-existing channels, Colorado Front Range (Coe et al., 2002) and (E) debris flows originating from rilling in volcanoclastic sediments, Vulcano, Italy (Ferrucci et al., 2005).

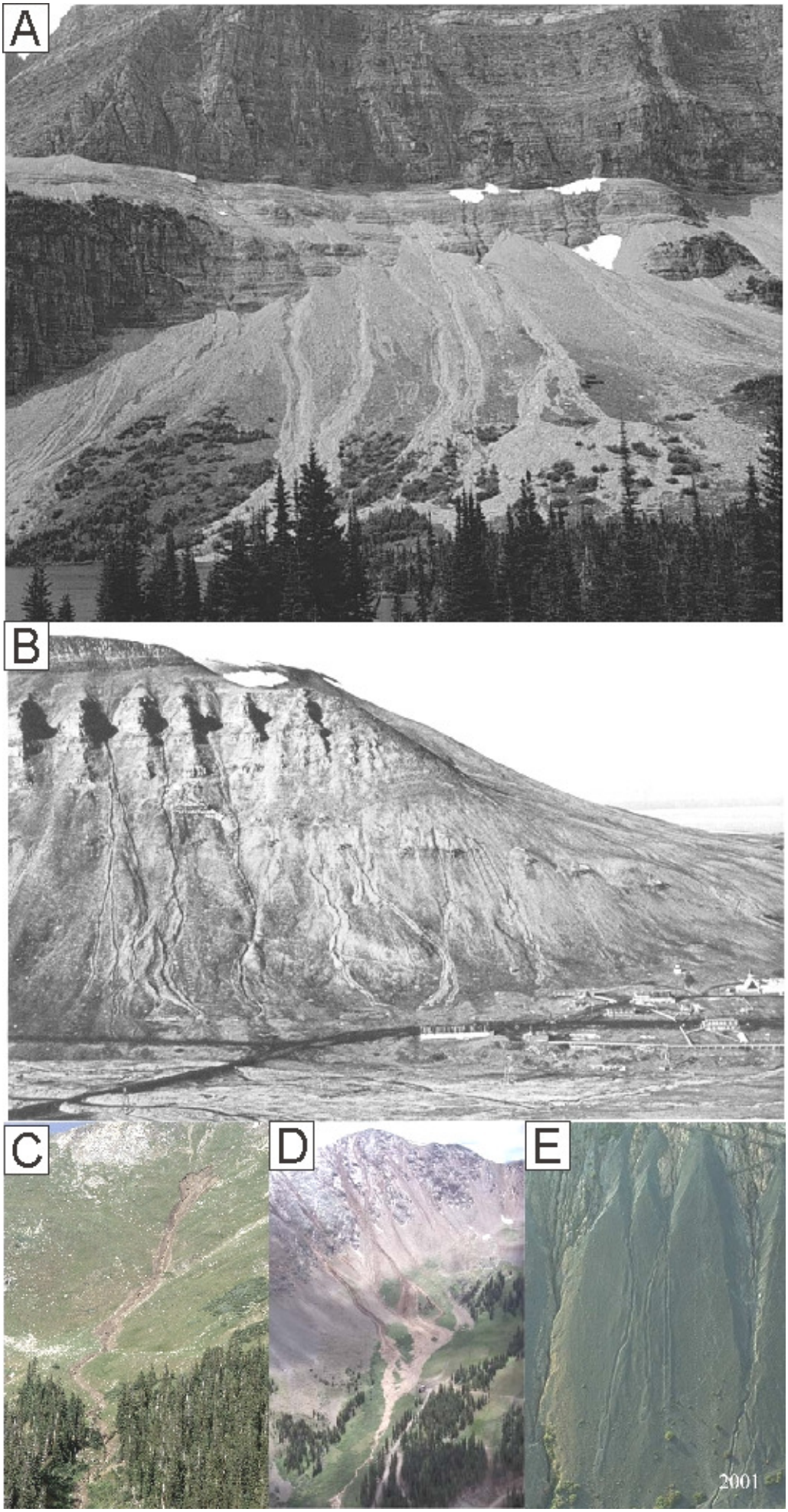
A
B
C
D
E
2001

The literature highlights some important differences between unconfined and confined flows: hillslope debris flows tend to start depositing at much higher slope gradients, are smaller in volume and have much lower runout, (i.e. they do not reach the base of the slope). For example, Lorente et al. (2003) observe 17.8° as the start of deposition for the hillslope debris flows in the Central Spanish Pyrenees, Rapp and Nyberg (1981) report deposition for hillslope debris flows on 30° slopes in Nissunvagge in Sweden and Larsson (1982) reports deposition at as much as 35° for hillslope debris flows in Longyear Valley, Spitsbergen. In an extreme example, the entirety of the deposits of small debris flows on the slopes of Vulcano Island, Italy were located on slopes ~ 30° and greater (Ferrucci et al., 2005). Guthrie et al. (2010) note that authors often record the onset of *net* deposition, rather than onset of deposition. Hence they suggest that the commonly quoted figures for the onset of debris flow deposition from the literature are often too low. In their study area they find that deposition occurs on slopes up to 35° for both confined and unconfined debris flows. The onset of deposition for confined debris flows is usually quoted as being on the upper fan surface: for example, 5° for Owens Valley, California (Whipple and Dunne, 1992), 5-10° Oregon Coast Range (May and Gresswell, 2004), and up to 10° for debris flows from Mt. Thomas, New Zealand (Pierson, 1980).

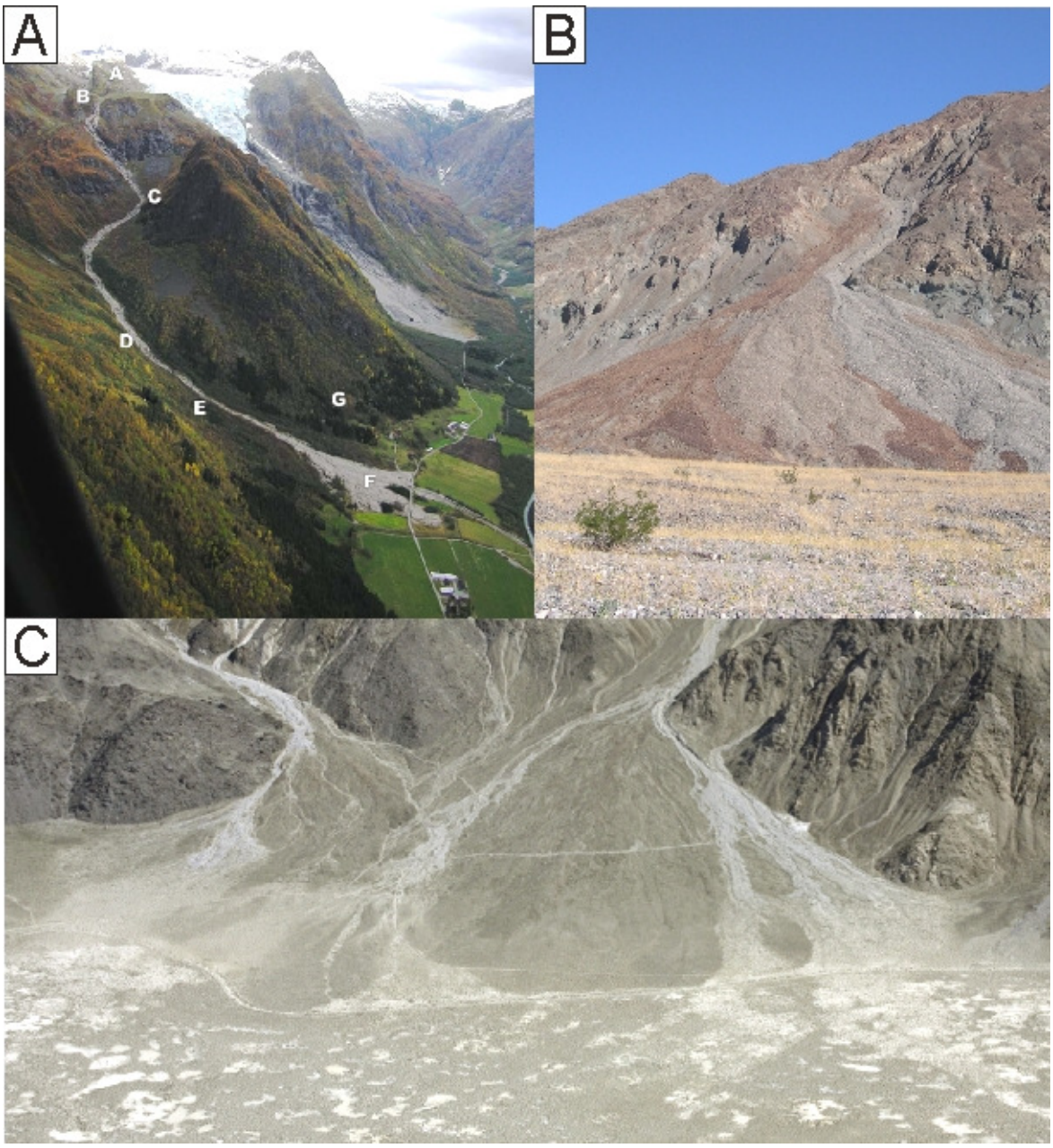

Figure 3-2. Examples of debris flow fans on Earth. (A) Small confined flow in Fjærland, Western Norway resulting from a glacial lake outburst. Little deposition occurs along the path and the majority of the deposition occurs on the fan. After Breien et al. (2008). (B) Steep debris flow fan, with small source area, in Death Valley. Image credit: Prof. Martha S. Gilmore. (C) Large debris flow fans in Death valley, Dolomite Fan, a result of large confined debris flows. After Hardgrove et al. (2009).

The literature also provides examples of the difference in runout distance and volume between unconfined and confined debris flows. Unconfined debris flows in Scotland are estimated to be up to hundreds of cubic metres in volume (Innes, 1985) with lengths of ~ 500 m (Luckman, 1992; Curry, 2000). The deposits of these debris flows do not extend the full length of the slope. In NW Iceland Decaulne et al. (2005) measured debris flows with lengths of ~ 700 m and volumes ranging from 100-3000 m^3 for

unconfined debris flows. Some of these debris flows were interrupted by the town, or the fjord, but most of the cohesive deposits remained on the slope (Decaulne, 2001). Larsson (1982) reported hillslope debris flows in Longyear Valley, Spitsbergen that are up to 400 m in length with volumes of 2-1800 m^3, and which do not reach the foot of the slope (Figure 3-1B). These three case studies can be compared to data presented in the review of predominantly confined debris flows by Rickenmann (1999). These debris flows have lengths from 300-90,000 m, volumes of 710-8,000,000 m^3 and the majority of them deposit onto debris fans (Figure 3-2) which have low gradients and are found beyond the foot of the slope (e.g. Harris and Gustafson, 1993).

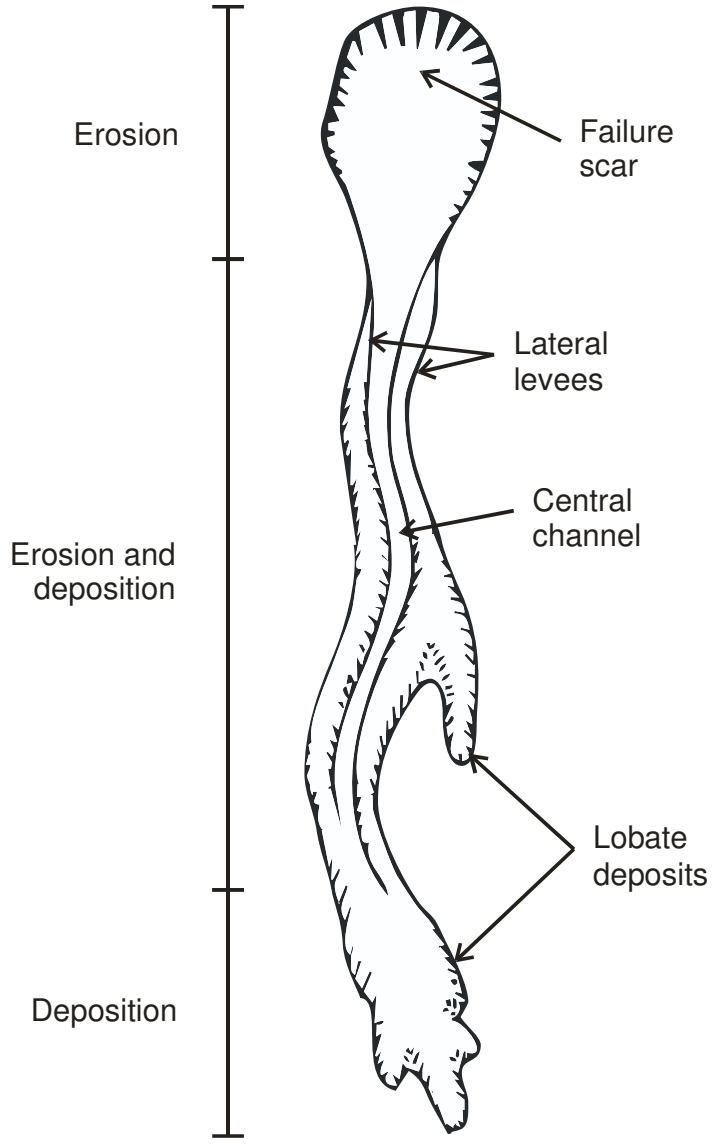

Figure 3-3. Sketch of a typical unconfined hillslope debris flow.

The two arguments that have been used against debris flow in forming gullies on Mars are (1) that gullies on Mars do not reach the base of the slope and (2) that deposition begins on relatively high slope angles (e.g. Kolb et al., 2009). However, as shown above, this is contrary to observations in the literature of unconfined hillslope debris flows on Earth. Because gullies on Mars are more similar morphologically to unconfined debris flows the focus of this review will be on this kind of flow.

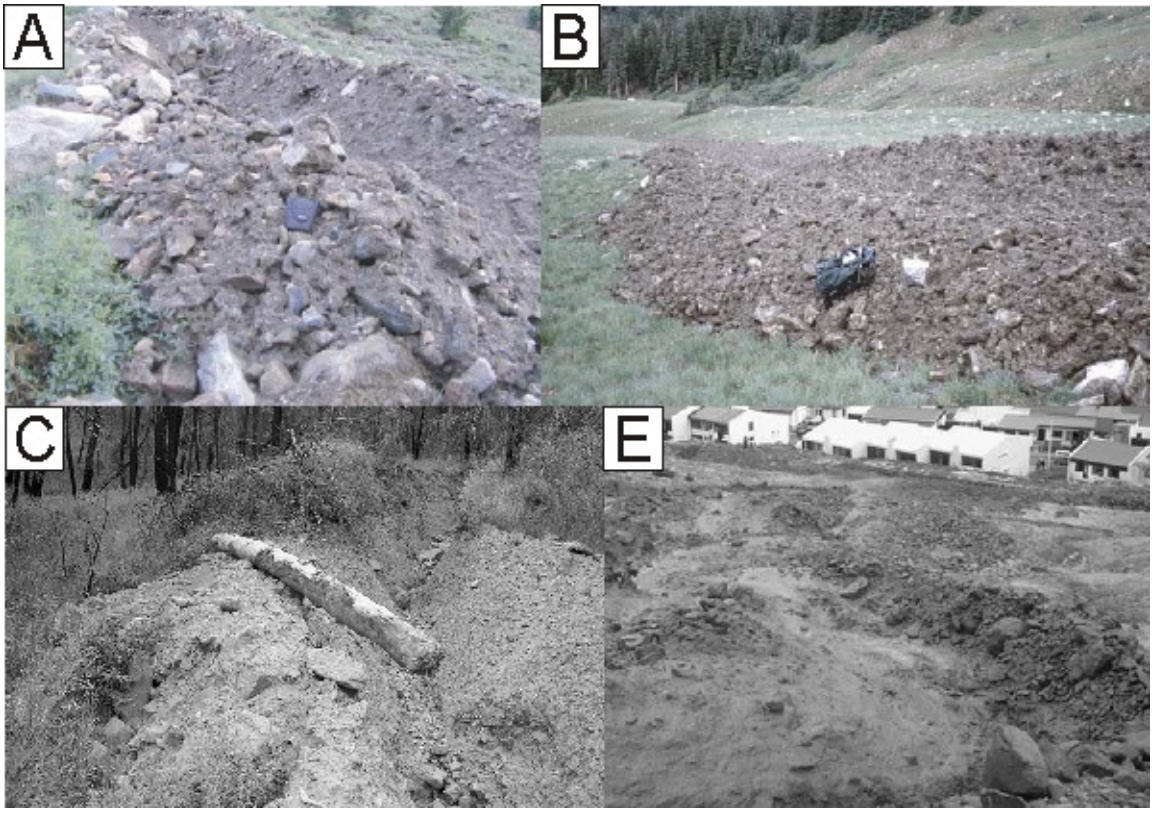

Figure 3-4. Debris flow channels and levees. (A) Unconfined debris flow in Colorado Front Range, camera case for scale. Image from Coe et al. (2002), (B) debris flow in Colorado Front Range, on west flank of Grizzly Peak, shown in Figure 3-1C, camera case for scale. Image from Coe et al. (2002), (C) Debris flow levees on Red Mountain, south of Glenwood Springs, Colorado, log is about 8 m long. Image from Santi et al. (2008), and (D) Unconfined hillslope debris flow during flow above Ísafjörður in NW Iceland. Image from Decaulne et al. (2005).

A simple hillslope debris flow is composed of three sections: erosion, mixed erosion and deposition and deposition (Figure 3-3). The source of a flow is in the erosion section and is often delineated by a failure scar (e.g. Larsson, 1982; Matthews et al., 1999), as shown in Figure 3-1C. Usually this is a discrete area defined by the outline of a rotational slide (e.g. Prior et al., 1970). Other modes of initiation (discussed in Section 3.3) produce different morphologies. Erosion during a debris flow is increased by its

turbulence, whilst the outer edges slow down and deposit lateral levees. Levees are hummocky, uneven, and often several metres in height, but can be > 10 m, depending on the scale of the flow (Figure 3-4). Continued erosion along a debris flow path is frequently termed bulking (e.g. Coe et al., 2008) and is an important contribution to the final deposition volume. When a debris flow ceases eroding it can come to a halt and form a terminal lobe, or can continue to progress while forming lateral levees, but not eroding, as shown by in-situ vegetation between levees (Rapp, 1960; Prior et al., 1970; Larsson, 1982; Luckman, 1992; Matthews et al., 1999). In a few cases the point where erosion ceases has been reported to be slope dependent. For example, Stratham (1976b) reports erosion ceasing at 16±0.25°, Fannin and Wise (2001) report the lowest limit of erosion on average as being 18.5° for unconfined flows, and Guthrie et al. (2010) report erosion on slopes as low as 5-10°, with confined flows generally showing erosion at a lower gradient than those that are unconfined.

Successive debris flows can build up terminal fans, which can become very large when there is sufficient sediment supply (Figure 3-2B and C). Although the sinuosity of debris flows is generally not mentioned explicitly in the literature, it is usually low (Figure 3-1) and seems to be caused by: (1) pre-existing topography or, (2) blockages formed by clast-rich areas of the flow. Asymmetry of the levees at bends has been reported and has been used to calculate velocity of a debris flow (Johnson and Rodine, 1984), but this is often at pre-defined stream bends (i.e. the flow is confined).

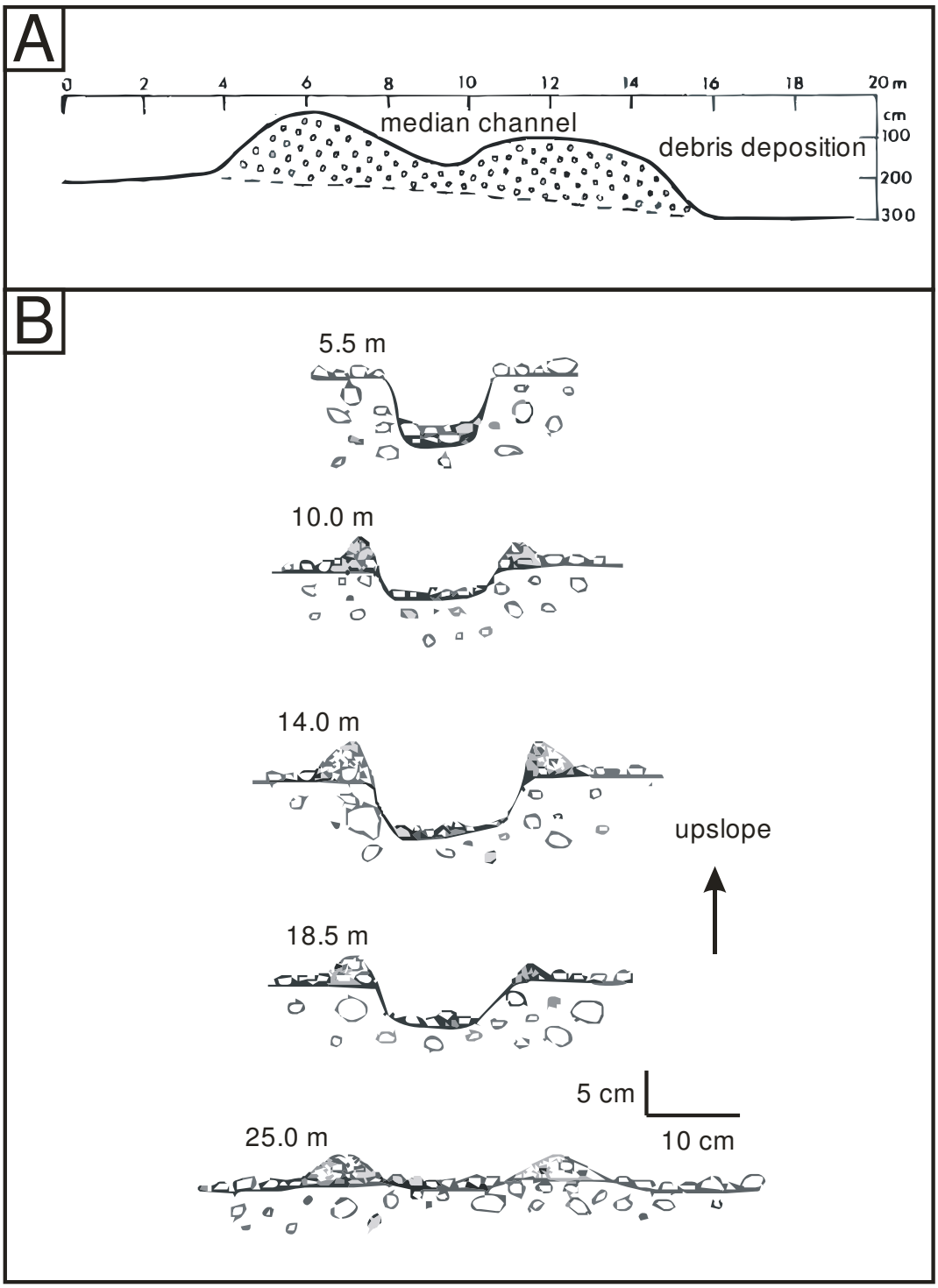

Figure 3-5. Typical debris flow cross sections taken from the literature. (A) Leveed deposits that are not eroding downwards from a debris flow in Longyear Valley, Spitsbergen. After Larsson (1982). (B) Typical sequence of debris flow cross sections, evolving through erosion, mixed erosion and deposition to just deposition. Despite the small scale of this flow, the same pattern is seen in much larger flows. The distance from the source of the flow is given to the right of each section. After Boelhouwers et al. (2000).

Debris flows are u-shaped, or rectangular in cross section (Figure 3-4 and Figure 3-5), but can also be v-shaped in erosive sections (e.g. Suwa and Okuda, 1980). Inner

channel walls are generally steep, e.g. Harris and McDermid (1998) measured inner channel slopes of over 30°. Debris flows can interact with old flows. For example, new debris flow levees are seen to follow the track of older ones, to overlap old levees and to punch through, or cross old levees (Sharp, 1942; Addison, 1987). Thus, caution must be taken when estimating deposit volumes for single events from levees that follow old debris flow tracks (Luckman, 1992).

3.3. Triggering and Composition

The triggering of debris flows is a stochastic process: there needs to be sufficient sediment supply for a debris flow to be possible, but also an event (usually meteorological) needs to occur to trigger the flow (Benda and Dunne, 1997). Debris flows occur at gradients below the stability of the host sediment and thus for a debris flow to occur the sediment has to become saturated in such a way that the pore-pressure exceeds the confining pressure, causing failure. The material only needs to be partially saturated to cause failure (Iverson et al., 1997; Imaizumi et al., 2006). In the literature these conditions are most commonly noted as being brought about by sudden heavy rainfall, or long-term persistent rainfall (e.g. Ben David-Novak et al., 2004; Decaulne and Sæmundsson, 2007; Godt and Coe, 2007; Crosta and Frattini, 2008; Morton et al., 2008). However, there are reported cases of debris flows being triggered by rapid snowmelt (Decaulne et al., 2005), ground-ice thaw (Harris and Gustafson, 1993), and natural damn breaks caused by glacial melting (Clague et al., 1985; Breien et al., 2008). It should be noted that the presence of ground-ice makes triggering of debris flows more likely as lack of infiltration promotes high pore water pressures in the regolith and aids basal sliding (Harris and Gustafson, 1993; Bardou and Delaloye, 2004).

Debris flows have several styles of initiation: (1) by landslips on open hillslopes and valley sides (Figure 3-1B & C), (2) by the formation of rills, which coalesce and trigger failure (Figure 3-1E), (3) by the mobilisation of sediments which have accumulated

in pre-existing depressions (Figure 3-1D) and (4) by the “fire hose” effect (Figure 3-1A). The “fire hose” mechanism (Johnson and Rodine, 1984) is characterised by the concentration of overland flow by chutes or depressions in the bedrock which becomes a debris flow when it impinges on sediments built up on the slope where it emerges. These mechanisms are morphologically distinct and are mutually exclusive. Carrara et al. (2008) found landslip to be the most common initiation mechanism in the Eastern Italian Alps, but Godt and Coe (2007) found that rilling was the most common mechanism in the Colorado Front Range, followed by “fire hose” and shallow landsliding in almost equal proportions.

Several authors report minimum angles for debris flow initiation. For example, Prior et al. (1970) note that none of the debris flows in their study area initiated at slope angles below 25°. However, this has not been supported by larger, more recent studies. For example, Godt and Coe (2007) found that debris flows initiate on slopes from 9-62°, with initiation by the fire hose mechanism having the lowest average initiation angle (~ 33°), followed by rilling (~ 36°), and then landsliding (~ 39°).

As noted by Klubertanz et al. (2009) the spatial location of debris flow triggering is a complex combination of material type (porosity, permeability, grain size distribution), sediment depth, saturation state and hydrology. This makes a generalised prediction of the location of debris flow initiation sites very challenging, although local studies have had some success, (discussed further in Section 3.6.1).

The deposits of debris flow are characteristically poorly sorted and reflect the sedimentology of their source area (e.g. Ballantyne and Benn, 1994). Most authors agree that debris flows require a proportion of clay-sized material; this enables the debris flow to maintain the high pore pressures required during flow (Iverson, 1997; Griffiths et al., 2004). A good example of this is provided by a study of two neighbouring alluvial fans in Death Valley, which are identical apart from their underlying geology (Blair, 1999). One fan has an underlying rock type that weathers to silt and clay and this fan is dominated by

debris flows. The rock type underlying the other fan produces neither fines nor clay and its weathering products have high permeability. This fan is dominated by alluvial processes. The exact proportion of fines within debris flows seems to be variable. For example, debris flow deposits in the Green River canyons of Dinosaur National Monument, USA were found to have between 7-23 % clay (Larsen et al., 2006), but deposits from small debris flows on Vulcano Island, Italy have clay contents of < 1 % (Ferrucci et al., 2005). Clay content can differ within the flow. For example, Sosio et al. (2007) found that the proportion of clay and fines decreased downstream. Water contents within debris flows are also very variable; Iverson quotes typical values of 20-60 % by volume in his review, but *in situ* sampling has revealed values of 9.6 to 11.9% (Berti et al., 1999).

Debris flows can carry boulders up to several metres in size. For example, boulders of up to 7 m diameter were recorded for a large confined debris flow, 300,000 m^3 in volume, in Serra do Cubatão, Brazil, (Kanji et al., 2008) and boulders several metres across were observed in unconfined debris flows of ~ 3000 m^3 in Iceland (Decaulne et al., 2005). The size of clasts was observed to decrease towards the end of the deposit by Kanji et al. (2008). However, Sosio et al. (2007) found that boulders of all sizes were evenly distributed along the whole length of the debris flow, and located preferentially at the front and levees. The ability of debris flows to carry large boulders combined with their capacity for inundation, make these types of flow both distinctive and very dangerous.

Several authors have found some weak organisation in debris flow deposits including: (1) long axis of clasts oriented downhill, with significant scatter, (2) clasts dipping at the same angle as the slope, and (3) coarse clasts located preferentially at the front and edges (Innes, 1983b; Ballantyne and Benn, 1994; Boelhouwers et al., 1998; Palacios et al., 1999). Newly deposited debris flows usually have a different colour from the surrounding landscape (Figure 3-1 and Figure 3-2) with clasts having a coating of mud that is subsequently washed away (Sharp, 1942) by rainfall (Figure 3-4).

3.4. Observations of active debris flows

Observed flow speeds of debris flows range from 0.8-28 m/s (see review by Rickenmann, 1999). *In situ* observations of debris flows have found that the excess pore pressures that trigger them are maintained for the whole length of the flow (Berti et al., 1999; Berti and Simoni, 2005; McArdell et al., 2007), which is used to explain their unusual mobility (compared to dry mass flows). This result was also obtained through simulation of debris flows in a true-scale flume (Iverson, 1997).

Eyewitnesses report that debris flows are very noisy and impacts of the rocks can be heard (Decaulne, 2001). While a debris flow is moving boulders are located at the advancing front (Breien et al., 2008), but they also have been seen to float and roll in the flow (Takahashi, 1981). Okuda (1989) placed seismometers and impact plates in the path of a confined debris flow in Japan and measured accelerations of up to 1 m/s^2 and impacts with a force of ~ 40 kPa. Pressure sensors or impact plates in the path of other debris flows have recorded normal pressures of 12-14 kPa (Berti and Simoni, 2005) and 23 kPa (McArdell et al., 2007). These impacts are another reason that this type of flow is so erosive (Stock et al., 2005).

Debris flows are not smooth continuous flows, but are pulsatory in nature, with pulses occurring with a frequency of minutes (Costa, 1984) up to hours (Decaulne, 2001). These pulses have been recreated in both large and small-scale laboratory experiments using a variety of Newtonian and non-Newtonian fluid types in the form of backward-moving and forward-moving pulses (see review by Zanuttigh and Lamberti, 2007).

Experiments on materials sourced from debris flow deposits and source areas reveal that the bulk rheology is broadly that of a Bingham fluid, (i.e. visco-plastic Iverson, 1997; Kaitna et al., 2007; Sosio et al., 2007). Observations from these experiments include: a central flow (termed a non-deformed plug) with slow and/or stationary sections on both sides and development of a clast-rich front are noted in the experiments in agreement with

field observations. Experiments have also confirmed modelling and field observations that debris flows are triggered by increased pore pressures (Moriwaki et al., 2004). However, these experiments have not explained all the features of debris flows; this cannot be done without consideration of the temporal and spatial variability of rheology (Iverson, 1997), brought about by interaction with a realistic spatially variable bed.

3.5. Setting and role in landscape evolution

Debris flows form part of a complete landform assemblage which, on Earth, is influenced by climatic and tectonic setting. For example, debris flows are very frequently associated with glacial terrain, occurring in paraglacial (i.e. recently deglaciated) and periglacial landscapes (areas proximal to glaciated areas and subject to intense freeze-thaw). They therefore are often co-located with glacial landforms, such as protalus ramparts (figures in: Whalley and Azizi, 2003; Harrison et al., 2008), moraines (Iturrizaga, 2008) and rock glaciers (Kneisel et al., 2007).

Paraglacial landscapes are profoundly affected by debris flows, as observed by Ballentyne and Benn (1994) and Curry (1999) in Fåbergstølsbreen in Norway. They found that the steep sediment-laden slopes are rapidly stripped by debris flows, forming a slope that has steep bedrock exposed in its upper section, a mid-slope dominated by deeply incised gullies, and a lower slope with low-gradient fan systems. The slope profiles evolve from steep, essentially linear profiles (resembling talus slopes, but sourced from moraine collapse) to profiles with steep linear upper sections and slightly concave lower sections (Figure 3-6). A similar pattern, but on a larger scale was observed by Iturrizaga (2008) in the Hindukush and Karakoram Mountains in India and Pakistan, but not explicitly linked to debris flow processes. This pattern of slope evolution was noted by Stratham (1976b) on scree slopes in Wales, but occurring over longer timescales. He observed that the screes contain deep gullies (often reaching bedrock) and debris flow cones which form at the base of the slope. These have an irregular surface because of a “criss-cross” of old levees. Over

time the straight scree slope profile is replaced by a more concave debris flow profile. The initiation of these flows occurs at 27-30°. The same evolution of scree slopes was observed in NW Scotland by Hinchcliffe and Ballentyne (2009) and they concluded that this sequence in slope evolution has been occurring throughout the Holocene. Another analogous system is the stripping of unconsolidated volcanoclastic materials by small debris flows from the outer walls of La Fossa cone on Vulcano Island, Italy. All these slope systems seem to be visually analogous to gullies on Mars that appear to be stripping the mantling material (Figure 3-6), described in Chapter 2.

Debris flow processes are intimately linked with the formation of many alluvial fans (e.g. Parker et al., 1998). A well-studied example is Death Valley (Figure 3-2B and C) where, in a large proportion of cases, debris flows are integral to the formation of the alluvial fans (Hooke, 1967; Blair, 1999). The prevailing theory is that steeper fans are formed by debris flow: i.e. Gardner (1989) stated that fans greater than 4° gradient have greater debris flow influence than those with gradients less than 4°. This is supported by recent evidence from high resolution topographic data from an airborne laser altimeter (Light Detection and ranging -LiDAR, or Airborne Laser Swath Mapping - ALSM). Staley et al. (2006) found that debris flows with higher internal shear strength produce fans with a higher overall gradient than debris flows with lower internal shear strength. Thus, by analogy, water flows should produce even lower gradient fans, as found by de Scally and Owens (2004). High fan surface roughness and low thermal inertia have been shown to be the principal characteristics of fans dominated by debris flow (Hardgrove et al., 2009).

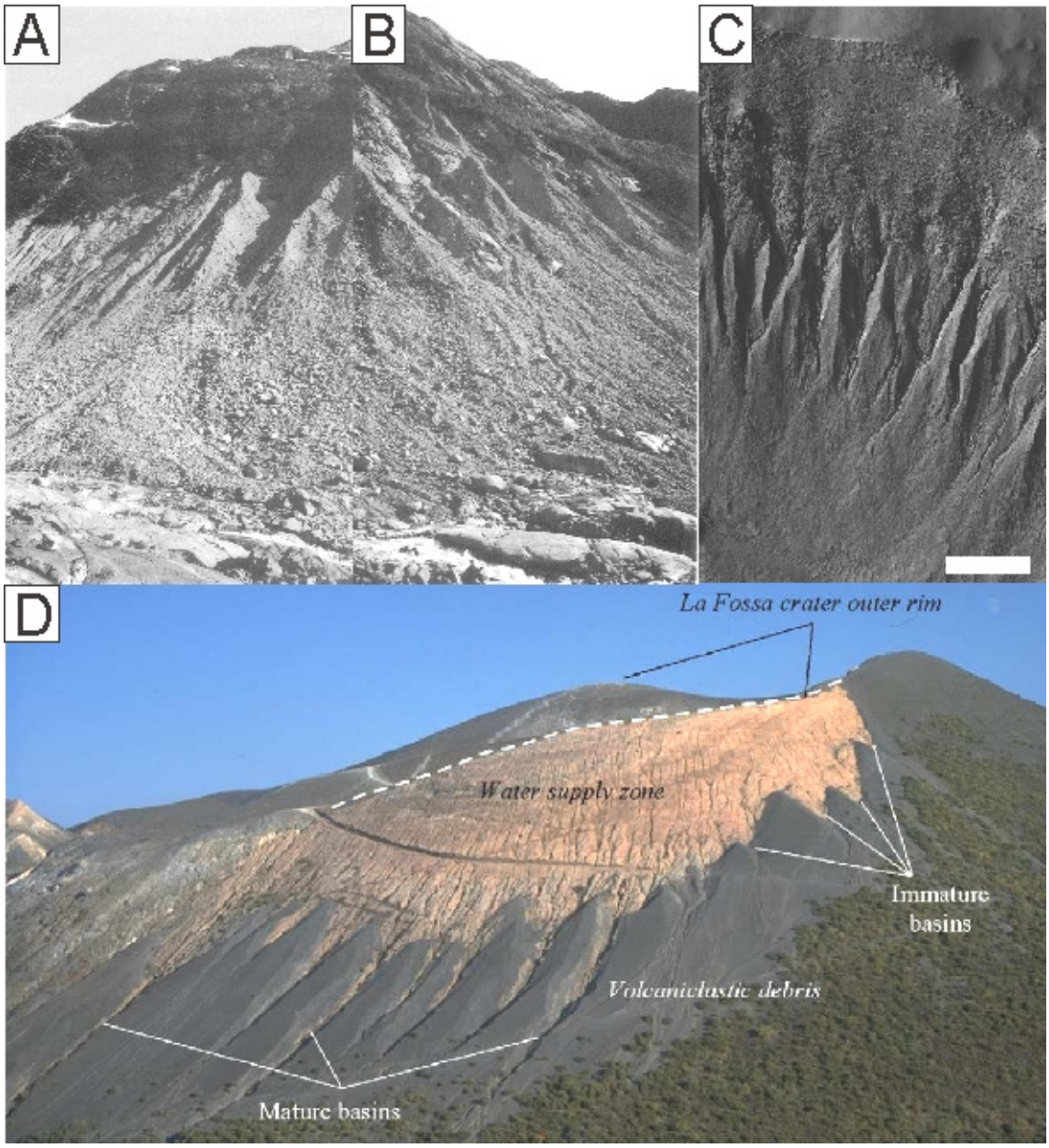

Figure 3-6. Comparison of rilling-initiated debris flows on Earth with mantle stripping gullies on Mars. (A) and (B) Slopes in Fåbergstølsdalen, where gullies cut into the drift deposits and debris flow deposits are seen in the fans in the foreground. Image from Ballantyne and Benn (1994). (C) Gullies stripping mantle deposits on Mars, HiRISE image PSP_002066_1425; scale bar in white is 250 m long. (D) Debris flows dissecting the unconsolidated volcanoclastic deposits on the side of La Fossa Cone on Vulcano Island, Italy. Image from Ferrucci et al. (2005).

However, it is not just arid areas that possess debris flow dominated alluvial fans; they occur in permafrost areas (Harris and Gustafson, 1993; Harris and McDermid, 1998) and humid areas (e.g. Winder, 1965; Coe et al., 2007). In addition, debris flows are generally not unique to periglacial, paraglacial and alluvial fan settings, but occur in other settings, such as the previously non-glaciated, humid, sedimentary mountains of Oregon Coast Range, USA (e.g. Stock and Dietrich, 2003; Kobor and Roering, 2004) and Toit's

Kloof, Western Cape, South Africa, (Boelhouwers et al., 1998), also on small volcanic cones in Cima Volcanic field, Mojave Desert, USA (Dohrenwend et al., 1986) and on the flanks of Mt Yakedake volcano, Northern Japan Alps (Suwa and Okuda, 1980).

These examples suggest that debris flows are an integral part of landscape evolution. They leave more profound signatures in the landscape than just the obvious surface alterations, such as levees or digitate deposits. It has already been shown that debris flows change the slope profiles of paraglacial valleys. Debris flows also contribute sediment to valley bottoms, which may then go on to become a confined debris flow, or be transported by fluvial processes (Benda et al., 2005). Their unique physics means that their broader morphologic signature can be separated from that of alluvial and dry mass wasting processes at the landscape scale (e.g. Montgomery and Foufoula-Georgiou, 1993; Lague and Davy, 2003; Stock and Dietrich, 2003). This signature can be quantified using plots of local slope against contributing drainage area ("slope-area plots") derived from topographic maps, or DEMs. The signature is twofold: firstly it is defined by a specific domain and secondly by a distinct trend in slope-area plots located between the hillslope and alluvial domains (Figure 3-7). Debris flow deposition has been found to define an additional domain within the alluvial domain at higher drainage areas and higher local slopes by Brardinoni and Hassan (2006), (see Figure 3-7); a result also confirmed by Mao et al. (2009). This type of analysis is only possible with high resolution topographic data, better than 1:25,000 topographic maps, or 10 metre per pixel DEMs (Tarboton et al., 1991).

The role of debris flows cannot be ignored if a successful result is to be obtained from long-term landscape evolution models, such as those designed to investigate tectonic and climatic signatures encoded in the landscape (Stock and Dietrich, 2006). The distinct signal of debris flow over both the long and short term allows its presence and relative

influence in the landscape to be assessed. This thesis aims to determine if this applied to planets other than the Earth.

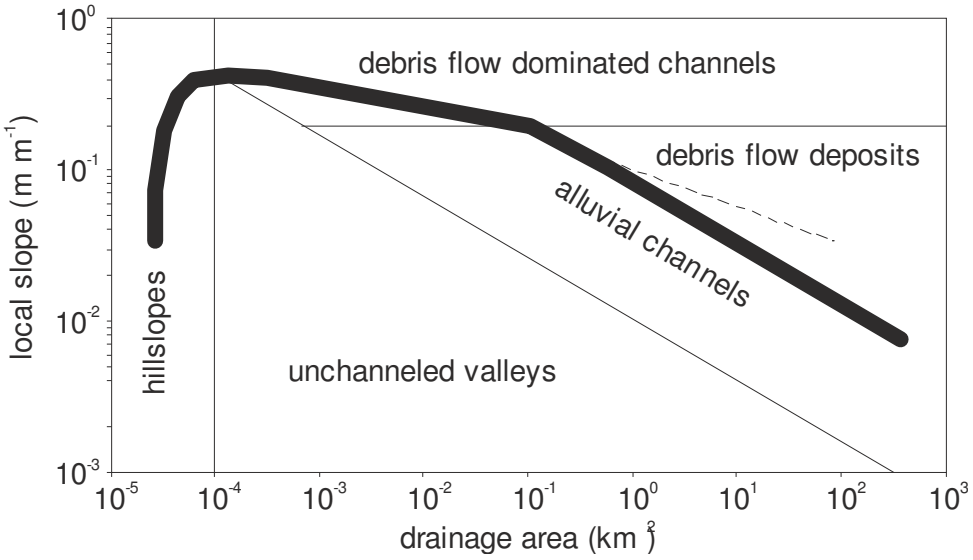

Figure 3-7. Slope-area plot after Montgomery and Foufoula-Georgiou (1993) and Braradioni and Hassan (2006). The process domains are delimited by thin lines and the dark line shows the typical trend of the data points for the catchment of a mature fluvial system in a soil-mantled landscape.

3.6. Debris flows as hazards

Hazard assessments have generally been performed for confined debris flows. They fall into two broad categories: (1) empirical relationships and (2) full flow-dynamical modelling. The former relies on field observations and the latter relies on the good understanding of the flow type and rheology of the debris flow. A brief review of these approaches is provided here.

3.6.1. Empirical Models

Empirical models are useful as they are easily applied, but they are usually only applicable to individual areas. They have been widely applied for both debris flow and other landslide movements. Rickenmann (1999) compiled empirical relationships for debris flows, using data from many studies of debris flows in many settings. The majority of these flows were in confined settings. He studied several characteristics of debris flows, including debris mass (with volume used as a proxy), peak discharge (23 flows), total travel distance, fall height (232 flows) and runout on fan (236 flows). To all these parameters he fitted a power

law relationship based on mass (volume). He also derived a relationship between mean flow velocity and slope, flow depth and discharge (373 flows).

Lorente et al. (2003) adapted the total travel distance relationship of Rickenmann (1999) for hillslope (unconfined) debris flows. They found that the 961 unconfined debris flows that they studied had a shorter total travel distance than the unconfined flows of Rickenmann (1999). The data presented by Rickenmann (1999) and Lorente et al. (2003) do in general follow their given relationships, but the scatter in the data spans an order of magnitude, which means that estimates of runout derived from these relationships have significant error bounds (e.g. a 100 m^3 debris flow dropping 100 m could have a runout anywhere between 30-200 m). Legros (2002) also supported the idea that runout distance in debris flows, and indeed other gravity flows, is more closely related to the initial volume than the fall height. Using data from 203 landslides and debris flows, he considered different classes separately. The data have a scatter of approximately a factor of 2-3 around the power-law relationship between volume and runout.

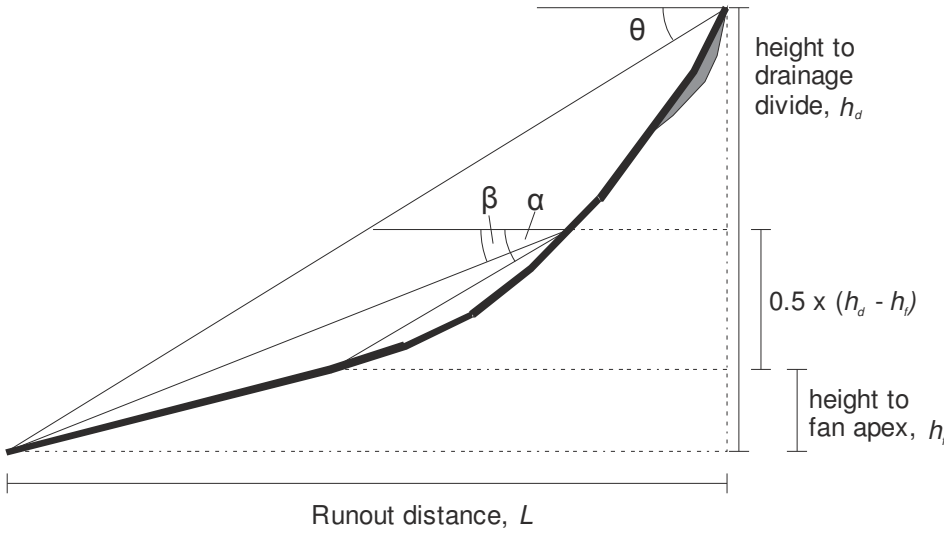

Figure 3-8. Diagram illustrating parameters used to construct empirical debris flow models. α is the fanhead angle and β is the runout angle from Prochaska et al. (2008). θ is the reach angle of Corominas (1996).

Corominas (1996) studied 204 gravity flows (of which 71 were debris flows) to develop an empirical relationship between the event volume and the angle of reach from

which runout can be ascertained. The angle of reach is measured between the top of the failure to the distal end of the deposits (θ in Figure 3-8). However, there is again significant scatter in the derived relationship: the r-squared of the fit is only 0.625, although debris flows treated alone have a better fit of r-squared = 0.763, but this still gives up to 250 m of error in runout for a debris flow with a 500 m fall height. Prochaska et al. (2008) used a similar approach and developed an empirical model from 20 debris flows to predict the runout of confined non-volcanic debris flows onto alluvial fans. They used the so-called average channel slope (ACS) method which was developed initially from avalanche studies. In their version they relate the fan head angle (α) to the runout angle (β), both measured from a fixed point located at the vertical midpoint between the drainage-divide and the fan apex (see Figure 3-8). They tested the model against three debris flow events that were not amongst those used the construction of their model and found runout lengths between 82 % and 131 % of the measured data. They showed that their model produces tighter estimates of runout than the empirical models of Rickenmann (1999) and Corominas (1996). The authors noted that this relationship would only be successful for debris flows in the same setting: i.e. modest sized confined flows with simple channels that debauch onto an alluvial fan. This model possesses the advantage that the volume of the flow does not need to be calculated. However, because it has been shown that runout increases with volume (e.g. Corominas, 1996), this model is only applicable for a small range of debris flows.

Iverson et al. (1998) produced a widely applied model called LAHARZ, which calculates the inundation of a debris flow from a DEM. This routine produces a set of potential debris flow inundation zones with an associated hazard rating based on their statistical analysis. It is based on empirical equations relating cross sectional area and inundation area to total volume. Berti and Simoni (2007) produced a similar model called DFLOWZ based on 27 debris flows onto alluvial fans in the Italian Alps. However, these

types of analysis are unreliable if the debris flows are unconfined over most of their length, as the equations are derived from confined lahars and debris flows. Also, these models do not attempt to estimate eroded volumes or deposition volumes along the flow.

Fannin and Wise (2001) produced an empirical–statistical model that calculates erosion and deposition per reach of the flow, with the governing equations dependent on whether the flow is confined, transitional, or unconfined. It is based on a study of 449 debris flow events in Queen Charlotte Islands, British Columbia, Canada. This model comes closer than other empirical models to describing the realistic behaviour of debris flows without full flow dynamic modelling and has been used by Lan et al. (2008) to assess the hazard from two debris flow tracks to the railway in the region of Klapperhorn Mountain, British Columbia, Canada. The model is limited by the fact that the user needs to have a good idea in advance of the path the debris flow will take and how wide it will be. Hence it is again better suited to debris flows that are confined for most of their length.

A similar approach was taken by Miller and Burnett (2008) to produce a more complex model. They used the expected locations of erosion and deposition to calculate the evolution of the debris flow volume along the flow. Hence, by finding the expected distance at which the debris flow volume became zero, this model can be used to predict overall debris flow runout. Their study used 46 debris flows in the Oregon Coast Range to calibrate their model. These systems were field-mapped and also analysed using data from the 10 m grid DEM. The following attributes were used to calibrate the model and then predict runout: cover class (forest, clearing, etc), slope gradient, scour type (erosion, mixed, or deposition) and confining channel width. Although this model produced good results for the author's test dataset, this type of model needs to be calibrated on extensive existing data before application and is yet again only applicable to confined debris flows.

The likelihood of debris flow occurrence in a particular location is called debris flow susceptibility. This has been calculated by several authors based on (1) statistical

analysis of the locations of previous debris flows – either by discriminant analysis, or linear regression (e.g. Tunusluoglu et al., 2008), (2) physical stability considerations (e.g. Borga et al., 2004). Carrara et al. (2008) investigated a range of physically and statistically based models and concluded that similar results were obtained, but that the largest differences were apparent between models that divide terrain based on slope-units and those that use a grid-based scheme. The model that provided the best fit to their data, comprising 7000 debris flows from 1950s onwards in Val di Fassa in the Eastern Italian Alps, was one based on discriminant statistical analyses of slope units. These models give good indications of broad areas that are at risk from debris flows, but not precise information about volumes of a particular event, or buildings/roads/etc that might be at risk.

3.6.2. Flow dynamics modelling

Full dynamic flow modelling reproduces many of the observed features of debris flows, but no model to date reproduces all the features. This is because the physics of these flows is poorly understood, for they are a complex mix of fluid dynamics and grain interactions.

A key observation of debris flows is that their source materials and final deposits behave like a solid, yet during transport these same materials act like a fluid. Iverson and Vallance (2001) rationalised this behaviour by considering a debris flow as a two phase fluid: interstitial liquid and the clasts, or grains. These two phases have different properties that allow the combined material to flow: the fluid exerts a pore-pressure, and the solid has a granular “temperature” (a measure of grain vibration). Iverson and Vallance (2001) assert that these two properties are not static, but change and exchange during flow. Ancey (2007) also divides a debris flow into solid and fluid interactions. They point out that modelling has often only considered the dynamics of one of the phases, or the bulk material, rather than the more complex problem of coupling the two phases. This has commonly been performed using one of three approaches: Bingham (the Herschel-Bulkley

and Casson are special cases of Bingham rheology), Coulomb, or Bagnold. Table 3-1 summarises the behaviours of these flow types.

Without modification these simple approaches do not allow all the properties of debris flows to be reproduced. For example, none of these approaches accounts for (1) lateral levees, (2) source and deposit material being solid, yet possessing the same components as the flow, (3) variable fluid pressures and (4) bed interactions. When in one dimension models can only be used along individual slope profiles, with measured cross profiles. This has significant limitations in terms of hazard modelling as debris flows interact strongly with topography, which contributes to flow spreading and flow concentration, which in turn determine the location of potentially dangerous deposition and erosion. One dimensional models are suitable for confined debris flows, but less so for unconfined flows.

Table 3-1. Summary of main debris flow physical models. After Ancey (2007).

<table>
<tr><th></th><th>Bingham (visco-plasticity)</th><th>Coulomb (plasticity)</th><th>Bagnold Grain Interactions</th></tr>
<tr><td>Shear rate dependence</td><td>Linear dependence of shear stress on shear rate</td><td>Shear stress is independent of the shear rate</td><td>At high values: shear stress is a function of the square of shear rate.</td></tr>
<tr><td>Normal stress dependence</td><td>Shear stress is independent of the normal stress</td><td>Shear stress is a linear function of the normal stress</td><td>Shear stress is independent of the normal stress</td></tr>
<tr><td>Two-phase flow effects</td><td>One phase homogeneous material – single constitutive equation</td><td>Two phase – normal stress is split into effective stress and pore pressure</td><td>One phase.</td></tr>
<tr><td rowspan="2">Yielding</td><td colspan="2">Below a certain threshold both behave like rigid or elastic bodies, above it they flow.</td><td rowspan="2">Below a certain threshold behaves like Newtonian fluid, in which shear stress is a linear function of viscosity and shear rate.</td></tr>
<tr><td>Threshold is constant.</td><td>Threshold depends on bulk friction angle and effective stress</td></tr>
</table>

Recently, significant advances in modelling have enabled more complex 2D models to be created, which also include more complex rheology models. The most commonly used models, discussed below, solve the momentum and continuity equations using a depth-averaged integration scheme to represent the third missing dimension. The performance of three single-phase rheological approaches will be discussed: Bingham, Coulomb and Voellmy. In addition, an example of a two-phase approach will be assessed.

3.6.2.1. Bingham Rheology

FLO-2D (O'Brien et al., 1993) utilises a grid-based calculation scheme to represent the 3D surface. A digital elevation model must be provided with associated roughness for each pixel and the duration and intensity of water flowing into the source area (the flow hydrograph). A model of the rheology of the material is provided by the user to define the flow type. For debris flows a so called “quadratic” rheological model is used, which is composed of a Bingham model with the addition of a turbulent term to account for the dispersive shear stress in the Bagnold model (Hübl and Steinwendtner, 2001). Bulking or erosion by the flow is not included in the model. It has been tested on unconfined as well as confined debris flows. It does not reproduce lateral levees, but usually produces realistic interaction of the deposits with obstacles, and reasonable lateral and distal extents of the deposits (Rickenmann et al., 2006).

3.6.2.2. Coulomb Rheology

Iverson (1997) suggested another method to approximate the two-phase nature of a debris flow: to consider it as a Coulomb grain flow, but include variable pore pressure. This method was tested against experimental results (Denlinger and Iverson, 2001; Iverson and Denlinger, 2001), but it was not tested on real flow, over uneven, realistic landscape. This model does not include erosion of the bed.

Mangeney et al. (2007) also used a modified Coulomb model to approximate the two-phase nature of the grain flow. They included the hysteresis behaviour of flows by using a variable Coulomb threshold dependent on Froude number, and including empirically-derived static and dynamic friction coefficients. They showed that this kind of model in unconfined conditions can reproduce the levee-channel morphology and also the small lateral lobes seen in natural debris flows and pyroclastic flows. However, the terminal deposits were not digitate and the simulation did not produce channel erosion.

3.6.2.3. Voellmy Rheology

The Voellmy fluid friction law replicates some of the attributes of a two phase material, without having to explicitly model it as such. It incorporates the Coulomb behaviour and a turbulent response. Pirulli and Sorbino (2008) found that the Voellmy rheology implemented in their model RASH3D did not produce a good match to observed deposits, compared with FLO-2D. However, they found that FLO-2D sometimes under-predicted deposit extents and RASH3D allowed the construction of more conservative hazard maps. Rickenmann et al. (2006) found that the Debris flow Finite Element Model by the Swiss Federal Institute for Forest, Snow and Landscape Research (WSL) with a Voellmy fluid friction law was able to generate some of the properties of debris flows: lateral and distal extents of deposits and the interaction of the deposits with obstacles. FLATModel (Medina et al., 2008a; Medina et al., 2008b) also uses Voellmy-type behaviour. However, the authors have explicitly included the pressure variations induced by slope and curvature and the entrainment of additional material. This model has been tested against real debris flows and replicates lateral levees, the extent of deposits and locations of erosion.

Although with modifications models using this rheology can replicate the majority of the features of debris flows, none of these models have been tested for unconfined flows.

3.6.2.4. Two-phase approach

Recent attempts to improve the numerical description of debris flows includes the coupling of the solid and fluid phase to better model the observed characteristics of debris flows (Hutter et al., 1996). This is an approach taken by Armanini et al. (2009) in TRENT-2D. They emphasised that one of the several limitations of using a single phase continuum model is that debris flows show spatial and temporal variations in rheology. Their model solved this problem by considering the exchange of momentum between the fluid and solid phases. The bed is considered to be erodible, a significant improvement as it allows for bulking of the flow. Empirically based boundary conditions (such as the range of sediment concentrations) have to be formulated to reduce the complexity of this model to allow calculation. Despite the improvement in modelling the physics of debris flow however, this model still failed to produce lateral levees and pulsing (which results in self-blocking and sinuosity) as seen in natural flows.

3.6.2.5. Summary

For all these models rheological constraints are needed, and these are derived in two ways, depending on the complexity of the model and number of parameters required: (1) from experimental work with debris flow deposits and (2) using extensive back calculation to compare with observed deposit geometry, flow depths and flow speed (although the latter two are rarely available). The flow hydrograph is a necessary input to many of these models and Rickenmann et al. (2006) showed that 2D models are particularly sensitive to changes in this parameter.

3.6.3. Summary of debris flow modelling

Hurlimann et al. (2008), summarised the conditions under which debris flow modelling is useful: (1) the method must specify a spatial distribution, and results must cover the entire study area; (2) the method applied should be able to incorporate different volumes as input

data; and (3) the output of the method should enable intensity determination without the need for the time and expense of a full two-dimensional flow model, requiring back-calculation to determine rheology and selection of the most appropriate flow-resistance law. These conditions suit empirical models, but urge a more sophisticated approach than has been taken to date. Authors such as Fannin and Wise (2001) have made good advances, but their work needs to be expanded and generalised. Empirical models developed for mass flows on Earth are certainly easier to apply to gullies on Mars than full dynamic flow models, and the application of such models (especially more sophisticated ones) might throw useful insights into the mechanics of such flows on Mars.

3.7. Conclusions

Debris flows have a wide range of morphologies and from visual inspection bear resemblance to gullies on Mars, both in terms of morphology and scale. Debris flows on Earth require unconsolidated material with a small fraction of fines, combined with water to create the raised pore pressures necessary for mobilisation. It is clear from the evidence in Chapter 2 that these conditions can also be met on Mars.

From review of the existing literature the process of debris flow is sufficiently distinctive to enable its recognition on Mars. Not only does it leave distinct micro- and macro- landforms, but it also leaves an impact on the landscape more generally. On Earth debris flows form as part of a wider landscape assemblage and this form of recognition and analysis could be extended to Mars. The recent availability of high resolution images of Mars' surface means that metre-scale albedo changes, clast-orientations, levees and lobate deposits can be observed. Simple morphometric measurements, such as long profiles and cross sections, should be useful in determining the influence of debris flows on Mars. More complex landscape-scale morphometric measurements, such as slope-area analysis, are now possible with high resolution digital elevation models of Mars. This opens up the possibility of whole-landscape topographic analysis on Mars.

The survey of the terrestrial debris flow literature highlights some areas in need of further work, namely (1) the dynamics of unconfined debris flows and their inclusion in hazard analyses, (2) the lowest limit of erosion and upper limit of deposition for debris flows which has been hinted at, but never explored thoroughly, and (3) the development of sophisticated empirical debris flow models based on topographic interactions (using high resolution data such as LiDAR).

The neglect of unconfined debris flows in the literature opens up a fruitful area for progress in terrestrial geomorphology and hazard studies, as well as providing an ideal analogue model for gullies on Mars which are unlikely to follow pre-existing fluvial channels or valleys. To explore this avenue of research, the rest of this thesis describes a systematic study of long profiles, topographic indices and hazard analysis of unconfined debris flows with the aims of (1) determining if debris flow is active in forming gullies on Mars and (2) to widen knowledge about the behaviour and hazard of unconfined debris flows on Earth.

Chapter 4. Debris flow gullies in Iceland – hazard and Earth analogue

4.1. Introduction

The majority of this chapter has been published as a peer-reviewed article in Geomorphology (Conway et al., 2010c). Sections 4.5.1, 4.5.3 and 4.7.6 are provided in addition to the published material and slight amendments have been made to the Background and Conclusions sections to reflect these additions.

4.2. Background

Debris flows move at great speed (e.g., 0.8-28 m/s from field measurements; Rickenmann, 1999) and are able to carry metre-size boulders (e.g., Clague et al., 1985; Kanji et al., 2008). They have great destructive ability and can pose a significant hazard to people and infrastructure. I have begun a new study in the Westfjords region, situated in the north-western tip of Iceland (Figure 4-1), where the infrastructure and local population are at considerable risk from a variety of slope-process hazards, including avalanches, landslides, slush-flows, rock falls, and debris flows. Many recent incidents related to snow avalanches have been serious: for example, 20 people died in a single avalanche in Flateyri in 1995 (Arnalds et al., 2004). These events have stimulated study of these processes in this region, and as a result government agencies have defined hazard zones (Arnalds et al., 2002). Debris flows have not caused major loss of life in this area in recorded history (Decaulne et al., 2005), but with the expansion of the traditional settlements from spits in the middle of the fjords toward the hillslope, it becomes increasingly likely that a debris flow will occur

that results in considerable destruction or death. Residents report the frequent blocking of roads by debris flows, and in 1999 several flows overcame the lower slope ditch (marked in Figure 4-3), which was built to protect the town and damaged houses in Ísafjörður (Decaulne et al., 2005). The main purpose of this study is to reassess the hazard posed to these new settlements using improved data on recent debris flows.

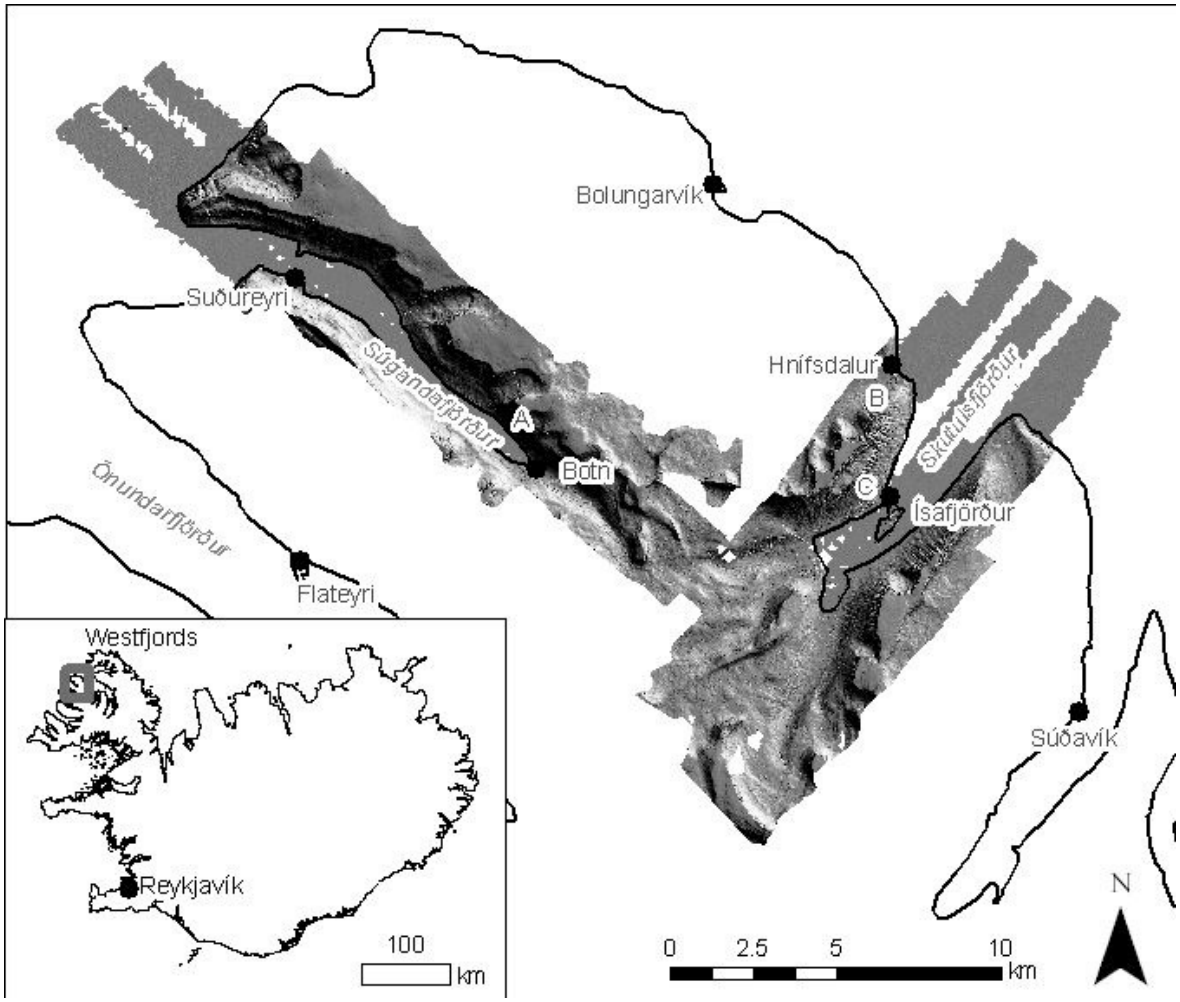

Figure 4-1. Inset: Map of Iceland showing location of main image (thick grey box). Main: hillshade representation of the NERC ARSF's LiDAR data collected in 2007 for Súgandafjörður and Skutulsfjörður, with locations in Fig. 2 marked A, B, C.

The focus of debris flow hazard prediction models is skewed toward so-called confined debris flows, which travel along pre-existing valleys, channels or torrents and emerge on to alluvial or debris fans (Rickenmann, 1999; Berti and Simoni, 2007; Gartner et al., 2008; Prochaska et al., 2008). In contrast, few studies concentrate on the hazard posed by hillslope-style debris flows (Fannin and Wise, 2001), which are not restricted by

pre-existing valleys over the majority of their length. Hillslope debris flows are common in steep terrain throughout the world, and these types of flows form significant recognised hazards in Iceland (Decaulne and Sæmundsson, 2007) and Scandinavia (Rapp and Stromquist, 1976).

Our study presents new results from quantification of the volume and pattern of debris flow deposits using topography from digital elevation models (DEMs) generated from differential GPS (global positioning system) measurements, and from LiDAR (light detection and ranging) data. This aim of the study is to improve hazard assessment in the region by empirical description of hillslope debris flows, and to provide a preliminary assessment of the suitability of debris flow as a process for forming martian gullies.

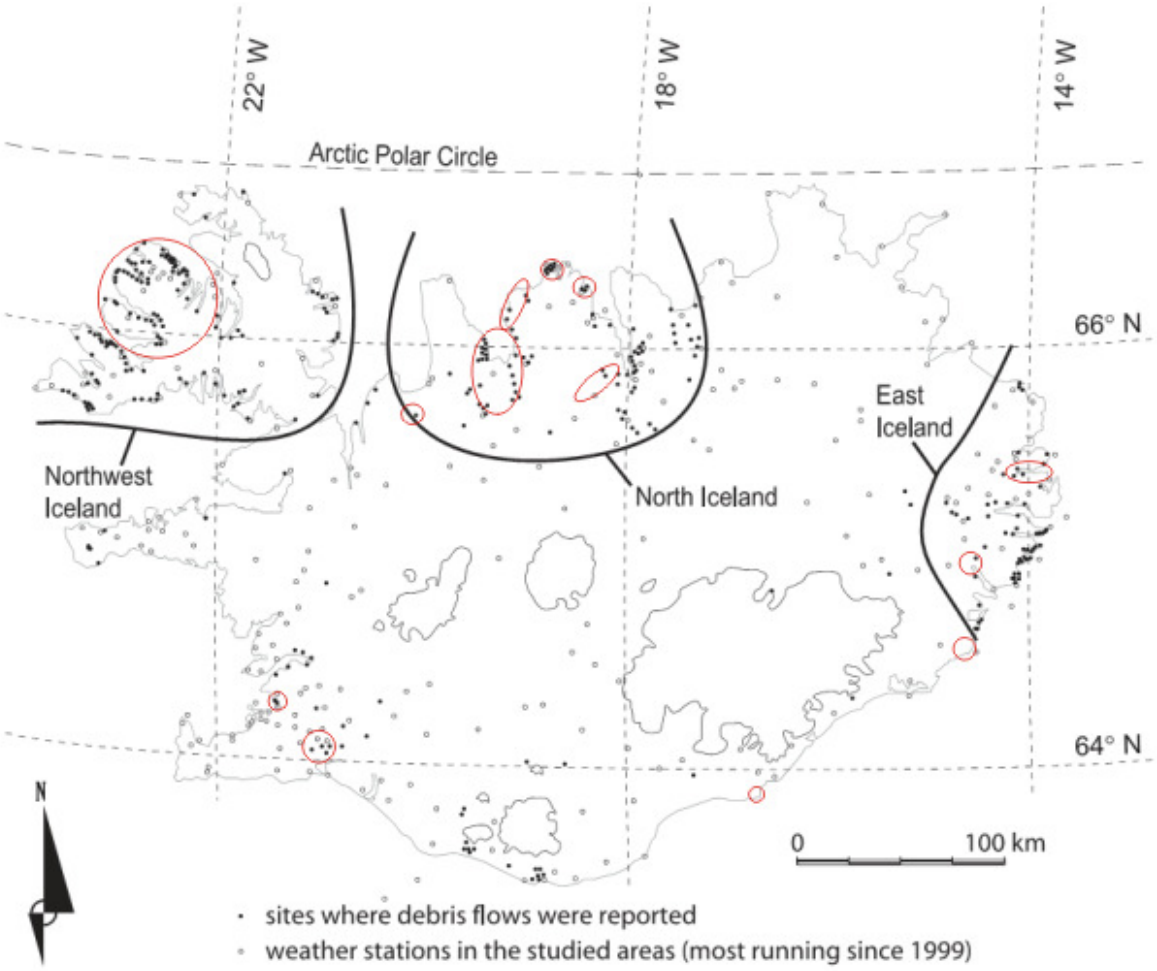

Figure 4-2. Map of Iceland, showing locations of debris flows mapped by Decaulne and Sæmundsson (2007). Red circles indicate locations where debris flows were observed by SJC in 2007 and 2008. Adapted from Figure 1 in Decaulne and Sæmundsson (2007).

4.3. Regional setting

Debris flows are located across Iceland in many different settings (Figure 4-2). A reconnaissance survey was performed around the perimeter of Iceland, and the site selected for surveying was chosen for its high frequency of debris flows. My study area in the Westfjords area of Iceland (Figure 4-1) is a typical post-glacial landscape consisting of deep fjords cut into a sequence of basaltic lava flows of Miocene age (~ 15 Ma). The hillsides in the Westfjords area rise from sea level to 700 m with average slope angles of 25-35°. The slopes are rocky and poorly vegetated; the dominant species are grasses and mosses on the soils and lichens on the rocks. The fjords themselves are incised into 2-30 m thick layers of basalt rock, which dip gently toward the SE (Decaulne et al., 2005). The slopes are very steep in the upper portion (~ 45°) and often form bedrock cliffs. The lower slopes comprise talus and relict debris flow deposits. The channels that dissect these slopes are principally incised by debris flows. These channels can lie as close together as 15 m, are densely packed along most of the slopes in the study area, and often span the entire slope from top to bottom (up to 1.5 km long in places). The area retains many inherited glacial features as well as active paraglacial features that include solifluction lobes and thick surface deposits of till on flat surfaces. Active slope processes are common here, most probably as a result of the post-glacial slope readjustment that has been ongoing over the last 10 ka since glacial retreat (Norðdalh, 1990). The temperatures in the area usually vary between -5 and 10°C with the 30 year mean annual precipitation being ~ 2000 mm/yr. Much of the precipitation falls as snow and snow patches can be preserved in shadow into the summer months. The maritime position of the Westfjords means that snow cover can be very variable and liable to thaw suddenly even in winter.

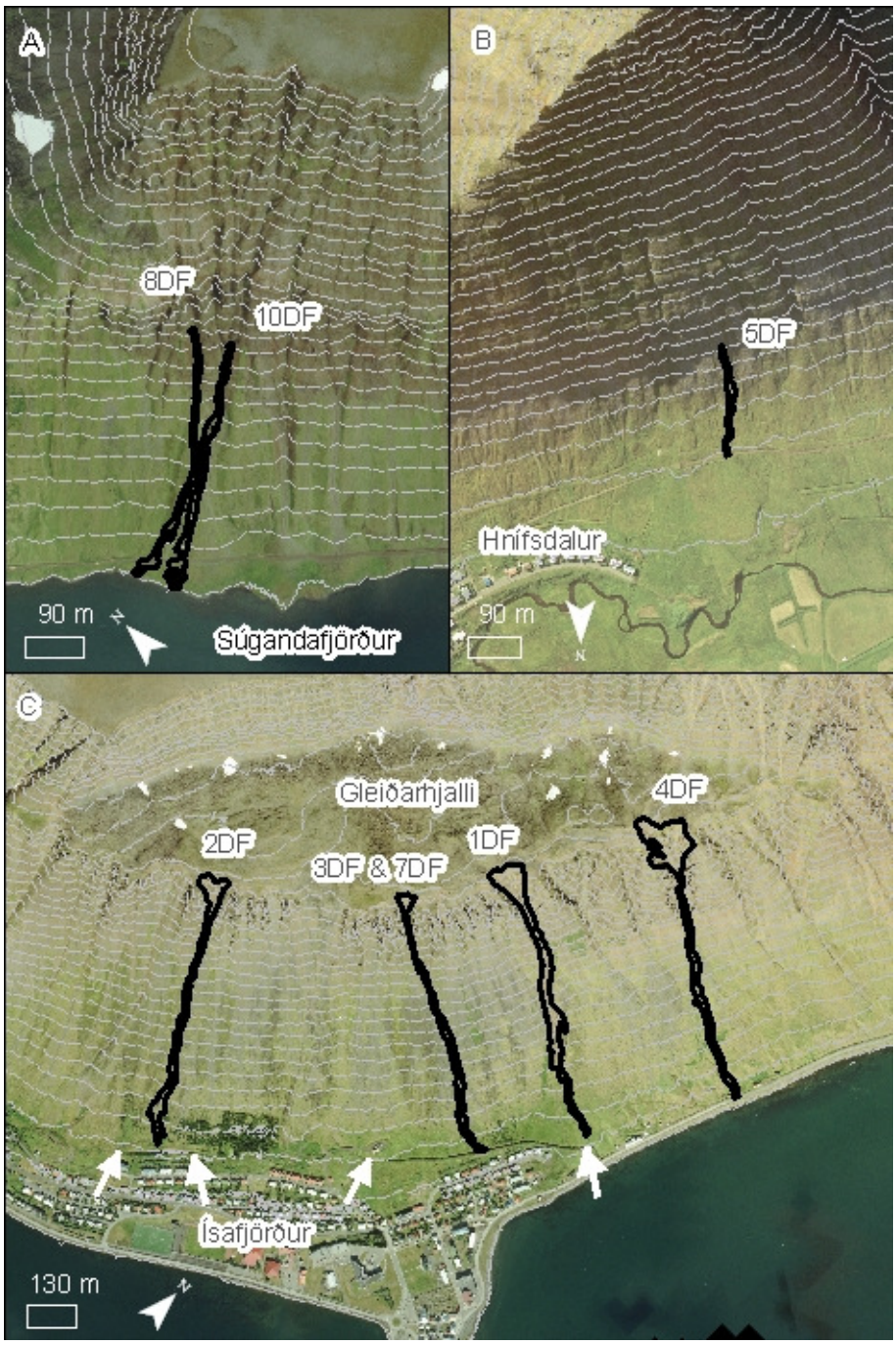

Figure 4-3. Air photographs of the study area obtained by NERC ARSF in 2007, with debris flows in this study marked with black outlines. Contours are at 20-m intervals. (A) Debris flows 8DF and 10DF are located on the east side of Súgandafjörður, north of Botn on the road to Selárdalur. (B) Debris flow 5DF is located to the south of Hnífsdalur above the valley road. (C) Debris flows 1DF, 2DF, 3DF, 4DF, and 7DF are located above the town of Ísafjörður, sourced from the Gleiðarhjalli bench. White arrows indicate the extents of the two main drainage ditches mentioned in the text.

The town of Ísafjörður is mostly located on a spit formed by the action of the sea, with expansion of the town over the last 50 years being accommodated along the basal slopes of the fjord. The slope above Ísafjörður (Figure 4-3C) is interrupted at ~ 450 m altitude by the Gleiðarhjalli bench, which slopes gently to the SE and is covered by ~ 30 m

of glacial sediments; these comprise gravelly to silty sand and subangular to subrounded clasts that range in size from centimetre to metre. On top of these deposits lie many centimetre to metre sized angular clasts derived from frost shattering of the bedrock and glacial clasts themselves. These sediments reach the angle of repose very quickly, as frost shattering promotes erosion of the bedrock cliff at their base and creep pushes the sediment body forward towards the bench edge. This means that the debris flows above Ísafjörður are not supply limited, but limited by the frequency of triggering events, unlike most other flows in the area (Glade, 2005).

Debris flows in this area are triggered by rapid snowmelt or prolonged rainfall (Decaulne et al., 2005; Decaulne and Sæmundsson, 2007). These processes saturate the sediment stack, which further destabilises the already unstable sediments. A debris flow is then triggered as a result of undercutting of these sediments by water emerging from beneath the sediment stack at the interface with the basalt bedrock. Rockfalls originating at the exposed edge of the debris stack have been observed immediately prior to a debris flow and are a probable cause of failure (Decaulne et al., 2005). The glacial till fails by rotational sliding and then forms a debris flow.

The mean interval between large flows is only 5 years (Decaulne et al., 2005). On other slopes in Iceland, debris flows are much less frequent and generally smaller because they are supply limited (Glade, 2005): the debris on the slopes must reach a certain thickness and steepness before it can slide (Ballantyne and Benn, 1994; Wilkerson and Schmid, 2008). The debris flows above the town of Ísafjörður provide a unique opportunity for study because (i) the frequency of large events is unusually high and (ii) the majority of the deposits are preserved on the slopes. This means that I have the opportunity to study very fresh debris flows in which the influence of post-depositional reworking is minimised, thus allowing more accurate quantification of erosion and deposition volumes and patterns.

In addition to the SE-facing slope above Ísafjörður, two additional sites (Figure 4-3A and Figure 4-3B) were selected because they had also experienced fresh debris flows just prior to the field visits in 2007 and 2008. Firstly, I studied an area to the south of Hnífsdalur, a village located to the north of Ísafjörður. Debris flows are much less frequent here than in Ísafjörður, but I investigated a small fresh flow sourced from the soil mantle on the slope above the valley road, which occurred here in late spring or early summer 2007. This flow originated, in all likelihood, as a failure triggered by concentration of overland flow that then eroded downslope before deposition. Secondly, on the north side of Súgandafjörður, debris flows regularly block the road and two fresh flows had cut off the road between Botn and Grensfjall between the 2007 and 2008 field visits. The flows originate by the "fire hose" (e.g., Johnson and Rodine, 1984; Coe et al., 2007; Carrara et al., 2008) mechanism in alcoves cut into the bedrock cliffs bounding the fjord. This triggering mechanism is characterised by the concentration of overland flow by chutes or depressions in the bedrock that evolves into a debris flow as it picks up material. This material has to build up by weathering and erosion of the bedrock before a debris flow can be formed (as described by Glade, 2005) hence the time between large events is much longer than at Ísafjörður. The source material is the product of frost shattering of material that has collected in these alcoves under the action of gravity. Interestingly, the flows did not originate from the top of the slope above the fjord (700 m asl) but from material accumulated at ~ 500 m or lower.

4.4. Materials and methods

4.4.1. Previous work and methodology for this study

Debris flow volumes are usually estimated from either the failure scar (e.g., Gabet and Bookter, 2008) or the deposits themselves (e.g., Decaulne et al., 2005). Traditionally this is done by measuring cross sections and long sections of the features, although the precise

method and associated errors are rarely reported (e.g., Decaulne et al., 2005; Gardner, 1989; Okuda, 1989; Rapp and Nyberg, 1981). Exceptions to this include Santi et al. (2008), who report errors as small as ± 23 % on volume estimation using the cross section technique with a slope profiler. They take into account the variation in technique between individuals and the use of differing locations for the cross sections, but do not include an error associated with estimating the pre-flow topography. A report that examined methods for estimating the erosion volumes removed by rills (Casali et al., 2006) recommended that sampling by microtopographic profile meter, which produces 50 points over 1 m to get an error of < 10% in volume calculation.

Empirical estimates of volumes have been derived from morphological data (e.g., Larsson, 1982; Innes, 1983a; Fannin and Wise, 2001), but these rely on a large sample size and their applicability varies by region. Empirical relationships from large data sets relating volumes, total travel distance, and other dimensions have been found for confined debris flows (Rickenmann, 1999) and hillslope debris flows (Lorente et al., 2003), but neither of these empirical approaches give information on the structure and pattern of deposition and erosion. Iverson, et al. (1998) produced a widely applied model called LAHARZ, which calculates the inundation of a debris flow given a DEM. This routine produces a set of potential debris flow inundation zones with an associated hazard rating based on their statistical analysis. It is based on empirical equations relating cross sectional area and inundation area to total volume. However, this analysis is not reliable if the flows are unconfined over most of their length, as the equations are derived from the study of 27 confined lahars originating from nine volcanoes. It does not attempt to estimate eroded volumes or deposition volumes along the flow. Fannin and Wise (2001) produced an empirical–statistical model that calculates erosion and deposition per reach of the flow, with the equations dependent on whether the flow is confined, transitional, or unconfined. It is based on the study of 449 debris flow events in Queen Charlotte Islands, British

Columbia, Canada. This model comes closer than other empirical models to describing the realistic behaviour of debris flows without full flow dynamic modelling.

Repeat stereo photogrammetry has been used to estimate overall slope denudation (Coe et al., 1997; Breien et al., 2008). Coe et al. (1997) used a 2 x 2 m grid, and achieved a volume error of ±5%. Breien et al. (2008) used a 3.3 x 3.3 m grid and achieved an error of ±10%. Neither study revealed the fine-scale structure of the debris flows (e.g., the levees were poorly resolved). In landslide studies LiDAR is often used in conjunction with other datasets, e.g., Chen et al. (2006) used DEMs derived from photogrammetry to compare with LiDAR topography. However, the lower accuracy of the photogrammetry and the difficulty in georeferencing all the datasets meant that the authors were only able to detect 10-100 m vertical changes. Good results have been obtained by comparing repeated LiDAR surveys (Scheidl et al., 2008) with estimated errors in the volume calculation ranging from just 9% up to 55%. No repeat LiDAR surveys have been performed in the Westfjords area, so I have used a combination of LiDAR data and differential GPS data to quantify the changes in morphology along the debris flows.

4.4.2. Data collection

A photographic survey of debris flows Iceland was performed in 2007 and again in 2008, which formed the basis for the qualitative comparison to gullies on Mars (Figure 4-2). Near Ísafjörður, eight debris flows (Figure 4-3) were surveyed using a Leica System 500 differential GPS in 2007-2008. Five debris flows were examined on the slopes above Ísafjörður (Figure 4-3C): one on the slope above Hnífsdalur in the adjacent valley (Figure 4-3B), and two on the east slopes of Súgandafjörður (Figure 4-3A). The relative timing of the activity of the debris flows in this study is shown in Table 4-1. A base GPS unit was positioned at the foot of the slope within 3 km of the rover GPS units. Point elevation data were collected by two roving units, with the operators collecting three or more epochs of data per point. To ensure high quality, data were not collected when the Global Dilution of

Precision (GDOP) value (which is calculated real-time from relative satellite positions) was > 7. A Leica System 800 Total Station (TPS) was used to collect additional data in 2008. The location and orientation of the TPS was obtained by collecting shared points with the GPS. The TPS collects point elevation data using a laser ranger equipped with accurate internal determinations of horizontal and vertical angles. The TPS could collect points at a maximum distance of 450 m.

Four main types of sampling were performed:

(i) channel long profile: recording the lowest point between the levees;

(ii) levee long profile: recording the maximum elevation of the levees on each side of the channel;

(iii) cross profiles: taken at ~ 50 m intervals (10 m for 5DF, 20 m for 7,8,10DF) along the debris flow; and

(iv) debris flow edge: only measured if the flow was well defined.

For each of these methods the topography was sampled at 0.5-2.0 m intervals, with more frequent sampling used where the topography changed more rapidly. This frequency of cross sections follows the scaled-up methodology advised by Casali et al. (2006).

Table 4-1. Dates of activity of the debris flows and dates of surveys described in this study. See Figure 4-3 for geographical locations of numbered debris flows. Numbers in brackets indicate the debris flow identification number in Decaulne et al. (2005) and * indicates debris flow occurred along the same track as the debris flow in the brackets.

Date	June 1999	June 2006	spring 2007	summer 2007	spring 2008	summer 2008
Event	2DF (1)	1DF	5DF	LiDAR and GPS survey	7DF (2DF*)	GPS Survey
	3DF (4)				8DF	
	4DF (5)				10DF	

The GPS data were supplemented with LiDAR data acquired using an Optech ALTM3033 instrument and aerial photography taken with a Leica-Wild RC10. These data were collected on 5 August 2007 by the U.K. Natural Environment Research Council's Airborne Research and Survey Facility (NERC ARSF; Figure 4-1). Seventeen flight lines were flown allowing the collection of 63 million LiDAR points and 63 aerial photographs.

The aerial photographs were orthorectified, mosaiced, and georeferenced using BAE System's SocetSet software.

Further processing of the LiDAR data was required to correct for between-track horizontal shifts of up to 2 m, which in steep areas results in an equivalent magnitude of vertical error. This problem has been highlighted by Favalli et al. (2009) who state that sub-metre scale measurements cannot be taken without correction for these between-track errors. To achieve this correction I used a least squares matching technique developed by Akca (2007b; 2007a), which matches the surface shape and LiDAR intensity between each track to align the tracks relative to one another. This adjusted data set was then georeferenced by aligning it to the GPS data collected in the 2007 campaign. This processing resulted in the cross-track and georeferencing errors in the LiDAR data being reduced to ~0.1 m vertically and < 0.25 m horizontally as detailed in Table 4-2.

Table 4-2. Summary of estimated measurement and processing error generated during GPS data collection and processing.

	Vertical Error (m)	**Horizontal Error (m)**
Human Error	0.05	0.05
GPS calculation error	max = 0.121	max = 0.043
-wobble of antenna	mean = 0.01	mean = 0.005
-constellation of satellites		
(number and position)		
LiDAR	~ 0.25 (extremes up to 2 considering the horizontal error)	~ 1-2
LiDAR (post adjustment)	~0.1	< 0.25
Kriging Error 1DF	Variable, max = 0.85, mean = 0.11	Not calculated
Kriging Error 5DF	Variable, max = 0.42, mean = 0.07	Not calculated
Kriging Error – GPS only	max ~ 1.0 mean ~ 0.3	Not calculated
Kriging Error –LiDAR + GPS	max ~ 1.4 mean ~ 0.5	Not calculated
Kriging Error – from buffer	max ~ 1.6 mean ~ 0.9	Not calculated

4.4.3. Generation of elevation models

To measure volumes of debris flows, I calculated the slope shapes before and after debris flows. In all calculations I used the last return LiDAR data where the height of the ground at the LiDAR shot point is calculated using the return time of the last laser light to reach

the receiver from that particular shot. I used these data to create a regional 5-m DEM using the LiDAR Explorer 2.0 extension for ArcGIS. This program uses the mean value of the LiDAR shots within each pixel to produce a smooth DEM and if necessary uses linear interpolation between the LiDAR shots to fill small data gaps.

The combined 2007 GPS and last return LiDAR survey data for the debris flows were converted into local 0.25-m DEMs for each debris flow. This was performed using the universal Krige interpolation method provided within the "Geostatistical Analyst" tool of ESRI's ArcMap software, which has been verified as a valid method for this type of data (Scheidl et al., 2008). I used Krige rather than Natural Neighbour, as recommended by Scheidl et al. (2008), because the Krige method allows inclusion of the expected asymmetry of the surface as well as the asymmetry of the sampling, and provides an estimation of the errors associated with the prediction. Because of the relatively low number of points compared to those processed by Scheidl et al. (2008), this processing was computationally inexpensive to perform — high cost being the main argument presented against this method by Scheidl et al. (2008).

For those debris flows that occurred before the LiDAR survey (1DF, 2DF, 3DF, and 5DF), the pre-flow morphology was estimated using the 2007 data alone. This was achieved by taking all the GPS and LiDAR points within a 5-m buffer around the boundary of the flow (i.e., excluding all the points that lie on the new debris flow) and performing a Krige interpolation based only on these points — in essence "smoothing out" the debris flow to estimate the preexisting topography. Where the debris flow is wide, especially in the alcoves, the interpolation was performed across large distances (of the order of 50 m). The post-flow surface was estimated using all of the 2007 data across the flow. For those debris flows which occurred after the LiDAR survey (7DF, 8DF, and 10DF), the pre-flow morphology was interpolated from the 2007 LiDAR and GPS data and the post-flow morphology derived from the 2008 GPS and TPS data.

4.4.4. Volume estimation and patterns

To assess trends in deposited volume over the length of the debris flow, the GPS points representing the margins of the debris flow were converted into a polygon shapefile using ArcGIS software. This polygon was then split into along-flow segments (Figure 4-4). These segments were equally spaced and lay perpendicular to the channel centre line (i.e., they were not necessarily of equal area). Section length was at 5-m intervals for all debris flows — apart from the small debris flow, 5DF, which had a 2-m interval. For each debris flow, an isopach map was produced by subtracting the post-flow surface from the pre-flow surface. Then for each segment, the total volume of erosion and of deposition was calculated by summing the negative and positive pixels, respectively, of the isopach map falling within the segment. To account for the varying areas of each segment, the volumes were divided by the area of the segment, giving a representative thickness of deposition and depth of erosion for each segment. The concept of representative thickness is a proxy for volume.

The segmented polygons were then used to generate statistics based on underlying topography. To analyse how the flow responded to variations in the regional slope morphology, I used a 5-m DEM produced from the LiDAR data. To analyse responses to the morphology produced by the flow itself, I used the higher resolution 0.25-m DEMs produced for each debris flow from LiDAR and GPS data. For each DEM, the mean slope angle and elevation were calculated using the standard tools provided in Spatial Analyst of ArcGIS. The slope angle is derived using the steepest downhill slope as calculated by fitting a plane through the eight nearest neighbours.

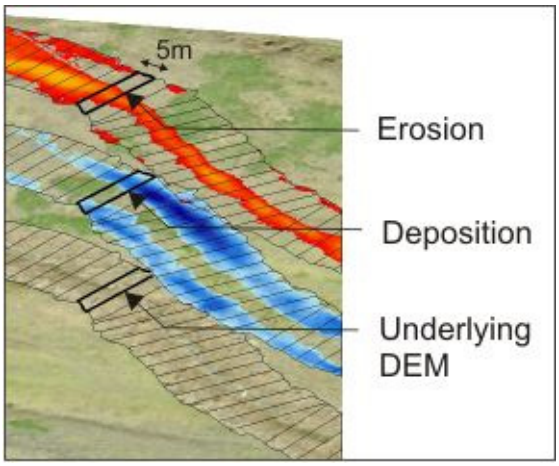

Figure 4-4. A schematic oblique three-dimensional illustration of how analysis was performed by segmenting the debris flows along-track. This figure shows debris flow 1DF, which has been split into segments 5 m wide at the channel centre-line. Summary statistics were derived for each of the segments from underlying data sets, such as isopach maps of erosion, deposition, and an underlying DEM.

To analyse patterns of erosion and deposition in all the flows together I normalised their individual segment erosion and deposition representative thicknesses. Normalisation is performed for erosion and deposition separately and is calculated by dividing representative thickness for each segment by the total representative depth or thickness for each flow (of erosion or deposition as appropriate) so that data for all the flows can be compiled together (otherwise the signal from the largest, freshest debris flow would dominate). This normalisation then adjusts for differences in both scale and age.

4.5. Results

4.5.1. Field observations – debris flows around Iceland

The locations of debris flows throughout Iceland have been documented by Decaulne and Sæmundsson (2007). Figure 4-2 shows their results and the locations of debris flows that I observed during fieldwork in 2007 and 2008.

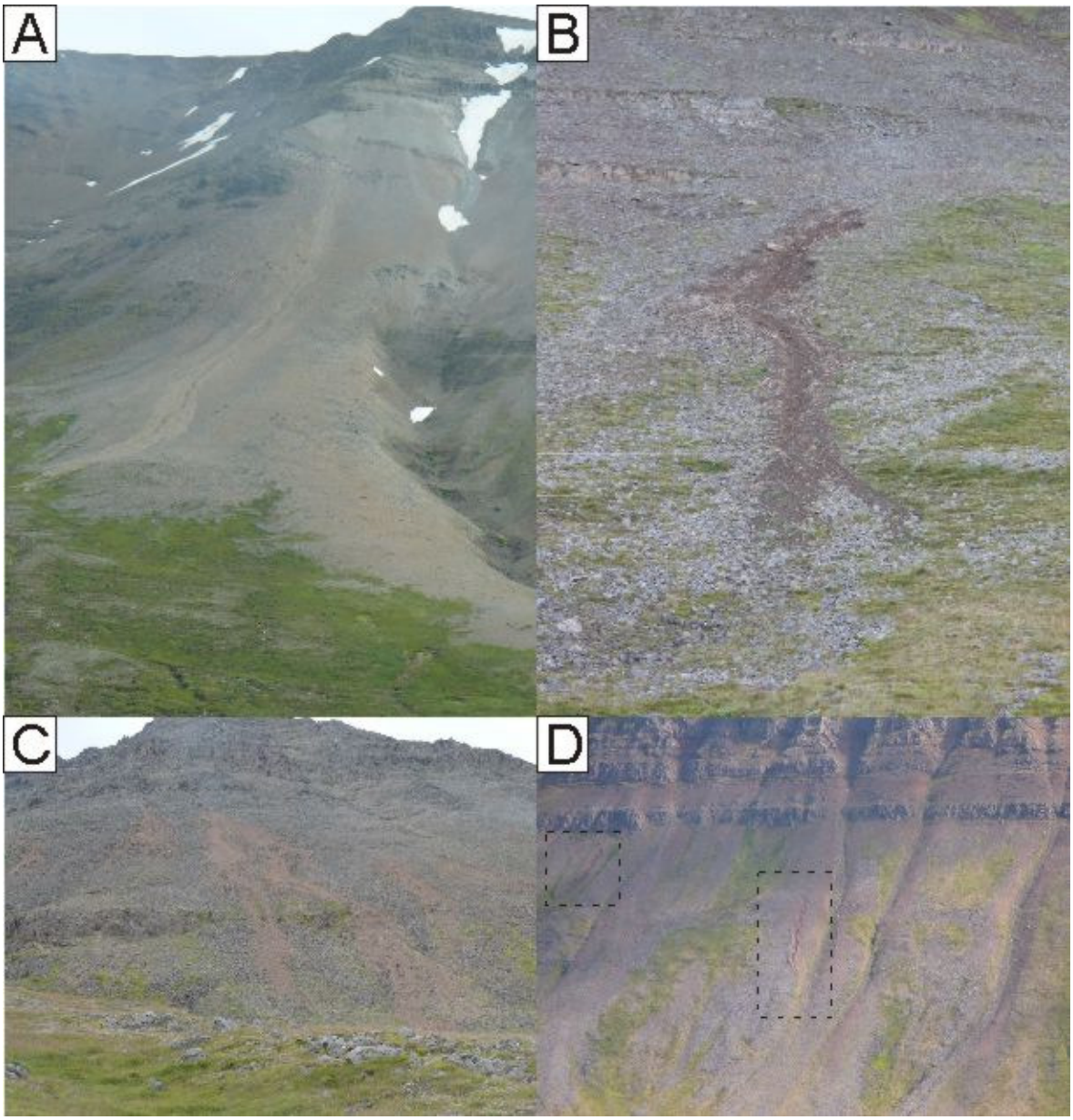

Figure 4-5. Examples of hillslope debris flows in Iceland. (A) debris flow on Hjallkarseyrarhild in the Westfjords, ~ 100-200 m long. (B) & (D) Small debris flows on the southern slopes of Skutulsfjorður (opposite Ísafjörður), all ~ 5 m wide. Dotted lines highlight the small debris flows in (D). (C) Debris flow on the hillside east of Vidilaekur, Eastfjords, ~ 50 m long.

Purely unconfined (hillslope) debris flows, such as debris flow 5DF in Hnífsdalur, which are on an open slope for their whole length, are common in Iceland. Some examples are shown in Figure 4-5. This type of debris flow starts with a slip scar, which is wider than the resulting flow and shallow, the base is usually flat with sharp scarps marking the edge of the scar. The deposits are the same as for those flows that are part-channelized, with lateral levees and digitate terminal lobes. These flows are often small in size, compared to part-channelised, or fully confined debris flows. They are located either

partially, or completely within talus slopes. In some cases they have a similar depositional morphology to their larger confined cousins (Figure 4-6A). In other cases they have a morphology that resembles a modified landslide more than a classic debris flow. An example of this form of flow is shown in Figure 4-5C: it is a blanketing digitate deposit without well-formed levees. Small debris flows on the southern slopes of Skutulsfjorður (Figure 4-5B and Figure 4-5D) have an intermediate morphology, with well-defined levees, but very digitate terminal deposits. In the field I observed that the debris flows on the southern slopes of Skutulsfjorður deposit material on similar slope angles to their initiation, with supply of material defining the down-slope extent of the deposits, rather than the slope angle. All these hillslope debris flows occur on very steep slopes (> 35º), however there seemed to be no systematic pattern as to the position in the slope where they initiate.

Confined debris flows are also common in Iceland; examples are shown in Figure 4-6. Debris flows were found with different proportions of their overall length being confined. Figure 4-6A shows the slope in the Westfjords, where two of the debris flows are confined for ~ 50 % of their length and have small fans. Principally unconfined debris flows are also located on this slope. Figure 4-6B shows an example in which a deep alcove leads straight into the debris fan, which has many levees over its surface. More developed systems are shown in Figure 4-6C and Figure 4-6D, in which large, deep alcoves lead to narrow bedrock gullies and debris flows emerge onto a wide and rough fan. On these fans the surface is constantly being reworked by debris flows, giving rise to this rough, leveed surface.

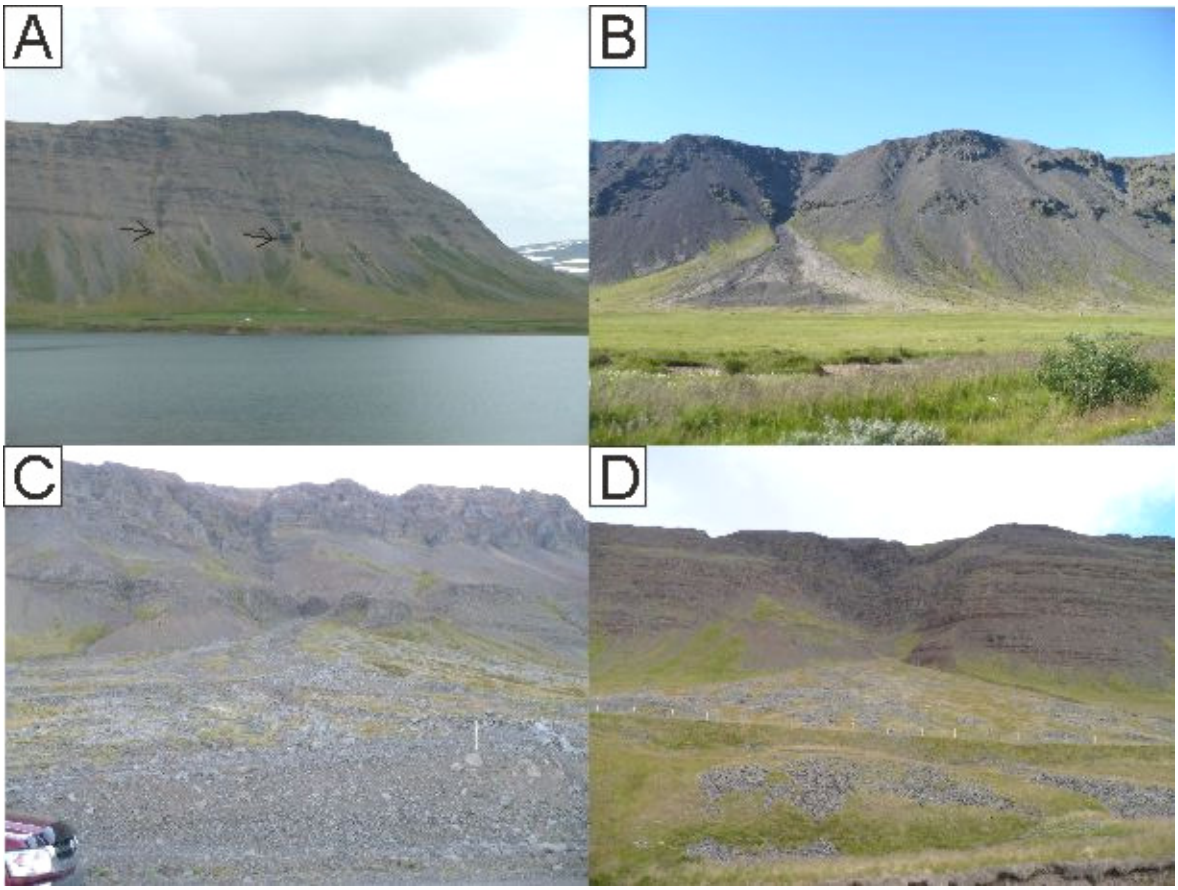

Figure 4-6. Examples of confined debris flows in Iceland. (A) Tindarfjall, on north side of Dýrafjörður, Westfjords, slope is ~ 600 m high. Arrows point to the two confined flows mentioned in the text. (B) South side of Ingólfsfjall near Selfoss, SW Iceland, the slope is ~ 300 m high. (C) East side of Reykjaströnd, north of Sauðárkrokur, northern Iceland, the slope is ~ 500 m high. (D) South slopes of Silfrastaðarfjall part of Blönduhlíðarfjöll, northern Iceland, the slope is ~ 400 m high.

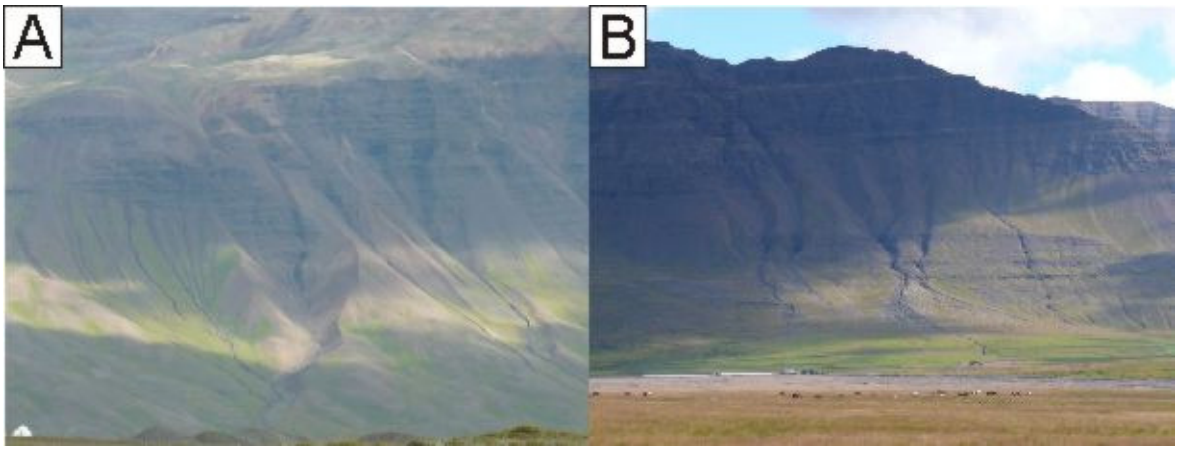

Figure 4-7. Examples of deeply incised confined debris flows in Iceland. Both slopes are about 500m high. (A) Debris flows on the western side of Vatnsfjall, northern Iceland, showing debris flows with different degrees of incision. (B)The slope above Kringlumýri, on Blönduhlíðarfjöll, northern Iceland.

A sub-category of the confined debris flows in Iceland is characterised by upper reaches deeply incised into talus, or colluvium, with a leveed terminal fan (two examples are shown in Figure 4-7). The incised reaches are v-shaped in cross section and as incision progresses more and more of the bedrock is exposed. However, because the bedrock takes much longer to erode, the alcove morphology is dominated by erosion of the talus.

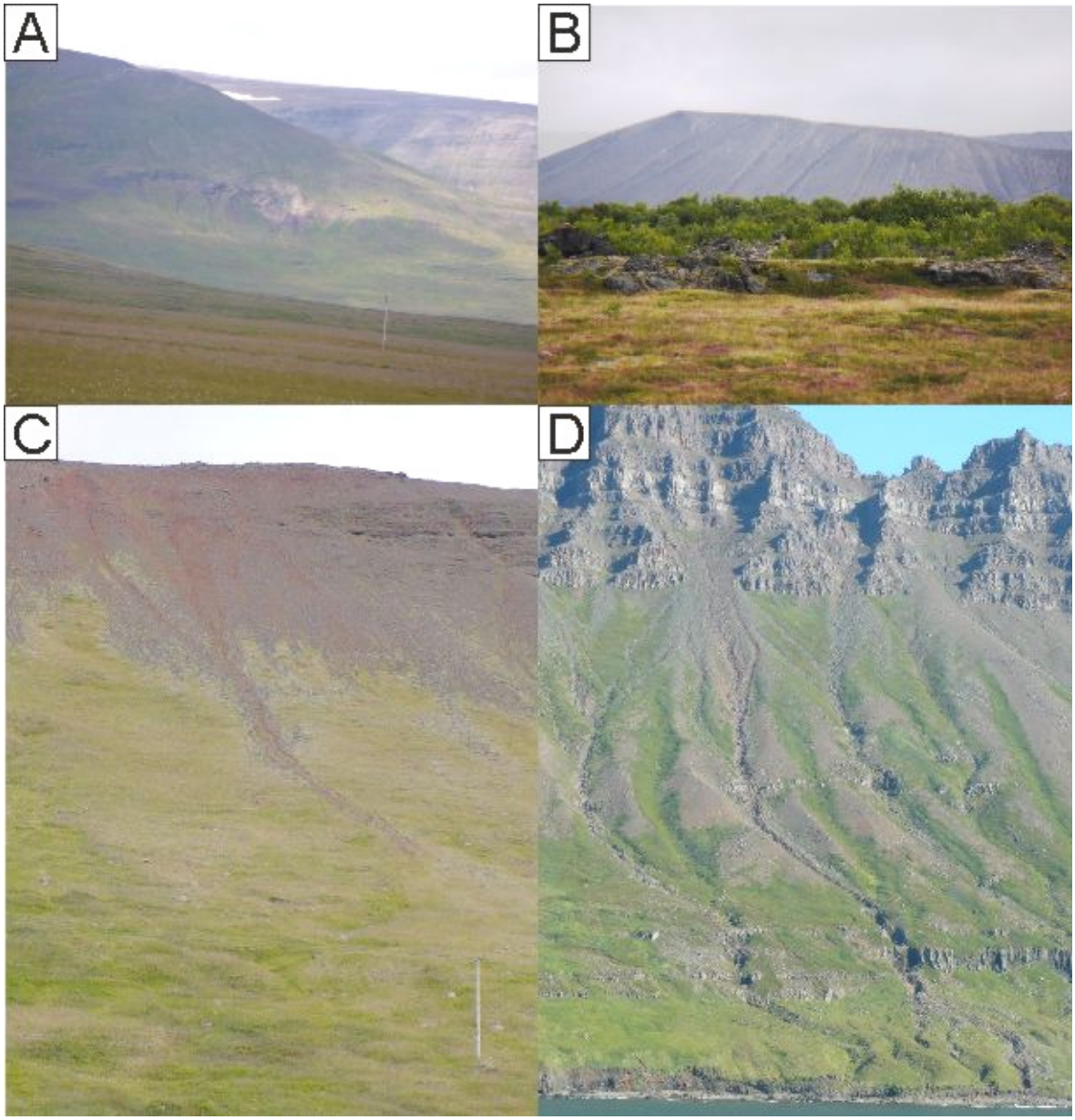

Figure 4-8. Examples of debris flows with unusual settings and different morphologies in Iceland. (A) Rounded alcoves on Southeast side of Breiðabólstaður, northern Iceland (~ 300 m high). (B) Alcoves and gullies on west side of Hverfjall pyroclastic cone (~ 150 m high). (C) Debris flows with tributaries on southeast slope of Bólstaðarhlíðarfjall (~ 200 m high). (D) Debris flows on north side of Seyðisfjörður, Eastfjords (slope is ~ 700 m high).

Figure 4-8 displays some of the other morphologies and settings of debris flows observed in Iceland that have resemblance to gullies on Mars. Figure 4-8A shows debris flows with very wide and rounded alcoves, which start part-way downslope, similar to the "widened" alcoves of Malin and Edgett (2000). Well developed alcoves and gullies formed by debris flows on Hverfjall, a monogenetic cinder cone near Mývatn, are shown in Figure 4-8B. These are similar to gullies incised into mantle deposits (see Figure 3-6 in previous chapter). Figure 4-8C shows a hillslope debris flow which has a tributary network, very digitate margins and which narrows downslope. This debris flow is similar to the new deposits discovered on Mars (Malin et al., 2006) and the "abbreviated" alcoves of Malin and Edgett (2000). The control of bedrock on some of the debris flow systems is shown by Figure 4-8D and also in Figure 4-6C. In both examples there are several points where the flows pass across bedrock layers, which temporarily cause the flow to become channelized. This emphasises that the influence of bedrock structure on debris flow morphology cannot be underestimated.

In addition, I made observations of springs on slopes in various parts of Iceland. Most occurred on open slopes and had little impact on the slope morphology (Figure 4-9A and C). Some were associated with debris flows (Figure 4-9D and E). Water seeps also occur in the alcoves of the debris flows sourced from Gleiðarhjalli bench above Ísafjörður (Figure 4-9B). Water runs from these springs all year round except when it is very dry. These springs are sourced from shallow aquifers, recharged from rainfall or snowmelt on the bench and slopes above. They are not responsible for the saturation of the material that produces the debris flows, but they do contribute to instability by undercutting the saturated material on the bench (Decaulne, 2001). It is assumed that a similar process is operating in debris flows shown in Figure 4-9D and E, as water was present, yet no debris flow had occurred.

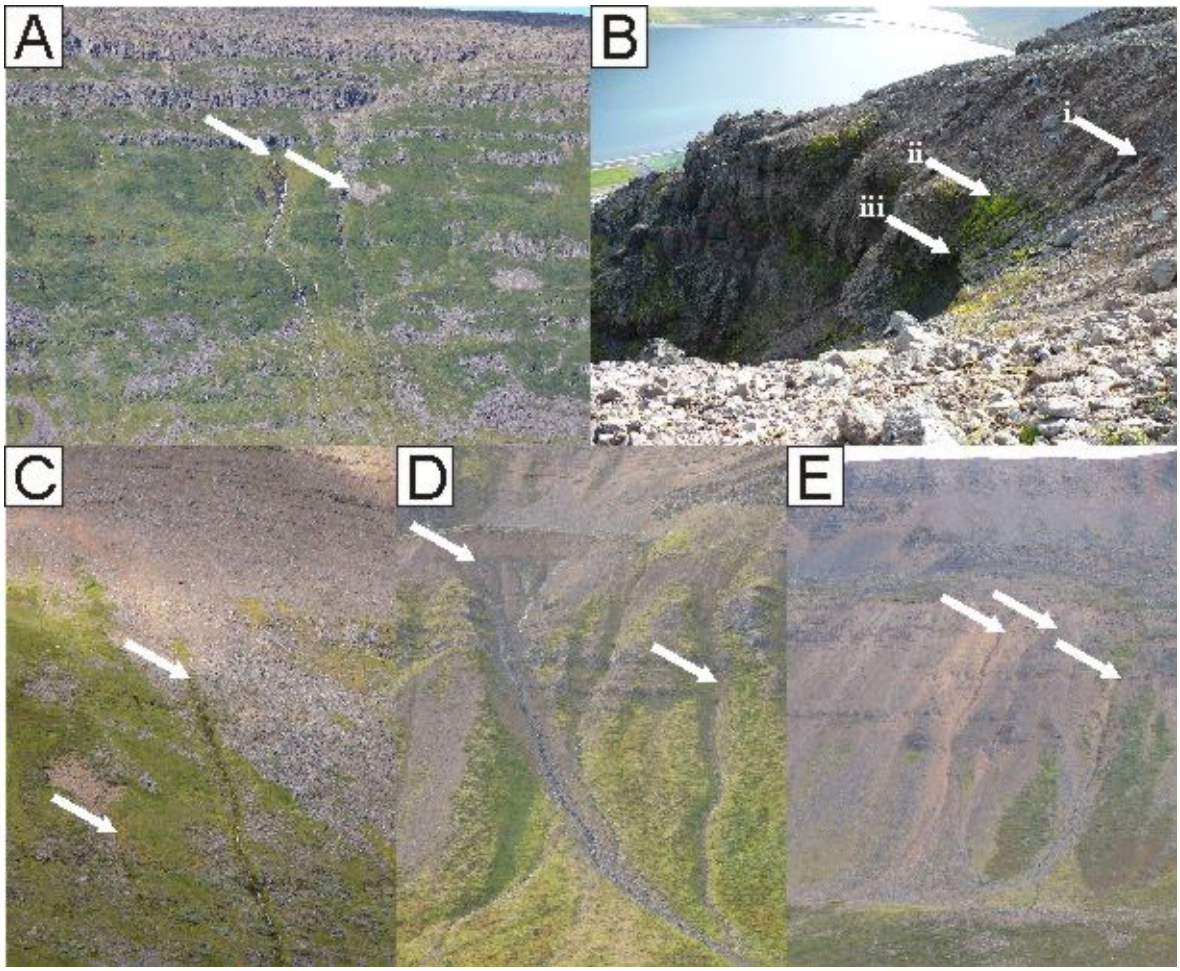

Figure 4-9. Examples of gullies in Iceland associated with springs. (A) Springs on west side of Skötufjörður, near Valahnúkur, Westfjords. (B) Springs in the alcove of a debris flow sourced from Gleiðarhjalli bench, above Ísafjörður. i indicates a small slip scar, ii indicates vegetation living on spring water and iii indicates the fully wetted sediment below. (C) Slope on the north side of Hnífsdalur in the Westfjords. Top arrow indicates a spring with no detectable impact on the slope and the bottom arrow shows a small spring that has caused a small failure above it. (D) Two springs associated with debris flows. Slope is located to the south of Mòafell, on road 82, northern Iceland. (E) Springs associated with small debris flows in the western slope of Barnadalsfjall to the north of Hofsós, northern Iceland.

4.5.2. Field observations – sources of materials

All the debris flows in this study form levees, and some exhibit a terminal lobe. The levees flank the channel, and when large and fresh have steep interior and exterior slopes. The levees all contain a fine matrix that supports the clastic material; however, the source material and age of the deposits varies between flows.

Decaulne (2001) observed that debris flows 2DF, 3DF, and 4DF were sourced from a rotational slide of the glacial material on top of Gleiðarhjalli bench. This material is characterised by the high content of subrounded to subangular clasts ranging from

centimetres to metres in size supported by 10-30% orange-brown fines (see grain-size analysis in Decaulne et al., 2005). I found that the materials that compose the levees in debris flow 1DF matched the glacial deposits, hence the composition of the levees reflects the composition of the source area. I used visual inspection and correlation to determine the source deposits of the remaining flows in this study (Table 4-3). The precise drainage areas for the Ísafjörður debris flows (1DF, 2DF, 3DF, 4DF, and 7DF) are difficult to determine, because much of the water flow occurs beneath the surface of the bouldery Gleiðarhjalli bench. I infer that the majority of the contributing area is from the Gleiðarhjalli bench, with some contribution from the small plateau above. The other debris flows (5DF, 8DF, and 10DF) have rockwall chutes upstream, which have small (or negligible in the case of debris flow 5DF) plateaus above them.

Table 4-3. Summary of materials and drainage areas for each of the debris flows in this study.

Debris flow ID	Source material	Estimated clast-size range (estimated median) m	Estimated percent fines	angularity	Upstream area
1DF	Glacial deposits	0.01 - 4 (0.3)	10-30	subrounded to subangular	Gleiðarhjalli bench
2DF	Glacial deposits	0.01 - 4 (0.3)			
3DF	Glacial deposits	0.01 - 4 (0.3)			
4DF	Glacial deposits	0.01 - 4 (0.3)			
5DF	Talus and soil	0.01 - 0.2 (0.05)	30-50	mainly angular	Rock chute
7DF	Weathering of bedrock and reworked material	0.01 - 1.5 (0.2)	< 5	subangular to angular	Rock chute
8DF	Weathering of bedrock	0.01 - 0.8 (0.1)			
10DF	Weathering of bedrock	0.01 - 0.8 (0.1)			

I have observed that debris flows usually take the path of a previous flow for at least the upper third of the total length. Levees that have been washed free of fines can be infiltrated by them again in a subsequent flow and in addition the levees can be built up in height. When flows are frequent, this means that caution is required when estimating the volume without knowledge of preexisting topography. Other authors have noted that levees are often reworked in subsequent flows, leaving almost no evidence of the previous flow, which leads to underestimation of historical frequency (e.g., Luckman, 1992).

Decaulne (2001) reported anthropomorphic removal of material from debris flows 2DF and 3DF because they affected the town. At debris flow 7DF, I observed that a significant quantity of material had been mechanically excavated from the ditch to the bank between the 2007 and 2008 field visits. These deposits were therefore not included in my study, and this anthropomorphic modification should be considered when drawing conclusions from volume data. I observed that large quantities of material had been moved from the road to the downslope verge in debris flows 8DF and 10DF, however, these deposits were included in my survey. As the deposits were moved by 5 m or less, which is on the same order as my sampling distance, I decided this was not sufficient to disrupt the conclusions based on the analysis of volumes in this study.

4.5.3. Field observations – changes over time

In 2006, when the deposit of debris flow 1DF was only a few weeks old, the clasts were masked by bright orange-brown fines, but these had been washed away by 2007, as shown in Figure 4-10A. It is apparent that stream flow between the levees had removed material (especially the fines) even by the time the first photograph was taken in 2006. By 2009 another small debris flow had occurred along the same path, reworking the material and making the debris flow appear fresher again. Figure 4-10B shows the source area of debris flow 5DF in 2007 and 2008. Between these photographs the scar has become much less distinct, mainly due to mass wasting, rather than cover by vegetation, and in < 10 years will be indistinguishable from the rest of the slope.

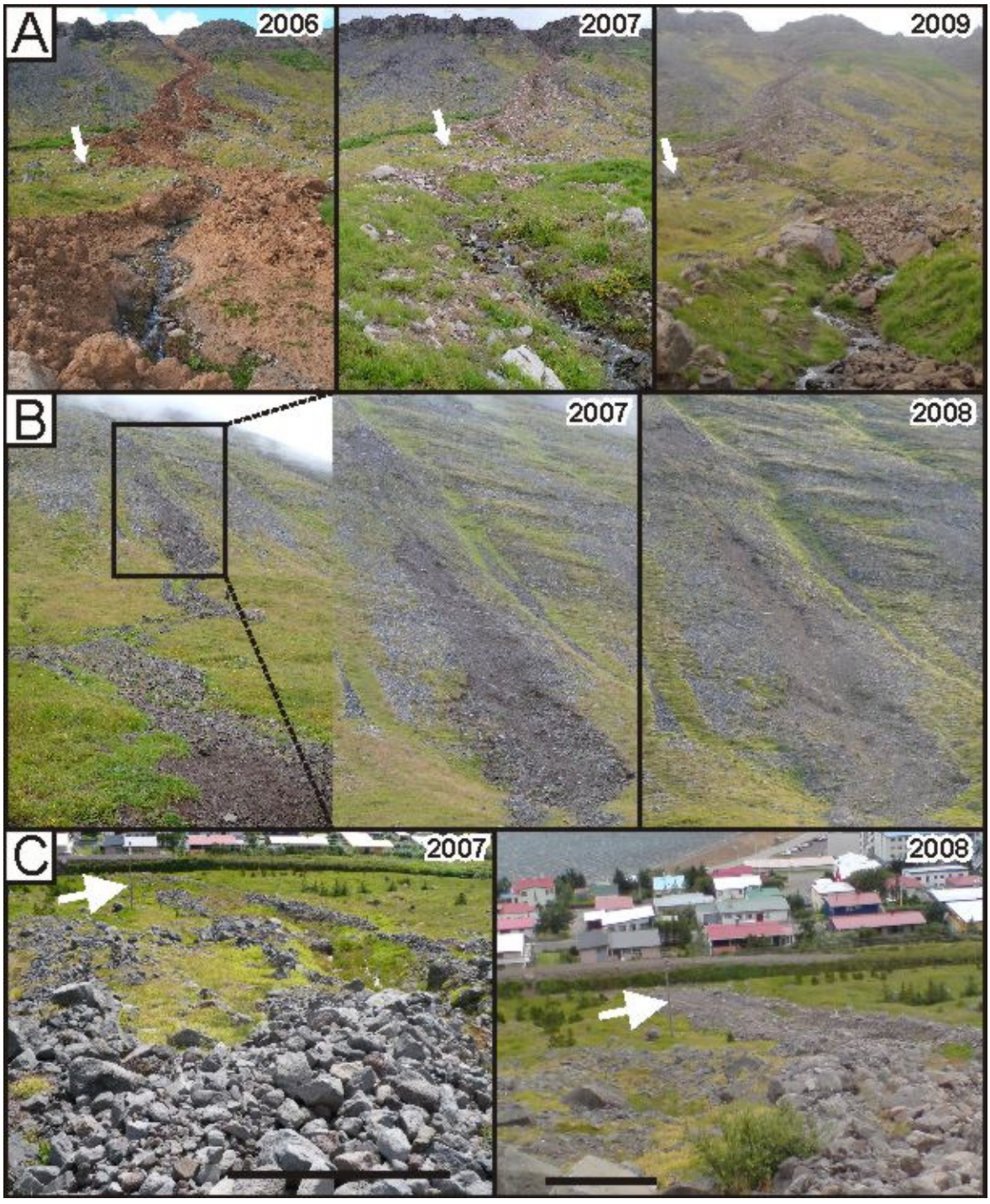

Figure 4-10. Examples of how debris flows in the Westfjords have changed over time. (A) Debris flow 1DF as it appeared in summer 2006, 2007 and 2009. Photos by AD, SJC and AD respectively. White arrow indicates the same boulder in each. (B) The source of debris flow 5DF in 2007 and 2008. (C) Debris flow 3DF in 2007 and debris flow 7DF, which covered the deposits of 3DF, in 2008. White arrow indicates the same telegraph pole in each photo.

By 2007, the 1999 flows (debris flows 2DF, 3DF and 4DF) were still cored with finer red-brown material in places, but the surfaces had been washed clean (e.g. 3DF, Figure 4-10C) and they had lost some volume (Table 4-2). From inspection of photographs taken shortly after the 1999 flows by A.D., these flows resembled the 2006 photo of debris

flow 1DF in Figure 4-10A. These older levees are often composed of a "skeleton" of cobble to boulder-sized sub-angular clasts, as shown in Figure 4-10C, and thus maintain some of their original volume. The 2008 photo of 3DF (i.e. 7DF, Figure 4-10C) shows the morphology when a flow has been reactivated. The vegetation right of the telegraph pole in 2007 has been masked by fines and boulders in 2008, the fines have been re-introduced between existing deposits and the new deposit spreading beyond the former boundaries.

I also found that the steep interior and exterior slopes of the levees rapidly degrades. From GPS measurements, slope angles in debris flow 1DF that were near-vertical in 2007, had declined to ~45° by 2008 and in 2008 debris flows levees from 1999 rarely exhibited slopes in excess of 30°. This decrease in slope is probably due to the removal of fines, which lowers the angle of repose and causes mass wasting of the deposits.

4.5.4. Debris flow volumes

Table 4-4 presents both measurements and estimates of volumes of the surveyed debris flows. According to the classification of Innes (1983b), these flows are medium-scale flows (except debris flows 5DF and 7DF which are small-scale flows). On the 1-10 magnitude scale presented by Jakob (2005) all the flows are rated as size class 2-3, with debris flow 5DF as size class 1-2.

Table 4-4. Summary of measured and estimated volumes and the other measured parameters of debris flows in this study. * indicates that the calculations performed do not include the debris flow source areas.

Debris Flow ID	Measured deposition m^3 (Standard Error)	Measured erosion m^3 (Standard Error)	Estimated deposition m^3 (Standard Error)	Estimated erosion m^3 (Standard Error)	Elevation Drop (m)	Length (m)	Area (m^2)	Mean Width (m)
1DF			8000 (±66%)	41,000 (±38%)	391	756	20 087	26
2DF			2000 (±134%)	16,000 (±62%)	322	732	13 323	19
3DF			1000 (±124%)	6000 (±100%)	396	728	9327	13
5DF			100 (±136%)	400 (±81%)	88	198	1427	7
7DF*	800 (±105%)	600 (±160%)	500 (±76%)	2000 (±70%)	394	721	3858	9
8DF*	1000 (±94%)	200 (±195%)	700 (±100%)	700 (±123%)	571	797	3192	7
10DF*	1000 (±91%)	500 (±105%)	800 (±88%)	2000 (±60%)	590	866	4029	10

To assess the performance of my method to estimate the pre-flow topography (see Section 4.4.3 for details) for debris flows 1DF, 2DF, 3DF, and 5DF, I also applied this method to debris flows 7DF, 8DF, and 10DF, where the pre-flow topography is known from the 2007 LiDAR survey. Table 4-4 shows the results of this analysis. My method tends to underestimate the overall volume of the flow by ~ 30-40 % and over-estimate the erosion of the flow by ~ 2-3 times. However, the overall volume of the erosion and deposition are not important for the following analyses, but the patterns of erosion and deposition are important. I find that the overall patterns of deposition and erosion are preserved when using my method of estimating pre-flow topography for all the debris flows (Figure 4-11).

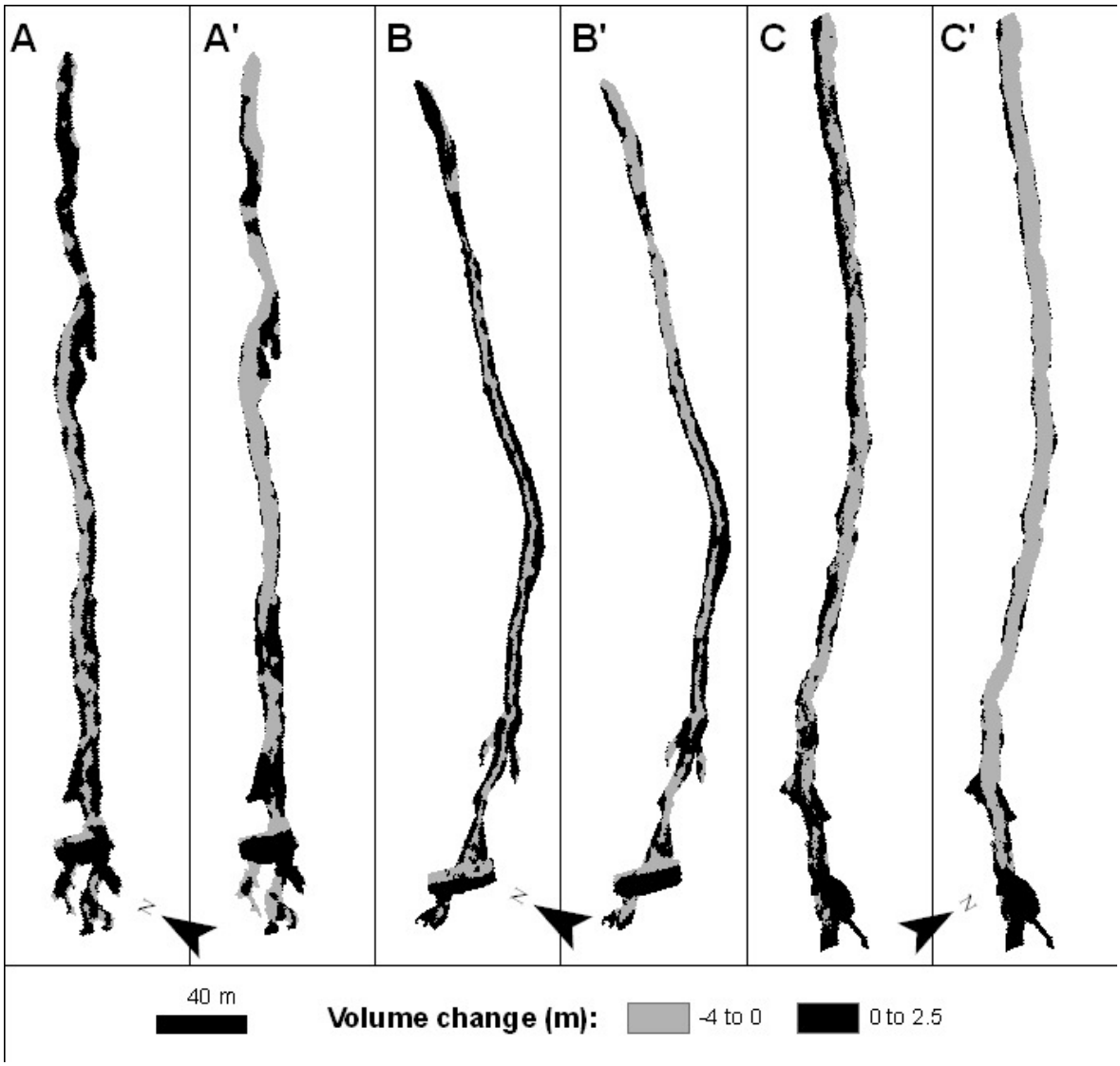

Figure 4-11. (A-C) Maps of the spatial relation between erosion and deposition as derived by differencing the LiDAR generated topography from the post-flow DEM for debris flows 10DF, 8DF, and 7DF, respectively. (A'-C') Maps for the same flows, with the base-topography used for differencing derived by Krige interpolation over the area of the debris flow (method described in Section 4.4.3).

The percentage errors appear large for all the flows (details of calculation in Appendix A) for the following reasons:

(i) for those flows without pre-flow data, the interpolation (described in Section 4.4.3) in the lower surface was performed over long distances, resulting in large estimate errors, especially in the source areas; and

(ii) because the error is expressed as a percentage, it is larger for the smaller debris flows (5DF, 7DF, 8DF, and 10DF) as the absolute error forms a larger percentage of their smaller volume. To put this in context, the average error on the deposition volume

relates to a ±20-cm thickness and the erosion volume corresponds to a ±42-cm thickness.

Despite the significant percentage errors that result from using the Krige interpolation over large areas without points (see Section 4.4.3 for details), it presents a superior approach than just taking a linear surface under the flow. It does so firstly, because the method uses the surrounding topography to estimate the pre-existing topography, and secondly, although the linear and Krige interpolation methods perform equivalently (see Table 4-5), the Krige method allows an estimate of potential error, whereas the linear method does not. In addition, I compared my volume results to those obtained by extrapolation of the cross-sectional areas calculated from cross profiles along the flow. I performed two calculations of the volume of debris flows 1DF and 2DF using this method: once using all measured cross sections and again using just three cross sections that are located at the same approximate position as those made by Decaulne et al. (2005). Both methods produced equivalent estimates for volumes (Table 4-5), although I must emphasise that when fewer cross sections are used greater care is required in ensuring that they are representative of the flow as a whole (e.g., recommendations of Casali et al., 2006). However, although extrapolation of cross-sectional area is adequate for estimating overall volumes, it cannot be used for detailed study of the patterns of erosion and deposition.

Table 4-5. Comparison of the results of Decaulne et al. (2005) with those from this study. Numbers in brackets in the first column indicate the debris flow identification number in Decaulne et al. (2005).

Debris Flow ID	Decaulne et al. (2005) estimated deposition (m^3)	Deposition (m^3) – this study	Deposition from linear lower surface (m^3) - this study	Deposition extrapolated from all cross sections (m^3) - this study	Deposition extrapolated from 3 cross sections (m^3) - this study
1DF	-	8287 (±66%)	11 584	7977	8359
2DF (1)	3000	1925 (±134%)	-	1770	2804
3DF (4)	1000	1119 (±124%)	-	-	-
5DF	-	136 (±136%)	128	-	-
7DF	-	800 (±105%)	531	-	-
8DF	-	1000 (±94%)	918	-	-
10DF	-	1000 (±91%)	806	-	-

4.5.5. Patterns in erosion and deposition

To demonstrate the overall patterns of erosion and deposition developed by debris flows, I have chosen two case studies, debris flows 1DF and 5DF, to illustrate the behaviour. The results from the calculation of total volumes of these debris flows are presented in Table 4-4, and the spatial distribution of volume over the flow in Figure 4-12. The scale of the two flows is very different, but they both show slope-dependent behaviour. The relationship between slope and the depositional regime is evident in Figure 4-12, with slope directly affecting the pattern and quantity of deposition as further detailed below.

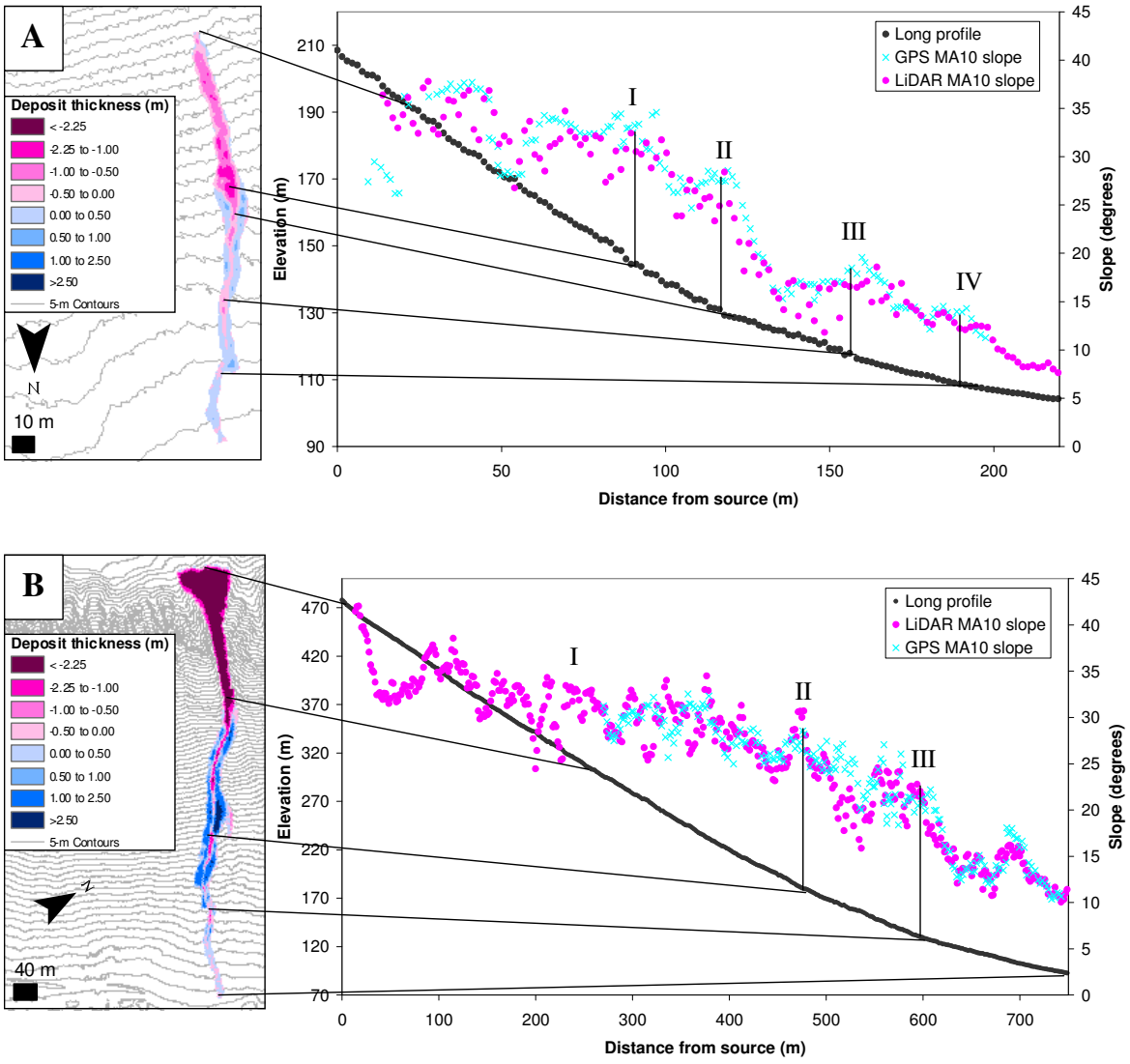

Figure 4-12. (A) Long profile and isopach map of debris flow 5DF. (B) Long profile and isopach map of debris flow 1DF. Contours on the isopach maps are at 5-m spacing. MA10 in the long profiles is the abbreviation for Moving Average over 10 data points. Black points correspond to elevation on the right-hand axis, and pink/blue points correspond to slope represented on the right-hand axis.

In debris flow 5DF (Figure 4-12A), a transition between the erosion and depositional regimes occurs at a sharp change of slope from 28° to 18°. The beginning of this slope change is marked II on Figure 4-12A. Above this, the point at which levees begin to form is marked by a slight decrease in slope, shown between I and II on Figure 4-12A. A slight decrease in deposition is matched by a slight increase in slope marked III, and a major peak in deposition occurs about 50 m from the end of the flow, matched by a drop in slope at IV. For 5DF, the complete cessation of erosion occurs somewhere between 25° and 17°, with deposition starting at 32° (Figure 4-12A). Field observations of *in-situ* grass between the levees confirm that erosion has stopped at this point. This flow remains mobile on slopes as low as 7°, but below the lobe at IV field observations show the deposits have very little relief.

The main erosional section of 1DF (where deposition is negligible) terminates at a slope angle of about 32° (marked I in Figure 4-12B). Below this point, erosion continues to take place in the centre of the channel, but temporarily ceases at the point where a secondary lobe breaks off from the main flow and restarts below this, marked II. The main depositional phase is also briefly interrupted over a short, steeper section (marked III) below which a brief pulse of deposition occurs before the deposition tails off on the lower slope section. The flow remains mobile on slopes as low as 10°. This is a relatively small flow for Ísafjörður, as it did not reach the fjord, nor the man-made drainage channel on the lower part of the slope.

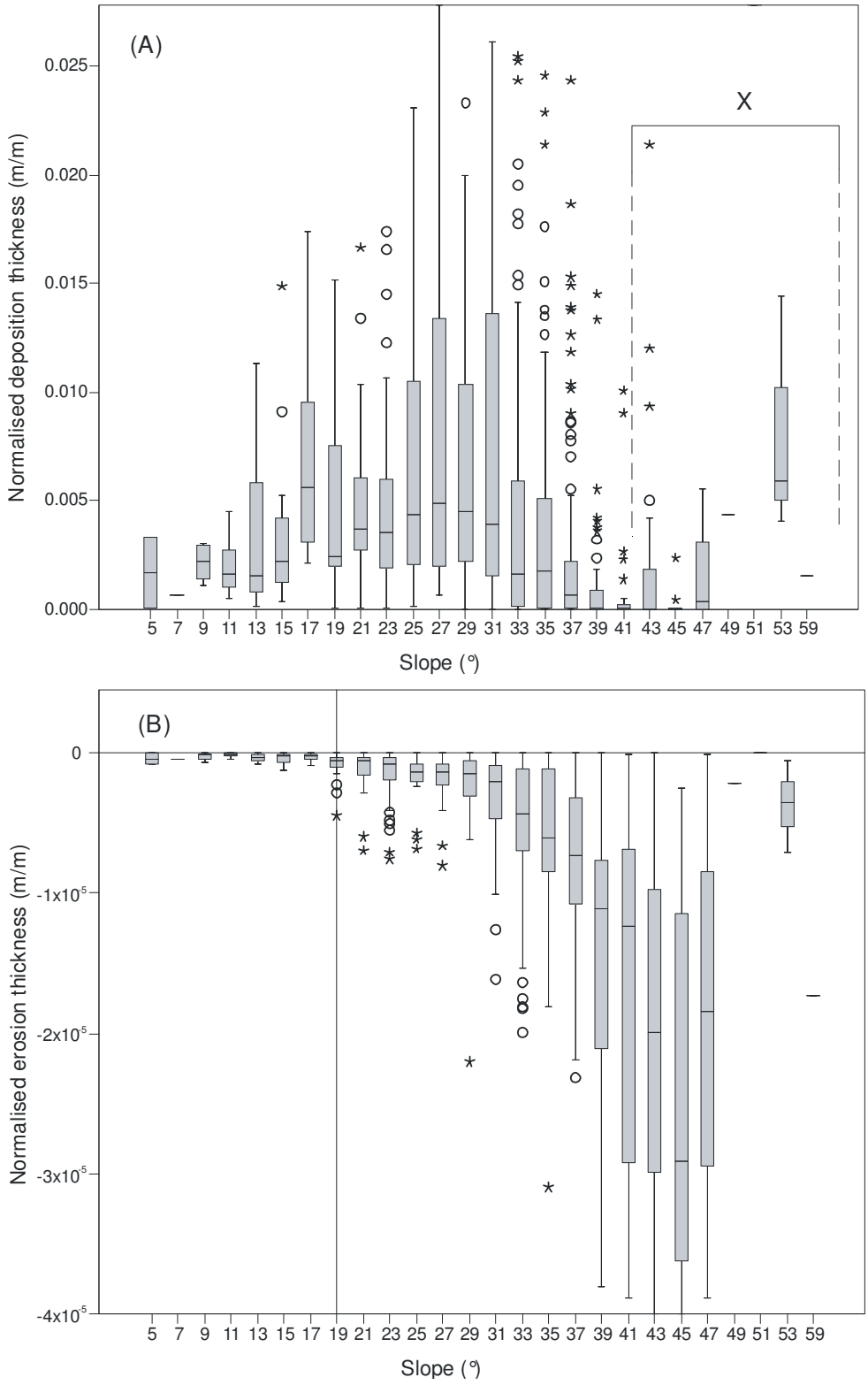

Figure 4-13. Box-plots showing the distribution of normalised representative deposition thickness (A) and representative erosion depth (B) with thickness plotted in 2° slope bins. Normalised thickness is calculated by taking the thickness of the flow in a given segment and dividing it by the total thickness for all segments (described in detail in section 2.4). All data from all debris flows are included. The boxes represent the first and the third quartiles of the distribution, with the black bar marking the median. The narrow bars mark the maximum and minimum of the distribution, with the circle symbols representing "mild" outliers (between 1.5 and 3 interquartile ranges beyond the bars) and the stars representing "extreme" outliers (above 3 interquartile ranges beyond the bars). The erosion slope threshold of 19° is marked by a vertical line in (B). In (A), X marks the region where there are artefacts from the interpolation technique, rather than a true signal. This problem occurred only within the alcoves.

Despite debris flows 3DF, 2DF, and 4DF being older flows (hence more eroded), the patterns in deposition and erosion are preserved. I can therefore analyse patterns of erosion and deposition in all the flows together using the methods described in Section 4.4.4. Figure 4-13 is a box-plot showing normalised representative deposition thickness (Figure 4-13A) and erosion depth (Figure 4-13B) against slope as a compilation of data for all the debris flows. Using Figure 4-13, I can then compare the onset of deposition and cessation of erosion in these flows with those found by other authors for hillslope flows. Note that the extension of the boxes above the zero-line in Figure 4-13A (marked X) at slope angles > 43° is an artefact because of the protrusion of bedrock surfaces in the alcoves of debris flows 2DF and 3DF above the interpolated surfaces.

Our results are interesting in that I find measurable deposition at slope angles of 37°. This is higher than reported by previous studies. Lorente et al. (2003) reported 17.8° as the onset slope for deposition; and Fannin and Wise (2001) reported unconfined (hillslope) flows as depositing at angles < 18.5° on average in the Queen Charlotte Islands, British Columbia, Canada, but their data show deposition occurring up to 38º in some cases (it is not clear, however, if these flows are exclusively hillslope debris flows). However, Larsson (1982) reported deposition at as much as 35° for debris flows in Longyear Valley, Spitsbergen, Norway. Matthews et al. (1999) reported deposition on slopes of up to 25º in Leirdalen, Jotunheimen, Norway; and Rapp and Nyberg (1981) reported deposition on 30° slopes in Nissunvagge, Sweden. For confined flows, deposition does not begin until much lower slope angles are reached on the fan (e.g., Staley et al., 2006; Prochaska et al., 2008). Hence, for the flows studied in this paper, deposition consistently begins at a much higher average slope angle than reported by the majority of other authors.

Fannin and Wise (2001) reported their lowest limit of erosion on average as being 18.5° for unconfined flows, but this lower limit has not been widely reported elsewhere in

the literature. From Figure 4-13B and Figure 4-12, apparently a lower slope erosion threshold exists of ~ 19° for debris flows in my study, marked by the vertical line in Figure 4-13B. This is reinforced by field observations of erosion occurring near the distal end of the debris flow coincident with an increase in local slope as shown in Figure 4-14. It is also consistent with the observation of *in-situ* grass between the levees of debris flow 5DF at a sudden decrease in slope below 19°. This phenomenon has been noted by other authors in other locations (Rapp, 1960; Luckman, 1992; Matthews et al., 1999), but not quantified.

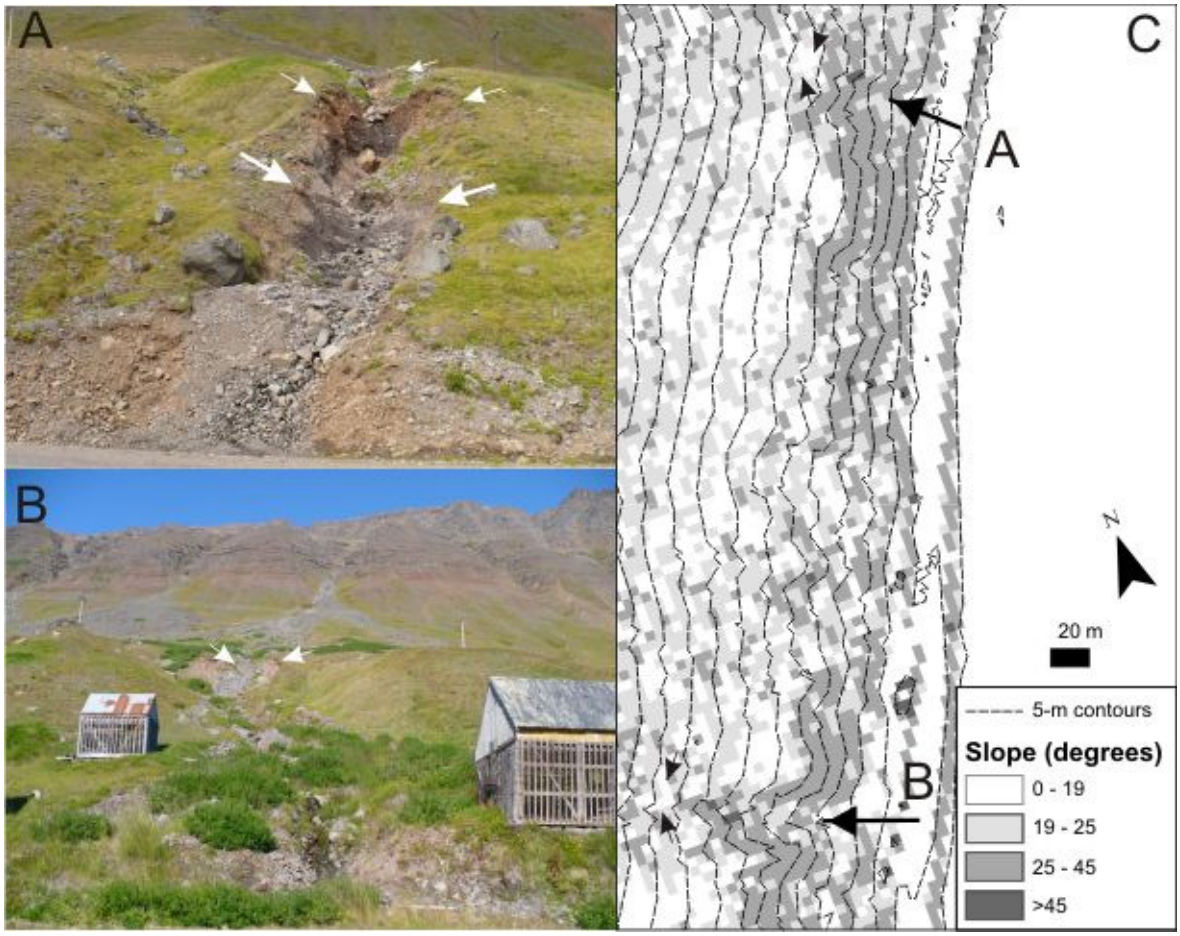

Figure 4-14. Erosion at the base of debris flows.(A) The base of the northernmost debris flow sourced from Gleiðarhjalli bench. (B) The base of debris flow 4DF. White arrows indicate the extent of the eroded channels. (C) Large black arrows indicate locations of photos (A) and (B) on a slope map of the 5-m DEM, with small black arrows showing increases in local slope that correspond to erosional sections picked out by the white arrows in (A) and (B).

4.6. Data analysis

4.6.1. Comparison with previous empirical relationships for debris flow total travel distance

Rickenmann (1999) used data from 232 confined debris flows from around the world to derive the following relationships:

$$L = 30(MH_e)^{0.25} \quad (4\text{-}1)$$

$$L = 1.9M^{0.16}H_e^{0.83} \quad (4\text{-}2)$$

where L is the total travel distance, H_e is the elevation difference between the source and the lowest point of deposition, and M is the magnitude or total volume. Equation (*4-1*) is a theoretical relationship between distance travelled and energy potential (MH_e), and the constant has been selected to approximate average total travel distance in the data of Rickenmann (1999). Equation (*4-2*) is the regression equation of L, M, and H_e that best fits Rickenmann's (1999) data. Similarly, Lorente et al. (2003) compiled data from 961 unconfined debris flows in the Flysch sector of central Spanish Pyrenees to derive the following relationships:

$$L = 7.13(MH_e)^{0.271} \quad (4\text{-}3)$$

$$L = -12.609 + 0.568h + 0.412s \quad (4\text{-}4)$$

where h is the elevation difference between the source and the starting point of deposition, and s is the average gradient of the source area in degrees. Lorente et al. (2003) used Eq. (*4-1*) as the basis for Eq. (*4-3*), but adjusted both the exponent and the constant to fit their data. Equation (*4-4*) is the result of a linear regression of the variables that had the highest correlation with total travel distance from Lorente et al.'s (2003) data.

For Rickenmann's (1999) Eq. (*4-1*), debris flow 1DF lies well above the line $x = y$ in Figure 4-15, which means its total travel distance is shorter than that predicted by this relationship. Using Rickenmann's (1999) Eq. (*4-2*), my debris flows 1DF, 10DF, and 8DF

all lie well above the $x = y$ line and therefore have a shorter total travel distance than predicted. This is because the elevation difference is more important in Eq. (*4-2*) than (*4-1*), giving a longer predicted total travel distance for 8DF and 10DF, which have greater elevation differences. For both the Rickenmann (1999) relationships (Eqs. *4-1* and *4-2*), my debris flows 2DF, 3DF, 5DF, and 7DF lie close to the $x = y$ line: the measured total travel distances match the predicted ones quite well. All the debris flows in this study lie well below the line for both of the relationships from Lorente et al. (2003), i.e., all the flows I have studied have larger total travel distances than would be predicted by Lorente et al. (2003). Existing relationships do not seem to fit my results very well, so I now proceed to develop my own empirical model in the following Sections.

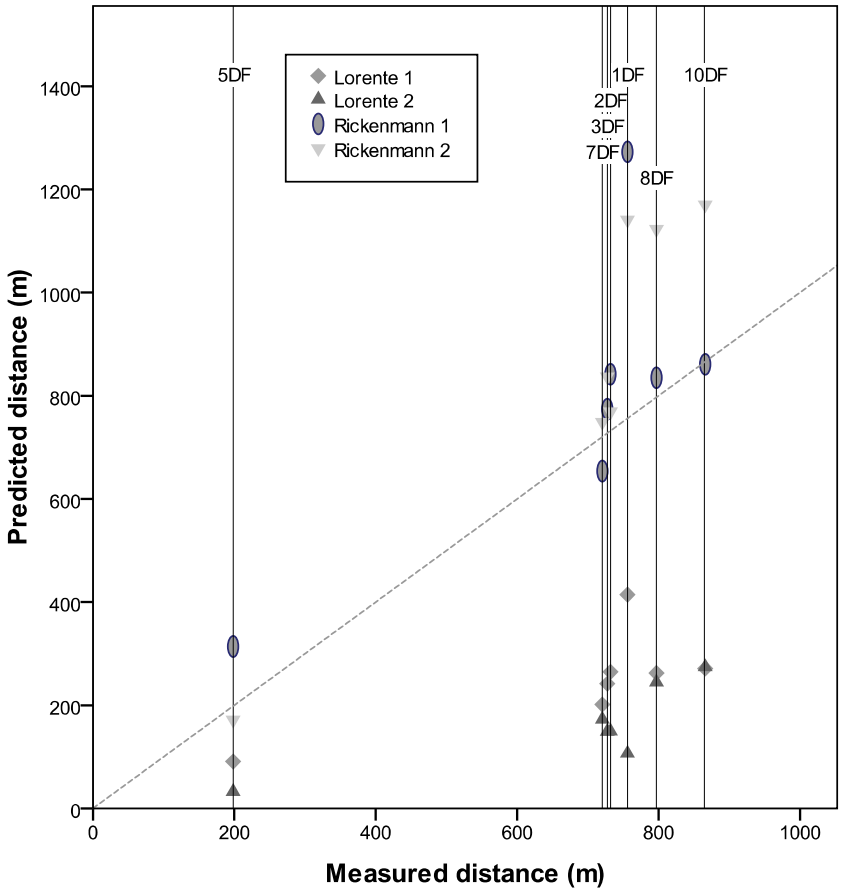

Figure 4-15. Plot of the total travel distance predicted for the debris flows in this study by the empirical relationships derived by Rickenmann (1999) and Lorente et al. (2003), against my measured total travel distance for the same debris flows. Rickenmann-1 refers to the relationship given in Eq. (*4-1*); Rickenmann-2 to Eq. (*4-2*); Lorente-1 to Eq. (*4-3*), and Lorente-2 to Eq. (*4-4*). The diagonal line is the equality line x = y.

4.6.2. Derivation of an empirical relationship for hazard prediction

By treating cumulative packets of the segmented debris flows from top to bottom as progressively larger subsamples of the main debris flow, I noticed predictable patterns in the pattern of deposition. Figure 4-16 shows a plot of cumulative average slope against cumulative normalised deposition thickness. Cumulative average slope (θ_n) was calculated for each segment ***n*** as follows:

$$\theta_n = \frac{\sum_{i=0}^{n} S_i}{n} \tag{4-5}$$

where S_i is the slope within segment i, and n is the number of segments counted from the source of the flow downward. The cumulative normalised deposition thickness (Z_n) was calculated for each segment n as follows:

$$Z_n = \sum_{i=0}^{n} \frac{Z_i}{Z_T} \tag{4-6}$$

where Z_i is the representative thickness for that segment, and Z_T is the sum of the representative thicknesses for all segments in the debris flow.

All the debris flows studied fall within a narrow range of cumulative average slope for a given representative thickness, and most have an initial steep section over which no deposition occurs. Deposition then begins at a cumulative average slope of 35-40°. The behaviour of the debris flows then falls into one of three groups: (i) those which then deposit linearly for the rest of their length (debris flows 2DF, 3DF, and 7DF), (ii) those with a sudden decrease in deposition before their terminus (debris flows 1DF and 8DF), and (iii) those which show strong initial deposition that tails off into a constant rate of deposition at lower slope angles (debris flows 5DF and 10DF). I can use these relationships to generate best-fit curves, allowing me to predict potential future flow behaviour.

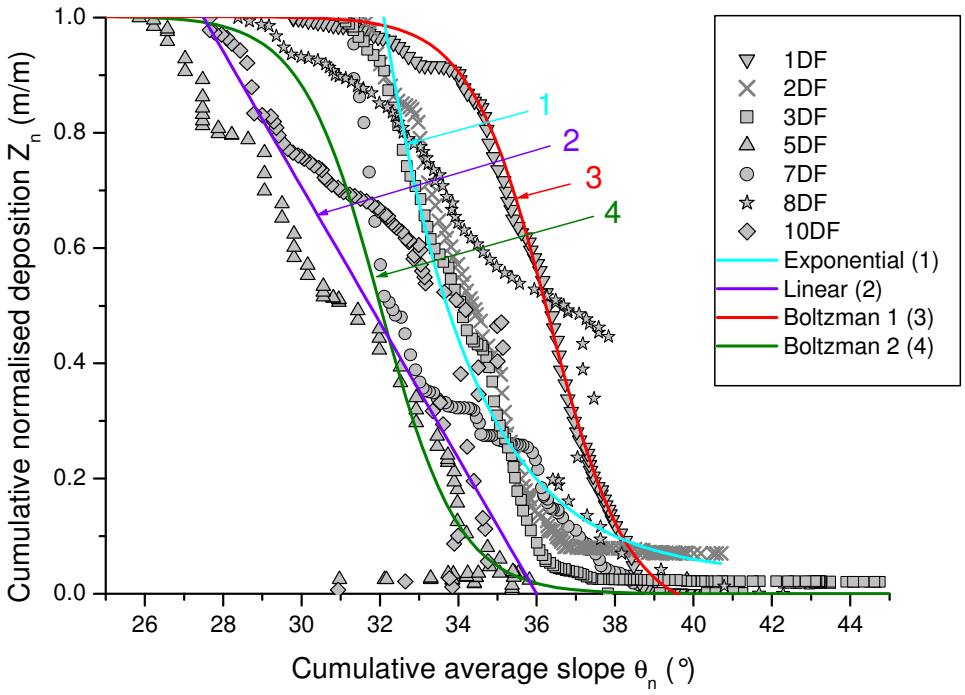

Figure 4-16. Graph showing normalised cumulative deposition thickness Z_n against cumulative average slope θ_n for all the debris flows in this study. The curves used in each of the models are 1 – exponential fit to debris flow 2DF, 2 – linear interpolation of data from flow 5DF, 3 –sigmoidal curve fitted to flow 1DF to delineate the upper limit of the envelope of curves, and 4 – sigmoidal curve following the lower limit of the envelope of curves, derived by translating curve 3 along the x-axis. See Section 4.6.2 and Appendix B for details.

4.6.3. Creating a hazard map from empirical relationships

Enough consistency exists in the relationship between cumulative average slope and cumulative normalised deposition thickness to fit curves to the envelope of the data points shown in Figure 4-16 (this process is described more fully in Appendix B). I have fitted three types of curves (Figure 4-16): linear (on the lower boundary, labelled 2 in Figure 4-16), sigmoidal (Boltzmann-family, to the highest average slope, labelled 3 in Figure 4-16 and lowest average slope, labelled 4 in Figure 4-16), and exponential (to the average, labelled 1 in Figure 4-16). These curves represent the patterns in behaviour labelled (i), (ii), and (iii) described in Section 4.6.2, respectively. I have then modelled the debris flow behaviours based on these curves along 19 simulated debris flow tracks (Figure 4-17). The tracks were generated from the lines of greatest fluid accumulation as derived from hydrological modelling of the LiDAR DEM using Arc Hydro Tools 9.0. Centrelines were

digitised from this accumulation model and then split or segmented at 5-m intervals, as per the empirical model (see Figure 4-4). The underlying slope for each of these segments was extracted from the DEM. These models require two inputs in addition to the flow paths: the planimetric area and the debris flow volume.

As debris flow 1DF was a relatively small event compared to those in 1999, I used its volume and planimetric area as an end member to estimate the thickness of deposits reaching the town on a set of 19 tracks shown in Figure 4-17. This volume was used as a starting point because larger flow volumes would result in greater thickness and greater runout distances, hence this provides a conservative estimate. The results of this modelling show that for models 2 and 4 upper parts of the town would be at risk from any debris flow; and for models 1 and 3 the flows do not have sufficient mobility to reach the town, no matter what the input volume and area. To demonstrate how the thicknesses change with increasing volume (and planimetric area), the thicknesses of debris reaching the town are tabulated for different input parameters for three example flow-paths (labelled on Figure 4-17 Model 1) for all four models in Table 4-6. The results from 1 and 3 emphasise that these types of flows rarely have sufficient mobility to reach the town, no matter what the input volume and area are for these two models.

Table 4-6. Model results for three example flows, marked on Figure 4-17, showing depth of the simulated flow on reaching buildings for various starting volumes and planimetric areas. The first data column shows results from using the volume and area for debris flow 1DF in the models. Starred entries indicate where the thickness of the flows is > 1 m.

Starting volume (m^3) : area (m^2)		**8 287 : 16,000**	**15,000 : 30,000**	**20,000 : 30,000**
flow 1	**model 1 (m)**	0	0	0
	model 2 (m)	1.22*	1.22*	1.5*
	model 3 (m)	0	0	0
	model 4 (m)	1.16*	1.16*	1.6*
flow 2	**model 1 (m)**	0	0	0
	model 2 (m)	0.96	0.96	1.28*
	model 3 (m)	0	0	0
	model 4 (m)	0.73	0.73	0.97
flow 3	**model 1 (m)**	0	0	0
	model 2 (m)	0.99	0.99	1.32*
	model 3 (m)	0	0	0
	model 4 (m)	0.12	0.12	0.16

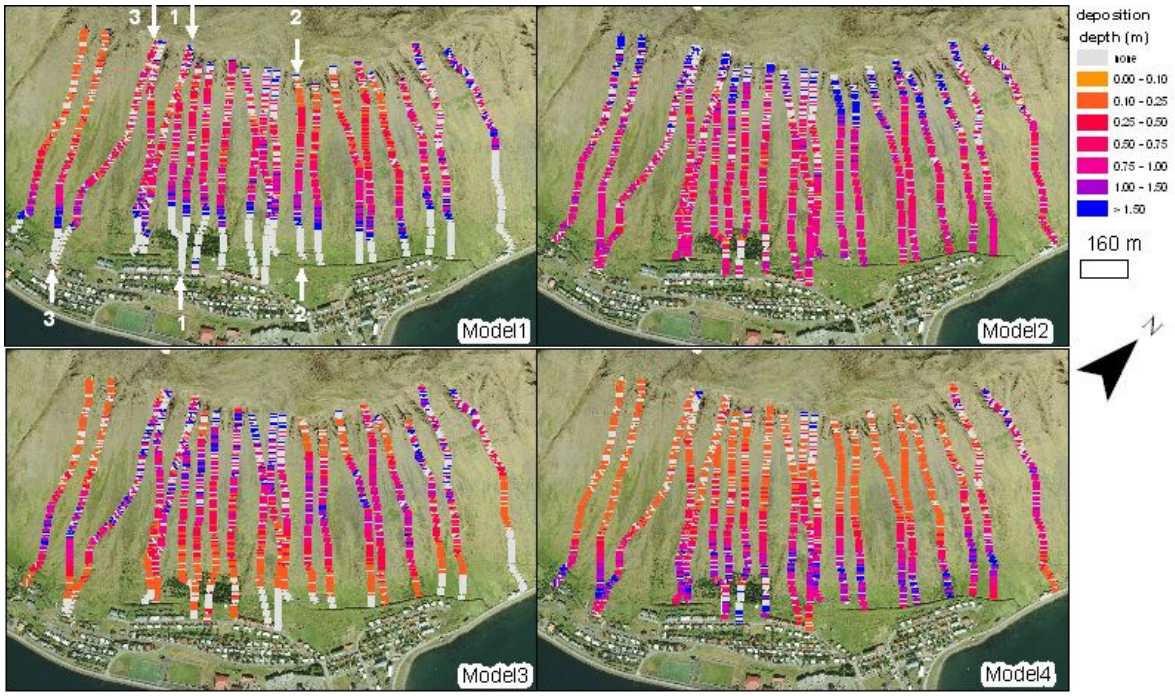

Figure 4-17. Graphic displaying the air photo mosaic of Ísafjörður taken by NERC ARSF overlain with model debris flow paths derived from different curves fitted to the normalised cumulative deposition thickness against cumulative average slope plot (Figure 4-16), using starting values given in Table 4-6, column 1. Arrows in upper left refer to tracks in Table 4-6.

4.7. Discussion

4.7.1. Reliability of volume data

Our method of estimating pre-flow surfaces has been tested on the debris flows for which I do have pre-flow data (7DF, 8DF, and 10DF), and it seems to underestimate deposition volumes and greatly over-estimate erosion volumes (Table 4-4). These tendencies are a result of the geometry of the pre-existing surfaces in this area, e.g. the primarily erosional source areas tend to be located within generally smooth concave topography and the depositional and mixed parts of the flow are on tilted planar topography with small wavelength variations. I do not have a debris flow > 1000 m^3 on which I can test this method, but it is likely that the percentage difference in calculating the deposition volume by this method would decrease with greater volume, as the absolute differences would increase only slowly. It is also likely that the percent difference in erosion volume would remain large, as the kriging is performed over larger source areas, leading to the absolute difference increasing with the volume. The estimate of the deposition cannot be improved

using this method, however the erosion estimate could be improved slightly by placing an upper limit on the allowed erosion thickness.

However, the interpolation on accurate GPS and LiDAR elevation data gives realistic ranges of volumes for these flows. Considering the inherent bias towards underestimation, the volume estimates are larger than previous estimates for this area: my "medium" flow 1DF has a volume of about 8000 m^3 compared to 3000 m^3 calculated by Decaulne et al. (2005) for a "large" debris flow 2DF in 1999 (Table 4-5). I have used several different methods to calculate the deposition volumes of 1DF and have found that all the results are consistent (Table 4-5). Debris flow 1DF is a medium-sized flow for this region, and the results are within realistic bounds for this scale of flow (Innes, 1983b). However, debris flow 1DF has the largest errors from lack of pre-flow data, and hence all other flows are better constrained and have more reliable volume estimates.

4.7.2. Patterns in deposition and erosion

Debris flows 1DF and 5DF show morphological evidence of the pulsing nature of debris flows in the patterns of their deposits. The break-off lobe in 1DF is probably a result of the first pulse, which was able to break over the pre-existing levees at the bend in the channel (Figure 4-12B – just above II). Later pulses blocked this path with their own levees and continued down the path of previous flows. For debris flow 5DF, a major peak in deposition is located about 50 m from the end of the flow (Figure 4-12A – III); this was also probably an original terminal lobe before a later pulse broke out through a levee above it. This later pulse formed small levees and then spread out into a sheet deposit, suggesting a higher mobility and, hence, water content. This demonstrates that a debris flow does not necessarily follow the line of greatest initial slope, but that earlier pulses can block further flow; this divagation behaviour of debris flows has been described by several other authors from deposits (e.g., Addison, 1987; Morton et al., 2008) and modelling (Zanuttigh and Lamberti, 2007). These field observations also point to the variable composition of the

pulses that form a debris flow event. Although my model does not incorporate these observations explicitly, I use the knowledge of this pulsing nature to expand and inform conclusions based on model results.

Debris flows continue to be mobile at low slope angles, with debris being transported at slope angles as small as 7-10°, although initiation seems to require a high slope angle (> 40°). I have measured little deposition at lower slope angles, and there are several possible reasons exist for this:

(i) The debris flows studied here exhausted the available material before reaching low slopes. I have not studied any very large, fresh flows that could perhaps continue depositing at low slope angles, as their material is not exhausted by deposition on higher slopes.

(ii) Any low-slope deposits within Ísafjörður or on roads remaining from historical flows would almost certainly have been cleared away.

(iii) Urbanisation on low slopes prevents debris flows from progressing unimpeded downslope.

(iv) Morphology of the slopes in Ísafjörður means that very low (<< 10°) slope angles are not abundant above the shoreline.

Previous studies (Decaulne, 2001) have suggested that deposition of lobes does occur at these low slope angles, but it is unclear if the water content is low enough within these mobile flows to maintain levees.

The ideal slope angles for deposition appear to be around 25°, enabling the outer edge of the flow to stabilise into levees while the main body of the flow remains mobile. Deposition begins to occur at much higher slope angles than reported for previous flows (e.g., Coe et al., 1997; Lorente et al., 2003). This potentially indicates that the flow deposits in the Ísafjörður region have a higher angle of dynamic friction or a higher viscosity (possibly related to lower water content or higher clay content) than previously

reported for debris flows. This is supported by field observations that the levees are able to maintain high external and internal slopes.

In the study area a threshold slope of 19° is observed, below which erosion completely ceases. Whenever this threshold is exceeded lower down the flow, erosion begins again as shown in Figure 4-14. This means that the debris flows are probably bulking (i.e., incorporating material eroded from along the flow path) as they progress downslope, although I was not able to estimate the amount of bulking, because of a lack of reliable data in the source areas.

4.7.3. Comparison with previous empirical relationships for debris flow total travel distance

Figure 4-15 shows how the debris flows studied here compare with empirical relationships for debris flow run-out distances derived by Rickenmann (1999) and Lorente et al. (2003).

Our debris flows fit best with the confined debris flows (Equation *4-1*) studied by Rickenmann (1999), but the total travel distance is greater than predicted from the hillslope debris flows studied by Lorente et al. (2003) in Flysch in the Pyrenees. This is surprising as the debris flows in my study area most closely resemble those of Lorente et al. (2003), being unconstrained hillslope flows rather than the confined torrent debris flows of Rickenmann (1999).

From this I infer that the larger debris flows in my area are generally more mobile than hillslope flows studied by Lorente et al. (2003), but less mobile than confined flows studied in a wide range of settings by Rickenmann (1999). However, the smaller flows have about the same mobility as Rickenmann's (1999) channelized flows. The higher mobility of these flows seems counter-intuitive considering their higher angle of dynamic friction or higher viscosity implied by observed high levee slopes and deposition at high local slope values (detailed in 4.5.1 and 4.5.5). However, Iverson (1997) concluded that the structure of the deposits does not reflect the properties of the original debris flow, and the

interplay of the flow's viscosity with the fluid and granular parts of the flow is poorly understood. I hypothesise that the high mobility compared to Lorente et al. (2003) is a reflection of the larger scale of the debris flows in this study. Clearly, the flows in my area do not closely match existing empirical relationships. I conclude that empirical prediction from simple models is insufficient here; and that without the application of more complex models, the prediction of future flow lengths in a given area can only be made by the analysis of detailed measurements of previous flows from the selected area. Here I present an example of how this could be implemented.

4.7.4. Developing a new empirical model for debris flow prediction

For the debris flows studied in the Westfjords, the relationship between slope and deposition does not strongly depend on the overall mass or the source material's grain size, grain size distribution, or angularity (detailed in Section 4.5.1). All the flows show similar basic patterns yet have different masses (Table 4-4) and comprise different materials (Figure 4-11, and Section 4.5.1). Both field observations and analysis of the isopach and slope profiles (Figure 4-12) point to a strong relationship between slope and deposition-erosion volume. From the isopach data, I have derived a predictive relationship for flows in this area. Figure 4-16 shows the data and trends in cumulative slope and normalised deposition thickness, as derived in Section 4.6.2 and Appendix B, which lead to this predictive relationship. As mentioned in Section 4.6.2, debris flows 2DF, 3DF, and 7DF do not have the sudden drop in deposition at low cumulative slope that is shown by most of the other flows. However, I believe that this is not a feature of the flow mechanics but a result of the deposits being later removed by anthropogenic mechanical excavation (Section 4.5.1). This removal has affected the normalisation in Figure 4-16, but I estimate that these deposits make up an insignificant fraction of the total deposition volume and therefore would not push these flows outside the main data envelope. I attribute the other differences between debris flows in Figure 4-16 to gross rheological differences and to the

variation in rheology of their constituent pulses. These differences are surprisingly small, however, considering the variation in topographical setting, source of material, fines content, clast size, angularity, and grain size distribution between the flows.

The data in Figure 4-16 form a discrete envelope that describes the way in which I expect a debris flow to evolve in terms of proportion of overall deposit thickness and hence volume with cumulative slope. Therefore, with a starting volume, planimetric area, and a DEM, this relationship can be used to predict overall total travel distance and deposit thickness at a given location.

4.7.5. Predicting hazard

I have used the empirical relationships described in Section 4.7.4 to simulate debris flow deposition and overall total travel distance along synthetic flow paths as explained in Section 4.6.3. Different flow behaviours are represented by the four models shown in Figure 4-16, and these have been simulated along the synthetic tracks. Models 2 and 4 always reach the houses no matter what the starting volume (Table 4-6; Figure 4-17). Models 1 and 3 never reach the houses, and again this is independent of starting volume (Table 4-6: Figure 4-17). As noted in Section 4.7.4, debris flows 2DF, 3DF, and 7DF do not have the sudden drop in deposition at low cumulative slope that is shown by most of the other flows; and these flows form the basis for creating model 1 (exponential). Hence, I can discount this model as being unrealistic for most debris flows. The sigmoidal (Boltzmann) models 3 and 4 seem to represent the inherent behaviour of most of the flows: an initial slow increase in deposition, a stable middle area with approximately constant deposition, and a sharp drop-off at low slope angles. However, the difference in terms of overall deposit thickness is not great between models 2 (linear) and 4 (sigmoidal), hence a simple linear model would suffice to implement this method, without the need to fit a precise curve to any particular flow.

Protective ditches have been dug above the town of Ísafjörður in two locations (marked in Figure 4-3) to protect the population and houses from debris flows. In my modelled flows, the flow thickness only matches the depth of the protective ditches (i.e., the flow only progresses past the ditches) when the flow is extremely large in volume (> 100,000 m^3 is an exceptionally large flow for this region). I should note that in reality the ditches were nearly overwhelmed (mud and water reached the houses) in 1999 (Decaulne et al., 2005) by 2DF and 3DF, which have estimated volumes of 3000 and 1000 $m^{3,}$ respectively (Table 4-5). I note that the ditches have since been widened (Decaulne, 2007). However, my model results show that medium-sized debris flows result in greater than 1 m of deposits at the eastern ditch, so two medium flows occurring close to one another in time and space would overwhelm this ditch and flows would reach the houses. Given that debris flows can be triggered simultaneously (e.g., Coe et al., 2007; Decaulne and Sæmundsson, 2007), this appears to be a plausible hazard. However, the frequency of occurrence of these multiple events is unknown for Ísafjörður, so I assume that this would be a comparatively rare event, but severe if it does occur. This analysis has enabled me to identify areas of the town at risk that would not be obvious otherwise. To prioritise any mitigation work done by the authorities, this model could be combined with estimates of most likely flow areas based on historical data and cost-benefit considerations. For example, although the electricity substation is unprotected, damage to it would be inconvenient but unlikely to cause loss of life, compared to residential properties.

Our model does not take into account the effect of the relative timings of multiple events nor the number of pulses in a single flow event. For example, a medium-sized flow could occur in a single pulse and stabilise on the slope with the terminal lobe at the ditch and rest of debris backed up behind it. However, such an event could also have many pulses, the first of which fills the ditch allowing the next pulses to ride over the top. These hypothetical events could have the same overall volume but very different outcomes. In

addition, the flow paths I have used in my model run down the steepest slope, but as noted previously, (Sections 4.5.1 and 4.5.5) debris flows do not necessarily conform to this path. However, the flow routes I have produced are representative of the slopes experienced by a debris flow as it progresses and therefore can be used as an indication of thickness of deposits expected for the flow, if not the exact path line.

Our model is an oversimplification of the behaviour of the flow, but it is conservative in its simplifications. The advantage of this model is that it meets the conditions of Hurlimann et al. (2008), which are (i) the method must specify a spatial distribution, and results must cover the entire study area; (ii) the method applied should be able to incorporate different volumes as input data; and (iii) the output of the method should enable intensity determination without the need for the time and expense of a full two-dimensional flow model, requiring back-calculation to determine rheology and selection of the most appropriate flow-resistance law. My model has a similar philosophy in this respect to Fannin and Wise (2001), although their model required the additional inputs of length, width, and azimuth of each reach in the debris flow. Their model also dealt with transitional and confined debris flows in addition to unconfined debris flows and also included bulking (incorporation of material eroded along the flow path). None of these additional factors are of importance in purely hillslope flows except bulking.

4.7.6. Potential application of results to Mars

Iceland is a good analogue to Mars, because (1) it has a similar lithology with horizontal to sub-horizontal layered basalts (2) glacially carved fjords have a similar shape to the pristine shape of impact crater walls – the setting for the majority of gullies, and (3) debris flows seem to occur almost everywhere in Iceland where there are steep, debris mantled slopes – a similar pattern to gullies on Mars. The debris in Iceland is provided by glacial sedimentation and mass wasting brought about by intense frost shattering. On Mars this debris could be supplied by aeolian deposition, impact breccia, or thermal stress (brought

about by extreme diurnal temperature oscillations) which causes mass wasting. Many debris flows in northern and north-western Iceland are triggered by snowmelt, as well as precipitation (Decaulne and Sæmundsson, 2007). The snowmelt-like triggering mechanism forms a more appropriate analogue for Mars than triggering by precipitation.

The water that triggers debris flows above Ísafjörður comes from a shallow groundwater source, but also requires the whole debris mantle to be saturated. This fits in with a similar model proposed for Mars by Gilmore and Phillips (2002), where melting ground ice percolates down to an aquiclude and flows along this layer until it intersects a crater wall. However, this model does not explicitly satisfy the condition that the slope materials need to be saturated. In Ísafjörður the groundwater undercuts the already saturated material, whereas in the Gilmore and Phillips (2002) model the water outbreak saturates the slope beneath, thus causing the slide. However, the debris flows in Ísafjörður have a different setting compared to the majority of debris flows in Iceland. There are many examples of debris flows in Iceland that are triggered by snowmelt without an accompanying groundwater source. These can be more appropriately compared to models of rapid ground-ice melting on Mars, either in the past (Costard et al., 2002) or possibly at the present day (Hecht, 2002; Christensen, 2003). These models seem to fit better as they allow whole-sediment saturation. In addition my observations of springs elsewhere in Iceland confirms that they are not always associated with debris flows and do not always have a topographic impact on the landscape.

At the resolution of HiRISE (25 cm/pixel) levees with large visible clasts are not apparent (e.g. Mangold, 2003). However, the survey of debris flows in the Westfjords and the rest of Iceland has confirmed that debris flows can occur in a wide range of materials, hence the absence of clast-rich levees in HiRISE images does not indicate that levees are not present at all. Another possibility on Mars is that large clasts could remain buried by fine material (Figure 4-10A) because there is no rainfall to remove the fines. Fresh debris

flows in Iceland often have albedo differences compared to the host slope, and this difference decays with time (Figure 4-10). This decay is due to vegetation growth, removal of fines and weathering of the freshly exposed rock surfaces. On Mars the decay in albedo could be brought about by aeolian reworking, or weathering. This could provide an explanation for the appearance of the light-toned deposits found by Malin et al. (2006).

In Iceland relict debris flows are not distinct from the host slope, even on non-vegetated slopes, despite still having levee-channel morphology. This makes them difficult to see in ordinary lighting conditions (Figure 4-18). This problem could certainly also apply to detecting levees on martian gullies.

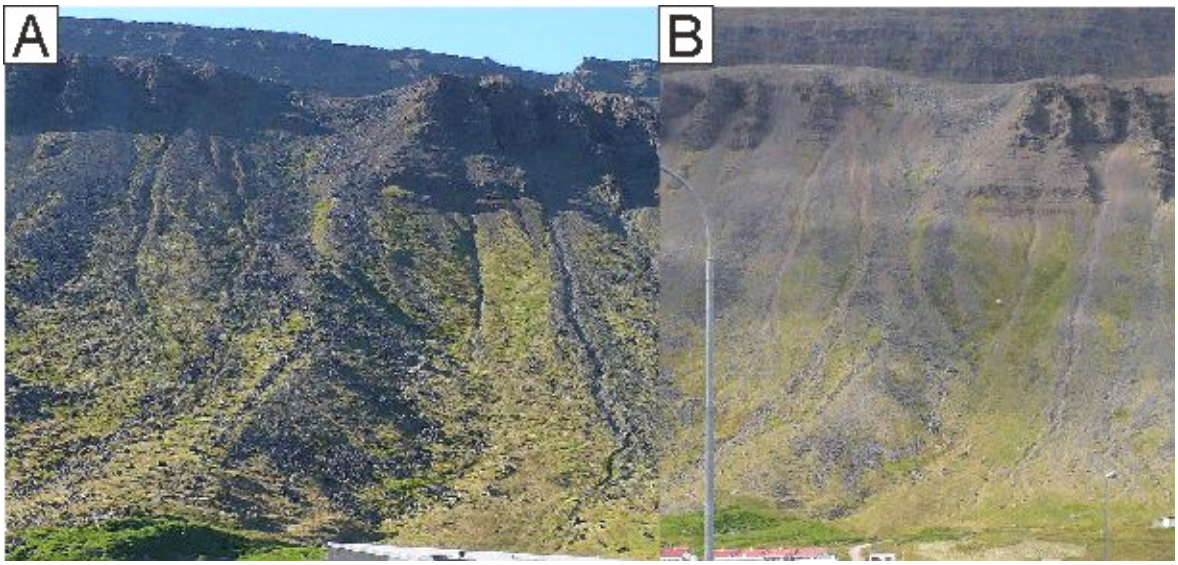

Figure 4-18. Example of how lighting angle affects the visibility of levees in Iceland. (A) View of slope above Ísafjörður, with a low sun angle in the late evening, with levees clearly visible and (B) the same slope, under midday lighting with levees difficult to see.

The range of morphologies of debris flows in Iceland closely matches the range of morphologies of gullies on Mars. Gullies in Iceland and on Mars have similar ranges of length, deposit shape, size of alcove and sinuosity. The exceptions are gullies located in the south polar pits and the "occupied" alcoves of Malin and Edgett (2000), which have no direct visual analogue in Iceland. The slip scars that form the source area for many hillslope gullies resemble simple gullies on Mars (e.g. Figure 2-7a). Figure 4-8 shows the limited examples of debris flows in Iceland with the "abbreviated" type alcoves of Malin and Edgett (2000). The "lengthened" and "widened" alcoves of Malin and Edgett (2000)

have the most obvious similarity to debris flows in Iceland. These debris flows are unconfined for most of their length, with an appearance similar to those studied near Ísafjörður. Like gullies on Mars the terminal deposits of debris flows in Iceland can be fans (Figure 4-6 and Figure 4-7), or single lobate deposits (Figure 4-5). However, without morphological measurements, the respective influences of pure water flow and debris flow are hard to distinguish and separate in Iceland. Hence, the visual analogue alone does not allow discrimination between the two formation processes in gullies on Mars.

Based on observations of debris flows in Iceland, Hartmann et al. (2003) proposed a model for the development of Icelandic debris flow gullies (Figure 4-19). From my observations this model appears to hold only on slopes that are deeply mantled by debris. In addition I have observed that all of the stages can coexist in one slope (e.g. Figure 4-7A), which suggests that there are different evolution rates on different parts of the slope. This model does not apply for slopes with a thin debris mantle, confined debris flows, or debris flows in which debris supply is sufficient for net-deposition over most of the length (e.g. Ísafjörður). The model is an over-simplification of the processes involved in debris flow and a true evolutionary trend can only be ascertained on a case-by-case basis. The use of a model of this kind for such a range of debris flow morphologies in Iceland is limited and is probably equally limited for the diverse morphologies of gullies on Mars.

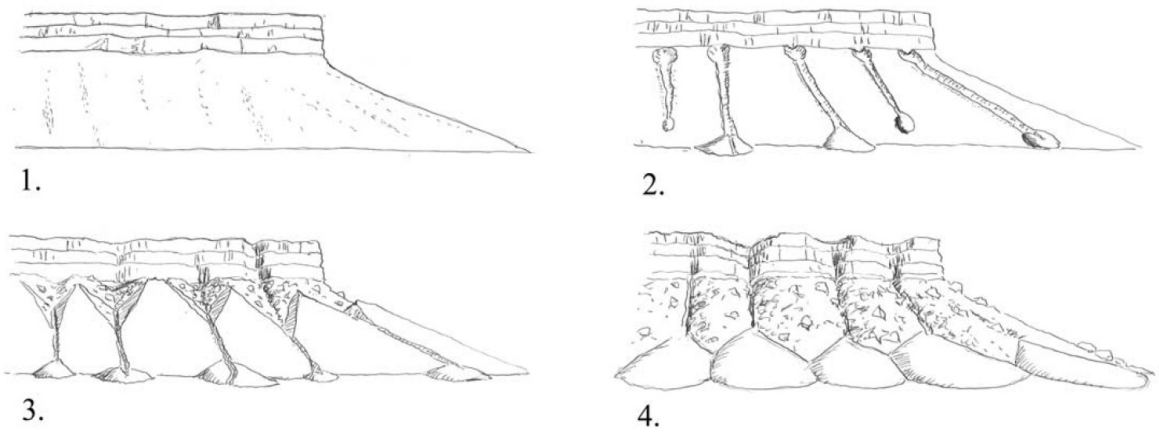

Figure 4-19. A model of the evolution of gullies on Mars, proposed by Hartmann et al. (2003). From Figure 6 in Hartmann et al. (2003).

For unconfined debris flows in Iceland deposition occurs on high slope angles compared to published results for terrestrial debris flows: many debris flows do not reach the end of the slope. This was the case for all unconfined debris flows and many partially confined debris flows. These observations fit with those of martian gullies, which sometimes deposit at high slope angles and do not reach the end of the slope.

In Ísafjörður I found there was a slope threshold for erosion by debris flows near the town. If such a slope threshold could be found on Mars, this would be indicative of debris flow processes. I have verified in this study that estimating the pre-flow topography is possible and represents the patterns of erosion and deposition reasonably well. Hence, if high resolution elevation data of suitable quality were available for Mars, then I could evaluate the erosion and deposition patterns of gullies on Mars. This analysis would not be complicated by the deflation of deposits due to washing out of fines by rainfall on Mars. These patterns would give insight into viscosity of the fluid and allow assessment of the contribution of debris flow to the formation of martian gullies.

4.8. Conclusions

(i) The length and pattern of deposition of a future debris flow of given volume can be estimated from slopes measured on DEMs for its predicted flow path. This conclusion is based on the fact that debris flows above Ísafjörður, in Hnífsdalur and in Súgandafjörður consistently showed similar relationships between cumulative average slope and normalised deposition thickness, despite each flow having wide differences in source materials and setting. This has allowed me to identify areas of the town of Ísafjörður previously not acknowledged as being at risk. I recommend areas that have been identified as medium risk or above not to undergo future development. I suggest that future work should include testing this model with additional data and extending it into other areas.

(ii) This model is notable for its simplicity, which allows future debris flow characteristics to be predicted without the need to determine the precise fluid dynamic parameters of the flow such as viscosity and velocity, which are required to implement more complex models.

(iii) I have found that erosion occurs when slope angles are > 19° in any part of the flow. Hence, any new development should be located in areas with slopes much less than this, in addition to being located away from areas highlighted as medium to high risk in the debris flow modelling.

(iv) Satisfactory estimates of debris flow volumes can be derived from well-placed cross profiles, as demonstrated by other authors, however patterns in erosion and deposition cannot be analysed using this method.

(v) Our method of estimating volumes using the Krige algorithm produces reasonable estimates of debris flow deposition volume, even when pre-flow data are absent. However without pre-flow data the deposition volume tends to be underestimated and the erosion volume greatly over-estimated, but the patterns in deposition and erosion are preserved and realistic bounds of error are given by this method.

(vi) Large hillslope-style debris flows above Ísafjörður, in Hnífsdalur and in Súgandafjörður do not fit existing empirical models developed using data from channelized torrent-fan systems or hillslope flows. Given their significant hazard potential, they therefore warrant more study. Furthermore, an extended study of the cessation point of erosion and the onset threshold of deposition in hillslope debris flows in other regions could lead to more generally applicable relationships. This in turn could provide an important link between the morphometric properties of debris flow deposits and the fluid dynamics of the flows themselves.

(vii) I have demonstrated that debris flows in Iceland are a good analogue for gullies on Mars in terms of (1) lithology and setting, (2) range of morphology (3) triggering

mechanism and (4) slopes on which erosion and deposition occur. Subjectively I have shown that the paucity of observations of levees in gullies on Mars could be due to lighting angle. The methods demonstrated in this study for determining the patterns of erosion and deposition without the information on the pre-existing topography could be useful for determining erosion and deposition patterns of gullies on Mars, given sufficient quality elevation data.

Chapter 5. Comparative Geomorphology

5.1. Introduction

The subject of Chapters 6 and 7 is comparative geomorphology between Earth and Mars. Some data and techniques are common to both chapters, and such the shared information will be described here. Parts of Sections 5.2.1 to 5.2.5, 5.3 and 5.4 have been taken from Conway et al. (2010a), submitted (and in review) for inclusion in the book "Planetary Geomorphology", a Geological Society of London Special Publication.

5.2. Analogue Sites on Earth

Figure 5-1. Location of study sites on Earth. Labels correspond to the letters used for site identification in the text.

Six study sites have been used on Earth in this thesis: Figure 5-1 shows their locations, Table 5-1 provides additional data and the following sections give further details on their

climate, setting and geology. These sites were chosen for two reasons: (1) they contained well documented or good examples of process end-members (dry mass wasting, debris flow or alluvial) and (2) they had high quality elevation data, either in the form of LiDAR, GPS, or stereo photgrammetry. Hillshade maps of these sites are presented in Chapter 7, Figure 7-2.

5.2.1. Site A – San Jacinto, California

This site is located in California along a splay of the San Andreas Fault, called the San Jacinto fault. This area is a desert with little rainfall and has undergone rapid recent uplift caused by the fault system. The landscape has a well developed ephemeral gully network with large alluvial fans. The vegetation is sparse, consisting of small scrub bushes. The underlying geology of the study area is mainly granite, schist and gneiss with minor outcrops of Quaternary "older fan deposits" (Moyle, 1982). This site forms an alluvial process end member.

5.2.2. Site B - Death Valley, California

This site is located a few kilometres NE of Ubehebe volcano in Death Valley, California. This is a desert area that has well developed ephemeral gully networks with large alluvial fans. There is little precipitation, although the nearby mountains receive as much as 85 mm of rain per year (Crippen, 1979). Debris flows are found on the fans in the area, but the primary process active in the gullies is alluvial deposition (Crippen, 1979). The bedrock consists of Palaeozoic sedimentary rocks (Workman et al., 2002). This site forms an alluvial process end member.

5.2.3. Site C – St Elias Mountains, Alaska

This site is located east of the abandoned town of Katalla, close to the recently de-glaciated mountain range of St Elias, near the coast of Alaska and on the border with Yukon, Canada. The area has been unglaciated for approximately the last 10,000 years (Sirkin and

Tuthill, 1987) and receives very high precipitation in the form of snow on the upper slopes and rain on the lower. My study area overlies Tertiary volcanic materials. The slope scarp was generated by an active fault: the Ragged Mountain Fault (Miller, 1961). The area was neither snow covered nor tree covered at the time of survey and the slopes are composed of steep bedrock cliffs that lead directly into large talus aprons. Debris flow tracks are apparent across this talus slope. This site forms a dry mass wasting process end member, but with significant influence from debris flows.

5.2.4. Site D – Front Range, Colorado

This site is located in the mountainous eastern side of the continental divide. The area was deglaciated around 14,000 to 12,000 years before present (Godt and Coe, 2007) and the landscape is dominated by glacially carved valleys. This area has many active debris flows (Coe et al., 2002; Godt and Coe, 2007) and has no permanent snowpack. The study slopes, located above the tree line, are dominated by Precambrian biotitic gneiss and quartz monzonite, scattered Tertiary intrusions, and various surface deposits, all of which host debris flows (Godt and Coe, 2007). The head and sidewalls of the cirques have large rockfall talus deposits, which also contain active debris flows. These slopes have little or no vegetation. This site forms a debris flow end member, but with influence from dry mass wasting.

5.2.5. Site E – Westfjords, Iceland

The site is located in NW Iceland and is dominated by fjords and glacially carved valleys. The last glacial retreat occurred approximately 10,000 years before present (Norðdalh, 1990). The valley walls have many active debris flows (Conway et al., 2010c) and on the slopes above Ísafjörður (Fig. 3g: study area E1) they occur in most years (Decaulne et al., 2005). The site has a maritime climate, so has high levels of both snow and rainfall, but

does not have permanent ice or snow patches. The site is underlain by Miocene basalts, although the debris flows occur generally in glacial till.

The DEM for NW Iceland was produced from the raw LiDAR point data collected by the UK's Natural Environment Research Council's Airborne Research and Survey Facility in 2007 using techniques described in Chapter 4 and by Conway et al. (2010c). This site forms a debris flow end member, but with influence from dry mass wasting.

5.2.6. Site K - La Gomera

Profiles of gullies were taken in south-western La Gomera, where the climate is semi-arid to fully arid. The island is volcanic in origin and volcanic activity ceased ~ 4 Ma ago (Ancochea et al., 2006) since which time the island has been subject to intense fluvial erosion (Llanes et al., 2009). The geology underlying the gullies studied is classified as Old Edifice (10-6.2 Ma) with a mixture of mostly horizontal bedded lavas, pyroclastic and breccia deposits. I collected the elevation data for the three short profiles with differential GPS in the field in May 2008 (using the same methods as described in Chapter 4). Additional data for these profiles (in areas to steep to reach by foot) and additional longer profiles were taken from a 10 m DEM from GRAFCAN (Canary Island Mapping Agency). This site forms an alluvial end member.

Table 5-1. Summary table for the study sites on Earth. Average elevation is given relative to datum, for A-D this is NAD 1983 and for Site E this is WGS 1984, in both cases the difference between the datum and sea level is approximately 60 m. Abbreviations: NCALM - National Center for Airborne Laser Mapping supported by the USA's National Science Foundation, ARSF – Airborne Research and Survey Facility supported by the UK Natural Environment Research Council.

Site	Location	Date Flown	Data Source	Approx. precipitation (mm/year)	Landscape-type	Latitude	Longitude	Average elevation (m)	Relief (m)
A	San Jacinto Fault	mid 2005	NCALM B4 Project	150	desert	33° 25' 58.55" N	116° 28' 57.55" W	597	677
B	Death Valley California	28/02/2005	NCALM	<85	desert	39° 38' 01.77" N	105° 49' 13.88" W	3664	1345
C	St. Elias, Alaska	02-15/9/2005	NCALM	2000	periglacial	60° 18' 18.59" N	144° 32' 14.98" W	490	831
D	Front Range, Colorado	30/09/2005	NCALM	600	periglacial	37° 04' 28.50" N	117° 26' 37.60" W	258	854
E	Westfjords, Iceland	05/08/2007	ARSF	700	periglacial	66° 04' 13.20" N	023° 07' 14.19" W	271	807
K	La Gomera, Canary Islands	n/a	GRAFCAN	~ 200	Semi-arid to arid	28° 07' 04.15" N	17° 20' 4.94" W	467	991

5.3. DEM study sites on Mars

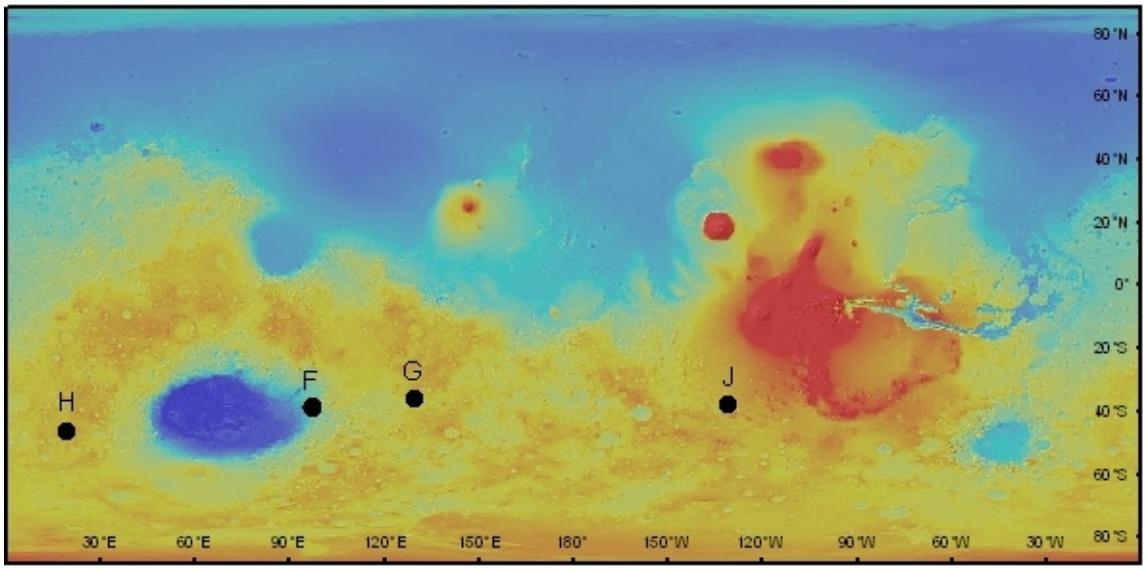

Figure 5-2. Study sites on Mars with DEMs.

Four sites were used as detailed study sites on Mars, restricted by the availability of HiRISE DEMs. Figure 5-2 shows their locations, Table 5-2 provides additional data and the following sections give details on the setting and surface textures. The location of these sites was dictated by the availability of suitable pairs of HiRISE images and all of these sites, except J, were processed and thus selected by the USGS (method detailed in Section 5.4). At the time of writing these were the only HiRISE DEMs of gullies available for me to use. These DEMs are time-consuming to produce, hence why there are fewer gully sites on Mars with DEMs than gully sites with HiRISE stereo image pairs. Hillshade maps of these sites are presented in Chapter 7, Figure 7-3.

5.3.1. Site F – Penticton Crater in Eastern Hellas

This site contains the very recent, light-toned deposits observed by Malin *et al.* (2006) and interpreted by them to be a recent "gully forming" event. These flows were later suggested by Pelletier *et al.* (2008) to be produced by dry granular flow. This slope does not have any well defined channels. The crater is very asymmetric, with the east and north rims being subdued in terms of elevation (the rim is nearly absent on the east side) whilst the southern rim is crisp and steep.

5.3.2. Site G – Gasa Crater in Terra Cimmeria

This ~ 7 km wide crater has well developed alcoves or indentations into the rim of the crater. Gully channels are most obvious on the west-facing to pole-facing slopes and the equator-facing slope lacks these well-defined alcoves and channels. The crater is located within a larger crater, which also has gullies on its west- to pole-facing slopes. There is no evidence of mantle deposits being present anywhere within this crater.

5.3.3. Site H – crater inside Kaiser Crater in Noachis Terra

The study crater, ~ 12 km across is located within the larger Kaiser crater, which not only has gullies down its own rim, but also gullies on the dunes within it (Bourke, 2005). Gullies in this crater have alcoves at various positions on the slope, which converge to form well-defined tributary networks. This slope has the subdued appearance often attributed to the presence of volatile-rich mantle deposits (Mustard et al., 2001).

5.3.4. Site J – crater in Terra Sirenum

This ~ 7 km diameter crater is located to the south of Pickering Crater in Terra Sirenum and contains pole-facing gullies. The equator-facing slope has no evidence of channels, but contains an apparently well developed talus apron with no evidence of mantle deposits.

Table 5-2. Summary table for the study sites on Mars. Average elevation is given relative to the Mars datum, as defined from the MOLA dataset. The average elevation has been estimated from the MOLA dataset and relief from the HiRISE DEMs.

Site	HiRISE image pair	Latitude	Longitude	Average elevation (m)	Relief (m)
F	PSP_001714_1415 PSP_001846_1415	-38.4°	96.8°	-2648	1124
G	PSP_004060_1440 PSP_005550_1440	-35.7°	129.4°	300	1205
H	PSP_003418_1335 PSP_003708_1335	-46.1°	18.8°	595	687
J	PSP_003674_1425 PSP_005942_1425	-37.4°	229.0°	1904	961

5.4. Creating HiRISE digital elevation models

For Mars I used four 1 m/pixel resolution DEMs produced using stereo photogrammetry from 25 cm/pixel HiRISE images. The DEMs for sites F, G, and H were produced by Chris Okubo (USGS) and the DEM for site J by SJC from publicly released HiRISE images using methods described by Kirk *et al.* (2008).

A brief summary of the stereo photogrammetry method is as follows. Firstly Experimental Data Records (EDR) HiRISE data must be acquired and then processed using ISIS3 (Integrated Software for Imagers and Spectrometers). Each HiRISE image is formed by a collection of 20 EDR images, two for each CCD (Charge Coupled Device). These EDR images are mosaiced and tone balanced using ISIS3. These pre-prepared images are then imported into SocetSet, a commercial software package used for stereo photogrammetry. SocetSet performs triangulation calculations which precisely calculate the external camera pointing and the internal camera properties. To generate the DEM SocetSet automatically identifies thousands to millions of matching points between the two images and calculates the stereo parallax vector and hence the elevation for each of them (additional details on this calculation are given in Appendix C). The DEM is produced by interpolation of these points.

The precision of elevation values in the DEMs used here can be estimated based on viewing geometry and pixel scale. For the DEM of site F, the attendant image pair PSP_004060_1440 (0.255 m/pixel) and PSP_005550_1440 (0.266 m/pixel) have a 12.6º stereoscopic convergence angle. Assuming 1/5 pixel matching error and using a pixel scale of 0.266 m/pixel from the more oblique image, the vertical precision is estimated to be $0.266/5/tan(12.6) = 0.24$ m (c.f. Kirk et al., 2003). DEMs for sites G through J have a similar magnitude of vertical precision. The pixel matching error is influenced by signal-to-noise ratio, scene contrast and differences in illumination between images. Pattern noise can also be introduced by the automatic terrain extraction algorithm, especially in areas of

low correlation. Manual editing is necessary to correct spurious topography in areas of poor correlation (e.g., smooth, low contrast slopes and along shadows).

Chapter 6. Statistical analysis of long profiles and morphological classification of gullies on Earth and Mars

6.1. Introduction

6.1.1. Long profiles as indicators of process

In the study of river geomorphology channel long profiles are used to show the change in elevation and slope of the channel with downstream distance (Hack, 1957). Slope long profiles preserve signatures from tectonics, climate, lithology and structure. Each of these factors modulates the dominant processes acting on the long profile and leaves a morphological heritage. Slope long profiles have been used to characterise the landscape change brought about by different processes, such as rockfall (Statham, 1976a), hillslope debris flows (Ballantyne and Benn, 1994) and gullying (Rowantree, 1991).

Certain properties are considered characteristic of a particular process. Rockfall dominated slopes tend to form steep linear slopes of scree or talus (Statham, 1976a). Hillslope debris flows tend to form a profile with a linear steep upper section and a concave lower section (Church et al., 1979; Larsson, 1982; Ballantyne and Benn, 1994). Water-worn gullies on Earth and more developed fluvial systems show a range of morphologies. However, the equilibrium state is considered to be a curve of exponential decay (e.g. Hack, 1957). This has been recently generalised to a power law relation of elevation to downstream distance (Goldrick and Bishop, 2007).

It has been noted that in mature fluvial systems, those parts of the channel long profile with a gradient greater than 0.03-0.1 are often dominated by debris flow processes (Stock and Dietrich, 2006). Several studies have found that the influence of debris flow deposition on a fluvial system decreases the concavity of the river channel profile (Brardinoni and Hassan, 2006; Mao et al., 2009) and can sometimes cause it to become convex (Hanks and Webb, 2006).

Little recent work has been done on discriminating process based on slope long profile measurements in small, relatively young systems on Earth. These systems have the benefit that they usually have a spatially uniform lithology, structure, climatic history and tectonic history and thus have a quantifiable morphological heritage. This should make process discrimination possible without interference from other factors. In this chapter I present data from ephemeral water-worn gullies and debris flow gullies on Earth that confirm the differences in long profile brought about by these two processes. I have then compared the results to gullies on Mars, to try to determine the process of gully formation there. In addition: (1) I compared non-gullied slope long profiles to gullied slope long profiles on Mars, (2) I looked for trends in visual properties and long profile properties, and (3) I tested whether the properties of craters determine the presence or absence of gullies within them.

The aims of these analyses were to (1) determine if long profiles on Mars preserve the signature of debris flow, or pure water flow, (2) test if gullies on Mars are formed by different processes and (3) look for global trends that might give clues as to the origin of the gullies on Mars.

6.1.2. Sites Studied on Earth

Five terrestrial analogue sites were studied. Two of these had debris flow as the dominant gully forming process: Colorado Front Range in the USA and the Westfjords of NW Iceland. Three had ephemeral water flow as the dominant gully formation process: Death

Valley, California; San Jacinto, California and La Gomera in the Canary Islands, Spain. Full site descriptions and data types were given in Chapter 5. In contrast to the other sites, none of the gullies in La Gomera had developed depositional fans and they terminated at the sea or the valley bottom. The long profiles in La Gomera in which data from the 10 m DEM were used were less accurate because of the low resolution of the DEM.

6.1.3. Sites Studied on Mars

I sampled gullies that had stereo HiRISE data coverage with greater than 50 % image overlap; these have a wide range of geographic locations and settings (Figure 6-1, Table 6-1). The selection of the study sites was limited by the spatial availability of suitable quality stereo pairs, but was not restricted by the availability of DEMs, which have an even more limited spatial coverage (Figure 5-2). Hence there is overlap in this study with the study sites in Chapter 7, but the sites are not so spatially restricted. Where it was possible, slope long profiles were also measured in non-gullied areas in the same image pairs. However, I found that slopes without gullies rarely had more than one HiRISE image, which prevented the sampling of craters or other slopes entirely free from gullies.

6.2. Approach

6.2.1. Identifying suitable image pairs on Mars

I extended the catalogue of Mars Orbiter Camera narrow angle (MOC-NA) images containing gullies compiled by Balme et al. (2006) up to orbit R10 and also added High Resolution Imaging Science Experiment (HiRISE) images up to the March 2009 Planetary Data System (PDS) release. Importantly, in both these catalogues all images were checked for gullies, hence those images excluded implicitly do not contain gullies. I added more images to the HiRISE catalogue by finding all images which overlapped with the image footprints included in the MOC-NA catalogue. The MOC-NA catalogue also contains information about the setting of the gullies and this was transferred to the HiRISE image

footprint database. HiRISE image pairs suitable for extraction of stereo elevation data were identified using the "Find Overlapping Polygons" script for ArcMap by Ken Buja which also allowed extraction of the overlapping area of the image pairs.

Table 6-1. Number of profiles collected and included in this study, with associated HiRISE image pairs. The criterion for excluding certain profiles is given in Section 6.3.1.

Image 1	Image 2	Number of gully profiles	Number of slope profiles	Excluded gully profiles	Excluded slope profiles
PSP_001508_2400	PSP_007666_2400	2	0	2	0
PSP_001528_2210	PSP_002214_2210	3	0	0	0
PSP_001552_1410	PSP_002172_1410	1	0	0	0
PSP_001578_1425	PSP_002066_1425	2	0	0	0
PSP_001684_1410	PSP_002027_1410	2	0	0	0
PSP_001714_1415	PSP_001846_1415	1	0	1	0
PSP_001714_2390	PSP_001846_2390	2	1	0	0
PSP_001823_1320	PSP_001691_1320	1	0	0	0
PSP_002014_1415	PSP_006695_1415	1	1	0	0
PSP_002425_1425	PSP_001792_1425	2	1	0	0
PSP_002884_1395	PSP_003517_1395	3	1	0	0
PSP_003096_1375	PSP_003940_1375	0	2	0	0
PSP_003215_1405	PSP_003492_1405	2	1	1	0
PSP_003302_1330	PSP_003170_1330	1	0	0	0
PSP_003498_1090	PSP_003353_1090	4	0	0	0
PSP_003511_1115	PSP_003287_1115	1	0	1	0
PSP_003557_1335	PSP_004058_1335	3	1	0	0
PSP_003583_1425	PSP_006629_1425	3	1	0	0
PSP_003596_1435	PSP_004229_1435	1	3	0	0
PSP_003627_1345	PSP_006963_1345	1	0	0	0
PSP_003649_1435	PSP_003794_1435	2	2	0	0
PSP_003674_1425	PSP_005942_1425	3	1	0	0
PSP_003675_1375	PSP_005877_1375	4	0	0	0
PSP_003708_1335	PSP_003418_1335	3	0	0	0
PSP_003954_1445	PSP_004310_1445	1	1	1	1
PSP_004024_1360	PSP_005646_1360	2	0	0	0
PSP_004167_1400	PSP_002888_1400	3	0	0	0
PSP_004804_1105	PSP_004949_1105	1	0	1	0
PSP_005054_1085	PSP_004988_1085	1	0	0	0
PSP_005319_1245	PSP_003842_1245	1	0	0	0
PSP_005550_1440	PSP_004060_1440	1	0	1	0
PSP_005576_1480	PSP_005286_1480	2	0	1	0
PSP_005586_1425	PSP_005731_1425	3	2	0	0
PSP_005587_1405	PSP_004176_1405	3	0	0	0
PSP_005595_1150	PSP_005160_1150	2	0	0	0
PSP_005739_1305	PSP_005673_1305	1	0	0	0
PSP_006922_2120	PSP_003942_2120	0	2	0	0
PSP_007062_1225	PSP_003515_1225	1	0	1	0
PSP_007085_1365	PSP_006162_1365	3	0	0	0
PSP_007110_1325	PSP_006820_1325	3	0	0	0
PSP_007112_1435	PSP_006545_1435	3	0	1	0
	TOTAL:	79	20	11	1

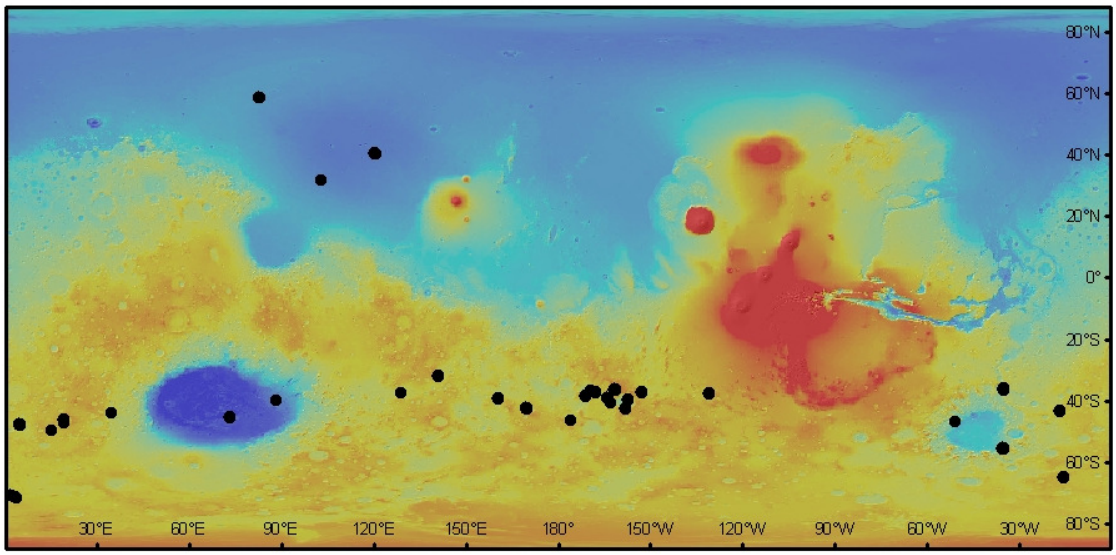

Figure 6-1. Global elevation map of Mars with locations of stereo HiRISE image pairs used for the profile analysis marked as black dots. Elevation data from MOLA gridded data.

From these image pairs I selected all those that contained gullies and had greater than 50 % overlap. This procedure produced a greater number of potential pairs than are flagged as stereo-acquisitions by the HiRISE team. Hence, it includes images that are not necessarily suitable for automated stereo matching due to, for example, differences in albedo, but which are suitable for manual stereo matching. These data were then manually filtered based on image quality. Some image pairs were rejected because they contained images that either had artefacts or were too blurred to identify matching points. Other image-pairs were rejected because they did not overlap in the correct location to cover either whole gullies or slopes of interest. The data were inspected in order of decreasing overlap. Table 6-1 lists the image pairs that passed these filtering procedures and have been used for the following analyses.

6.2.2. Extracting topographic profiles on Mars

I adapted a manual point matching method developed by Kreslavsky (2008) for capturing point elevation data from Reduced Data Records (RDR) HiRISE images. Details of the Kreslavsky (2008) method are given in Appendix C. A summary of the procedure that I have followed is given below.

Using ESRI's ArcGIS I created point shapefiles, one for each image within a stereo pair. Matching points, such as boulders, were identified and digitised in both images. The estimated error for this matching is 1-3 pixels. Points along the line of the gully profile were digitised at 50-100 m spacing, but this spacing varied according to the availability of features to match. Each point was classified as one or more of the following: "pre-gully", "alcove", "channel", "debris apron", or "debris apron width marker". The classifications were allocated as follows:

(1) pre-gully – any part of the slope included in a profile that was above a gully;

(2) alcove – any area where the flow appeared to be confined (e.g. the channel was confined by bedrock, or deep incision) and principally erosive;

(3) channel – any area where the flow appeared to be unconfined and erosive, i.e. the channel was free to migrate over an open slope;

(4) debris apron – any area where the flow was seen to be depositing; and

(5) debris apron width marker – two of these were placed, one at either side of the flow at the furthest lateral extent of the debris apron for that gully.

Digitisation was started at the top of the slope and continued to the base of the debris apron. For slopes without gullies, all points were classed as "pre-gully" and the profile was judged to be complete at the end of the scree-slope or debris fan. Each gully was given a unique identification number. For each point the x and y coordinates were extracted in map-space and converted to pixel coordinates using the projection information and image resolution on the ground supplied in the image metadata (PDS label file). The pixel coordinates were given from the top left corner of the image and positive in the top-to-bottom and left-to-right directions. These coordinates were passed through the script developed by Kreslavsky (2008) and the output, consisting of the x, y, z coordinates and error field in metres were appended directly to the shapefiles. The coordinates were given relative to the centroid of the point array, rather than to Mars datum. The error term not

only contains the error associated with the errors in digitisation, but also the error brought about by the assumptions made about the image geometry; further details can be found in Appendix C. A discussion of what this error represents in terms of a vertical offset in metres is discussed in Section 6.3.1.

6.2.3. Analysis of the Long Profiles

All the long profiles were analysed to collect the following information: total planform length, total elevation difference, start-to-end gradient (slope of *AB*, Figure 6-2), radius of curvature, concavity (3 methods, detailed below) and the relative position of the maximal concavity. These profile statistics were collected both for the part of the profile that contained the gully and the whole slope long profile. The length and the maximum, minimum and mean slopes were calculated for each individual portion of the gully (pre-gully, alcove, channel, debris apron). In addition, the following were also calculated: debris apron width to length ratio, the debris apron length as a proportion of the overall length, the pre-gully length as a proportion of the overall length and the overall range of slope.

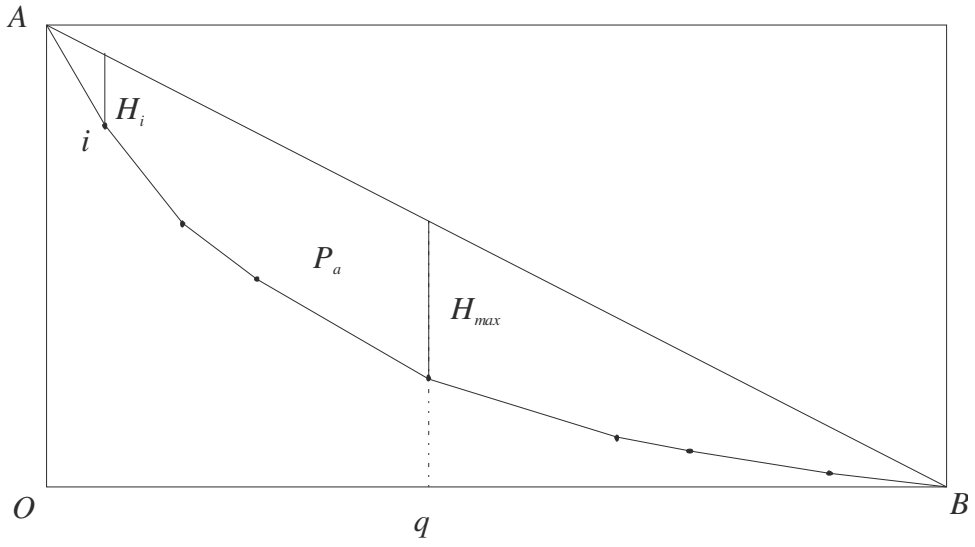

Figure 6-2. Annotated sketch of a typical long profile. *A* is the source and *B* is the distal end, with P_a representing the area between the straight line *AB* and the profile, H_i is the elevation difference between the straight line and the profile at point *i* and H_{max} is the maximum value of H_i with *q* the horizontal distance associated with it. Hence E_q is the distance *Oq* normalised by *OB*.

Concavity was derived using three methods:

(1) Following Demoulin (1998) I calculated the area between the straight line connecting the source to the distal extent of the deposits and the profile (P_a, Figure 6-2) expressed as a percentage of the triangle's area (AOB, Figure 6-2). P_a only included portions of the profile that dropped below the straight line. This parameter is used by Demoulin (1998) as a proxy for the area eroded, A_{ero}. In addition I calculated the position of the maximal concavity ($E_q=O_q/OB$, Figure 6-2), which is the distance to the point in the profile where the difference between the profile and the straight line is the greatest (H_{max}), normalised by the distance OB. This is otherwise known as the "Kennedy Parameter" (Allison and Higgitt, 1998). The smaller E_q the better graded the profile, conversely the larger A_{ero} the better graded the profile, i.e. the more similar the profile to an "ideal" river profile following a curve of exponential decay.

(2) I calculated the concavity index (θ) of Goldrick and Bishop (2007), which is the gradient of the best-fit line in the plot of log slope against log distance. Negative values mean that the profiles are concave and positive that the profiles are convex.

(3) The relative concavity index (CI) of Phillips and Lutz (2008) was also calculated, in which the sum of the distances between the profile and the straight line (H_i, Figure 6-2) is divided by the number of segments and normalised by the overall height drop (AO, Figure 6-2). CI ranges between 1 and -1, with negative values indicating convexity, positive concavity and 0 is a linear profile.

The radius of curvature was calculated by fitting a circle to the profile and taking its radius as a measure of the curvature of the profile.

6.2.4. Validation of the point-matching method

I tested the Kreslavsky (2008) method against published DEMs in order to (1) verify that the assumptions made in the method are not detrimental to the results and, (2) to determine a value of output error beyond which data should not be used for further analysis. I

compared the results from profiles analysed by the Kreslavsky (2008) method to profiles taken from four HiRISE DEMs, detailed in Chapter 5, (Table 5-2). The vertical precision of these DEMs is estimated to be ~ 0.24 m. Hence the error in elevation is very small and for the purposes of this project, considered as "truth" in terms of comparison with the results of the point matching method. The position of the points in the DEM profile was matched to be as close as possible to the position of the points in the manual profiles. Approximately 1 m of positioning mismatch was introduced by transferring the profile points to the DEM profile.

6.2.5. Additional information for long profiles on Mars

Additional attributes were recorded at the sites of long profile collection on Mars including: latitude of image centre, longitude of image centre, presence of polygonal structures (Figure 6-5E), presence of sinuous channels (Figure 6-5F), linear gully density (gullies per km of slope section), gully setting, alcove type, fan type, and whether the gullies occur in a discrete part of the slope and nowhere else ("patch"), or gradually appeared ("progressive"; Figure 6-4). Gully settings were defined as one of the following: inner crater rim (e.g. Figure 2-7a), outer crater rim, crater central peak, crater central pit, valley wall, hill, dune (e.g. Figure 2-7e) and polar pit (e.g. Figure 2-7b). Fan types were divided into single types (Figure 6-5C) and interlaced types (Figure 6-5A), in which single fans occur on their own; interlaced fans interact with fans from other gullies. Each of these categories contained the subjective sub-categories: small, medium and large. An additional category was "amorphous" (Figure 6-5B), which represented deposition that could not be divided into fans. Alcove types were divided broadly into open and closed. Closed types were those which have a discrete upper terminus delimited by a break in slope, and open were those which did not possess this clear boundary. Closed types were divided into single and lobate. Open types were divided into: rockwall chute, bouldery chute and wide. The different alcove types are illustrated in Figure 6-3.

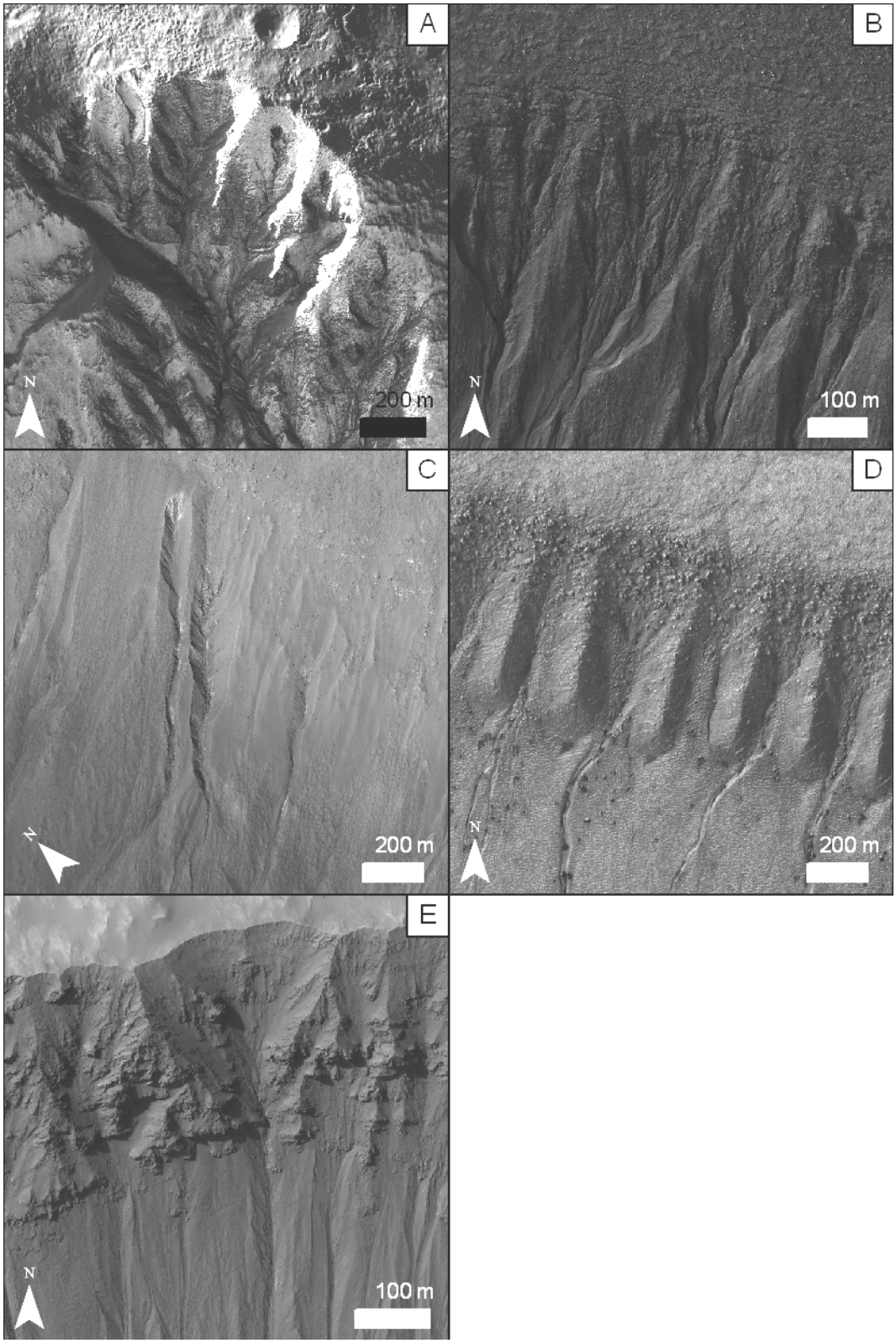

Figure 6-3. Examples of alcove types on Mars. (A) Closed lobate type, part of image PSP_001552_1410. (B) Open wide type, part of image PSP_001792_1425. (C) Single closed type, part of image PSP_002884_1395. (D) Bouldery chute type, only found in the polar pits, part of image PSP_003498_1090. (E) Rockwall chute type, part of image PSP_005586_1425. Image credit: HiRISE team, UofA/NASA.

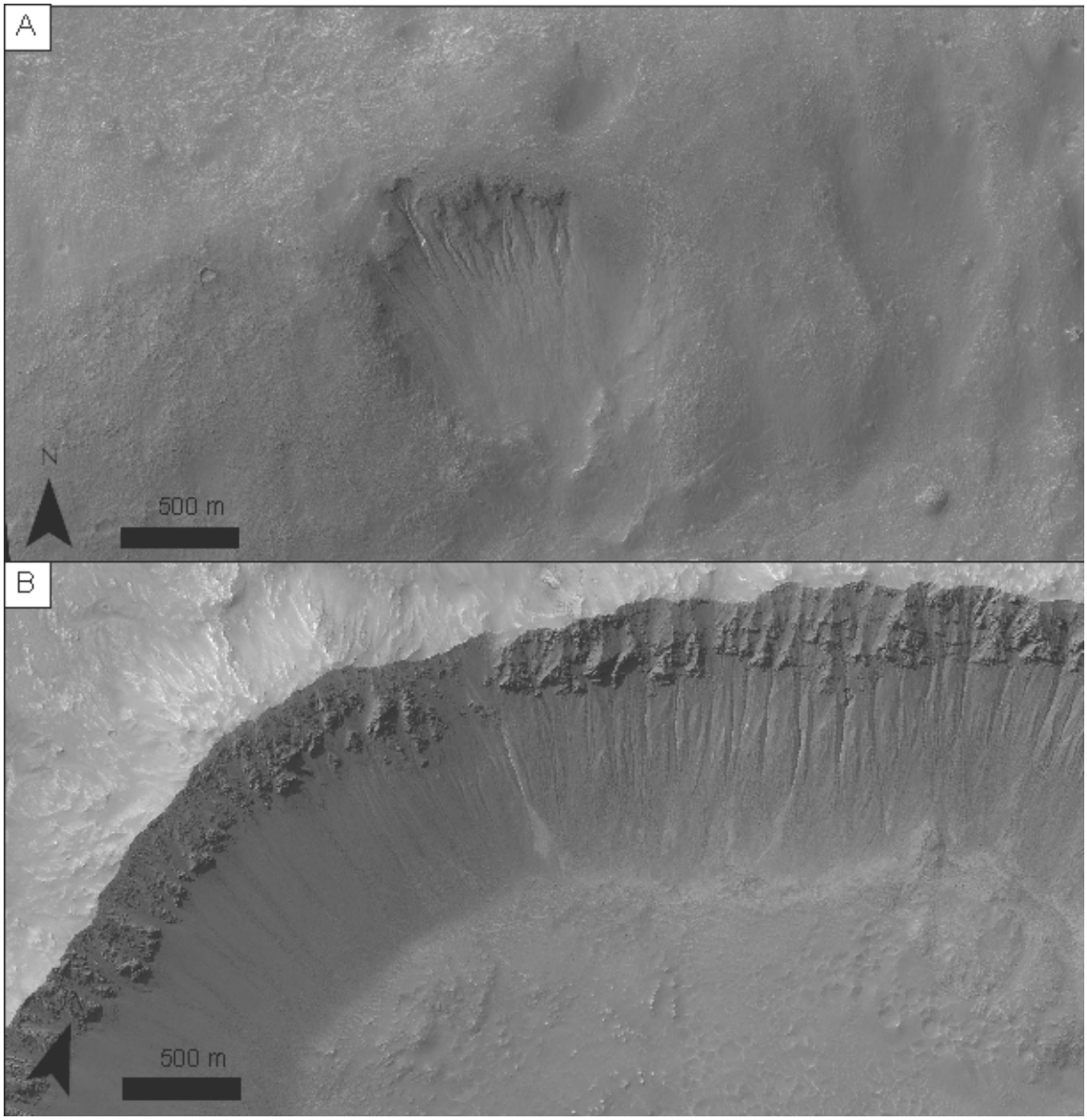

Figure 6-4. Examples of patch and progressive gully types. (A) Patch types are where gullies occur in a discrete part of the slope and nowhere else. HiRISE image PSP_005701_1445, credit NASA/JPL/UofA. (B) Progressive types are where gullies occur across a slope but gradually disappear along the slope, i.e. the slope appears to go from gully-dominated to mass wasting dominated. HiRISE image PSP_005586_1425, credit NASA/JPL/UofA.

6.2.6. Extracting long profiles on Earth

The same system of digitisation and classification, as outlined in Section 6.2.2, was applied to long profiles on Earth. However, there was no need to run the points though the script developed by Kreslavsky (2008), because all the sites on Earth had elevation data, which could be directly interrogated.

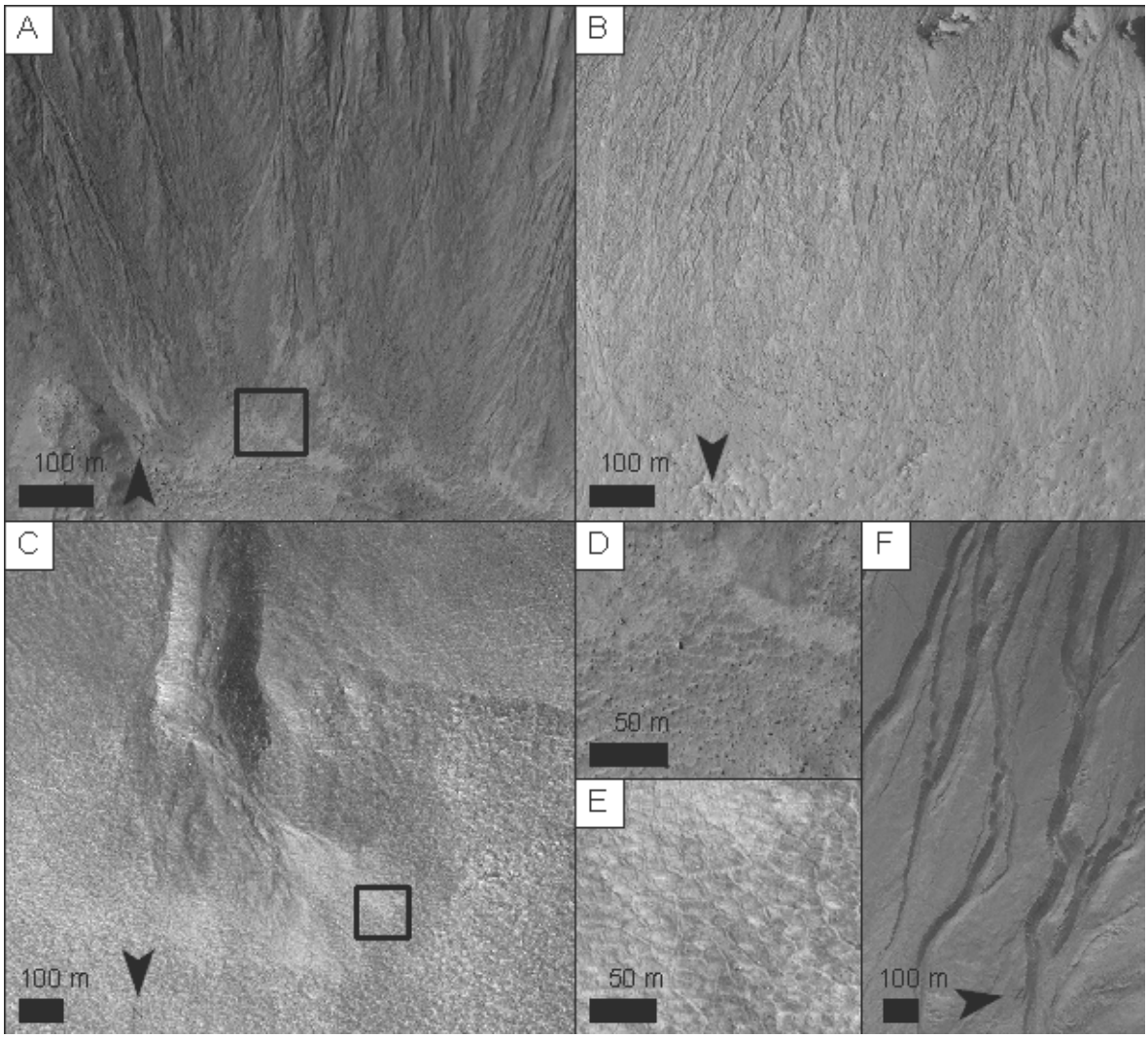

Figure 6-5. Examples of different fan types, polygonal structures and sinuosity. (A) Example of the interlaced fan type, with low sinuosity channels. Black box is an approximate location of (D). HiRISE image PSP_005586_1245, credit NASA/JPL/UofA. (B) Amorphous fan type, in which different fans cannot be separated easily. HiRISE image PSP_003557_1335, credit NASA/JPL/UofA. (C) Single fan type, in which no other fan overlaps with it. Black box is an approximate location of (E) HiRISE image PSP_001714_2390, credit NASA/JPL/UofA. (D) Example of surface without polygonal structures. (E) Example of surface with polygonal structures. (F) Example of channels with sinuosity HiRISE image PSP_003583_1425, credit NASA/JPL/UofA.

6.2.7. Craters on Mars

The majority of martian gullies are found within craters (e.g. Balme et al., 2006). To assess if gullies occur inside craters with particular properties I linked the HiRISE and MOC-NA gullies catalogue described in Section 6.2.1 to the GT-57633 crater catalogue of Salamunićcar and Lončarić (2008). I converted the radii of the craters given in GT-57633 in decimal degrees into radii in kilometres using the equidistant projection for latitudes $< 60°$ and the polar stereographic projection for latitudes $> 60°$. Using the x and y

coordinates of the crater centres and their radii I created circles to represent their rims. I then determined which images from the HiRISE and MOC-NA catalogue overlapped with the rims (polylines) of the craters. From this I was able to determine: (1) those crater rims that hosted gullies, (2) those that had overlapping images but no gullies and (3) those that had no coverage in the catalogue. It is possible that craters classed as not having gullies could host gullies on parts of the rim that have not yet been imaged, however this was considered to be a relatively small proportion. Using the gridded Mars Orbiter Laser Altimeter (MOLA) data the depths of the craters were ascertained by taking the difference between the maximum and minimum elevation pixels within the crater. The maximum slope within the crater was calculated from the MOLA slope map generated using the slope tool within ArcMap's Spatial Analyst extension. The depth, diameter and maximum slopes of the craters were then compared for those with and without gullies.

The crater depth and maximum slope derived from MOLA data are both likely to be underestimates. MOLA shot size is 130 m with an along-track spacing of 300 m. MOLA gridded data are interpolated in the cross-track direction (over > 1 km in some instances) and some of the additional detail included in the along-track direction is smoothed out. Hence MOLA has insufficient resolution to capture maximum rim height, minimum crater elevation and local slopes, which are all features with length scales < 100 m.

6.3. Results

6.3.1. Validation of the point-matching method

The difference between the profile parameters (detailed in Section 6.2.3) calculated for the DEM profiles and the profile parameters from profiles calculated by the Kreslavsky (2008) method are shown in Table 6-2. Two of the profiles (PSP_001714_1415, Gully ID 1 and

PSP_005550_1440, Gully ID 1) have high estimates of stereo error and correspondingly also have large differences between the DEM profile and manual profile parameters.

Table 6-2. Differences between profile parameters for stereo-point analysis and DEM analysis. "nm" stands for not measured, because that slope section type was not present.

Image 1	PSP_001714_1415	PSP_003674_1425	PSP_003708_1335	PSP_003708_1335	PSP_005550_1440
Gully ID	1	4	1	2	1
Difference in total length %	-7.74	-7.62	-0.76	-0.31	-12.28
Difference in total height %	-7.89	-0.18	3.65	3.69	2.15
Difference in average channel slope (°)	nm	nm	1.30	0.47	9.09
Difference in minimum channel slope (°)	nm	nm	1.54	-0.22	6.88
Difference in maximum channel slope (°)	nm	nm	2.10	0.61	59.05
Difference in average pre-gully slope (°)	4.61	2.06	0.88	0.83	nm
Difference in minimum pre-gully slope (°)	-3.57	1.26	-0.35	0.56	nm
Difference in maximum pre-gully slope (°)	46.43	-1.89	2.11	0.64	nm
Difference in Area of Erosion (Aero)	-0.10	0.02	0.02	0.05	0.33
Difference in best fit circle radius (m)	-490	-298	-1011	-345	-7979
Difference in Relative Concavity Index (CI)	-0.126	0.005	0.011	0.005	0.044
Difference in relative position of maximal concavity (Eq)	0.068	-0.002	-0.005	0.001	0.331
Difference in Concavity Index (θ)	-0.30	-0.01	0.01	-0.03	0.23
Difference in start-end gradient	0.02	-0.05	-0.01	-0.01	0.01
Mean error value	0.00	-8.80	0.50	0.88	-6.52
Standard deviation of error value	36.12	2.92	1.10	6.01	126.77

Reassuringly the profiles with low error estimates also have small differences between their parameters. This is a good first indication that the error output of the Kreslavsky (2008) method is a reasonable estimate of the real error. These profiles have at worst 2° differences in slope, 7 % difference in length, and 3.5 % difference in elevation.

For the concavity measures: CI should range between -1 and 1, so differences < 0.01 are very good; E_q should be between 0 and 1, so differences << 0.01 are extremely good; θ has values of down to -1 in Goldrick and Bishop (2007), so differences of < 0.01 are very good, and A_{ero} can have values of up to 0.5 (Demoulin, 1998), so differences of 0.05 are reasonable. However, it is clear that the best-fit circle radius parameter is very sensitive to the relative position of the points, because it has large differences between the profiles, despite the differences being low for the other parameters. Hence, this parameter has been excluded from future analyses.

The error output by the Kreslavsky (2008) method was compared to the real error, the combined stereo error of every consecutive pair of points in the profile was calculated using the standard formula $\sigma_Z = (\sigma_A^2 + \sigma_B^2)^{0.5}$, where σ_Z is the total uncertainty, and σ_A and σ_B are the uncertainties of the two points. The first point of the pair was then fixed at the same elevation in the DEM profile and the manual profile and the difference in elevation between the two methods calculated for the second point. The plot of the combined stereo error against this elevation difference is shown in Figure 6-6. Although there is no obvious trend of the stereo error with the elevation difference, it is clear that even if the stereo error is of the order of ~ 15 m this corresponds to an elevation difference of 5 m in the worst case and more likely < 2 m. This elevation difference can lead to errors in slope calculations of the order of ~ 1°, or 3° at worst. Reassuringly, very large stereo errors (> 100 m) correspond to very large elevation differences. The mean stereo error was not reliable as an indicator of error for the whole profile. Stereo errors often fluctuated around zero, so a profile with average error of zero could have extreme positive and negative values, as demonstrated by profile 1 of PSP_001714_1415 in Table 6-2. The standard deviation was a better guideline and a cut-off value of 20 m was chosen to provide a criterion to discriminate between profiles to include and those to exclude from further analysis. From visual inspection a value of around 20 m for the standard deviation was due

to a single outlier. A total of 2116 points were measured and of those 7 % had an error greater than 20 m, 15 % had an error of greater than 10 m and 27 % had an error of greater than 5 m. Using the 20 m cut-off, 12 profiles and 7 image pairs were eliminated from the study sample of 99 profiles (Table 6-1) in a total of 41 images.

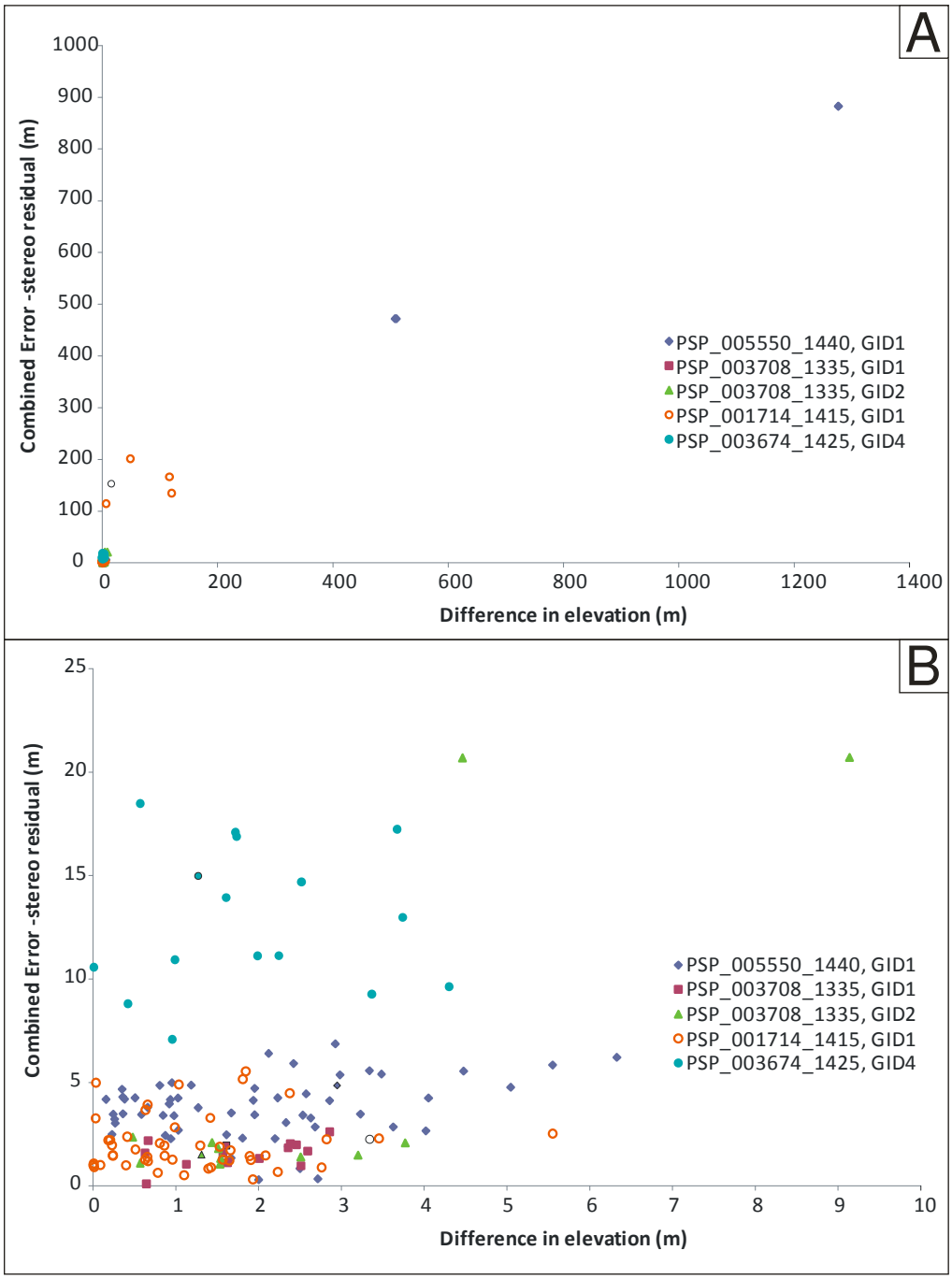

Figure 6-6. Error analysis of stereo method of Kreslavsky (2008). (A) All the data points and (B) the same data, but enlarged near the origin.

6.3.2. Comparing Earth and Mars

6.3.2.1. Profile lengths and ratios

All the profiles used in this study are shown in Figure 6-7 and Figure 6-8. Gully length against height is shown in Figure 6-9. Alluvial gullies (Death Valley, San Jacinto and La Gomera, Figure 6-7C, D and E, and Figure 6-9) have a wide range of lengths and heights, and have a range of profile shapes. Some of the alluvial gullies are very concave (Figure 6-7C and Figure 6-7E) and all of the gullies in Death Valley and San Jacinto have moderate to high concavity. In contrast, gullies in La Gomera can have very linear profiles (Figure 6-7E). Errors in digitisation due to the coarse resolution of the DEM led to the uneven shape of some of the profiles in La Gomera. At 10 m per pixel the DEM sometimes captured the channel minima and sometimes the lip of the gorge, leading to a sawtooth shape in some of the profiles. Compared to alluvial gullies, debris flow gullies (Colorado Front Range and Iceland) have a restricted range of lengths, heights and profile shape. Their profile shape is slightly concave and, compared to alluvial gullies, very consistent in shape, especially in NW Iceland (Figure 6-7B). Many of the profiles have a basal concavity, i.e. they are more concave in the lower parts. Martian gullies have an even wider range of lengths, heights and profile shape. Some martian profiles are convex in profile, most have a "pre-gully" slope, before the gully begins and the majority are concave in profile. Gullies from Noachis Terra have particularly marked concavity (Figure 6-8D). Martian non-gullied slope long profiles tend to have very linear profiles (Figure 6-8F), but several show marked concavity. From these simple comparisons some qualitative differences between alluvial, debris flow and martian gullies seem to be apparent. An in-depth, quantitative analysis of the profiles is given in the following sections.

6.3.2.2. Discrimination analyses

Canonical discrimination analysis (McLachlan, 2004) was performed on the profile parameters to: (1) enable the identification of the parameters that were important for separating alluvial and debris flow gullies, and (2) to determine if martian gullies have unique characteristics that could separate them from terrestrial gullies. Canonical discrimination analysis attempts to find a linear combination of variables that best separates any given groups. The first function is the linear combination for which the separation is maximised. Standardised versions of the variables (i.e. the variables are transformed so that their mean is 0 and their variance is 1) are used in this analysis as it allows assessment of the relative importance of the variables within each discriminant function. The number of functions derived is one less than the number of groups.

Table 6-3 shows: (1) the function coefficients that best separate terrestrial alluvial gullies, terrestrial debris flow gullies and martian gullies, and (2) those coefficients that best separate debris flow and alluvial gullies on Earth. This table reveals that the greatest differences between the data can be seen if you consider the following variables: average alcove slope, average debris apron slope, eroded area (A_{ero}), relative Concavity Index (CI), position of maximal concavity (E_q) and gully start-end gradient. I excluded the ratios of debris apron length to width and debris apron length to gully length, because (1) not all gullies had this information and (2) from a separate discriminant analysis they were shown to be less important parameters. The maximum and minimum slopes of alcove channel and debris apron were also excluded from this analysis because, (1) they are based on single values, and so were susceptible to errors from anomalous points and (2) they correlate very strongly with the average values of slope anyway.

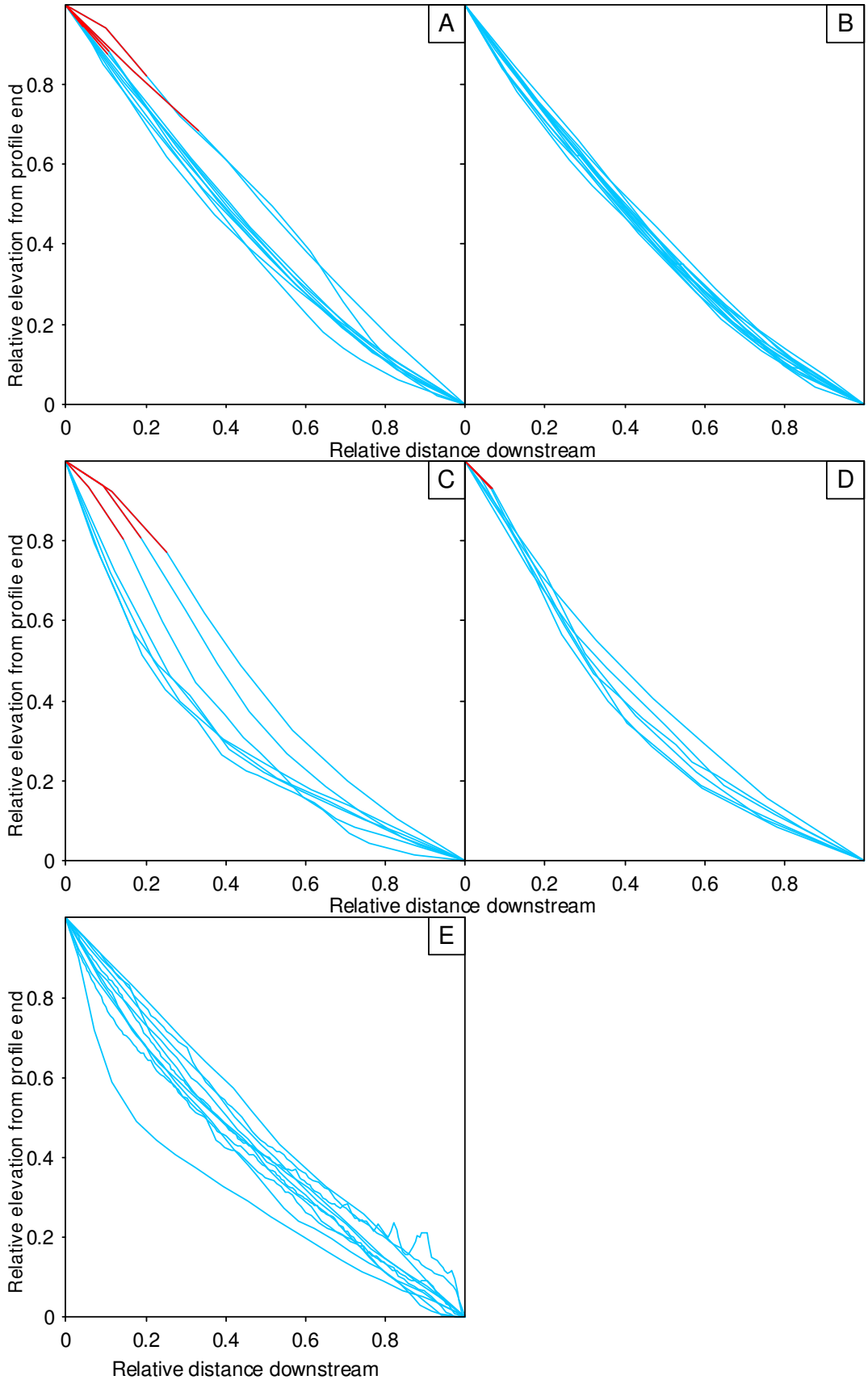

Figure 6-7. Profile data from Earth. Red portions of the line are parts of the slope pre-gully and blue is the gully. (A) Debris flow gullies in the Colorado Front Range, USA. (B) Debris flow gullies in NW Iceland. (C) Alluvial gullies along the San Jacinto fault, California. (D) Alluvial gullies in Death Valley, California. (E) Alluvial gullies in SW La Gomera, Canary Islands, Spain.

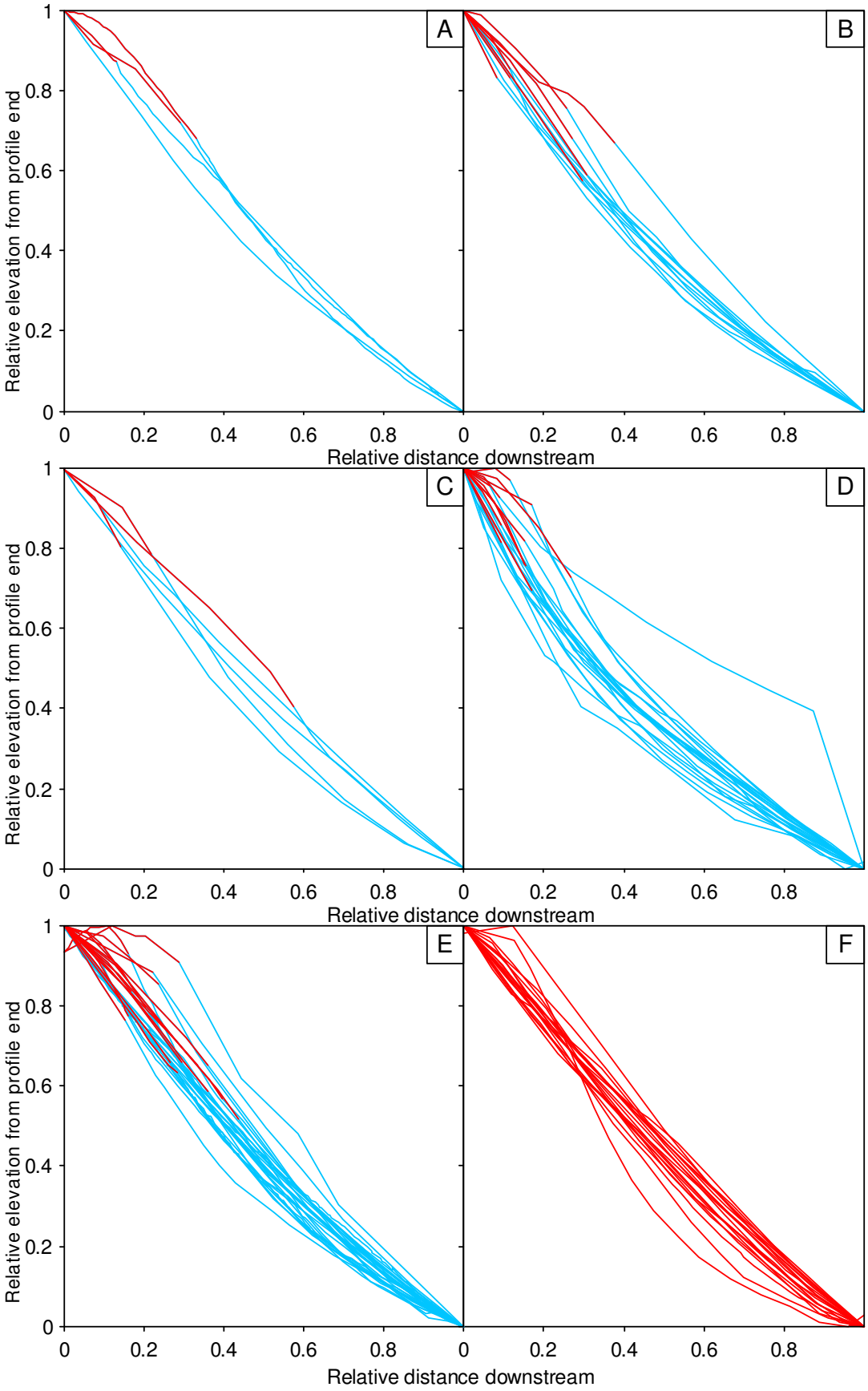

Figure 6-8. Profile data from Mars. Red portions of the line are parts of the slope pre-gully and blue is the gully. Gullies in the (A) Argyre region, (B) Eastern Hellas region, (C) Northern hemisphere, (D) Noachis Terra, (E) Terra Sirenum and (F) slope long profiles without gullies.

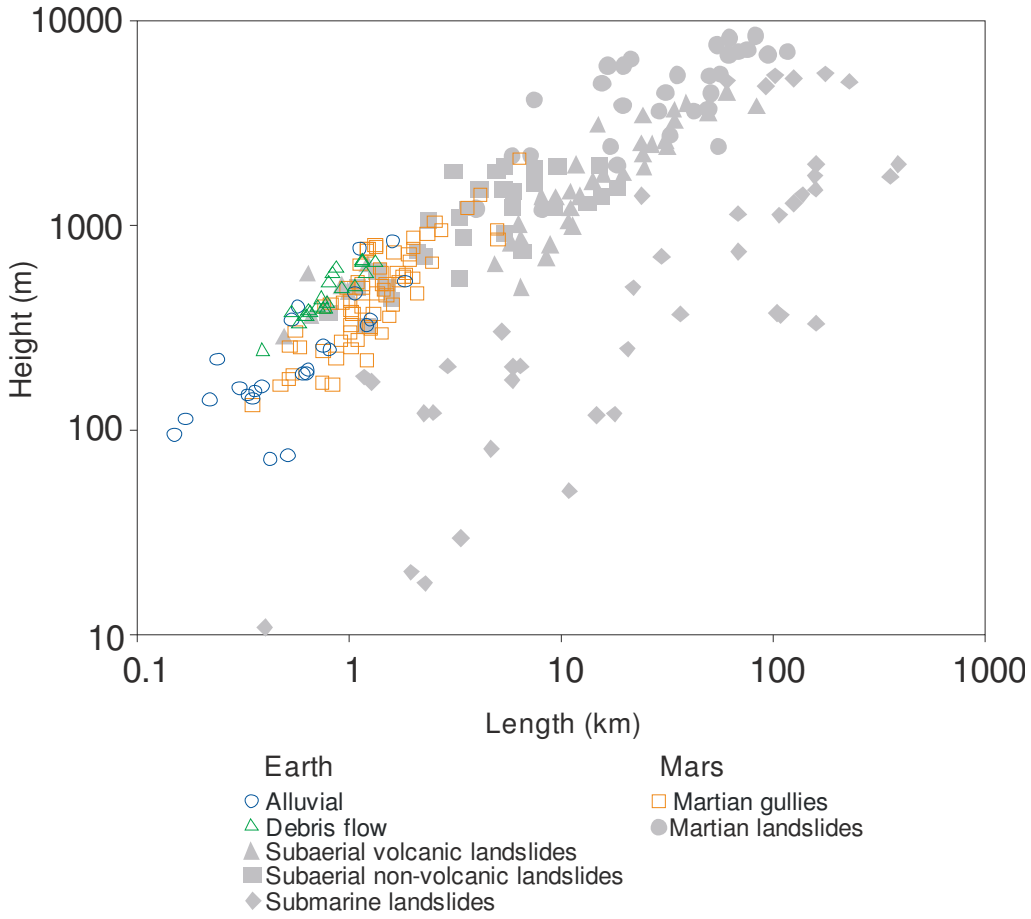

Figure 6-9. Log-log plot of height against length for gullies on Mars and Earth compared to landslides of Legros (2002). My data are represented as hollow symbols and data of Legros (2002) as filled grey symbols.

Table 6-3. Standardized Canonical Discriminant Function Coefficients for separation of terrestrial alluvial gullies, terrestrial debris flow gullies and gullies on Mars, and alluvial and debris flow gullies on Earth only. The more important the parameter the higher the magnitude of its coefficient, and coefficients with absolute values > 0.5 are highlighted.

	Earth and Mars		Earth Only
	Function		Function
	1	2	1
Slope Range	-.230	.059	-.879
Average Alcove Slope	1.611	-.451	1.659
Average Channel Slope	-.218	.347	-.515
Average Debris Apron Slope	.687	.284	.425
Erosion Area (A_{ero})	.285	.600	.774
Relative Concavity Index (CI)	-.996	.338	-.522
Position of maximal concavity (E_q)	.423	.542	.852
Concavity Index θ	-.020	.475	.352
Gully height	.302	-.446	.596
Gully Length	.268	.547	.421
Gully start-end gradient	2.116	-.951	.441

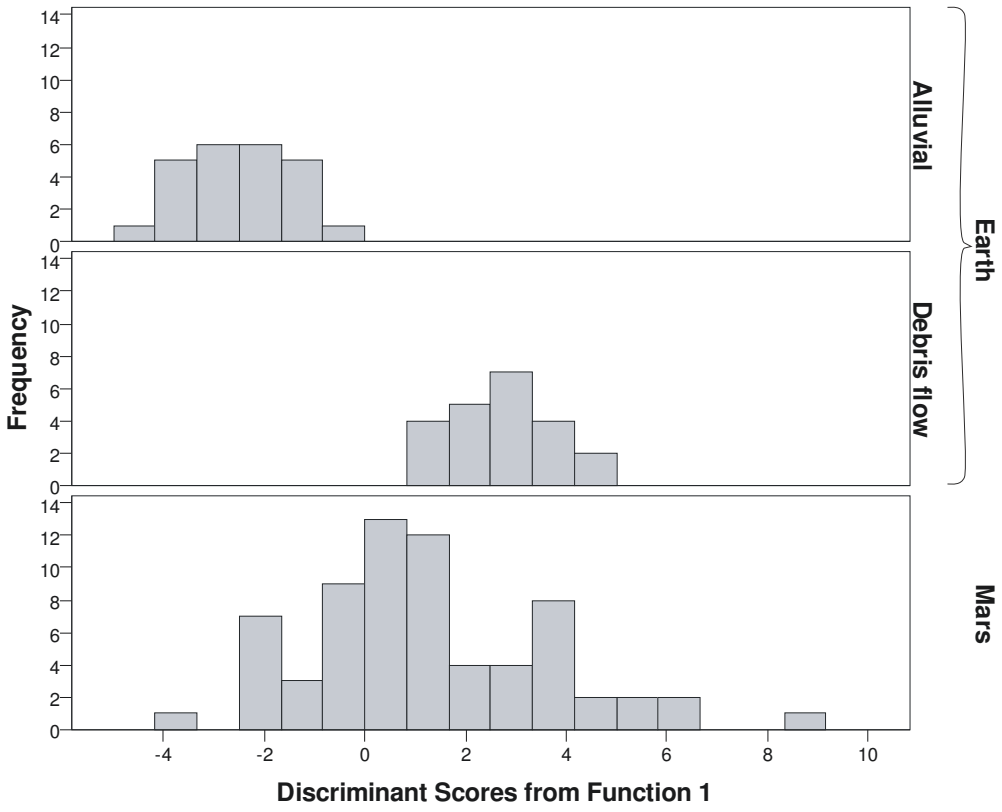

Figure 6-10. Stacked histograms of the discriminant score calculated from the coefficients in Table 6-3 for terrestrial alluvial, debris flow and martian gullies.

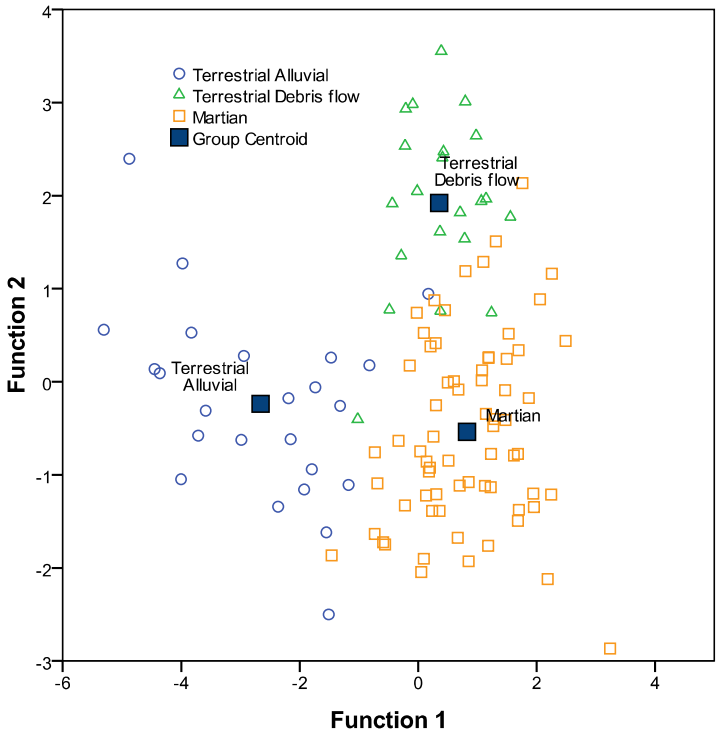

Figure 6-11. Canonical discriminant functions derived to separate gullies on Earth (Alluvial and Debris flow) and Mars, shown in Table 6-3.

Figure 6-10 shows the discriminant function calculated to best separate alluvial and debris flow gullies on Earth, but applied to gullies on Mars as well. Although the martian data overlap both the alluvial and debris flow data for Earth, they overlap more with debris flow gullies than alluvial gullies. Figure 6-11, a plot of the two canonical discriminant functions that best separate alluvial, debris flow and martian gullies, shows that gullies on Mars can be separated from those on Earth, but that there is some overlap, especially with debris flow gullies.

Figure 6-12 to Figure 6-16 show scatter plots of the identified important variables; the significant results are:

(1) Alluvial gullies tend to have lower values of E_q compared to debris flow gullies (Figure 6-13).

(2) Alluvial gullies have a range of CI concavity values, but debris flow gullies are confined to low CI values (Figure 6-13).

(3) Alluvial gullies tend to have lower debris apron slope, alcove slope and overall start-to-end gradient compared to debris flow gullies (Figure 6-12, Figure 6-14 and Figure 6-16).

(4) The data for debris apron slopes demonstrate the least overlap between the alluvial and debris flow gullies.

(5) Debris flow gullies occupy a distinct domain at high average alcove slopes and high E_q (Figure 6-14), a signal which is not as clear for the other slope parameters.

(6) The martian gullies overlap with both the alluvial and debris flow data in almost all cases, with the notable exception that for a given slope parameter (e.g. start-end gradient Figure 6-16, or average debris apron slope Figure 6-12) martian gullies tend to have a lower value of CI, i.e. lower concavity than either alluvial or debris flow gullies.

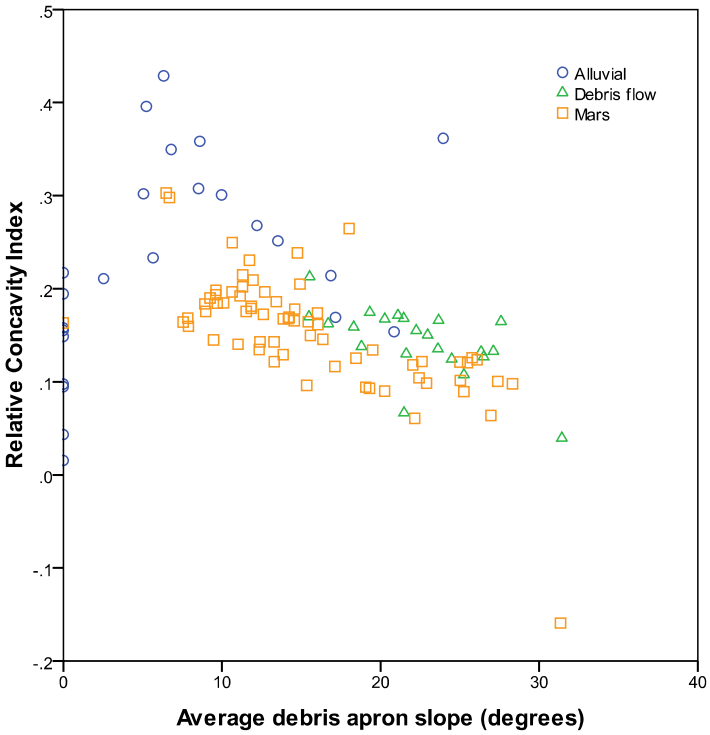

Figure 6-12. Plot of Relative Concavity Index (CI) against average debris apron slope for gullies on Earth and Mars.

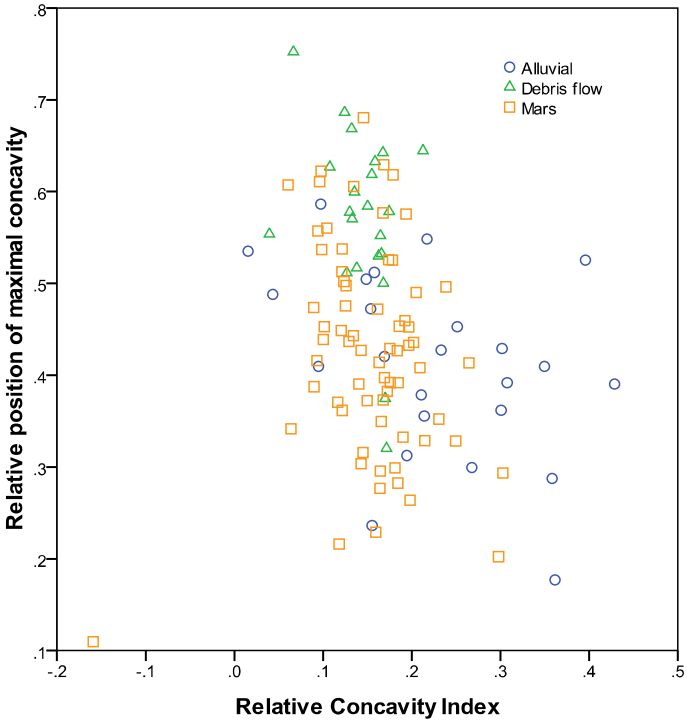

Figure 6-13. Plot of the relative position of the maximal concavity (E_q) against the Relative Concavity Index (CI) for gullies on Earth and Mars.

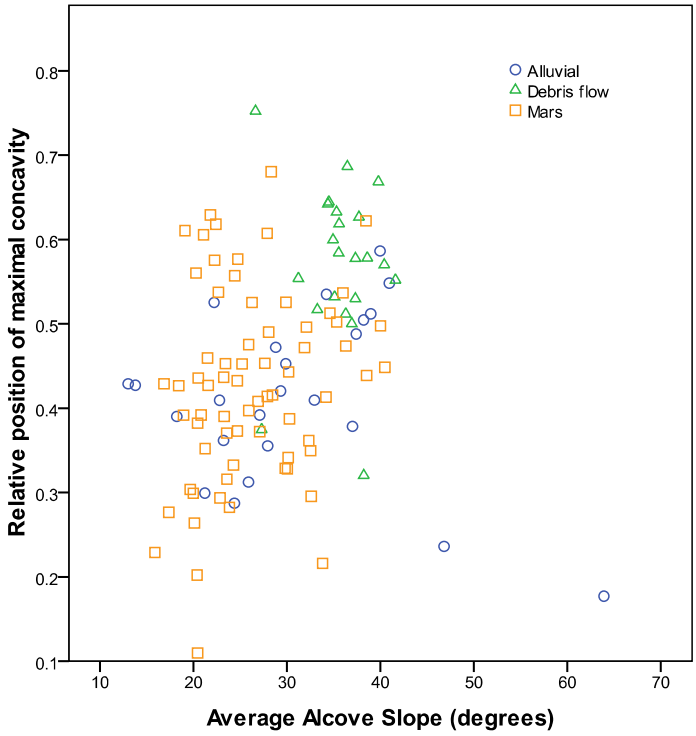

Figure 6-14. Plot of the relative position of the maximal concavity (E_q) against the average alcove slope for gullies on Earth and Mars.

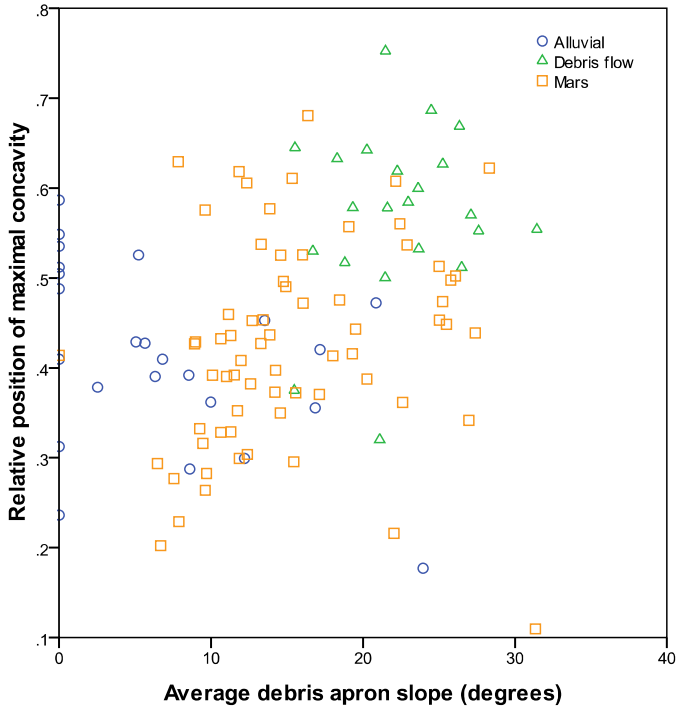

Figure 6-15. Plot of the relative position of the maximal concavity (E_q) against the average debris apron slope for gullies on Earth and Mars.

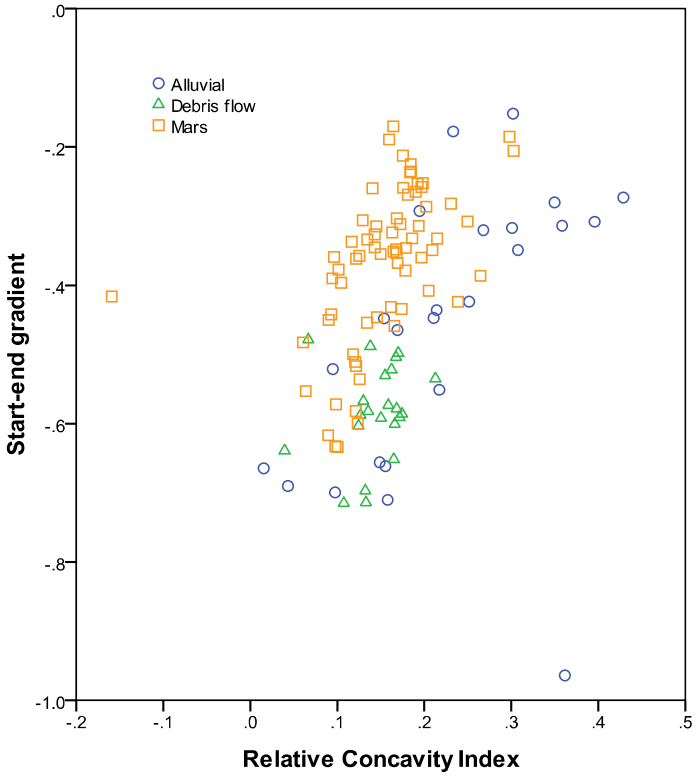

Figure 6-16. Plot of the start-end gradient against the Relative Concavity Index (CI) for gullies on Earth and Mars.

6.3.3. Gullies on Mars

6.3.3.1. Comparison of gully profiles to non-gullied slope long profiles

Two discriminant analyses were performed to attempt to separate gully profiles from non-gullied slope long profiles on Mars. Firstly, a discriminant analysis was performed that compared non-gullied slope long profiles with gully profiles that included the pre-gully section, and secondly a discriminant analysis was performed that compared non-gullied slope long profiles with gully profiles not including the pre-gully section. The second analysis, not including the pre-gully section, gave the best separation of the two groups and the resulting discrimination function coefficients are shown in Table 6-4. The histograms comparing the distribution of the discriminant function for the two groups (Figure 6-17) reveal that although the groups overlap, they are separable.

Scatter plots of the important variables show some interesting patterns. CI and θ (concavity) indices both show that gully profiles are generally more concave than non-

gullied slope long profiles and have a lower value of E_q (Figure 6-18). It is particularly notable that, for a given height or length, gully profiles have a greater concavity than non-gullied slope long profiles (Figure 6-19). From closer inspection of the data most of the gullies that have similar concavities for a given height are those with the rockwall chute alcove type. Neither the start-to-end gradient nor the range of slope separate the non-gullied slope long profiles from the gully profiles when plotted against any of the other parameters.

Table 6-4. Standardized Canonical Discriminant Function Coefficients for separation of non-gullied slope long profiles and gully profiles on Mars. The more important the parameter the higher the magnitude of its coefficient.

	Function
	1
Profile height	0.718
Profile length	-0.389
Profile start-end gradient	0.294
Erosion Area (A_{ero})	0.214
Relative Concavity Index (CI)	-0.338
Position of maximal concavity (E_q)	0.591
Concavity Index (θ)	0.693
Slope Range	-0.211

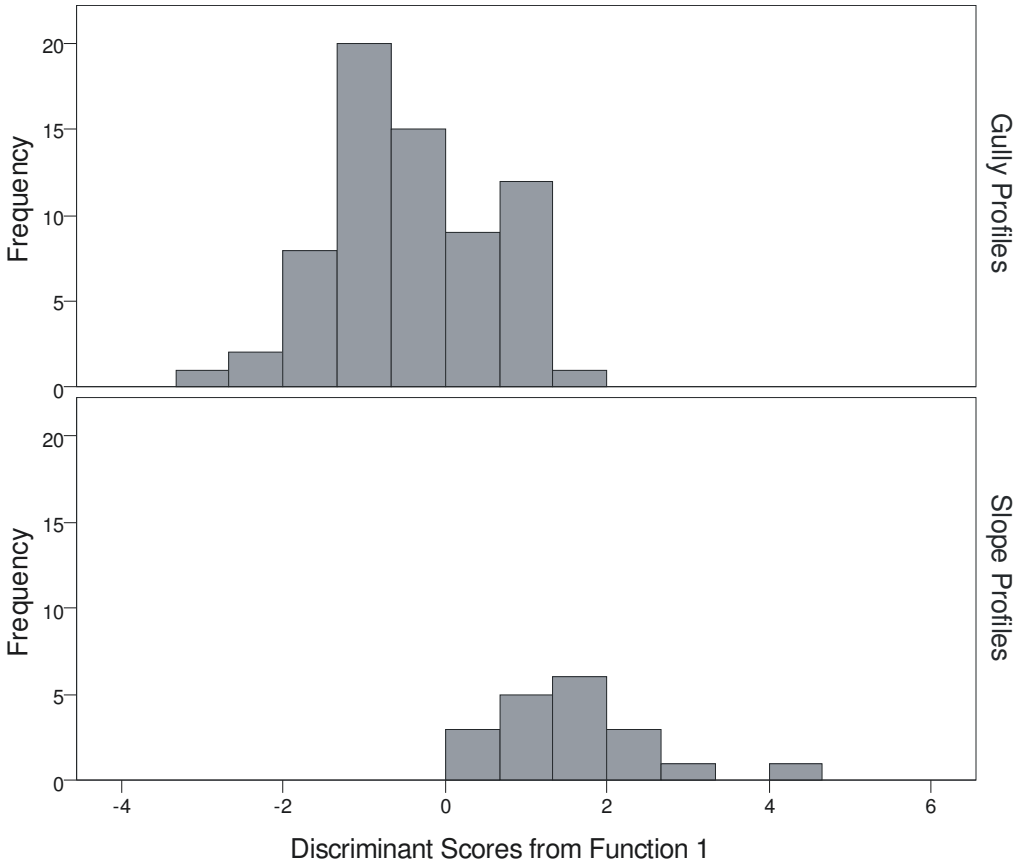

Figure 6-17. Stacked histograms of the discriminant score calculated from the coefficients in Table 6-4 for martian gully profiles and martian slope long profiles.

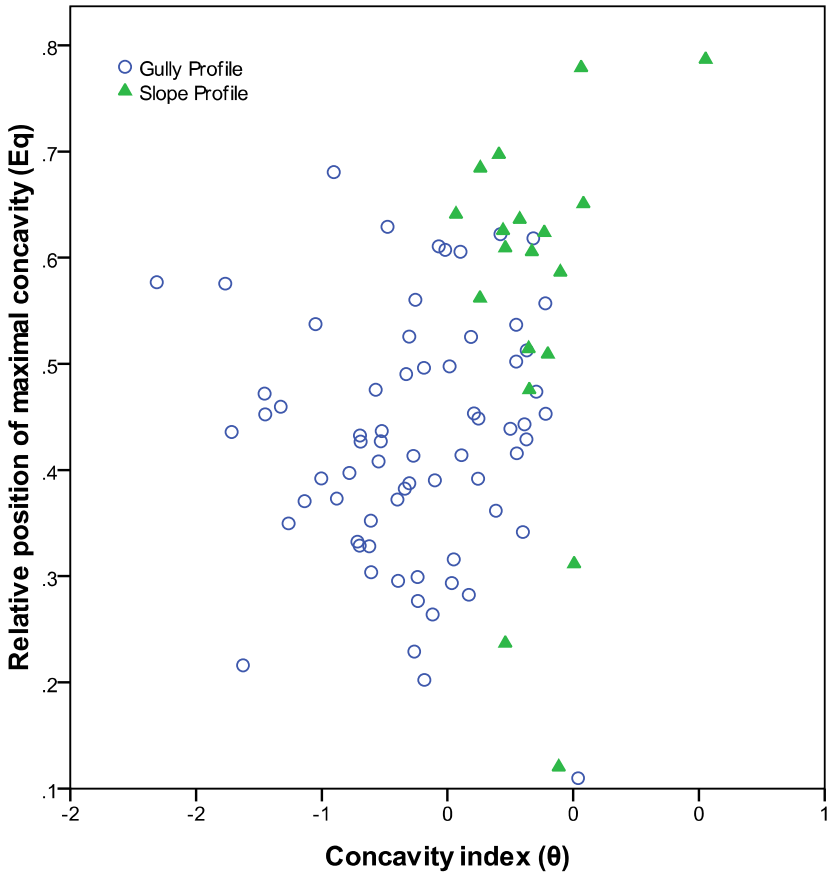

Figure 6-18. Plot of the relative position of the maximal concavity (E_q) against the concavity index (θ) for non-gullied slope long profiles on Mars and gully profiles that do not include the pre-gully section.

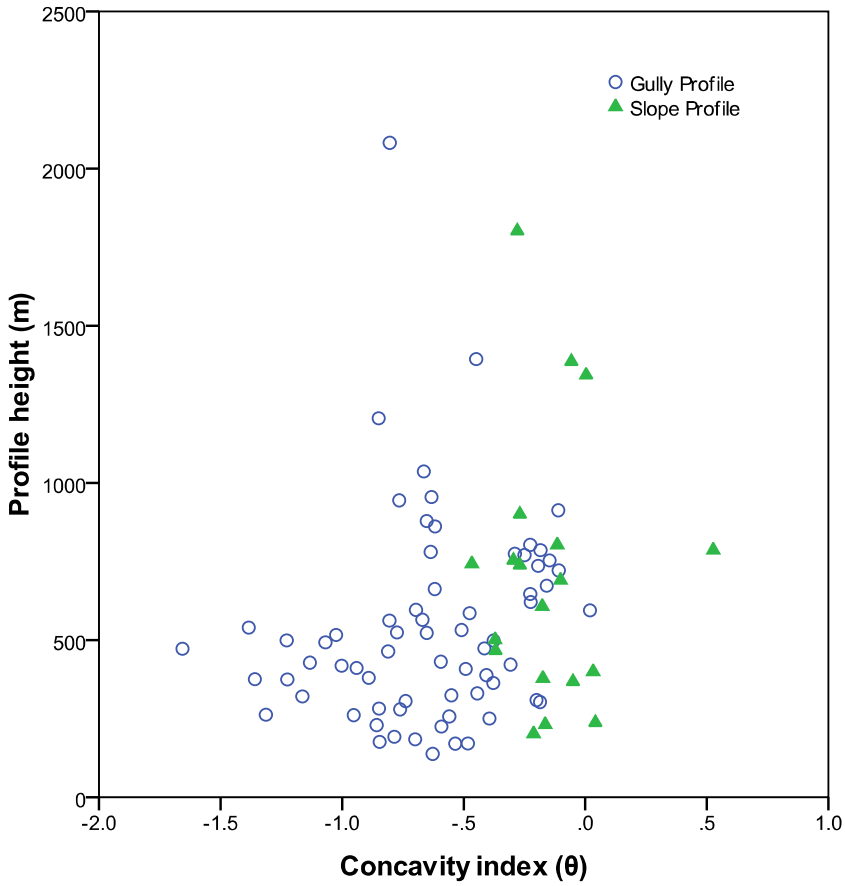

Figure 6-19. Plot of profile height against concavity index (θ) for non-gullied slope long profiles on Mars and gully profiles that do not include the pre-gully section.

6.3.3.2. Groupings of gullies on Mars

Discriminant analyses were performed for all the additional attributes recorded for martian gullies including: presence of polygonal structures, presence of sinuous channels, gully setting, alcove type, fan type, and if the gullies formed a patch, or gradually appeared. This analysis was performed to investigate whether visually separable attributes also carried a morphological signature. If a link were to be found then visual attributes alone could be used to draw morphological conclusions, hence widening the data available. However, only the alcove type groups could be separated. Table 6-5 shows the canonical function coefficients and Figure 6-20 the associated scatter plot. The plot reveals that the rockwall chute type and bouldery chute types are distinct from the others. The closed types form a cluster, or sub-group within the open wide types, hence showing a close relationship. Figure 6-21 shows concavity index (θ) plotted against E_q and Figure 6-22 alcove slope

plotted against debris apron slope, for the different alcove types. Open wide types and closed types are more concave than rockwall chute types. Closed single types have a higher E_q than closed lobate and open wide types. Rockwall chute types have the highest slopes, bouldery chute the lowest slopes and the closed types fall in between. Open wide types span a range of slopes, but do not extend to the high slopes of rockwall chute types.

Table 6-5. Standardized Canonical Discriminant Function Coefficients for separation of different alcove types within gullies on Mars. The more important the parameter the higher the magnitude of its coefficient.

	Function			
	1	2	3	4
Absolute Latitude	1.659	.144	.073	.483
Proportion of profile pre-gully	.848	-.631	.184	.722
Debris apron width to length ratio	-.475	-.466	-.533	.601
Debris apron length normalised to gully length	-.387	-.221	-1.413	.374
Slope Range	-.071	-.264	.173	.051
Gully density (Nr./km)	.644	.213	-.222	-.252
Average Alcove Slope	.566	1.144	1.615	-.361
Average Channel Slope	.061	-.171	-.290	-.217
Average Debris Apron Slope	-.094	.741	1.468	-.921
Gully height	1.749	-.159	-.992	.641
Gully Length	-2.409	.269	.876	-.759
Gully start-end gradient	1.157	.630	2.146	-1.117
Erosion Area (Aero)	.521	-.477	.247	-.129
Relative Concavity Index (CI)	.149	-.126	.205	.037
position of maximal concavity (Eq)	.177	.520	.973	.430
Concavity Index θ	1.300	-.203	.155	.434

Despite the other attributes not being separable, some additional observations could be made. In terms of gully setting, it was found that gullies in the polar pits had the lowest slopes for all the slope parameters. Gullies that co-occurred with polygonal structures generally had the lowest slope values. There was a weak trend of E_q with aspect (Figure 6-23), where south-facing gullies have the lowest E_q and north facing the highest.

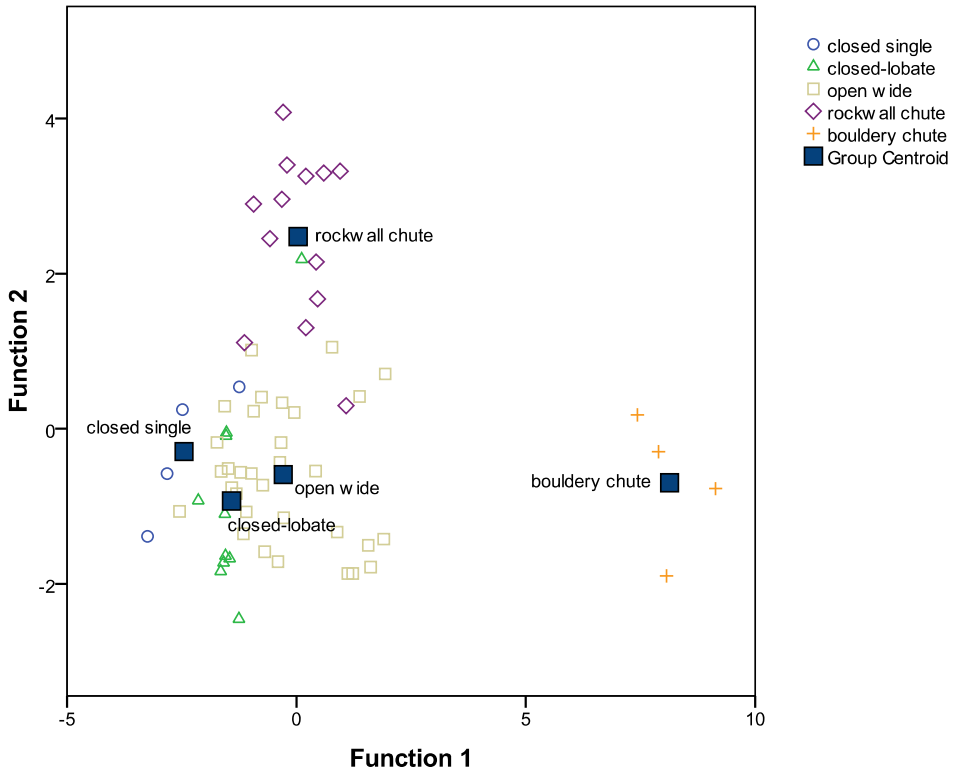

Figure 6-20. Canonical discriminant functions derived to separate different alcove types in gullies on Mars, shown in Table 6-5.

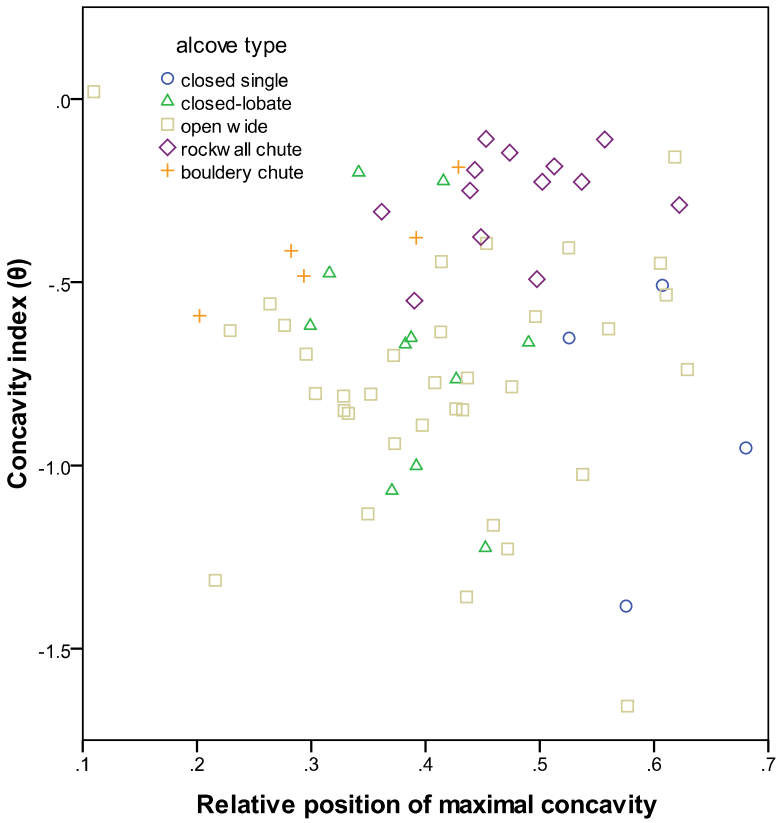

Figure 6-21. Plot of concavity index (θ) plotted against the relative position of the maximal concavity (E_q) for different alcoves types in gullies on Mars.

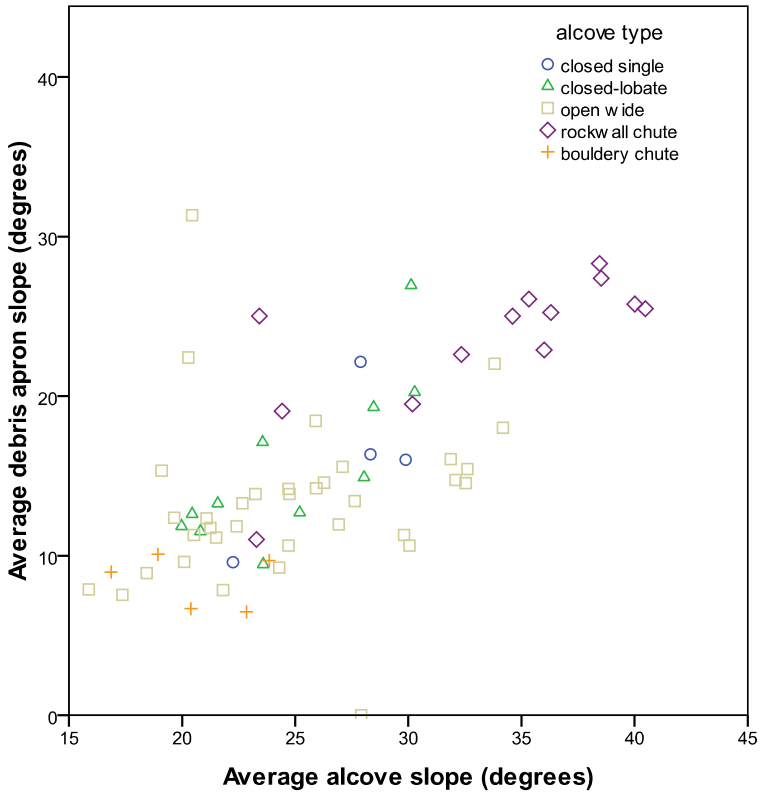

Figure 6-22. Plot of average debris apron slope against average alcove slope for different alcove types in gullies on Mars.

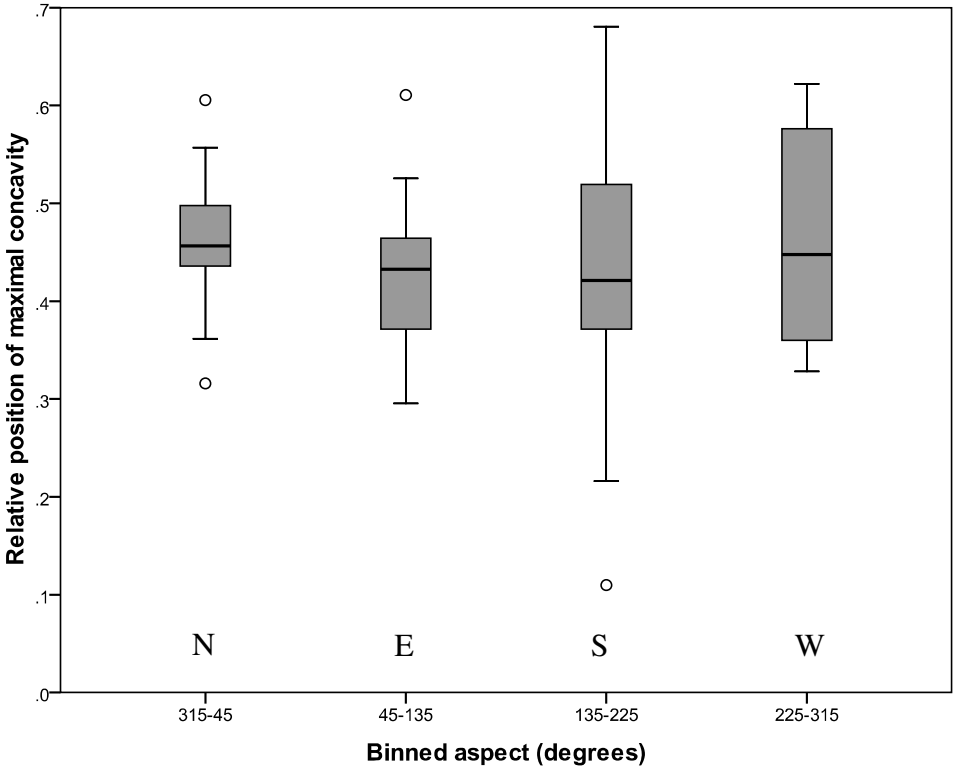

Figure 6-23. Boxplot of the relative position of the maximal concavity (E_q) against binned aspect for all martian gullies, except the polar pits. The boxes represent the first and the third quartiles of the distribution, with the black bar marking the median. The narrow bars mark the maximum and minimum of the distribution, with the circle symbols representing "mild" outliers (between 1.5 and 3 interquartile ranges beyond the bars). The outliers are included in the calculation of the median and quartiles.

6.3.3.3. Latitudinal trends of gullies on Mars

Both average alcove slope and start-end gradient of the long profiles decreases with increasing latitude (Figure 6-24 and Figure 6-25). Start-end gradient decreases both in non-gullied slope long profiles as well as gully profiles with increasing latitude (Figure 6-25). Gully profiles generally also show a decrease in E_q (Figure 6-26) and an increase in concavity (Figure 6-27, only CI index shown, but A_{ero} and θ have similar trends) with increasing latitude. These trends are less marked, or absent, for the slope long profiles. Figure 6-28 shows that some gullies co-occur with polygonal structures from 36.6° to 73.3°, however all gullies co-occur with polygonal structures at > 50° and polygonal structures are not found co-occurring with gullies < 36.6°.

Gullies are found in discrete patches at almost all latitudes (except 40°-43.3° and > 66.6°; Figure 6-29). However, gullies that gradually appear on slopes ("progressive" gullies) peak between 36.6°-40° and decline sharply, disappearing at 50° and only occur again in the polar pits at latitude of ~ 70°. Gullies occurring in patches have a similar range of slopes compared to progressive gullies, but the progressive types have the highest slopes (Figure 6-24). Figure 6-25 also shows the decrease in frequency of gullies with increasing latitude (with the exception of the highest latitudes). Figure 6-30 shows that gully density also tends to decrease with increasing latitude (with the exception of the polar pits at the highest latitudes). Figure 6-31 shows that the rockwall chute alcove type and both the closed alcove types only occur at lower latitudes (< 45°). The open wide types occur over a large range of latitudes (35°-65°), but only the bouldery chute types (which are all classed as polar pit gullies) occur at high latitude (~ 70°). The closed single types are the only alcove type present at the lowest latitudes (< 35°).

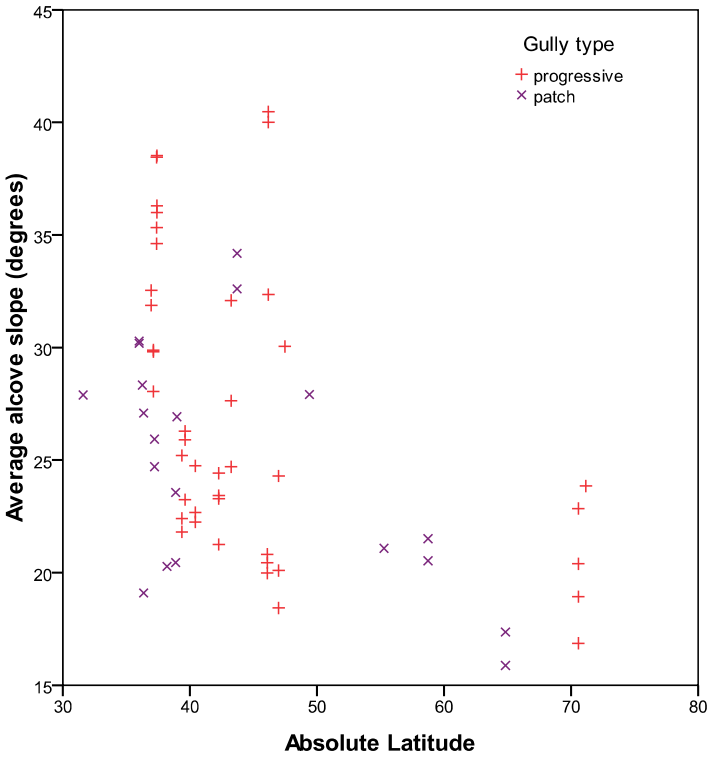

Figure 6-24. Average alcove slope against absolute latitude for all gullies on Mars, differentiated by patch, or progressive types.

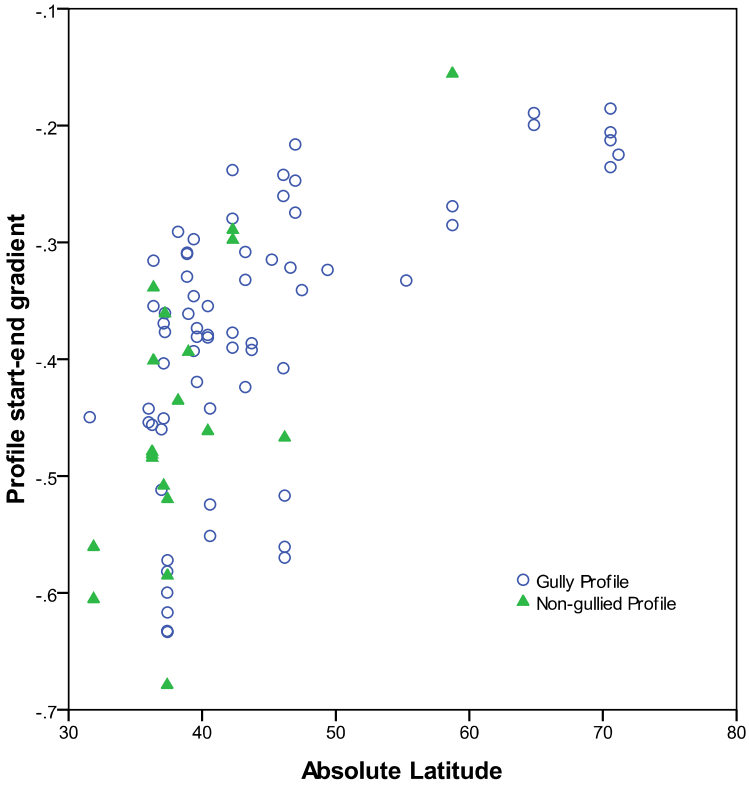

Figure 6-25. Profile start to end gradient against absolute latitude for all gullies and non-gullied slope long profiles on Mars. Note: steeper slope angles are located towards the lower end of the *y*-axis.

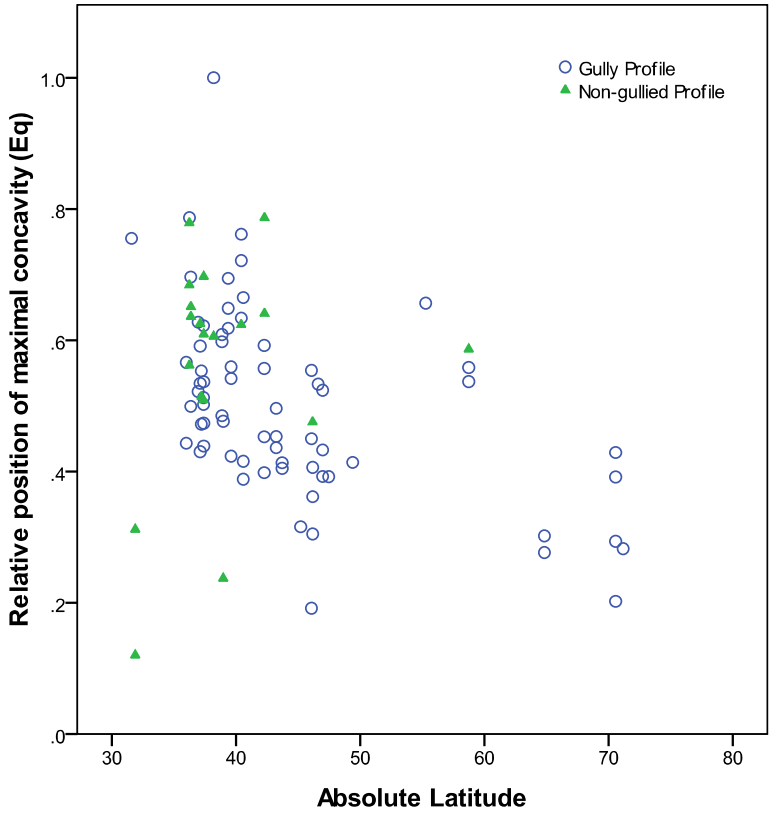

Figure 6-26. Plot of relative position of the maximal concavity (E_q) against absolute latitude for all gullies and non-gullied slope long profiles on Mars.

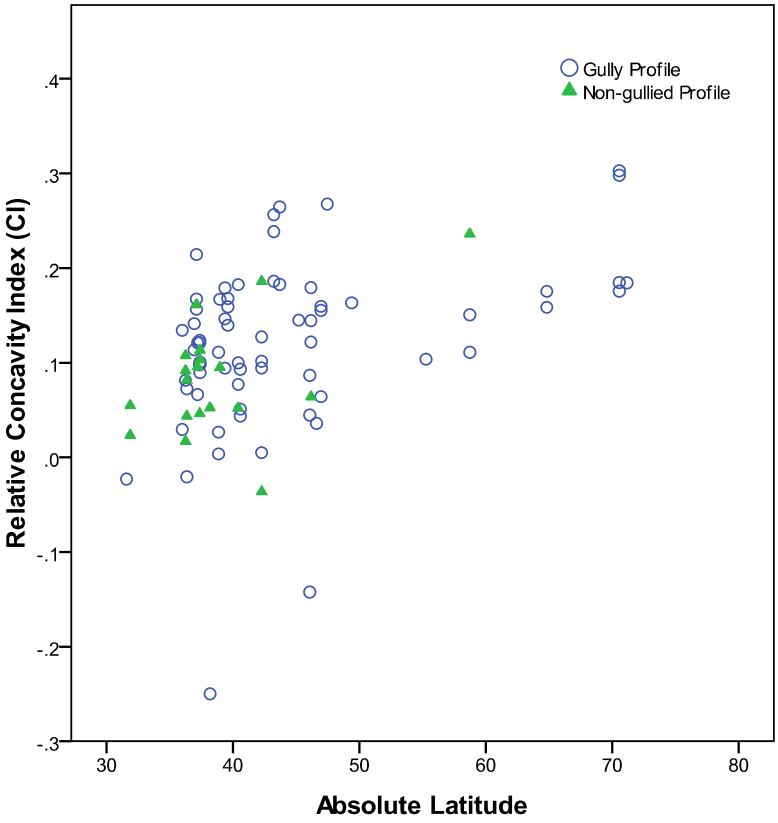

Figure 6-27. Plot of Relative Concavity Index (CI) against absolute latitude for all gullies and non-gullied slope long profiles on Mars.

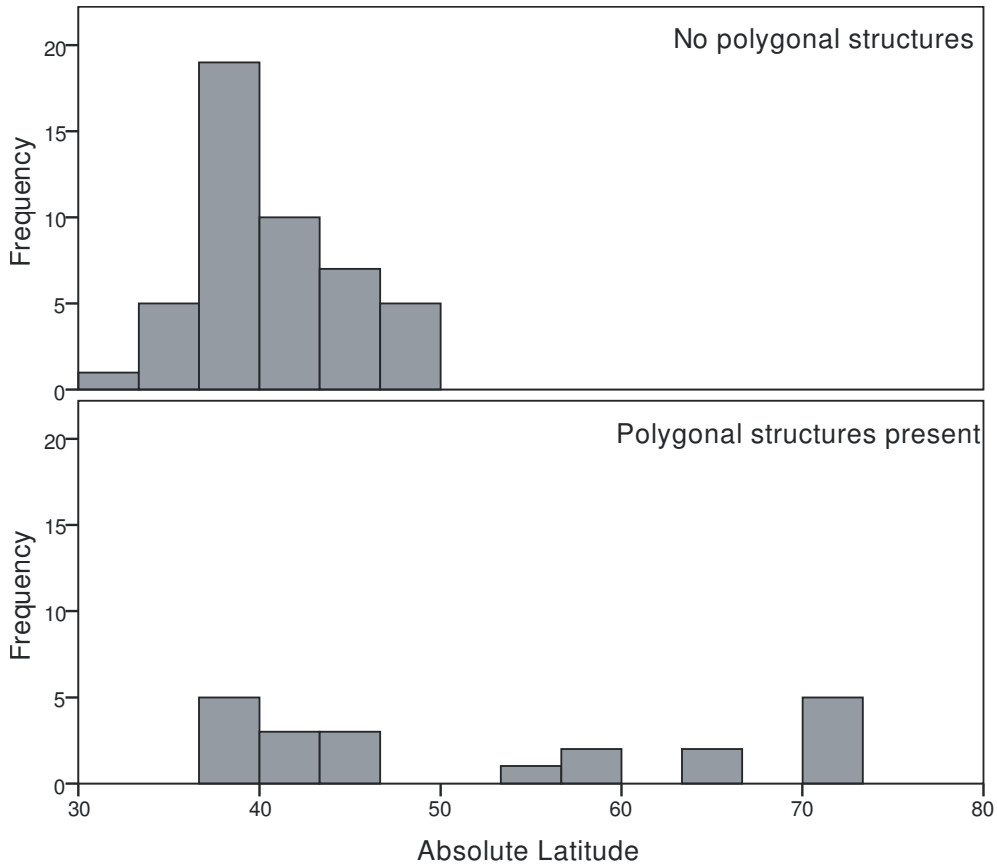

Figure 6-28. Latitudinal distribution of gullies that co-occur with polygonal structures, compared with those that do not.

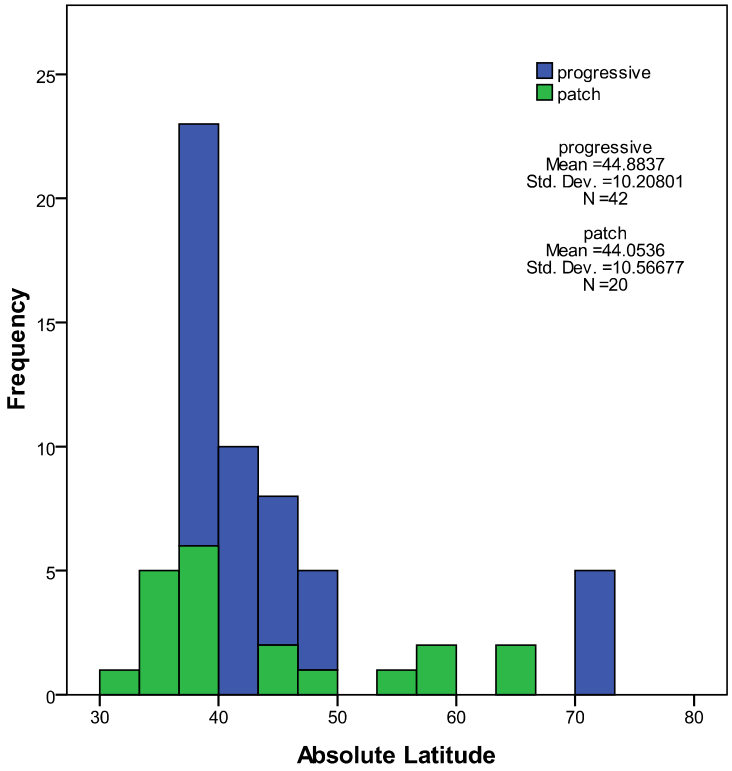

Figure 6-29. Stacked histogram of the latitudinal distribution of gullies on Mars that occur in patches and those that occur on whole slopes "progressive".

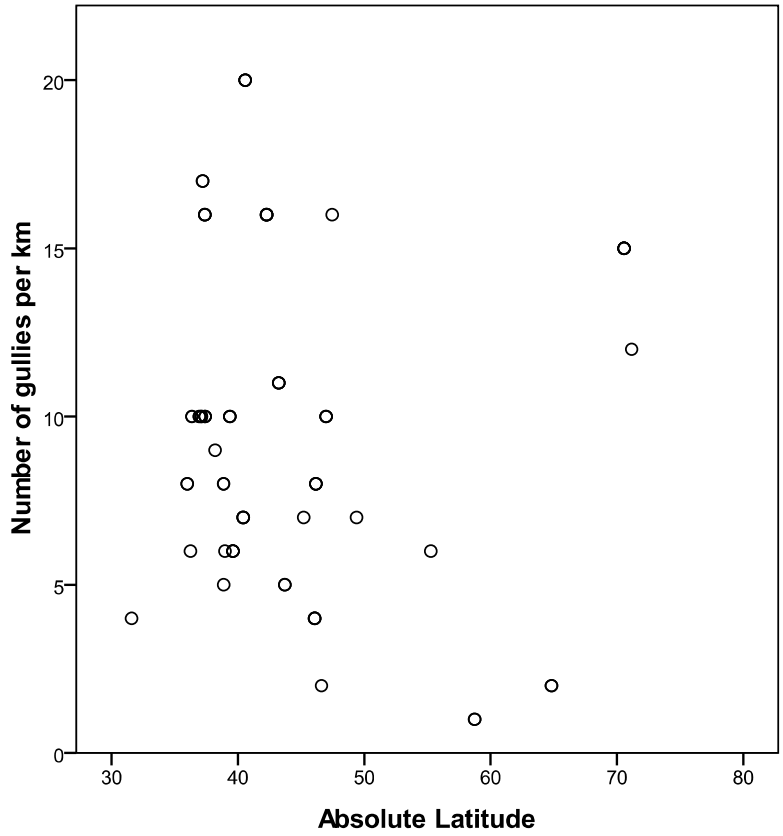

Figure 6-30. Plot of gully density against latitude.

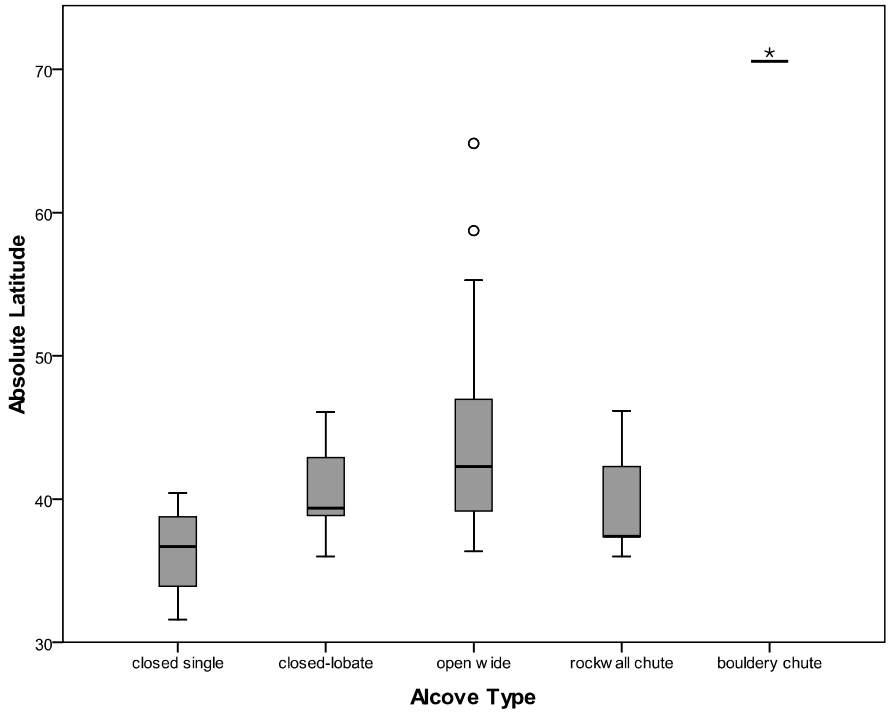

Figure 6-31. Boxplot of absolute latitude per alcove type for gullies on Mars. The boxes represent the first and the third quartiles of the distribution, with the black bar marking the median. The narrow bars mark the maximum and minimum of the distribution, with the circle symbols representing "mild" outliers (between 1.5 and 3 interquartile ranges beyond the bars) and the stars representing "extreme" outliers (> 3 interquartile ranges). The outliers are included in the calculation of the median and quartiles.

6.3.4. Crater Gullies on Mars

The maximum slopes found inside impact craters generally decrease with increasing latitude and craters containing gullies are those with the highest maximum slopes for each latitude band (

Figure 6-32). The mean of the maximum slope of craters containing gullies lies above the upper quartile of the general population, giving strength to this result. Considering the coarse resolution of the MOLA data (one pixel is ~ 500 m) the maximum slope within craters is going to be underestimated, but despite this a trend is detectable.

Figure 6-33 shows the plot of depth against diameter for craters with and without gullies broken down by latitude bands. Craters with gullies have a similar distribution in terms of depth and diameter as the general crater population, but are much less numerous. However, there seems to be a slight bias for craters containing gullies to be deeper for a given diameter than the general population.

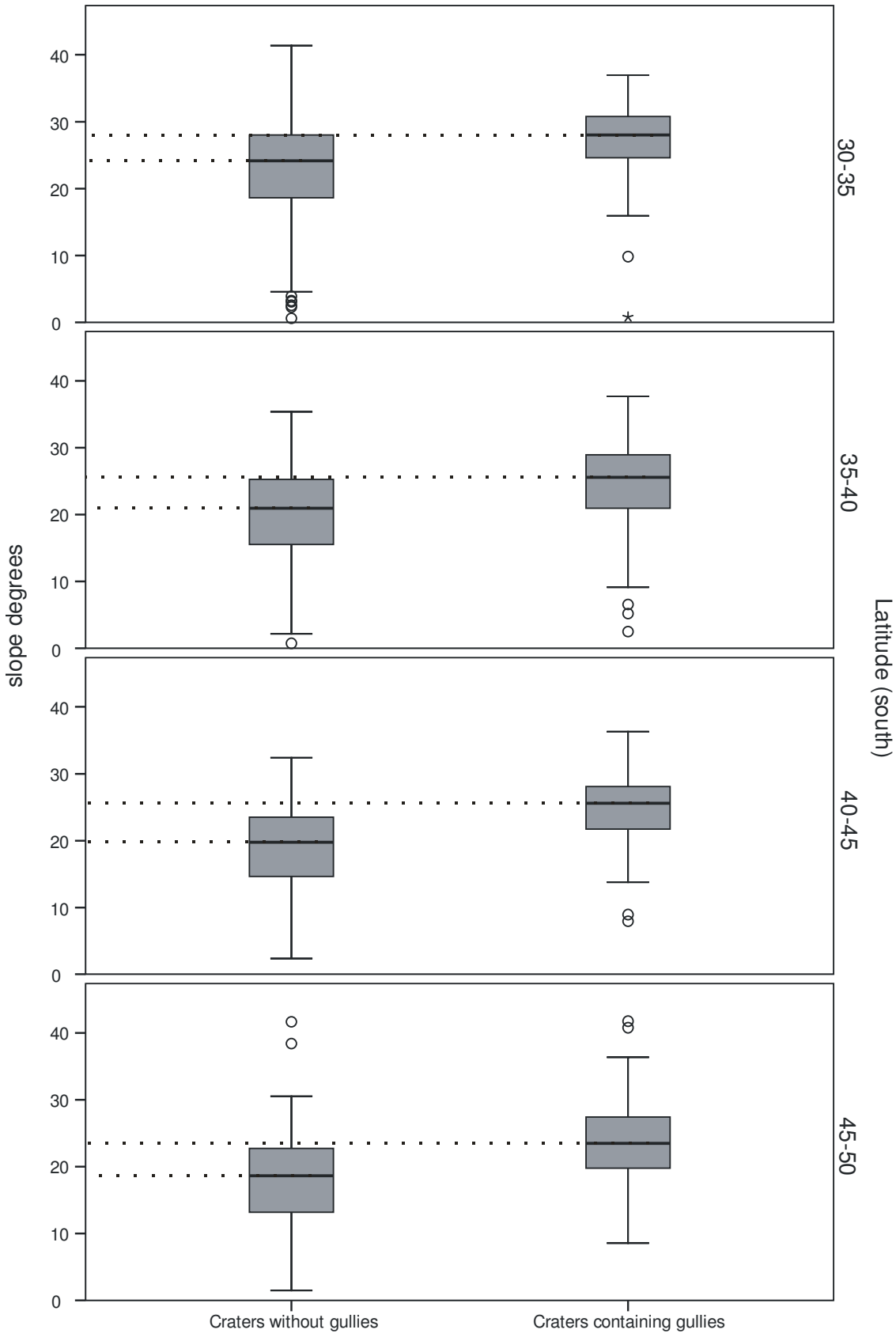

Figure 6-32. Stacked boxplots for three latitude bands of maximum slopes found inside craters with and without gullies in the southern hemisphere of Mars. The boxes represent the first and the third quartiles of the distribution, with the black bar marking the median. The narrow bars mark the maximum and minimum of the distribution, with the circle symbols representing "mild" outliers (between 1.5 and 3 interquartile ranges beyond the bars) and the stars representing "extreme" outliers. The outliers are included in the calculation of the median and quartiles.

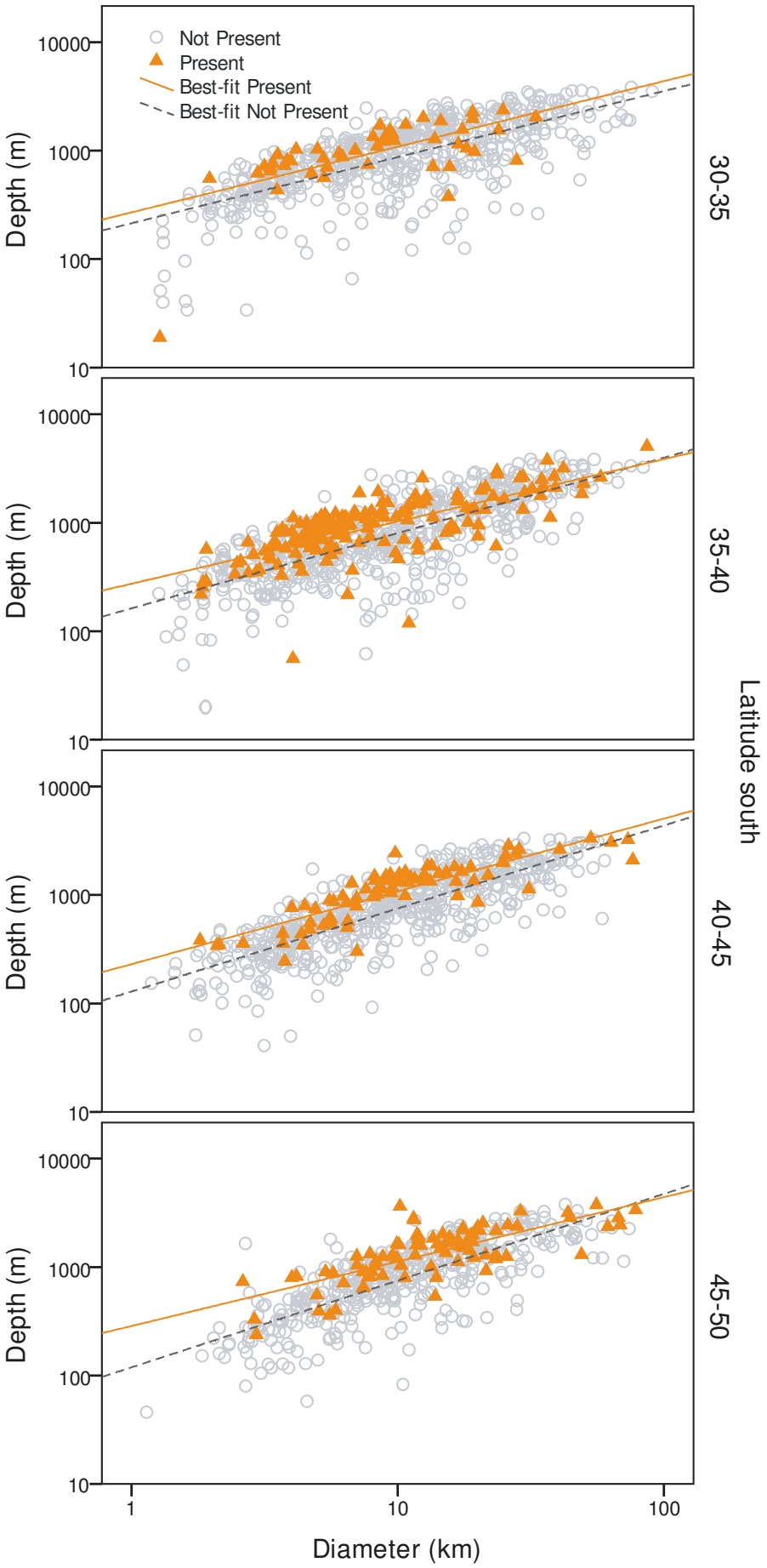

Figure 6-33. Stacked plots for three latitudinal bands of the depth against diameter for craters in which gullies are present and for those in which gullies are not present in the southern hemisphere of Mars. Two best-fit lines are included for data with gullies are present and for those where they are not.

6.4. Discussion

6.4.1. Comparing Gullies on Earth and Mars

The profile dimensions of gullies on Mars are similar to those generated by debris flow and alluvial processes on Earth. Figure 6-9 shows the total horizontal runout distance and total fall height data for landslides on Earth and Mars compiled by Legros (2002) plotted with all of my data for gullies on Earth and Mars. Some of the landslides included by Legros (2002) are technically large debris flows. My data form a continuation of the landslide data towards lower lengths and heights. However, the gully data continue the trend for landslides on Earth and are located away from the data for landslides on Mars. The alluvial data should not necessarily follow the same patterns as landslides and debris flows on this plot. Alluvial gullies are controlled by flow of water, rather than a granular flow, and hence do not necessarily have a fixed runout distance. For mature alluvial systems the length of the profile is expected to be very much longer than the height, but in the small systems that I studied, the length and height are almost equivalent. For debris flows the plot in Figure 6-9 gives an indication of the mass and scale of the flow and, if the gullies on Mars are controlled by debris flow, then they are flows of small to medium scale.

Discriminant analysis reveals that profiles of gullies formed by debris flow and ephemeral water flow are distinct on Earth. However, the martian gully data overlap with both debris flow and alluvial gullies on Earth. There is some suggestion from the discriminant analyses that gullies on Mars lie closer to the debris flow than alluvial gullies (e.g. Figure 6-10). In particular, the values of concavity index (θ) for alluvial, debris flow and martian gullies are low compared to that found for mature streams by Goldrick and Bishop (2007). Erosion area ($A_{ero)}$ and the position of the maximal concavity (E_q) span equivalent ranges to those found for rivers in Belgium by Demoulin (1998) except that some of my data have higher values of E_q (especially for the debris flow and martian gullies). The relative concavity index (CI) spans an equivalent range in my data, but never

gets as high as those found by Phillips and Lutz (2008) for alluvial rivers in disequilibrium. However, the disequilibrium bedrock rivers of Phillips and Lutz (2008) all have negative values, hence are generally convex-up in profile, and only a single martian gully has a negative value of CI. In general the alluvial and martian gullies have the highest CI, followed by the debris flow gullies and lastly the martian ungullied slope long profiles.

These comparisons indicate that my data from Earth or Mars do not represent mature fluvial systems, but instead these indices demonstrate that they are relatively immature systems. This is no surprise for the Earth data as these gullies are forming on recently exposed landscapes (recently de-glaciated, uplifted, or erupted). The relative immaturity of gullies on Mars compared to the alluvial gullies that I studied on Earth, means that if fluvial processes are acting, then they have not reached the level of maturity indicative of millions of years of development on Earth. Thus, if gullies on Mars are alluvial, then gully forming events on Mars are less frequent, and/or less intense than on Earth. However, debris flow gullies on Earth also form immature fluvial profiles, because their profiles are characterised by a basal concavity, resulting in a high E_q, and low concavity (confirmed by this study and data from Church et al., 1979; Larsson, 1982; Ballantyne and Benn, 1994). Hence, the relatively immature nature of the gullies on Mars could be due to a dominance of debris flow. The debris flow gully profiles on Earth have generally taken less than 10,000 to 15,000 years to form (Norðdalh, 1990; Godt and Coe, 2007), deglaciation forming an upper limit and over this time debris flows have only occurred episodically (Decaulne et al., 2005). As gully profiles are similar on Mars, this could suggest that either gullies on Mars have developed with the same frequency over the same time period, or with a higher frequency over a shorter time, or a lower frequency over a longer time.

6.4.2. Gullies on Mars

6.4.2.1. The effects of gullies on slope long profiles

The majority of the martian gully profiles can be separated from the martian non-gullied slope long profiles (Figure 6-17). This observation is made the more significant because all the sampled non-gullied slope long profiles are proximal to gullies, which means that apart from the gully formation they have experienced similar conditions. Gully profiles show a greater concavity (lower θ) and lower position of the maximal concavity (E_q) compared to non-gullied slope long profiles; both of which are indicators of fluvial maturity. This means either that (1) gullies have a significant impact on the long profiles of slopes, or that (2) gullies only form on slopes with particular pre-existing properties and do not impact the long profile significantly. The fact that non-gullied slope long profiles cannot account for the full variety of gully profile morphology, despite being located in close proximity (and hence the initial slope long profiles should be very similar), suggests that (2) is not the case. However, sampling of a greater number of non-gullied slope long profiles proximal to gullies and of non-gullied slope long profiles away from gully formation (e.g. in the equatorial regions) would be required to completely rule out this possibility. Assuming therefore that (1) is correct, this means the shape of the majority of gully profiles are strongly indicative of a water-flow process, be that debris flow or pure water flow, for the formation of gullies on Mars. The fact that there is significant overlap between non-gullied profiles and gullied profiles indicates that some gullies have little impact on the long profile and without visual observation a gullied profile would not always be distinguishable to a non-gullied profile.

Downward departure from the expected relationship of crater depth to diameter is taken as an indicator of above average relative crater age (e.g. Boyce et al., 2005; Boyce and Garbeil, 2007). In general it is expected that as craters get older, their rims become subdued and their cavities infill, reducing their depth, but with little effect on crater

diameter, hence older craters in general are located lower in Figure 6-33. Craters with gullies are not found at the extremes of the crater depth-diameter plot, but they are distributed throughout the entire population, though they concentrate at higher values of depth. Hence, all craters independent of depth, diameter and apparent relative age are able to host gullies, as long as they occur within the appropriate latitudinal band though they are more frequent in deeper craters.

6.4.2.2. Are there different gully types on Mars?

I have found that gullies with different alcove types (Figure 6-3) can be separated from one another in terms of profile parameters, using discriminant analysis. Closed alcove types and open wide types have strong similarities in terms of profile parameters, which may suggest a relationship between them. As the location of the maximal concavity is linked to maturity for profiles on Earth, by analogy this would imply that single closed types are the least mature and closed lobate and open wide types the more mature members of this group. Hence, it is possible that these gully types might be members of a morphological evolutionary sequence. Rockwall chute alcove types and bouldery chute types (which are made up of polar pit gullies and vice versa) form their own distinct groups. Rockwall chutes form the steepest and most linear gully profiles; overlapping with non-gullied martian slope long profiles and debris flow profiles on Earth. This presents two possible explanations (1) that the bedrock contributes a dry mass wasting component to an alluvial signal, which tends to make the profile more linear, or (2) that debris flow is the dominant process in forming this type of gully. The large separation in analysis space of the polar pit gullies suggests that the formative mechanism may be somewhat different from the other types.

Figure 6-34 shows the distribution of data for each alcove type compared to the data from alluvial and debris flow gullies on Earth, using the discriminant function calculated in Section 6.3.2.2. This function places rockwall chute gullies closest to debris

flow gullies on Earth and bouldery chute types closest to alluvial gullies. The other alcove types are split across the two processes. The apparent difference in formation process of the different alcove types could be due to the inherent difference in the morphological heritage of the slopes, or a difference in the frequency, intensity and/or type of gully-forming process. It is likely to be a combination of these factors. It is possible that these observations are simply a result of the small sample size for some gully types. A larger sample size for each of these types would assist in clarifying these observed trends.

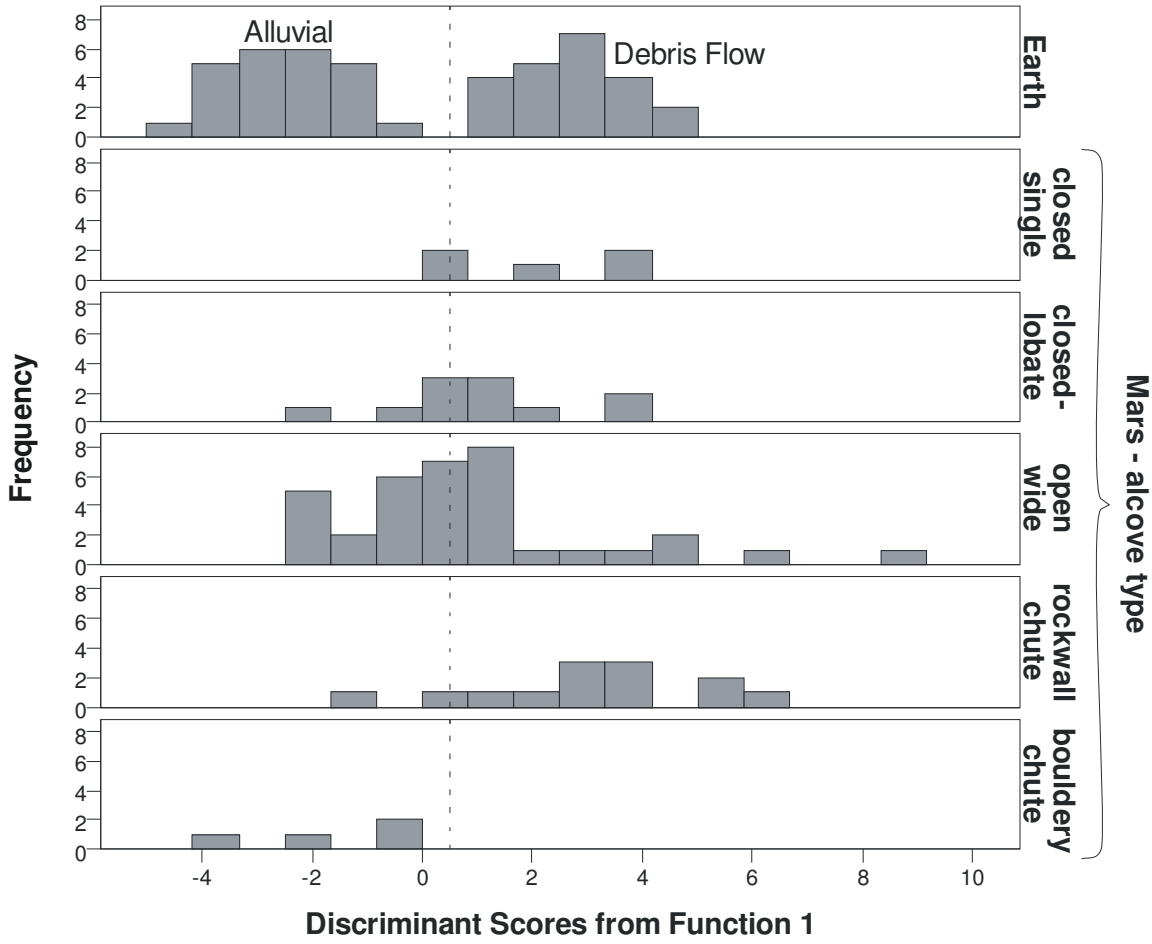

Figure 6-34. Stacked histograms of the discriminant score calculated from the coefficients in Table 6-3 for terrestrial gullies and each different alcove type for gullies on Mars.

The other groupings of morphological parameters for gullies on Mars do not show any significant separation. This could be for two reasons (1) the attribute is neither affected by, nor affects profile shape, or (2) the groups are poorly defined and/or there are insufficient sample numbers. Explanation (2) does not apply to sinuosity, however. It is likely that the fan classification suffered from insufficient sample numbers.

6.4.2.3. Latitudinal Trends

Analysis of the gully long profiles shows that gullies have lower slope angles at higher latitudes. Analysis of the crater population shows that craters containing gullies also have lower slopes at higher latitudes (in line with the overall population of craters that do not contain gullies). Gullies whose alcoves are carved into bedrock (rockwall chute type) occur only at lower latitudes. On Earth, exposure of bedrock generally only occurs at high slope angles and, as gullies of this alcove type have high slopes, it suggests that this is also the case on Mars. The general decrease in slope angles with increasing latitude agrees with the findings from MOLA roughness data of Kreslavsky and Head (2000), in which topography becomes progressively subdued with increasing latitude. However, it is important to note that gullies always occur on the steeper slopes for each latitude band. This is in agreement with the findings of Reiss et al. (2009), who found that gullies occurred in Hale Crater but not the neighbouring Bond Crater primarily because Hale Crater contains steeper slopes. This requirement for steep slopes to form gullies can partially explain the decreasing number of gullies with increasing latitude.

The confinement of gullies to steeper slopes suggests that the process by which gullies form is dependent on slope. If I assume from the results so far that these gullies are carved by water flow or ice melt, then this could mean that either (1) the process that carves the gullies can only be triggered on steeper slopes, (2) water-ice can only be accumulated on steeper slopes, (3) water can only be melted on steeper slopes, (4) steep slopes are inherently more erodible, or (5) a combination of the above. If the process requires steep slopes, then a good candidate would be debris flow, in which steep slopes are required to trigger failure, although at angles much less than the angle of repose (e.g. Larsson, 1982; Stock and Dietrich, 2003). This could be confirmed if a lower threshold of slope was found for gully formation. The MOLA data are of insufficient resolution to confirm this, however, and insufficient higher resolution topographic data currently exists.

The slope constraint does not apply to alluvial gullies which form on almost any slope angle (e.g. Rowantree, 1991). Hecht (2002) and Kossacki and Markiewicz (2004) suggested that steep slopes (especially those containing hollows) are able to provide good microenvironments for melting of water on Mars. Dickson and Head (2009) among others have shown that hollows on steep slopes form effective frost hollows on Mars. Hence, the limitation to steep slopes cannot distinguish between alluvial and debris flow processes.

My results agree with previous studies that have shown a sharp decrease in the frequency of gullies with increasing latitude, with the exception of the polar pits (e.g. Balme et al., 2006; Dickson and Head, 2009). However, I have also shown that the linear density of the gullies and that the proportion of gullies that gradually appear on slopes (progressive) decreases with increasing latitude. This is either because (1) there is a higher occurrence of the steep slopes needed to form gullies, and/or (2) that the climatic conditions at lower latitudes were/are particularly suitable for gully formation. I can rule out option (1) as a dominant factor because the percentage of craters with steep slopes that contain gullies changes with latitude (Figure 6-35). Hence, Figure 6-35 suggests that at latitudes between 35°S and 50°S climatic conditions must have been particularly suitable for gully formation.

Because gully formation has been more intense at lower latitudes, then it might be expected that the gully profiles would become more "mature" (i.e. evolve towards a more fluvial profile) at lower latitudes. However, the opposite is the case: gully profiles become more linear and the position of the maximal concavity becomes closer to the bottom of the slope (the smaller E_q the better graded the profile). This could mean: (1) gully profiles on Mars evolve differently to those on Earth, and/or (2) different gully forming processes occur at different latitudes and/or (3) gullies are not the dominant slope process and the profile shapes instead reflect other processes. The fact that the non-gullied slope long profiles only weakly follow the trends in CI and E_q (Figure 6-25 and Figure 6-26) and

gully profiles are more generally separable from non-gullied slope long profiles suggests option (3) is not the case.

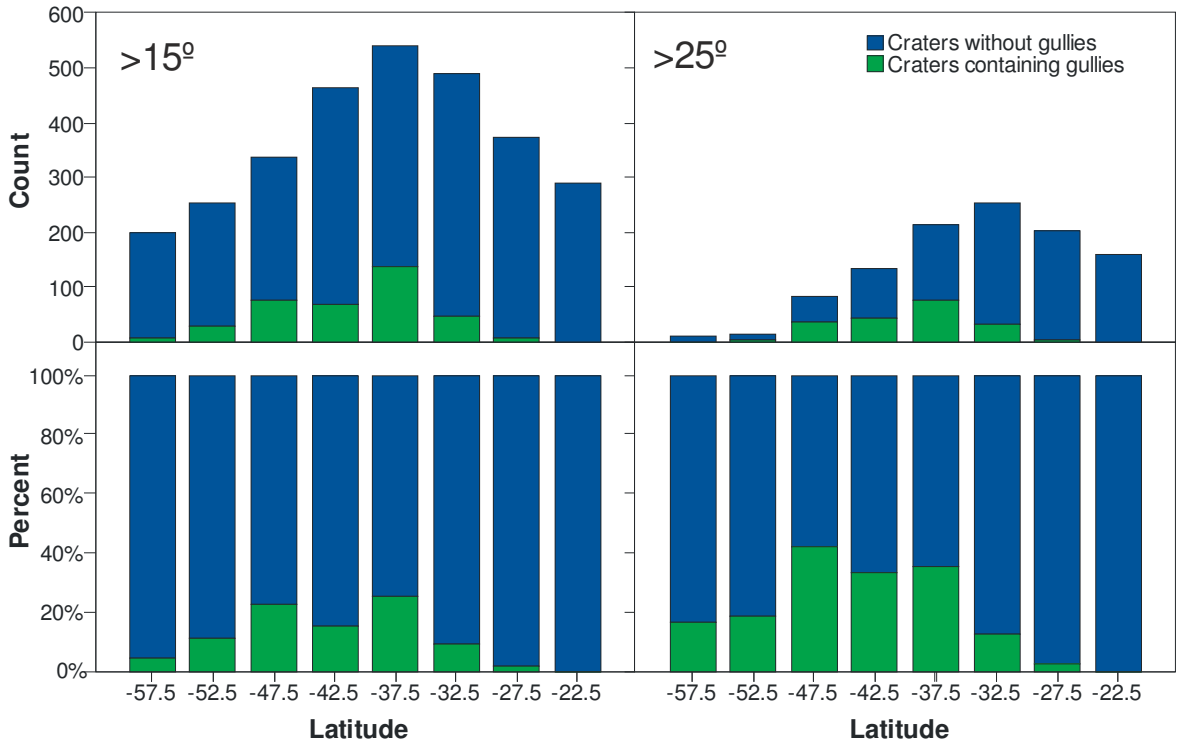

Figure 6-35. Histograms showing the latitudinal distribution of craters with internal maximum slopes of greater than 15° and greater than 25°, which also show the relative proportions of craters that contain gullies to those that do not. Upper panels show the absolute numbers of craters in each latitude band, whereas the lower panels show the relative proportion of craters of each type in each latitude band.

Gullies located at high latitudes (i.e. polar pits) are most similar to alluvial gullies on Earth, but gullies at lower latitudes share profile properties with debris flow gullies on Earth, with rockwall chute gully types showing the strongest similarities to debris flows on Earth, Figure 6-34. This suggests that gully formation process could be latitude dependent. This is supported by Figure 6-36, which shows the distribution of data for three latitude bands compared to the data from alluvial and debris flow gullies on Earth using the discriminant function calculated in Section 6.3.2.2. There is a slight trend, with profiles changing from debris-flow-like to alluvial-like with increasing latitude.

An additional factor to consider is that gullies at very high latitudes always co-occur with polygonal structures and the proportion of gullies that occur with polygonal structures increases with increasing latitude. As polygonal structures are generally

interpreted to be indicative of near surface ice (e.g. Mangold, 2005; Levy et al., 2009a) then: (1) this could affect the gully-forming process, as suggested by Levy et al. (2009b) and/or (2) the long-term presence of this ice could mean ice-creep has substantially altered the pre-existing slope structure as suggested by Kreslavsky and Head (2003). If the polygons are indicative of ground ice that was present at the time of gully formation, this could provide an explanation for the change of process with latitude. Near-surface ground ice has the potential to inhibit infiltration (e.g. Bogaart et al., 2003) and therefore might prevent debris flows from occurring, thus only allowing pure-water flow. If this were the case, it might be expected that channels would be shallower and longer. Another explanation is that the ground ice itself melts to form gullies, as suggested by Levy et al. (2009b), and because the location of ground ice is not slope dependent (unlike atmospheric accumulation), then it is possible for melt to be formed on any slope. Hence, melt formed on lower slopes cannot mobilise sediment and form debris flows.

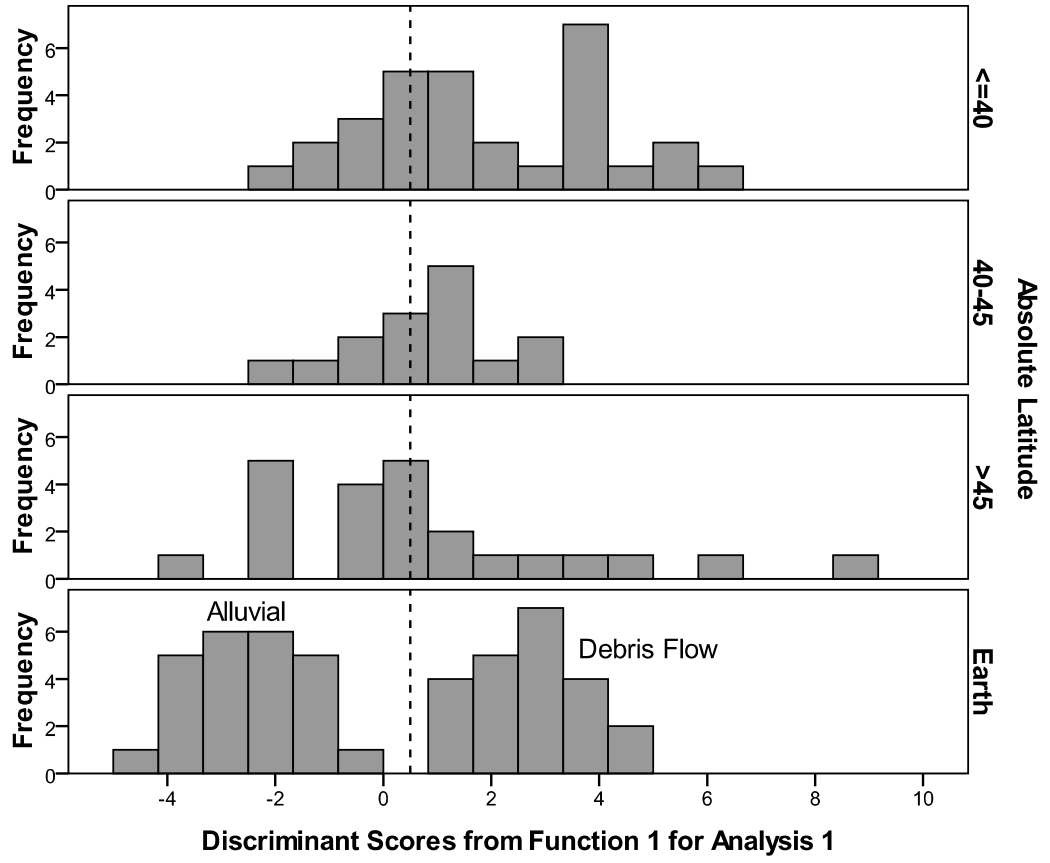

Figure 6-36. Stacked histograms of the discriminant score calculated from the coefficients in Table 6-3 for terrestrial gullies and for three different latitudinal bands of gullies on Mars.

The presence of these latitudinal trends is an indication of the influence of climate on both the slope long profiles generally and the gully-forming process in particular. This supports the gully formation model proposed by Costard et al. (2002), whereby gullies are formed by melting of near surface ice on pole-facing slopes under high obliquity. An additional support for insolation control of gully formation is the presence of a weak trend in the position of the maximal concavity with aspect (Figure 6-23), with south-facing slopes presenting more mature gully systems. This trend would be expected if formation occurred under past orbital conditions of high obliquity, because pole-facing (i.e. south facing in the southern hemisphere) slopes would receive more insolation for a longer time duration (see Figure 2-4). The high intensity of gully formation at latitudes of ~ 40° provides a good constraint for future modelling as it reveals that this latitude band must have been both a site of preferential accumulation and melting.

6.5. Conclusions

The stereo point matching method developed by Kreslavsky (2008) is particularly useful for collecting a large quantity of simple elevation data rapidly and I have shown that it is sufficiently accurate to produce reliable results.

Gullies on Mars overlap with both alluvial gullies and debris flow gullies on Earth, in terms of long profile properties. Gullies on Earth and Mars are both visually similar and similar in terms of scale, slope angle and slope curvature. Discriminant analysis indicates that gullies on Mars have slightly more affinity with debris flow gullies than alluvial gullies on Earth. Comparison of non-gullied slope long profiles and gully profiles on Mars reveals that gully profiles tend to have a greater concavity and lower relative position of the maximal concavity than non-gullied slope long profiles. This is additional evidence that gullies on Mars are both (1) causing distinct morphological change on the surface of Mars and (2) formed by a process that is similar to gully formation on Earth, which inherently involves liquid water.

Gullies with different alcove types on Mars have different profile properties. I found that: (1) polar pit gullies (~ 70°S) are the most morphologically distinct and are closest in form to alluvial gullies on Earth, (2) gullies with rockwall alcoves form another distinct group, but are most similar to debris flow gullies on Earth, and are restricted to latitudes below 45°.

Gullies form a greater linear density (i.e. a greater number of gullies per km of slope section) and have a greater frequency at latitudes around 40° and are more likely to occur across whole slopes rather than as isolated patches. Although the frequency of steep slopes increases to a maximum at 30-40°S my results show the proportion of steep slopes containing gullies increases faster. This indicates the latitudinal band around ~ 40° is or was particularly suitable for gully formation. In combination with the observation that pole-facing gullies are the most mature, this observation supports the climatic model of gully formation suggested by Costard et al. (2002).

The latitudinal trends in gully density, alcove type, co-occurrence with polygonal structures and profile parameters suggest a dominance of gullies formed by pure water flow at high latitude and a mixture of debris flow and gullies formed by pure water flow at lower latitudes. This could be related to (1) ground ice distribution, as indicated by the presence of polygonal structures, which could inhibit infiltration and prevent the sediment saturation needed for debris flow, or influence the amount of water available (2) the decrease in slope angle at high latitudes, which could prevent the triggering of debris flows, or (3) other climatic influences, which control the amount of water and the timing and distribution of melting/accumulation.

From a wider study of all craters known to contain gullies; gullies can occur in craters of any age or size, but have a preference for those craters containing above average maximum slopes. Hence, the gully-forming process requires steep slopes: either for water

accumulation and/or melting, or to trigger the gully-forming process (in which case the process would be debris flow).

Chapter 7. The determination of martian gully formation processes by slope-area analysis

7.1. Introduction

This Chapter has been submitted and is in review as part of Conway et al. (2010a): a book chapter in "Planetary Geomorphology" a Geological Society of London Special Publication. This Introduction and Sections 7.3.1, 7.3.2 and 7.4.1 have been abridged to avoid repetition.

The amount of water required to carve channels, and transport and deposit sediment differs substantially between debris flow, pure water/brine flow and granular flow. Determining the amount of water available at the martian surface is important for questions of martian climate, hydrology and the study of potential martian habitats. Hence, an accurate determination of active processes is needed that in turn can constrain the quantity of fluid required to form gullies. Quantitative geomorphological study can provide the tools to discriminate between these three processes. The recent availability of high resolution digital elevation models (DEMs) of Mars has opened up the possibility of using quantitative geomorphic methods that have, until now, been restricted to analysing landscapes on Earth. By taking well-developed slope-area analyses and other geomorphic process indicators for the Earth and applying them to Mars, this study aims to give insights into both the processes that formed the gullies on Mars and the source of any water involved.

7.2. Approach

I used three geomorphic tools commonly applied in terrestrial geomorphology to determine active processes forming gullies on Mars: slope-area plots (Figure 7-1a), Cumulative Area Distribution (CAD) plots (Figure 7-1b) and wetness index maps. These analytical techniques are described in more detail in the following sections. They are usually used to assess active processes within catchment areas and other larger-scale landscape analyses. To test whether they are equally applicable to smaller areas, I first applied them to five study sites on Earth at an equivalent scale to gullies on Mars. Glacial areas were preferred as these have: (1) a geologically short and finite slope-development history and, (2) their default slope-profile strongly resembles that of fresh impact craters (compare relationships in Garvin et al. (1999) and Brook et al. (2008)). However, suitable quality data could not be found for the alluvial end-member process in glacial environments, so two desert study sites were included as well.

When I was satisfied that different geomorphic processes could be discriminated on Earth using slope-area plots, CAD plots and wetness index maps, I applied these analyses to slopes containing gullies on Mars.

7.2.1. Slope-area and Cumulative Area Distribution (CAD) methods

The stream power law was first proposed by Hack (1957) and has been widely used to investigate landscape evolution on Earth (e.g., Kirby and Whipple, 2001; Stock and Dietrich, 2003). It is based on the detachment- and transport-limited rate of bedrock erosion, otherwise known as the shear-stress incision model, which is stated as follows:

$$S = kA^{-\theta} \qquad (7\text{-}1)$$

where S is local slope, A is upslope drainage area, k is a process related constant, which is different for detachment and transport cases, and θ is the concavity index, which is process dependent. It has also been noted that if the drainage area is plotted against the

local slope for drainage basins then process domains can be defined in log-log plots as shown in Figure 7-1a (after Montgomery and Foufoula-Georgiou, 1993). Brardinoni & Hassan (2006) added an additional domain in which systems dominated by debris flow deposition occupy that part of the alluvial domain of Montgomery & Foufoula-Georgiou (1993) which is located towards higher drainage areas (Figure 7-1a). This domain was proposed from field observations and has since been supported by additional observations by Mao et al. (2009) in a different field area. Process information can be obtained both from the position of the data points relative to defined domains on this slope-area plot, and also from the trend of the data within these domains, for example whether the data points plot in a concave, convex, upward trending, or downward trending curve (Tucker and Bras, 1998). The general trend for an alluvial system is shown in Figure 7-1a, which passes through several process domains. The data for such plots are generally derived from digital elevation models or topographic maps. The slope and contributing area data are either extracted from only the channel, or the whole drainage basin, depending on the focus of the study. In Figure 7-1a these data are taken from every pixel contained within the catchment of the whole fluvial system (encompassing valley hillslopes, tributaries, main channels and estuary system) sampled at a single point in time.

Cumulative Area Distribution (CAD) is the probability distribution of points in the landscape having a drainage area greater than any particular area, A^*. The log-log plot of $P(A>A^*)$ against A^* gives information on the processes acting within a catchment (Perera and Willgoose, 1998; McNamara et al., 2006). Interpretation of this index varies, but usually it is split into three areas: (1) at small drainage areas the plot usually evolves from convex to concave, and represents diffusive erosion, (2) intermediate drainage areas are linear in a log-log plot and this is thought to represent incision (i.e. channel formation), and (3) at large drainage areas there are small steps where major tributaries join the channel (Figure 7-1b). McNamara et al. (2006) split domain (1) into three sub-domains (Figure

7-1b): (1a) a convex section, representing hillslopes that diverge and do not gather drainage, (1b) a linear and steep section in a log-log plot, indicating hillslopes with convergent topography and, (1c) a concave section, which they suggest is a reach dominated by pore-pressure triggered landsliding, including debris flows which are triggered by this mechanism.

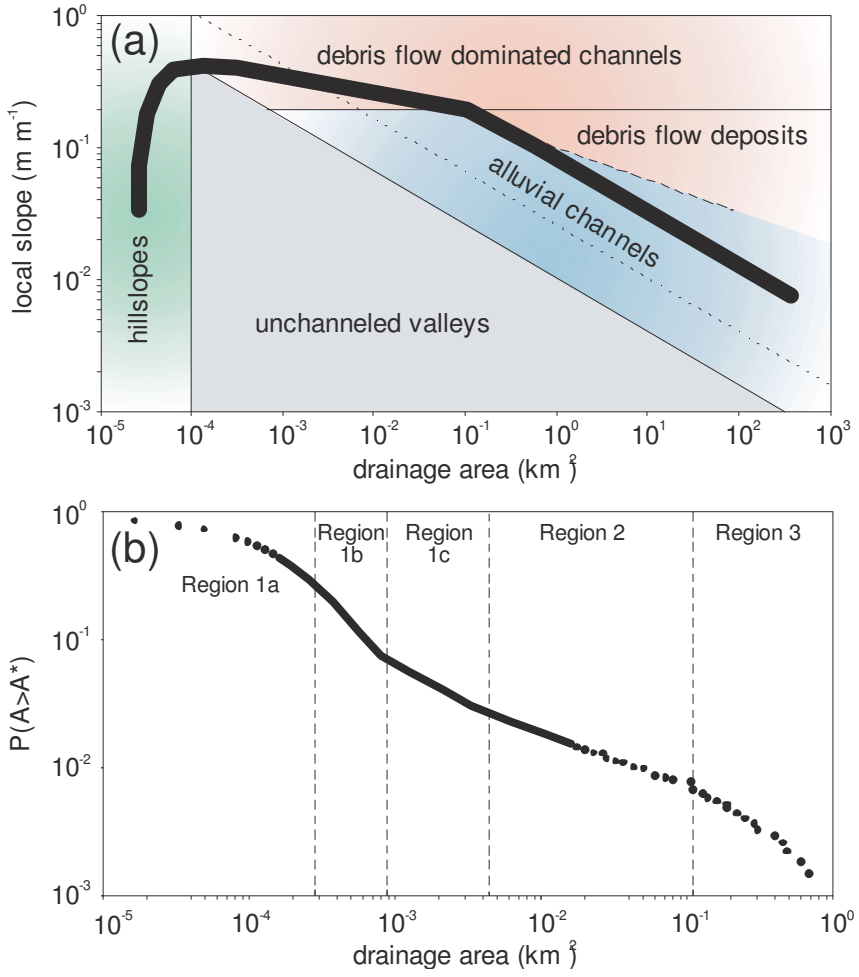

Figure 7-1. Modified slope-area plot of Figure 3-7 and Cumulative Area Distribution (CAD) plots, showing typical process domains on Earth. (a) Slope-area plot from Montgomery & Foufoula-Georgiou (1993) with the additional domain of Brardinoni & Hassan (2006) indicated with a dashed line. The dotted line indicates the adjustment to the alluvial domain boundary considering the gravitational acceleration of Mars. The thin lines delimit the domains and the thick line shows the typical trend of the data points from a well-developed fluvial system. (b) CAD plot from McNamara et al. (2006). P(A>A*) represents the probability of a point in the landscape having a drainage area greater than the given drainage area, A*, on the x-axis. Region 1a represents hillslopes that diverge and do not gather drainage. Region 1b represents hillslopes with convergent topography. Region 1c represents pore-pressure triggered landsliding or debris flow. Region 2 represents incision, or channel formation. Region 3 has large steps where large tributaries join the channel.

7.2.2. Application of slope-area method to Mars

The reduced gravitational acceleration of Mars shifts the boundary of the alluvial slope-area domian vertically (dotted line in Figure 7-1a). This means that the unchanneled domain extends to higher slopes for a given drainage area for Mars (extending into the alluvial and debris flow domains for Earth); however the hillslope domain is unaffected. Appendix D gives details of the calculations performed to account for the gravitational acceleration of Mars. The relative gradients and curvatures of the trends described by the alluvial data in slope-area plots are unaffected by the reduced gravity. I have not been able to revise the position of the domain added by Brardinoni & Hassan (2006) as a function of gravitational acceleration because this domain was added empirically, based on field observations.

The slope threshold for dry mass-wasting or landsliding in loose material is the same as on Earth (Moore and Jakosky, 1989; Peters et al., 2008). The slope thresholds for pore-pressure failure are also unaffected by the difference in gravitational acceleration. Hence there would be no change to these process domains or trends for either dry mass wasting or pore pressure triggered processes such as debris flow.

7.3. Study areas

7.3.1. Earth

All the study sites on Earth are located in the northern hemisphere and most are within the continental USA. Chapter 5 provides a summary and data sources for the sites and Figure 7-2 shows the setting of the areas studied in this chapter. From the six sites described in chapter 5, five contained suitable study areas for slope-area analysis:

7.3.1.1. Site A – San Jacinto, California

For my analyses I used three study areas that contained small complete gully systems, including sources, channels and debris aprons, but avoided large fan systems and debris

aprons from neighbouring systems (Figure 7-2a and Figure 7-2b: study areas A1, A2 and A3).

7.3.1.2. Site B - Death Valley, California

I chose two study areas (Figure 7-2c: study areas B1 and B2) with gully systems that were not affected by neighbouring alluvial fans or gully systems so only receive local, low levels of rainfall.

7.3.1.3. Site C – St Elias Mountains, Alaska

Debris flow tracks are apparent across this talus slope, especially in study areas C3 and C4. Debris flow might have occurred in study area C3 (Figure 7-2d). Study area C1 has no evidence of debris flow processes (Figure 7-2d).

7.3.1.4. Site D – Front Range, Colorado

Three of my study areas (Figure 7-2e and Figure 7-2f: study areas D2 to D4) include debris flows located on talus. By way of contrast, I also examined a partially vegetated slope (study area D1) that seems to be unchanneled and dominated by creep processes (Figure 7-2e).

7.3.1.5. Site E – Westfjords, Iceland

From this site I chose a study area above the town of Ísafjörður that has very active debris flows (Figure 7-2g: study area E1), two study areas with less active debris flows and more alluvial processes (Figure 7-2g and Figure 7-2h: study areas E2 and E3), and one study area dominated by talus processes, although there are some debris flow tracks visible (Figure 7-2h: study area E4). All these study areas have patchy vegetation, but no trees.

7.3.2. Mars

All the gullies that I studied on Mars were located on the inner walls of craters in the southern hemisphere (see Chapter 5 for full site descriptions). Slopes both with and without gullies were analysed for comparison.

7.3.2.1. Site F – Penticton Crater in Eastern Hellas

I used two study areas within this ~ 7.5 km diameter crater for my slope-area analyses, shown in Figure 7-3a and Figure 7-3b. Study area F1 is located over the equator-facing light-toned deposits (Figure 7-3a) and study area F2 on the west-facing crater wall which contains small gullies (Figure 7-3b). These gullies appear to be incised into "mantle deposits" (Mustard et al., 2001). The mantle is hypothesised to be the remnants of a previously extensive volatile rich deposit (e.g., Mangold, 2005).

7.3.2.2. Site G – Gasa Crater in Terra Cimmeria

I chose sections on the pole-facing (study area G3; Figure 7-3c), west-facing (study areas G1 and G2; Figure 7-3d) and equator-facing (study area G4; Figure 7-3e) slopes.

7.3.2.3. Site H – crater inside Kaiser Crater in Noachis Terra

I chose study areas that encompass the drainage area of two gullies (study area H2), a single gully (study area H1) and also the slope section as a whole (study area H3), all of which are shown in Figure 7-3f. I chose study area H4, an area of the slope not affected by gullies, for comparison (Figure 7-3f).

7.3.2.4. Site J – crater in Terra Sirenum

I analysed an equator-facing slope (study area J1; Figure 7-3g) which has no evidence of channels but contains an apparently well developed talus apron. There is no evidence of mantle deposits being present on this slope.

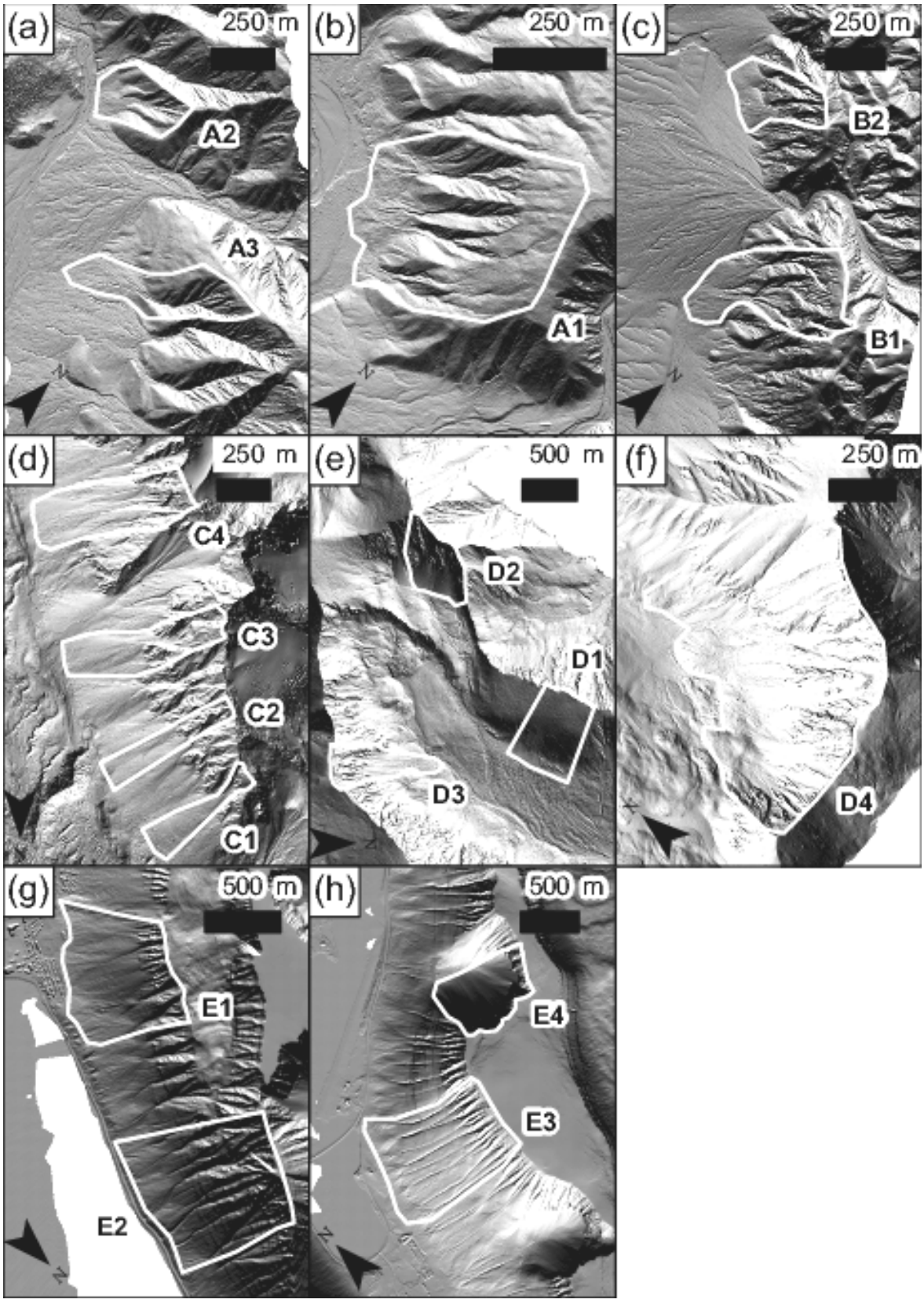

Figure 7-2. Hillshade representations made from digital elevation models of the study site locations on Earth. Areas included in this study are outlined and labelled in the Figure. (a) and (b) Site A, San Jacinto, California. (c) Site B, Death Valley, California. (d) Site C, St Elias Mountains, Alaska. (e) and (f) Site D, Front Range, Colorado. (g) and (h) Site E, Westfjords, NW Iceland.

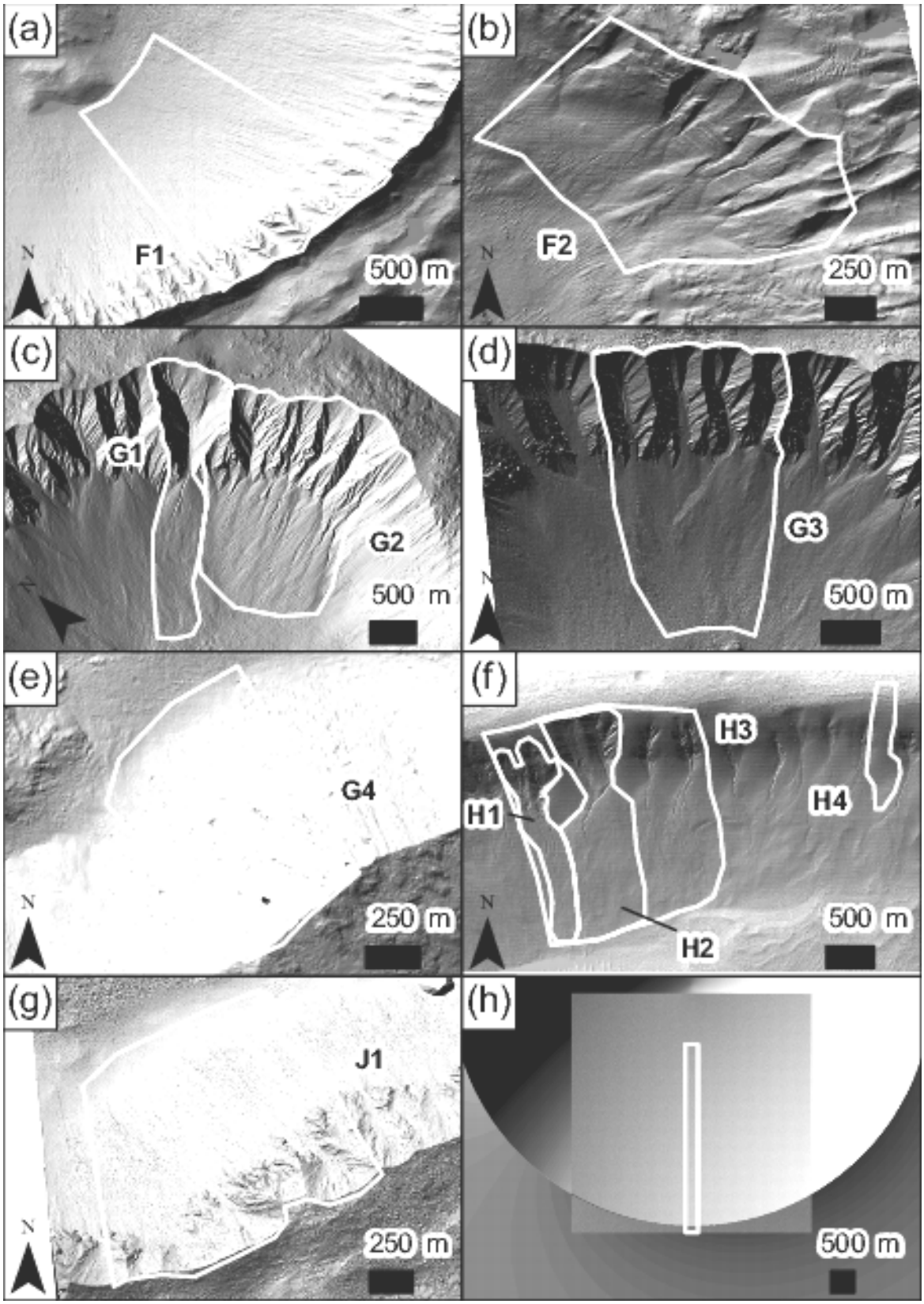

Figure 7-3. Hillshade representations made from digital elevation models of the study site locations on Mars. Areas included in this study are outlined and labelled in the Figure. (a) and (b) Site F, Penticton Crater in Eastern Hellas. (c), (d) and (e) Site G, Gasa Crater in Terra Cimmeria. (f) Site H, a crater inside Kaiser Crater in Noachis Terra. (g) Site J, a crater in Terra Sirenum. (h) The 10 km diameter synthetic crater, in which the square area is where the pink noise has been applied.

7.4. Method

7.4.1. Datasets and generation of digital elevation models

Slope-area analysis is only possible with high quality elevation data, preferably at a resolution better than 10 m per pixel, or 1:25,000 map scale (Montgomery and Foufoula-Georgiou, 1993; Tarolli and Fontana, 2009). For each of the terrestrial sites 1 m resolution DEMs were derived from airborne laser altimeter (LiDAR) data. These were then resampled to 5 m resolution to match the Mars data as described below. Chapter 5 gives details on the data sources for the study sites on Earth.

Significant metre-scale noise present in the DEMs of sites G, H and J had an extremely detrimental effect on preliminary slope-area analyses. Hence, all the DEMs were resampled to 5 m per pixel before the reanalysis was performed.

Finally, a synthetic crater was constructed (Figure 7-3h) to test whether the results from the Mars study sites in general reflected the process, or instead were a result of the geometry imposed by the impact crater setting (all the Mars study areas were on the inner walls of bowl-shaped depressions, but none of the ones on Earth were). A 10 km diameter synthetic crater was created by applying a smooth parabolic radial profile, which was derived by fitting curves through non-gullied radial profiles of the craters in sites F and G. Metre-scale "pink" (also called "1/f") noise was added to simulate a natural rough surface (Jack, 2000).

7.4.2. Derivation of drainage area and local slope

Representative slope sections were chosen in each DEM (Figure 7-2 and Figure 7-3). For Earth, these were chosen to represent end-member and intermediate process domains, including dry mass wasting, debris flow and alluvial processes. On Mars, some areas were chosen that covered the complete slope on which gullies are found, whilst others covered a single gully system, or non-gullied slope for comparison.

The slope and the flow directions of each pixel in each DEM were determined using a "Dinf" algorithm. This algorithm gives flow directions in any direction, rather than only towards one of the eight neighbouring pixels (Tarboton et al., 1991). This has been shown to produce better results from slope-area analysis because it gives a more accurate approximation of the real path of flow through the landscape (Borga et al., 2004). For each pixel, the accumulation of flow was calculated from the flow directions by summing the number of pixels located upstream, and multiplying by the pixel area. These analyses were performed using the TauDEM extension for ArcGIS, based on the algorithms developed by Tarboton (1997). For each DEM the "wetness index" was also calculated. This is the natural logarithm of the ratio of contributing area to slope. It provides information on the connectivity of the landscape drainage and ability of the surrounding landscape to deal with drainage (Woods and Sivapalan, 1997). All the DEMs underwent the same processing steps.

Finally, the slope data were extracted in 0.05 wide logarithmic bins of drainage area in square metres. Hence, the bins have unequal and increasing spacing in units of square metres, but equal spacing in logarithmic space. Therefore the bin-boundaries in square metres, where a is the lowest boundary, are given by x, calculated as follows:

$$\log_{10}(ax^n) = 0.05 \tag{7-2}$$

$$x = \left(\frac{10^{0.05}}{a} \right)^{1/n}, n = 1,2,3,... \tag{7-3}$$

The slope-area and CAD plots were constructed using these binned data. Binning data in this way makes the trends in slope-area and CAD plots clearer and is a commonly used display technique (e.g., Snyder et al., 2000).

7.5. Results

7.5.1. Earth

Initially I chose two study areas with talus and one with active creep. The slope-area analysis results for these are shown in Figure 7-4a. The study areas with well developed talus (E4 and C1) show the following pattern on log-log plots: (1) at small drainage area the curves are initially flat, (2) there is then a linear decrease in slope with increasing drainage area and, (3) the curve then becomes horizontal again at higher drainage area with a lower slope value. Talus slopes that have a mixture of processes (e.g., C2) show a curve that (1) drops off linearly in log-log plots and, (2) then flattens at higher drainage areas.

The CAD plot (Figure 7-5a) provides additional information: the talus-dominated study areas have a very smooth convex shape. The gradient of the curve is low until the drainage area is between 0.0001 and 0.001 km^2 after which the curve drops sharply and continues to steepen with increasing drainage area.

The soil creep diffusive process study area (D1 in Figure 7-4a) shows a distinctive signature in slope-area plots: (1) The curve is initially horizontal to gently downwards sloping. (2) Between drainage areas of 0.00001 to 0.0001 km^2 the slope increases linearly with increasing drainage area. (3) There is then a marked slope-turnover at which the curve switches to decreasing slope with increasing drainage area. The soil creep diffusive process study area resembles the talus slopes in CAD plots (D1, Figure 7-5a).

Figure 7-4b and Figure 7-6b show the debris flow study areas that are influenced by talus processes and Figure 7-4c and Figure 7-5c show those that are more influenced by alluvial processes. Generally in slope-area plots debris flow produces a curve that drops off linearly in log-log plots, flattening off before finally dropping away steeply. The difference between the talus study areas (e.g. C2, Figure 7-4a) and the debris flow study areas influenced by talus (Figure 7-4b) is subtle in some cases. In a similar way the difference between the debris flow areas influenced by talus processes (Figure 7-4b) and those

influenced by alluvial processes (Figure 7-4c) is also subtle. Without field information it would be difficult to differentiate talus dominated and debris flow dominated slopes reliably in slope-area plots (e.g., compare Figure 7-4a, C2 and Figure 7-4b).

However, in CAD plots it is possible to differentiate between the two process types. The debris flow dominated study areas (Figure 7-5b and Figure 7-5c) show the following pattern: (1) the curve drops away from the horizontal slowly (but faster than the talus slopes) at small drainage areas, (2) the curve then either dips down linearly, or follows a flattened convex path and, (3) at high drainage areas the curve drops away sharply with increasing drainage area.

Study areas modified by ephemeral water flow have distinct signatures in slope-area plots (Figure 7-4d) and in CAD plots (Figure 7-5d). In slope-area plots they show a shallow linearly decreasing trend at small drainage areas, followed by a steep linear drop at higher drainage areas. The CAD plot drops away from the horizontal slowly and then dips down linearly (or even with a concave profile) until the tail of the curve drops sharply off at the highest drainage areas.

7.5.2. Synthetic Crater

The slope-area and CAD plots for the synthetic crater are easily differentiated from the process study areas that I have examined on Earth. In slope-area plots the synthetic crater produces a hump-backed curve (Figure 7-6d): at small drainage areas the curve rises steeply, then levels off and drops at high drainage areas. In appearance the curve is nearest to study area D1, the area dominated by diffusive creep (Figure 7-4a). In CAD plots (Figure 7-7d) the line follows a smooth convex arc, similar to that shown by talus on Earth, except that there is no break in gradient.

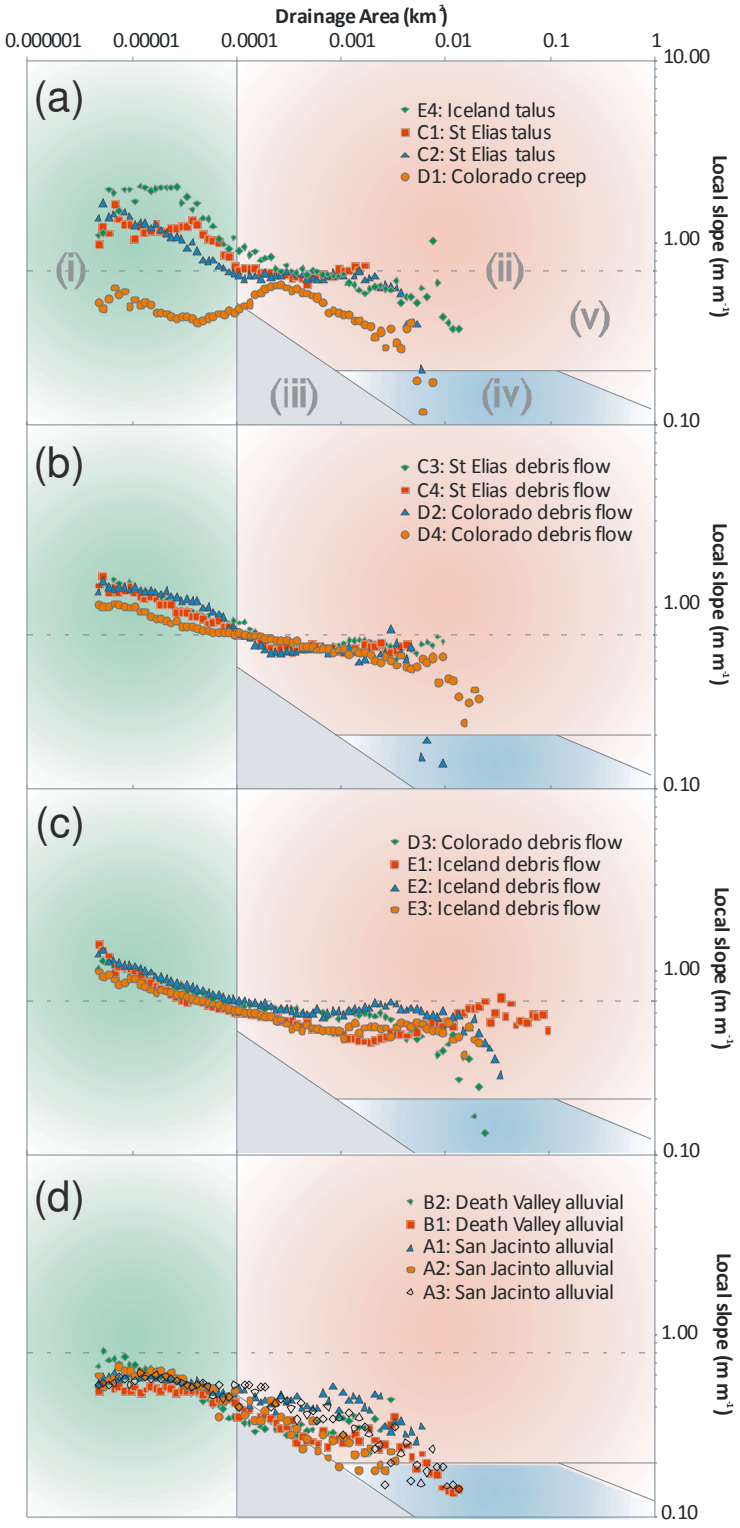

Figure 7-4. Slope-area plots for study areas on Earth. Marked with solid grey lines are the domains of Montgomery & Foufoula-Georgiou (1993) and Brardinioni & Hassan (2006), as shown in Figure 7-1. Labels are included in (a), but omitted for clarity in the other plots and are as follows: (i) hillslopes domain, (ii) debris flow dominated channels, (iii) unchanneled valleys, (iv) alluvial channels and (v) debris flow deposition domain. The horizontal dotted line represents the threshold for unconsolidated dry mass wasting at 0.7 gradient, equivalent to 35° slope. (a) Plots for those areas dominated by talus and creep processes. (b) Plots for those areas dominated by debris flow, with some influence from talus processes. (c) Plots for those areas dominated by debris flow, with influence from alluvial processes. (d) Plots for those areas dominated by ephemeral water flow, or alluvial processes.

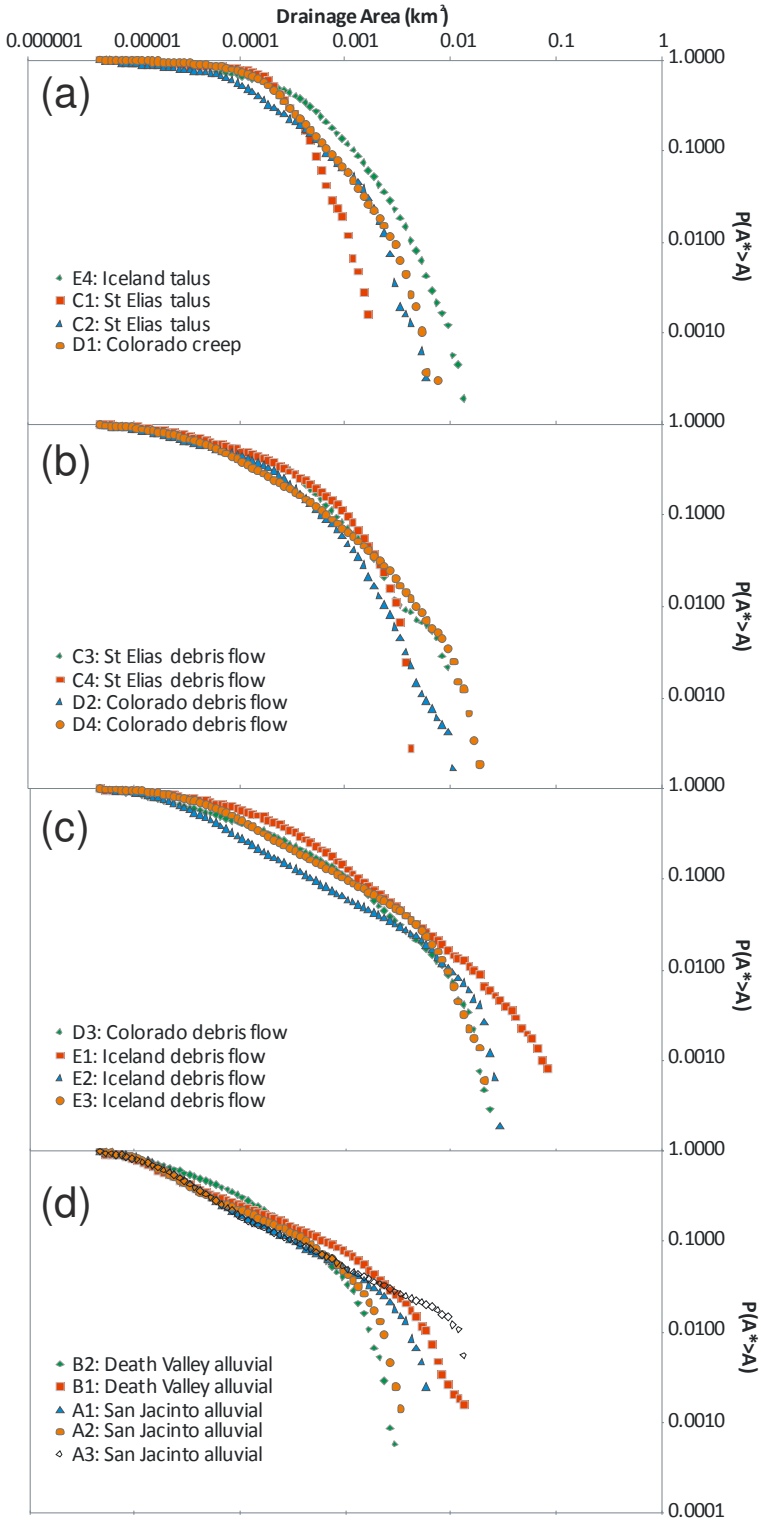

Figure 7-5. Cumulative Area Distribution plots for the study areas on Earth. (a) Plots for those areas dominated by talus and creep processes. (b) Plots for those areas dominated by debris flow, with some influence from talus processes. (c) Plots for those areas dominated by debris flow, with influence from alluvial processes. (d) Plots for those areas dominated by ephemeral water flow, or alluvial processes.

7.5.3. Mars

The slope-area plots for sites F and G (Penticton Crater and Gasa Crater inner slopes) closely resemble one another (Figure 7-6a and Figure 7-6b). The resulting curve can be divided into three zones: (1) A short initial increase in slope with increasing drainage area, followed by a slope-turnover at very small drainage areas. (2) A linear or slightly concave decreasing slope trend with increasing drainage area that continues for most of the plot. (3) Finally, at the largest drainage areas, there is a steep decrease in slope with increasing drainage area. For study area F1 there is a distinct and linear decline in slope with drainage area, whereas for study areas F2, G1, G2 and G3 this section is slightly concave. The drop-off at the highest drainage areas occurs at lower absolute drainage area values than for site G. In the CAD plot, study areas F1 and G4 have a smooth convex form, whereas study areas F2, G1 and G2 all have a nearly linear, flattened section at intermediate drainage areas (Figure 7-7a and Figure 7-7b). Study area G3 lies close to F1, G1 and G2 but without any sign of flattening.

The slope area plots for gullies in study areas H1, H2 and H3 (Figure 7-6c) can be split into three sections as follows: (1) At small drainage areas the curve is sub-horizontal with a subtle upward trend. This trend is more apparent for the data from individual gullies than the data obtained from the whole slope-section and is somewhat variable between gully systems. (2) At intermediate drainage areas there is a transitional zone, occurring at different drainage areas for each gully system, in which slope drops off markedly with drainage area. (3) At higher drainage areas there is a gently declining relationship between slope and drainage area, which is the same for all the gully systems.

The non-gullied study area (H4) is also shown in Figure 7-6c. This study area has a hump-back shape, resembling that seen for the synthetic crater. The hump occurs across the same slope values as the transition zone (2) for the gullied slopes. In CAD plots (Figure 7-7c) study areas H2 and H3 have a flattened section at intermediate drainage areas,

followed by a steepening decrease at higher drainage areas. The study area without gullies (H4) has a curve that is convex and initially declines slowly, before dropping off steeply. Study area H1 has a less flattened profile than study areas H2, or H3 and it seems to be a mixture between slope types typified by gullied study areas H2 or H3 and ungullied study area H4.

In slope-area plots, study area J1, an ungullied slope, shows a slope-area turnover at small drainage areas, followed by a decreasing and slightly concave trend in slope with drainage area (Figure 7-6d). There is a slight upturn at the highest drainage areas, but this is likely to be an artefact caused by a lack of pixels in these bins. In CAD plots (Figure 7-7d) study area J1 has a very smooth convex curve.

The slope and drainage area of the gully head initiation points were recorded for site H. These data are displayed on Figure 7-6c. This analysis was not performed for site F because edge contamination and noise made it impractical. The analysis was also omitted for site G because the gullies start at the top of the slope, so would by definition occur at the lowest drainage areas. Interestingly, the locations of the gully heads cluster around the range of drainage areas of the transitional section in the slope-area plot, but are located at higher slope values.

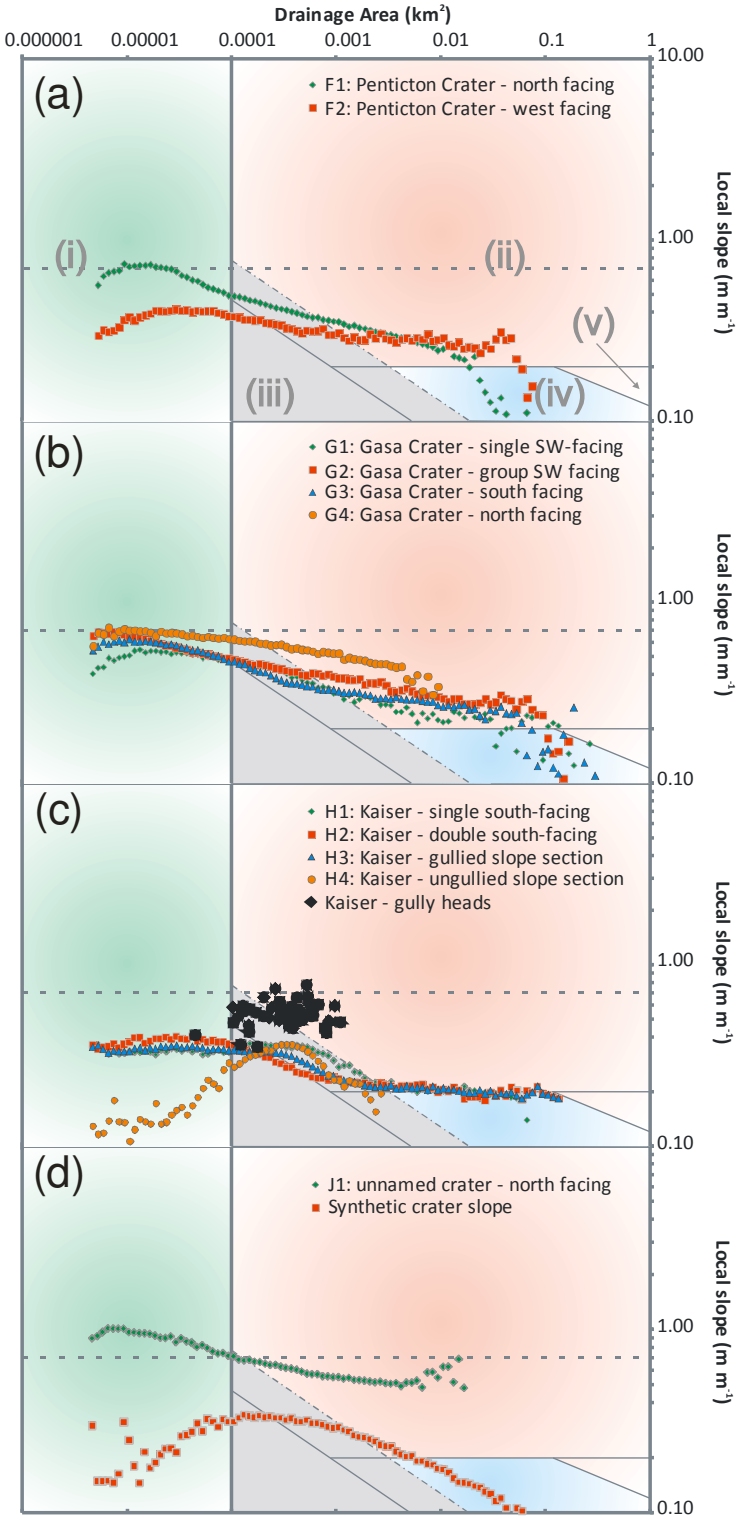

Figure 7-6. Slope-area plots for the study areas on Mars. Marked with solid grey lines are the domains of Montgomery & Foufoula-Georgiou (1993) and Brardinioni & Hassan (2006) established from Earth-based studies, as shown in Figure 7-1. Labels are included in (a), but omitted for clarity in the other plots and are as follows: (i) hillslopes domain, (ii) debris flow dominated channels, (iii) unchanneled valleys, (iv) alluvial channels and (v) debris flow deposition domain. The horizontal dotted line represents the threshold for unconsolidated dry mass wasting at 0.7 gradient, which is equivalent to a 35° slope. The dash-dot line represents the adjustment of the alluvial domain when taking into account Mars' gravitational acceleration. (a) Plots for Site F, Penticton Crater in Eastern Hellas. (b) Plots for Site G, Gasa Crater in Terra Cimmeria. (c) Plots for Site H, a crater inside Kaiser Crater in Noachis Terra. (d) Plots for Site J, a crater in Terra Sirenum and the 10 km diameter synthetic crater.

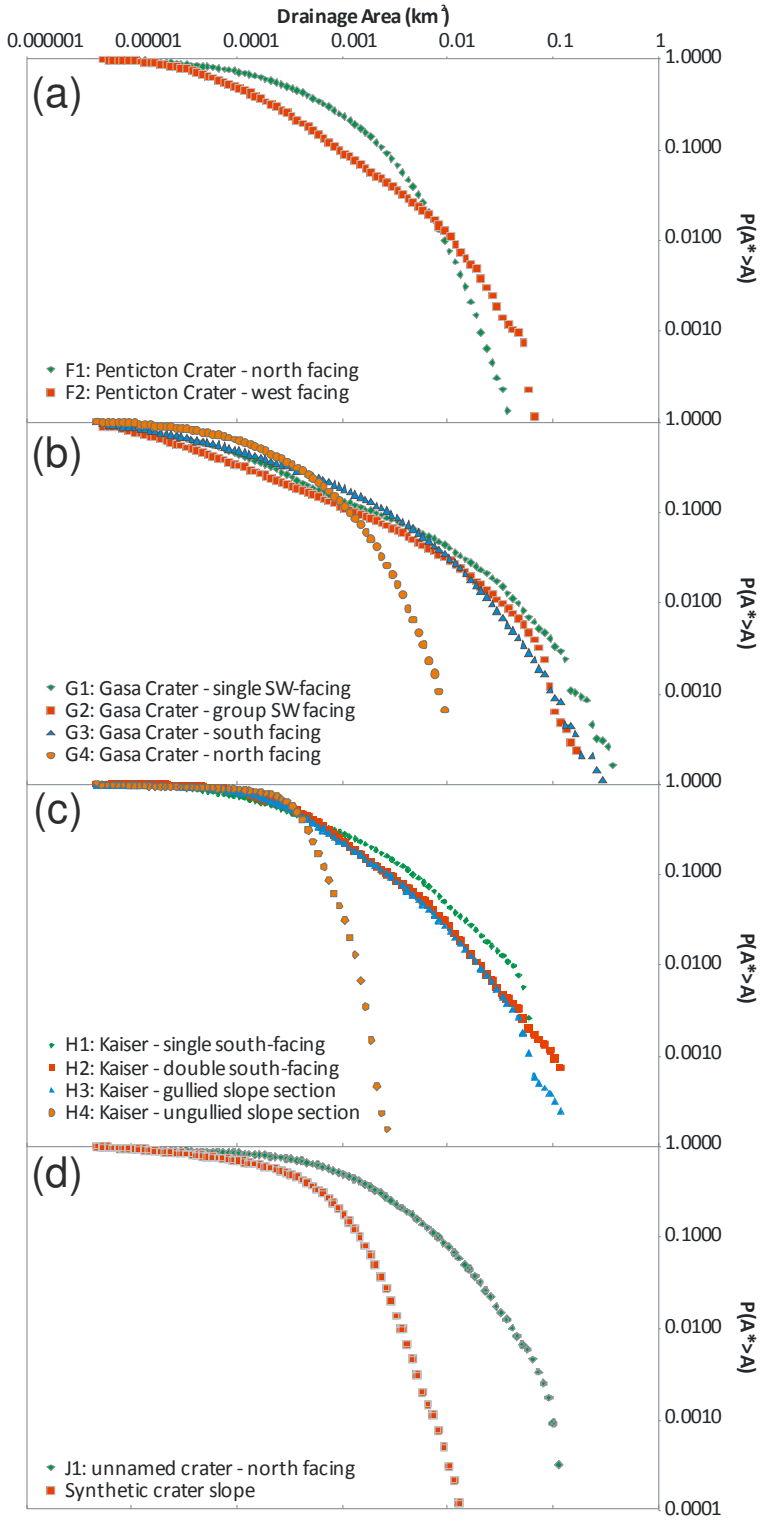

Figure 7-7. Cumulative Area Distribution plots for the study areas on Mars. (a) Plots for Site F, Penticton Crater in Eastern Hellas. (b) Plots for Site G, Gasa Crater in Terra Cimmeria. (c) Plots for Site H, a crater inside Kaiser Crater in Noachis Terra. (d) Plots for Site J, a crater in Terra Sirenum and the 10 km diameter synthetic crater.

7.6. Wetness Index on Earth and Mars

The spatial distribution of the slope-area data is most easily visualised using a wetness index map. Maps of wetness index are presented for Earth (Figure 7-8) and for Mars (Figure 7-9). The alluvial study areas in Earth sites A and B show very low overall wetness indices – only the channels have significant wetness index (Figure 7-8a, Figure 7-8b, and Figure 7-8c). Debris flow study areas are slightly more complex (Figure 7-8d, Figure 7-8e, Figure 7-8f, Figure 7-8g, and Figure 7-8h): the slopes generally have moderate wetness index, but there are localised paths along which the wetness index is higher. Site E (Figure 7-8g and Figure 7-8h) is the best example of this pattern, but it is also the area with the highest influence of overland flow. For site C (Figure 7-8d) this signature is poorly-developed, but this site has been influenced by talus processes. The creep-dominated study area, D1, has moderate wetness index throughout (Figure 7-8e). The talus study areas C1, C2 (Figure 7-8d) and E4 (Figure 7-8h) show lobe-like areas of low wetness index with widening streaks of higher wetness in between.

On Mars, study area F1 (Figure 7-9a) and the synthetic crater (Figure 7-9h) have similar wetness maps: the slope generally increases in wetness going downhill and there are quasi-linear streaks of higher wetness that increase in value going downslope. Study area F2 (Figure 7-9b) has overall low wetness, apart from concentrated lines of high wetness within the gully alcoves, that spread and become more diffuse in the debris aprons. A similar overall pattern is shown for study areas G1, G2 and G3 (Figure 7-9c and Figure 7-9d), but the ridges around the alcoves have very low wetness. Study area G2 in particular (Figure 7-9c) shows very concentrated slightly sinuous high wetness lines on its debris apron. However this part of the DEM contains significant noise, making it hard to judge whether this is simply an artefact. Study areas G4 (Figure 7-9e) and J1 (Figure 7-9g) have similar wetness index maps: there is low wetness at the crest of the slope and where bedrock is exposed and the wetness generally increases downslope, but this trend is

superposed with diffuse linear streaks of higher relative wetness. Site H (Figure 7-9f) has generally moderate wetness, with the alcoves and channels of the gullies showing focussed high wetness flanked by much lower wetness, and the debris aprons having generally high wetness with diffuse downslope streaking.

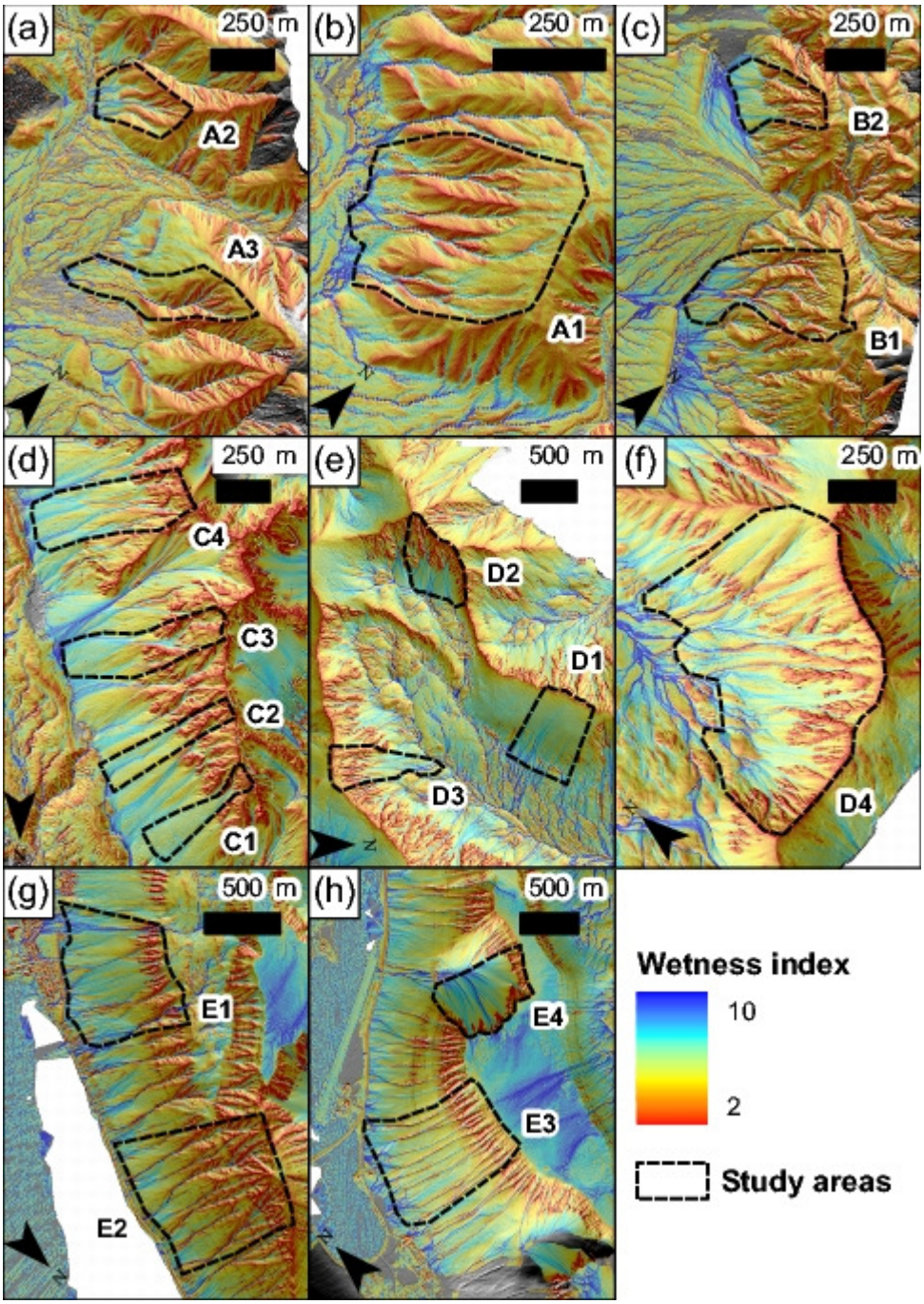

Figure 7-8. Wetness index maps made from digital elevation models of the study site locations on Earth. Areas included in this study are outlined and labelled in the Figure. (a) and (b) Site A, San Jacinto, California. (c) Site B, Death Valley, California. (d) Site C, St Elias Mountains, Alaska. (e) and (f) Site D, Front Range, Colorado. (g) and (h) Site E, Westfjords, NW Iceland.

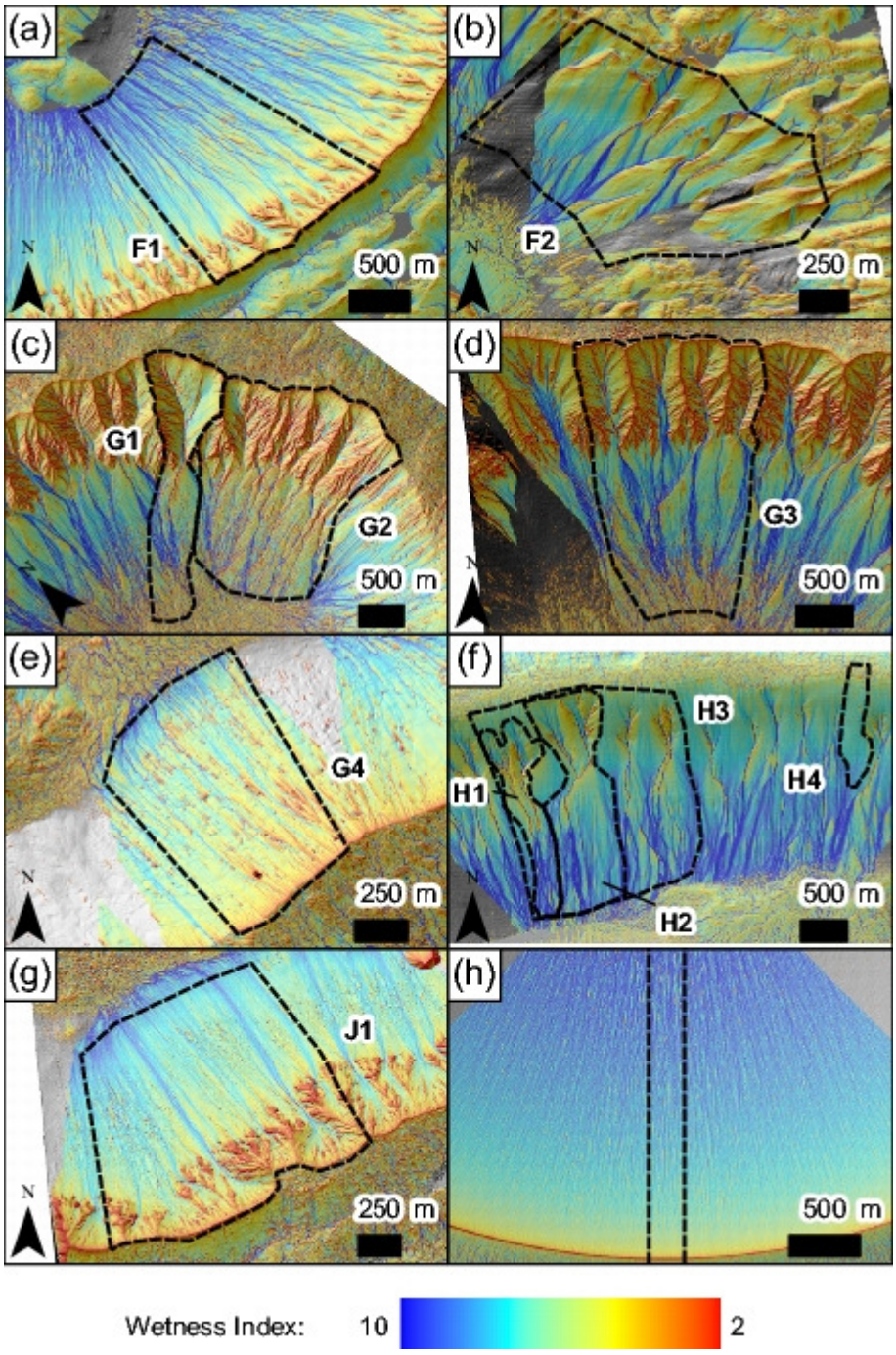

Figure 7-9. Wetness index maps made from digital elevation models of the study site locations on Mars. Areas included in this study are outlined and labelled in the Figure. (a) and (b) Site F, Penticton Crater in Eastern Hellas. (c), (d) and (e) Site G, Gasa Crater in Terra Cimmeria.(f) Site H, a crater inside Kaiser Crater in Noachis Terra. (g) Site J, a crater in Terra Sirenum. (h) 10 km diameter synthetic crater.

7.7. Discussion

7.7.1. Comparison of Earth data to previously published slope-area process domains

There are two interlinked methods of determining slope processes from slope-area plots:
(1) The data points fall within *domains* in the plots which have been found both theoretically and empirically to relate to particular processes, and
(2) The data points exhibit *trends and gradients* that provide information on active processes.

I compared my data from Earth to the slope-area process domains of Montgomery & Foufoula-Georgiou (1993) and the additional domain added by Brardinoni and Hassan (2006), shown as solid lines in Figure 7-4. The data from my creep, talus and debris flow analyses fall into the debris flow domain of Montgomery & Foufoula-Georgiou (1993). However, some of my debris flow data start to drop into their alluvial domain at the highest drainage areas. Because they are small systems with limited drainage areas, however, only a few points fall within the alluvial domain. Some of my data approach the additional domain added by Brardinoni & Hassan (2006), but do not extend towards sufficiently high drainage areas to enter it (Figure 7-4c). My data from the alluvial systems (Figure 7-4d) fall into both the debris flow and alluvial domains. They start to trend downwards in slope-area plots at lower drainage areas than my debris flow systems.

Tucker & Bras (1998) simulated the effects of different dominant processes on slope-area plots and I now compare their model results to the patterns in slope-area plots shown by my data. My talus systems (Figure 7-4a) closely fit their model of a landscape dominated by landsliding (which includes the process of debris flow). In slope-area plots my talus data have an initial flat section at small drainage areas, which represents the slope threshold for the rock wall failure and so differs between localities. At higher drainage

areas the curves are again flat, representing the failure threshold of loose talus, which is consistent for all areas at approximately 0.7 gradient, equivalent to a slope of approximately 35°. This is the typical angle of repose for unconsolidated materials (Chandler, 1973; Selby, 1993) and is shown by a dotted horizontal line in Figure 7-4 and Figure 7-6. Between these two horizontal sections there is a transition where the dominance shifts from rock wall failure to unconsolidated talus failure.

Within the framework of Tucker & Bras (1998) the pattern shown by the debris flow slopes on Earth (Figure 7-4b and Figure 7-4c) is most consistent with the transition from unsaturated landsliding (dry mass wasting of both talus and rock wall) to pore-pressure triggered landsliding (which I interpret to also include debris flow), in a landscape dominated by landsliding. The presence of processes with a slope failure threshold cause data in slope-area plots to fall along horizontal lines. Hence, as the process dominance changes from rock wall failure (highest threshold) to unsaturated landsliding (intermediate threshold) to saturated landsliding (lowest threshold) the curve declines and levels off at the slope value of the saturated landslide threshold in that particular area. As each physical locality has its own saturation threshold, this horizontal section occurs at different slope values for different localities but is always located below the dry stability line at 0.7.

In slope-area plots, my data from alluvial systems on Earth (Figure 7-4d) show a simple decline of slope with drainage area, possibly steepening at higher drainage areas. The data are scattered at drainage areas > 0.0001 km^2, due to the limitations of the small sizes of the gully systems available. This meant a relatively small number of pixels were used to generate each point, leading to random scatter. However, even taking into account the scatter, the data are below the slope threshold for dry slope failure at 0.7 slope, which suggests a gradual transition from pore-pressure dominated landsliding to fluvial processes.

The main feature of my creep-dominated hillslope data (D1, Figure 7-4a), is a turnover from increasing slope with drainage area to decreasing slope with drainage area. One of the alluvial systems in site A (study area A3) shows a weak slope-turnover at the lowest drainage areas but none of the other plots show this feature. The slope-area turnover is shown in Figure 7-1 and is generally expected to occur in slope-area plots (e.g., Tucker and Bras, 1998) and usually occurs in, or close to, the "hillslope" domain of Montgomery & Foufoula-Georgiou (1993). The turnover represents a transition from slopes dominated by diffusive processes (which include soil creep often modified by plant roots and other biota) to those dominated by advective, or alluvial processes. Within the diffusive processes domain in slope-area plots, slope increases with drainage area. The reason that most of my data do not show this turnover is that the slopes I studied lack stable vegetation (Dietrich and Perron, 2006; Marchi et al., 2008).

The pattern shown by my alluvial systems and some of my debris flow systems (slow decline at small drainage areas followed by a steep decline at higher drainage areas) has been shown from numerous remote sensing and field studies to mark the transition from the colluvial (including debris flow) regime, to that of a fully fluvial regime (e.g., Lague and Davy, 2003; Stock and Dietrich, 2003; Stock and Dietrich, 2006). Some have described the transition as a separate linear portion of the plot between the colluvial and the fluvial (Lague and Davy, 2003) and some as a gradual curved transition (Stock and Dietrich, 2003). However, both are consistent with Tucker & Bras' (1998) transition from pore-pressure triggered landsliding into a fully fluvial system. My plots do not show a well-developed alluvial regime, but this is due to the use of high resolution data of very small areas rather than large, well developed fluvial catchments.

In summary, my terrestrial data are consistent with published slope-area process domains, provide reassurance that the method is applicable and that the Mars data can be

used to infer process in a similar way. Furthermore, improved process discrimination can be made by considering CAD profiles in addition to slope area analysis.

7.7.2. Comparison of Earth data to published CAD process domains

Comparison of all my CAD plots for Earth (Figure 7-5) to the published process domains for CAD (Figure 7-1) reveals that my data do not follow the generally cited trends. This is possibly because I am studying small areas, rather than large catchments. However, the shape of the curve outlined by my data in CAD plots does allow process discrimination and does follow some of the framework outlined by McNamara et al. (2006). Specifically region 1 on Figure 7-1 has three sub-regions whose shapes can be recognised in my datasets. The talus data (Figure 7-5a) and synthetic crater (Figure 7-7d) are both convex in their CAD plots, resembling most closely region 1a of McNamara et al. (2006). They describe this region as representing "hillslopes that diverge and do not gather drainage." my alluvial data and some of my debris flow data show a flattening of the CAD plot curve in the middle region, giving a steep linear section corresponding to either region 1b or region 2 (Figure 7-1b) which McNamara et al. (2006) describe as slopes that are convergent (1b), or channel-forming (2). Two debris flows (E2 and E3 in Figure 7-5c) show a concave section, which would correspond to region 1c of McNamara et al. (2006) and which they attribute to pore-pressure triggered landsliding or debris flow.

The similarity of talus and debris flow in slope-area plots can be attributed to their similarly linear long profiles. However, the two processes produce different patterns in CAD plots because talus slopes tend to disperse drainage but debris flow slopes tend to converge drainage. This can also be seen in the wetness index plots (Figure 7-8). This difference of behaviour in CAD and wetness plots, in addition to the information from the slope-area plots, shows that I can detect slopes dominated by alluvial, debris flow and dry mass wasting on the basis of these parameters, even for small catchments such as

individual gullies or debris flow tracks. Therefore I can apply these methods of process discrimination to Mars.

7.7.3. Process domains for gullies on Mars

In slope-area plots all the Mars slope sections, except study area J1, fall below the slope threshold for dry mass wasting (dotted line in the plots in Figure 7-6). This means that talus-like dry mass wasting is not a dominant process in these areas. However, study area J1, visually similar to talus on Earth, is not only above the slope threshold for dry mass wasting, but also bears a signature similar to talus on Earth in the combination of its slope-area plot, CAD plot and wetness index map.

Within the process domains of Montgomery & Foufoula-Georgiou (1993) the majority of the Mars data lie within the debris flow domain, with some data located in the alluvial domain and some on the boundary of the debris flow deposition domain added by Brardinoni & Hassan (2006). The difference in gravity between Earth and Mars requires an upwards slope adjustment to the alluvial channels domain boundary line (see Figure 7-1a) in slope-area plots (Appendix D), but does not change the gradient of the line. This is marked by the dash-dot line on the plots in Figure 7-6. The shift places more data in the unchannled domain, but does not place any additional data into the alluvial or debris flow domains. The distribution in itself does not provide very detailed information on the formation mechanisms for gullies. However, by combining slope-area trends, CAD plots and wetness index maps I can make more detailed assessments. I examine each of the study areas on Mars in turn and then discuss the overall implications for the gully formation processes.

7.7.3.1. Synthetic Crater

The pattern in slope-area plots of the interior of impact craters is a result of the inherent shape of the crater slope which in turn is due to the impact process and the modification

that occurs immediately afterwards. The slope of a fresh impact crater is concave and exponentially shaped in profile (Garvin et al., 1999). Thus in slope-area plots it resembles a well-developed alluvial system on Earth (e.g., Hack, 1957). In CAD plots, however, the synthetic crater data show a similar pattern to that of talus slopes on Earth, indicating that, at short length-scales, this type of slope cannot channelize flow on its own. This interpretation is supported by the wetness index plot (Figure 7-9), which shows a slowly coalescing flow, rather than discrete areas of fluid concentration.

7.7.3.2. Site F – Penticton Crater in Eastern Hellas

In slope-area plots the slope-turnover is well expressed for both study areas in site F (Figure 7-6a). This suggests a strong diffusive or creep influence on both slopes. Study areas F1 and F2 both resemble either poorly developed talus or debris flow in slope-area plots. In the CAD plot (Figure 7-7a), however, study area F2 has the distinctive profile associated with debris flow, whereas study area F1 more closely resembles talus. Talus processes can only be active in study area F1 at small drainage areas, where it lies on the dry mass wasting threshold in slope-area plots. Hence the shape of the CAD curve must be explained by another process, which has a slope threshold but does not concentrate drainage. This unknown process must be pore-pressure triggered as it is below the slope for dry mass wasting. In addition, the wetness plot reveals that study areas F1 and F2 are very different: study area F1 has a similar wetness index map to the synthetic crater (Figure 7-9h), whereas study area F2 resembles debris flow areas on Earth (e.g., Figure 7-8f) with strongly concentrated high wetness within alcoves and channels, becoming more diffuse down slope on the debris aprons.

The combined evidence suggests that the east-facing slope, which contains small gullies, has been modified by debris flow, whereas the equator-facing slope is more similar to dry mass wasting deposits. This agrees with the interpretation of Pelletier et al. (2008),

who, using numerical modelling, concluded that the new bright toned deposits on this slope were more similar in form to deposits of dry granular flows than debris flows.

7.7.3.3. Site G – Gasa Crater in Terra Cimmeria

In the slope-area plot for site G (Figure 7-6b), the slope-turnover occurs at very small drainage areas (one or two pixels) and is thus partly abbreviated. This suggests that creep has not strongly influenced this site. This interpretation is supported by the observation that the gully heads originate at the very top of the slope. Study areas G1, G2 and G3 resemble either poorly developed talus on Earth (study area C2, Figure 7-4a) or debris flows on Earth (Figure 7-4b and Figure 7-4c) in slope-area plots. However, in CAD plots (Figure 7-7b) they have a flattened mid-section, resembling debris flow systems on Earth. Their wetness index plots (Figure 7-9c and Figure 7-9d) have strong similarities with debris flow systems on Earth (e.g., Figure 7-8g), showing flow concentration in the alcove and channel, with more diffuse flow on the debris apron. Study area G2 (Figure 7-9c) shows a similar pattern of wetness index to the alluvial systems on Earth, with focussed flow throughout.

In slope-area plots (Figure 7-6b) study area G4 has a flatter profile than study areas G1, G2 and G3. The drop in slope at high drainage areas in G4 is probably an artefact of the low number of pixels included in the last 5 to 10 points. In the CAD plot (Figure 7-7b), study area G4 has a similar shape to talus systems on Earth (Figure 7-5a). The talus interpretation for G4 is supported by additional evidence: (1) there is no evidence for channels (Figure 7-3e), (2) the wetness index plot (Figure 7-9e) is similar to talus slopes on Earth and (3) part of the slope-area curve lies on the threshold for dry mass wasting (Figure 7-6b). The dip of the slope-area curve away from the threshold for dry mass wasting suggests that another process with a lower slope threshold is acting, either without having an effect on the CAD plot, or with the same CAD plot as talus. I hypothesise that this may be the same unknown process noted in study area F1.

The combined evidence suggests that the pole- and east-facing slopes of the crater have been affected by debris flow processes and the equator-facing slope by mass wasting and an unknown process.

7.7.3.4. Site H – crater inside Kaiser Crater in Noachis Terra

Our ungullied study area (H4) shows patterns in slope-area (Figure 7-6c) and CAD plots (Figure 7-7c) very similar to the synthetic crater and creep slopes on Earth. The difference between this study area and the gullied study areas (H1 to H3) is presumably a result of the process of gully formation. Study areas H1 to H3 do not have slope-area plots (Figure 7-6c) that fit easily within the framework established so far. However, if I refer to the modelling work of Tucker and Bras (1998) then the patterns in slope-area plots can be explained. At small drainage areas my curves for study areas with gullies have a horizontal or slightly positive trend compared to my non-gullied study area, which has a definite positive trend. This suggests the weak influence of diffusive processes (which generate a positive relationship in slope-area plots) combined with slope threshold processes (which tend to produce horizontal trends). As all the data are below the dry mass wasting threshold, this threshold process is likely to be a pore-pressure triggered process, such as debris flow. At intermediate drainage areas there is a transitional region which occurs at a similar drainage area to the slope-turnover in the non-gullied section. At high drainage areas, the gullied study areas show a slightly decreasing sub-horizontal trend, as opposed to the non-gullied study area which has a well defined decrease in slope with drainage area. This also can be attributed to a pore-pressure triggered threshold process but at a lower slope threshold than the previous process. In CAD plots (Figure 7-7c) study areas H1 to H3 are consistent with debris flow processes. The wetness index plots for these study areas (Figure 7-9f) are similar to terrestrial debris flow study areas which have been influenced by alluvial processes (e.g., site E, Figure 7-8g and Figure 7-8h). This suggests that the first pore-pressure threshold in slope-area plots is due to debris flow and the second lower one

due to an unknown process, which may be the same unknown process affecting sites F and G.

In slope-area plots, the gully heads on this slope (Figure 7-6c) coincide with the drainage area of the slope-turnover in study area H4 and the transitional study areas of H1 to H3. This coincident relationship matches the observations made by many authors who have studied gullies on Earth (e.g., Hancock and Evans, 2006). My channel heads lie in the domains attributed to "unchanneled" and "pore-pressure landsliding channel initiation" processes (McNamara et al., 2006). Notably the gully heads occur below the dry mass wasting threshold, again suggesting that my gullies are initiated by a pore-pressure threshold process. The gully heads occur on slope gradients of 0.25, similar to those described by Lanza et al. (2010), but at drainage areas an order of magnitude lower. This is possibly due to the different approach used by Lanza et al. (2010) to measuring the contributing area, and possible differences in their interpretation of the location of channel initiation. The co-occurrence of the gully heads with the slope-turnover in slope-area plots suggests that the gullies are a result of whole-slope drainage, either at the surface or shallow subsurface. This is evidence for a distributed source, and thus argues for the surface melting model for martian gully formation, and against the aquifer source model. Further, this observation provides additional evidence that a threshold process, probably debris flow, is forming these gullies.

From the combination of the slope-area, CAD and wetness plots I infer that the gullies in this crater are produced by debris flow and were initiated by surface, or near subsurface, flow of water. Creep and an unknown process were likely to have been the dominant processes on the ungullied crater slopes. This is consistent with the setting of these gullies within the ice-rich mantle deposits which is likely to be susceptible to melting, providing a distributed source of water for the gullies.

7.7.3.5. Site J – crater in Terra Sirenum

Unlike the other areas I have studied on Mars, parts of the slope-area data for study area J1, at lower drainage areas (Figure 7-6d) are above the threshold slope for dry mass wasting. This is an indication that rock-strength limited dry mass wasting is occurring in the upper parts of the slope. In CAD plots (Figure 7-7d) this study area has the classic shape of a talus or creep slope. However, the slope-area trend shown by study area J1 is very different from that of the synthetic crater (Figure 7-6d), which I assume to have been similar to the starting point for study area J1. This assumption carries the implication that the slope in study area J1 has evolved over time from concave to linear in profile. Study area J1 shows a very similar trend in slope-area plots to study area G4 (Figure 7-6b). As discussed previously for study area G4, in the framework of Tucker & Bras (1998) such a pattern is likely to reflect a gradual transition from the dominance of a dry mass wasting threshold at higher drainage areas to the dominance of a pore-pressure triggered slope threshold due to an unknown process at lower drainage areas. The wetness index map shows that the slope is mainly quite dry, except for some diffuse linear areas, again resembling talus slopes on Earth. The combination of the slope-area plot, CAD plot and wetness map suggests a dominantly dry mass wasting evolution of this slope, which fits well with the visual observations.

7.7.3.6. Solifluction on slopes on Mars

In many of the Mars study sites I have identified an unknown process that is responsible for a second, lower-slope pore-pressure triggered threshold in the slope-area plots. However, this process seems to have a CAD plot that is similar to talus on Earth, i.e. it does not concentrate drainage. As suggested by Tucker & Bras (1998) another threshold process which would produce a similar response in slope-area plots to pore-pressure induced landsliding is solifluction, which in frozen landscapes comprises the combined action of gelifluction and frost creep, and describes the slow, down slope movement of

water-saturated debris or soils. Solifluction requires freeze-thaw to generate elevated pore-pressures and occurs at lower slope angles than pore-pressure induced failure, which can trigger landslides and debris flow (Harris et al., 2008). This process is consistent with the recent observations of periglacial landform assemblages on Mars (Balme and Gallagher, 2009; Balme et al., 2009; Soare and Osinski, 2009).

7.7.4. Implications for the formation process of martian gullies

Dietrich & Perron (2006) suggested that the lack of biotic processes on Mars would promote erosion by rilling and gullying and stripping of the fine surface materials, given a suitable water source. This would lead to a slope-area plot that lacked a distinct slope-turnover, similar to Death Valley (our site B – Figure 7-4d). However, inspecting the trends in the slope-area plots for the Mars systems in Figure 7-6, one of the most apparent differences from Earth is the *presence* of this slope-turnover. This indicates that creep is a more dominant process on Martian hillslopes than on those I studied on Earth, contradictory to the predictions made by Dietrich & Perron (2006). The creep signal in slope-area plots on Earth is induced predominantly by biota, hence on Mars creep must be facilitated using a different mechanism. Perron et al. (2003) observed, using Mars Orbiter Laser Altimeter (MOLA) data, that slopes on Mars have average gradients well below 35° and suggested that ice-driven creep is the cause. This provides an explanation for the signals seen in my slope-area data from Mars. In accordance with their results, most of the slopes I studied on Mars also have average gradients well below 35°, with the exception of slope J1, whose average gradients are partially above 35°.

Virtually every gully that I have studied on Mars has the distinct signal of debris flow as the dominant gully-forming process. The notable exception is area F1, the slope containing the new light-toned deposits. However, this area does not include gullies of a normal form (Figure 2-1) as it lacks well-defined alcoves and channels. Examination of a greater number of DEMs containing gullies would be needed to confirm debris flow as the

main gully-forming process on Mars. However, if this is the principal mechanism, it has several important implications for the formation of gullies on Mars:

(1) The hyperconcentrated sediment and low infiltration rates could protect the water from evaporation.

(2) The energy released by grain interactions within the flow could retard freezing.

(3) Basal freezing (Conway et al., 2010b) or a permafrost layer could facilitate the saturation of the sediment that is required to generate the high pore water pressures to trigger debris flow.

(4) Expected depositional features include levees and lobes.

(5) Expected erosional features include discrete slip scars.

Points 1-3 of this list are hard to observe or test, but the erosional and depositional features can be detected in the high resolution HiRISE images. Failure scars have been noted by other authors (Dickson and Head, 2009) from HiRISE images and are present within my study areas. Depositional lobes have also been noted by many authors (Levy et al., 2009b; Lanza et al., 2010). Visual observations have been made of debris flow levees (Lanza et al., 2010) but DEMs from HiRISE are not yet of sufficient quality to show the topographic signature of debris flow levees. High quality DEMs would allow the estimation of individual flow volumes (Conway et al., 2010c), which could be used to constrain models of gully formation. This should be a priority for future work, as it would allow precise estimates of water contents.

A debris flow, once triggered, results in more erosion and deposition with less water than pure water flow. This means that the high discharges invoked by other workers (Heldmann et al., 2005; Hart et al., 2009) would be unnecessary to form martian gullies. Modelling has shown that surface melting produces only small amounts of liquid water (Williams et al., 2009). This has been one of the major criticisms of the surface melting

model. However, if gullies are formed mainly by debris flow, points (1) and (2) above indicate that relatively small amounts of water are needed.

7.7.5. Implications for the water source of martian gullies

The observed relationship in slope-area plots between the slope-turnover and the location of gully-heads in site H on Mars is an important observation and indicates that the transition from concave to convex topography is closely linked to gully formation. This would not be expected in an aquifer system: channel formation would be controlled predominantly by the location of aquifer bodies rather than the shape of the landscape (Fetter, 2001). My work indicates that a widely distributed source of surface or shallow subsurface flow in site H would be the most satisfactory explanation. Because my data do not show a definite trend in slope-area plots, this indicates that the channels originate from shallow sub-surface flow (Hattanji et al., 2006; Jaeger et al., 2007a; Imaizumi et al.), or more likely surface flow in a soil-poor landscape (Larsen et al., 2006). A potential source for this near surface water is the mantle deposits which have been observed on both this slope and in site F2.

The development of equally spaced incised alcoves in site G can either be attributed to geological controls (e.g., faulting), or landscape self-organisation from an interlinked debris flow-alluvial system (Perron et al., 2009). Considering (1) that I conclude debris flow to be the dominant gully-forming process on this crater slope, and (2) the lack of these organised alcoves on the equator-facing slope; it would seem most likely that these are self-organised alcoves formed as a result of active erosion of the gully-forming processes. This kind of self organisation requires a landscape that responds to a distributed water source as on Earth rather than an aquifer source.

Kreslavsky & Head (2003) and Kreslavsky et al. (2008) found that pole-facing slopes between 40-50° latitude in both hemispheres were systematically gentler than equator-facing slopes. They suggest that this is due to insolation asymmetry and melting of

ice on pole-facing slopes during periods of high obliquity, similar to the model proposed by Costard et al. (2002) for gully formation on pole-facing slopes. My study sites also show this asymmetry: pole-facing slopes are longer, have a greater variety of slope angles and are more concave, whereas the equator-facing slopes are shorter, have a more uniform distribution of slopes and are more linear. There is a marked difference in geomorphological process between crater walls with different aspects in the two craters that I studied (sites F and G). The observed asymmetry of process and form supports the model of a climatic influence on gully-formation and general slope development of the craters.

7.8. Conclusions

I have shown that the use of quantitative geomorphological analysis techniques commonly applied on Earth are also capable of discriminating between different active processes on Mars. Specifically I have validated the use of slope-area plots, cumulative area distribution (CAD) plots, and wetness index maps on small slope sections of less than one square kilometre. I have shown that pure water (alluvial) flow, debris flow and dry mass wasting dominated slopes can be satisfactory discriminated on Earth. By applying these techniques to four areas of Mars containing recent martian gullies I have found that debris flow is the dominant gully-forming process. However, I have also shown that, as on Earth, gully formation on Mars is a complex process: slopes on Mars have been affected by a variety of processes that lead to a mixture of signals from my geomorphological analyses. Despite this, I have not found the distinctive geomorphological fingerprint of pure water flow on slopes that host gullies. Its absence, however, does not prove the absence of the process. My results are consistent with the possibility that ice driven creep and solifluction are, or have been recently, active in modifying crater slopes on Mars.

From the location of gully heads within the landscape, and by studying the form of alcoves, it is apparent that at least two of the sites examined contain gullies which have

been formed from a widely distributed source of water. This is most easily explained by a surface melting source for the water. I agree with Costard et al. (2002) that the most likely cause of this melt was increased insolation during past high obliquity excursions. My observation of an asymmetry in process and form around the impact craters provides additional support for this model.

Our geomorphological evidence for debris flow as an active process in forming gullies is reinforced by visual observations. Debris flow as a process leaves distinct geomorphological features, such as failure scars and lobate deposits, which have been observed both here and in previous studies (Dickson and Head, 2009; Levy et al., 2009b; Lanza et al., 2010). Unfortunately the topographic data on Mars are not yet sufficient for the discrimination of these features and flanking levees in DEMs, which would allow accurate estimation of individual flow volumes and thus prediction of the volumes of water needed to form the gullies (Conway et al., 2010c).

Chapter 8. Experimental study of sediment transport by water flowing under martian conditions: application to gullies on Mars

8.1. Motivation and context

The bulk of this chapter has been submitted to the journal Icarus and is currently under review. I have abbreviated Section 8.1 to avoid repetition, and amendments have been made where appropriate for the thesis format.

The aim of this study is to investigate the sediment transport capability of liquid water on hill slopes under current martian conditions. This is important for the understanding of the potential role of liquid water in forming recent martian gullies (Malin and Edgett, 2000). Hecht (2002) proposed that metastable liquid water could form almost anywhere on present-day Mars if there are steep slopes. I therefore explore how the ambient conditions (and hence stability of water) inhibits or enhances erosion, sediment transport and deposition. Constraining the behaviour of interacting water and sediment under current martian conditions could help develop future models that describe gully formation on Mars.

No experiments to date have attempted to produce flows under the low temperature and pressure experienced on the present day martian surface. I recognise that I cannot replicate the effect of gravity easily in an experiment including a hypobaric chamber and I make no attempt to compensate for this. I stress that these experiments are directed at the

process level. Any comparisons that I make between the forms of the structures produced by my experiments are simply comparisons between different temperature and pressure regimes at Earth's gravity and should not be interpreted as direct analogues for landforms seen on Mars. I do not attempt to scale up my experiments spatially, as studying metre-scale sediment motion is sufficient to draw initial conclusions about sediment transport. For example, processes occurring in the source area of gullies would initially be small-scale, involving small amounts of water and small amounts of sediment transport. We recognise that these results therefore are not universally applicable, but give indications of the likely effects and consequences of the environmental conditions on Mars on sediment transport by water.

8.2. Method

8.2.1. Chamber description

The test bed was contained within a cylindrical low pressure chamber 2 m in length and ~ 1 m diameter. The test bed was a 1 m long, 0.1 m deep rectangular metal tray of trapezoidal cross section measuring 0.50 m across at the base and 0.54 m across at the top. A ~ 5 cm deep layer of various combinations of unconsolidated material was placed in this tray to form the sediment substrate. The tray was placed on a copper cooling plate and the whole test bed was set at angle of 14° (Figure 8-1). All the experiments used water containing no dissolved salts. For the control experiments performed at ambient pressure, the water was introduced through a 14 mm diameter hose connected to a container ~ 5 m above the chamber. For experiments at low pressure, the water was introduced from a calibrated container placed outside the chamber, at the same level as the source hose – the difference in pressure was enough to drive the water into the chamber. The flow rate was kept constant at 0.08 litres per second for all experiments. Thus each experiment lasted approximately 30 seconds; hence a total of 2.5 l of water was used. Inside the chamber, the

source hose was positioned centrally on the rim of the tray. Water was thus introduced onto the top of the sediment body. Water was not introduced underneath or directly onto the surface of the sediment to avoid ice blockages in the hose. A solenoid valve within the end of the hose allowed external control over the release of water. A diffuser was located below the solenoid valve to dampen the horizontal velocity component of the water. The sediment substrate was chilled using a cooling plate in contact with the entire base of the tray. The cooling plate, a copper slab, was cooled by interior flow of liquid nitrogen. Baffles within the cold plate distributed the cooling effect of the liquid nitrogen evenly throughout its area. The pressure in the chamber was actively controlled using a vacuum pump and was maintained at ~ 7 mbar for the Mars analogue experiments.

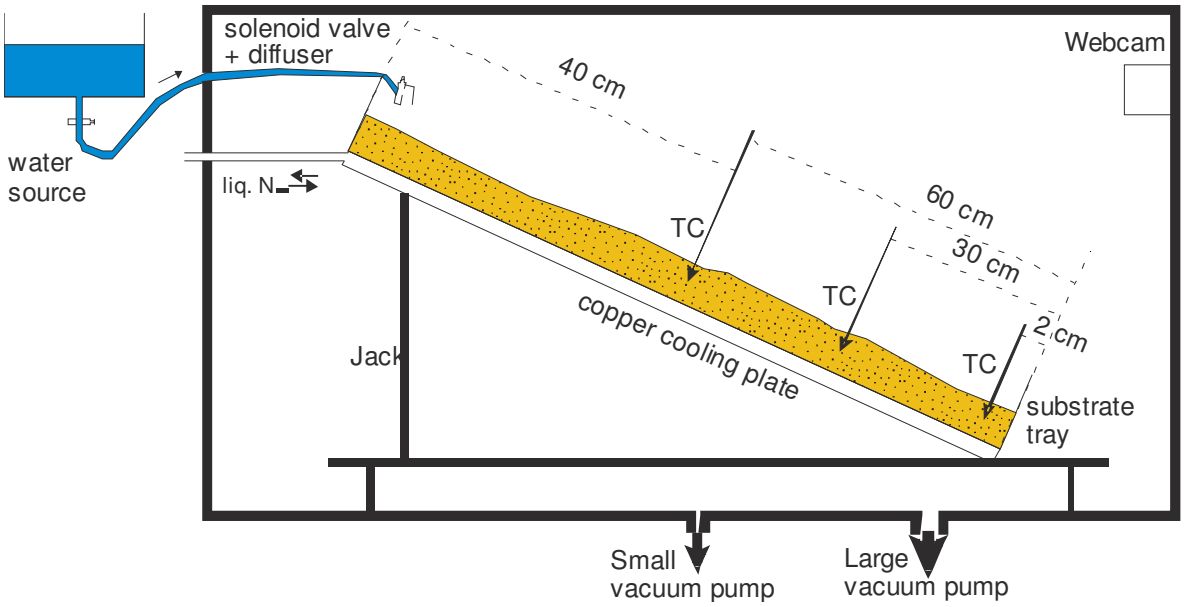

Figure 8-1. Diagram of the experimental apparatus. Dark bounding box represents the hypobaric chamber. TC stands for thermocouple.

8.2.2. Instrumentation

Three pairs of thermocouples were placed within the sediment at 2 cm depth and 14 cm from the edges of the tray at the longitudinal distances marked on Figure 8-1, and shown in plan view in the inset of Figure 8-4. Their output was recorded at one second intervals by a datalogger. In all low temperature experiments the average temperature was below -20 ºC before the experiment was run, representing an above average, but not unexpected local

surface temperature for Mars (e.g. Haberle et al., 2001). For six of the experiments the water temperature was pre-chilled to 5 ºC and for three further experiments the water was pre-chilled to 0.5 ºC. The temperature of the water was varied to simulate possible martian gully processes: the warmer temperature might be expected for an aquifer outburst (e.g. Heldmann and Mellon, 2004) and the colder water to form as a result of near-surface ice melt (e.g. Costard et al., 2002).

All experimental runs were monitored and recorded using an internal and external webcam (with different view angles) and a digital camera. This allowed playback and detailed observations to be made of the evolution of the flow, the morphology, and the relative timings of events. Once each experiment had finished, photographs were taken of the sediment surface and also of exploratory excavations made to investigate the sub-surface changes to the sediment body. For low temperature/low pressure experiments the chamber was opened only after the temperature on all thermocouples was observed to be dropping – this was taken as an indication that freezing of the water was complete – thus allowing the preservation of any sedimentary structures present.

Figure 8-2. Photograph of profiler used to measure cross sections for volume calculations. The tray is 54 cm across at the top.

Cross sections were measured with a profiler (Figure 8-2) before and after the experiment to enable measurement of the volume of sediment transported. The profiles were measured at marked 10 cm intervals along the tray, including both ends. The profiler allowed the surface of the test bed to be measured by a grid of 8 x 11 points, accurate to about 0.1 cm in height, before and after each run. After the experimental run was complete, further measurements at higher spatial resolution were made where the surface height changed abruptly – for example at the edges and tops of levees, channel walls, or at the ends of lobes. Volumes of erosion and deposition were derived from these data as described in Section 8.4.1.

8.2.3. Sediment characterisation

I used two different sands to evaluate the effect of grainsize and a more natural, poorly sorted material – rock crush – to investigate the effects of a broad grainsize distribution. Specifically, the substrates used were: (i) Leighton Buzzard DA 16/30, a medium sand, (ii) Leighton Buzzard RH T, a fine sand and, (iii) poorly sorted rock crush containing particles ranging in size from fine silt to gravel. The sands are both composed of quartz grains and their size distributions were measured by dry sieving (Atkinson, 2008). The rock crush is a mixture of crushed igneous rocks, including basalt and granite. The grainsize distribution of the rock crush was measured using the wet sieve method and hydrometer to British Standard BS1377 Part 4:1990 by Soil Property Testing Ltd, Huntingdon, UK. Quantitative grain size data are shown in Table 8-1 and Figure 8-3.

Table 8-1. Sediment characterisation, in which D50 represents the modal grainsize of the distribution.

	Bulk density (kgm^{-3})	Particle density (kgm^{-3})	Porosity	D_{50} (mm)	Permeability (ms^{-1})	Angle of repose (°)
Rock Crush	1910	2680	0.403	1.8641	$2.23x10^{-4}$	41.0
Medium Sand	1700	2680	0.576	0.6144	$5.21x10^{-3}$	34.5
Fine Sand	1680	2680	0.595	0.2301	1.31x10-3	33.5

The permeability of each material was measured using the falling head method (Head, 1982) by Soil Property Testing Ltd, Huntingdon, UK and is shown in Table 8-1. Bulk density, particle density and porosity (Table 8-1) were ascertained prior to permeability testing using the standard methods as described in Head (1982). The angle of repose of the materials was measured by gently forming a loose conical pile of sediment and averaging two measurements of the incline of the slopes formed. The angle of repose was very similar for the two sands (33-35°), but much greater for the rock crush (41°). The angularity of the sediments was determined by microscopy: the sand grains were sub-rounded to well-rounded in shape, the rock crush had sub-angular to angular grains.

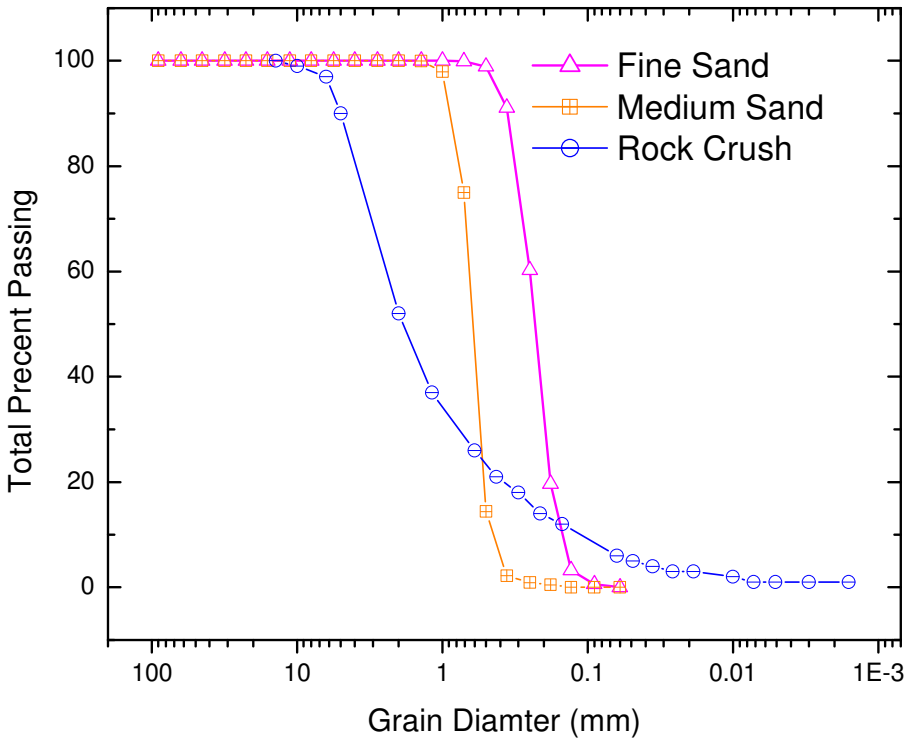

Figure 8-3. Plot showing the grainsize distribution of the sediments used in this study. The results of Atkinson (2008) are given for the fine and medium sands and the results from Soil Property Testing Ltd., Huntingdon, UK for the rock crush.

Grain compositions and grain size distributions have been shown to be widely variable on Mars from in-situ observations from Viking (Clark et al., 1977; Moore and Jakosky, 1989) through to the Mars Exploration Rovers (e.g. Jerolmack et al., 2006; Cabrol

et al., 2007; Sullivan et al., 2008) and from remote sensing observations that use thermal inertia as a proxy for grain size (e.g. Fergason et al., 2006). The materials used as simulants are somewhat more restricted (e.g. Peters et al., 2008; Sizemore and Mellon, 2008), but still have a range of physical and chemical properties. Although I am exploring the effects of material parameters, rather than simulating Martian regolith *per se*, the physical properties of the materials used in this study are certainly within the bounds of possible martian surface materials. Very fine material was avoided due to technical and health and safety restrictions, rather than its inapplicability to Mars.

8.3. Results

8.3.1. Summary

Table 8-2 provides a summary of the results and Appendix E contains the video recordings of all the experiments performed in this study. An annotated example of a complete low pressure and temperature experiment is shown in Figure 8-4. For each sediment type, three experiments were performed at low temperature and low pressure, one was performed at room temperature but low pressure, and one performed at ambient pressure and room temperature. Within the low temperature/low pressure experiments, two were performed with water at ~ 5 ºC and one with water at ~ 0.5 ºC. The appearance of the sediments at the end of each experiment is shown in Figure 8-5.

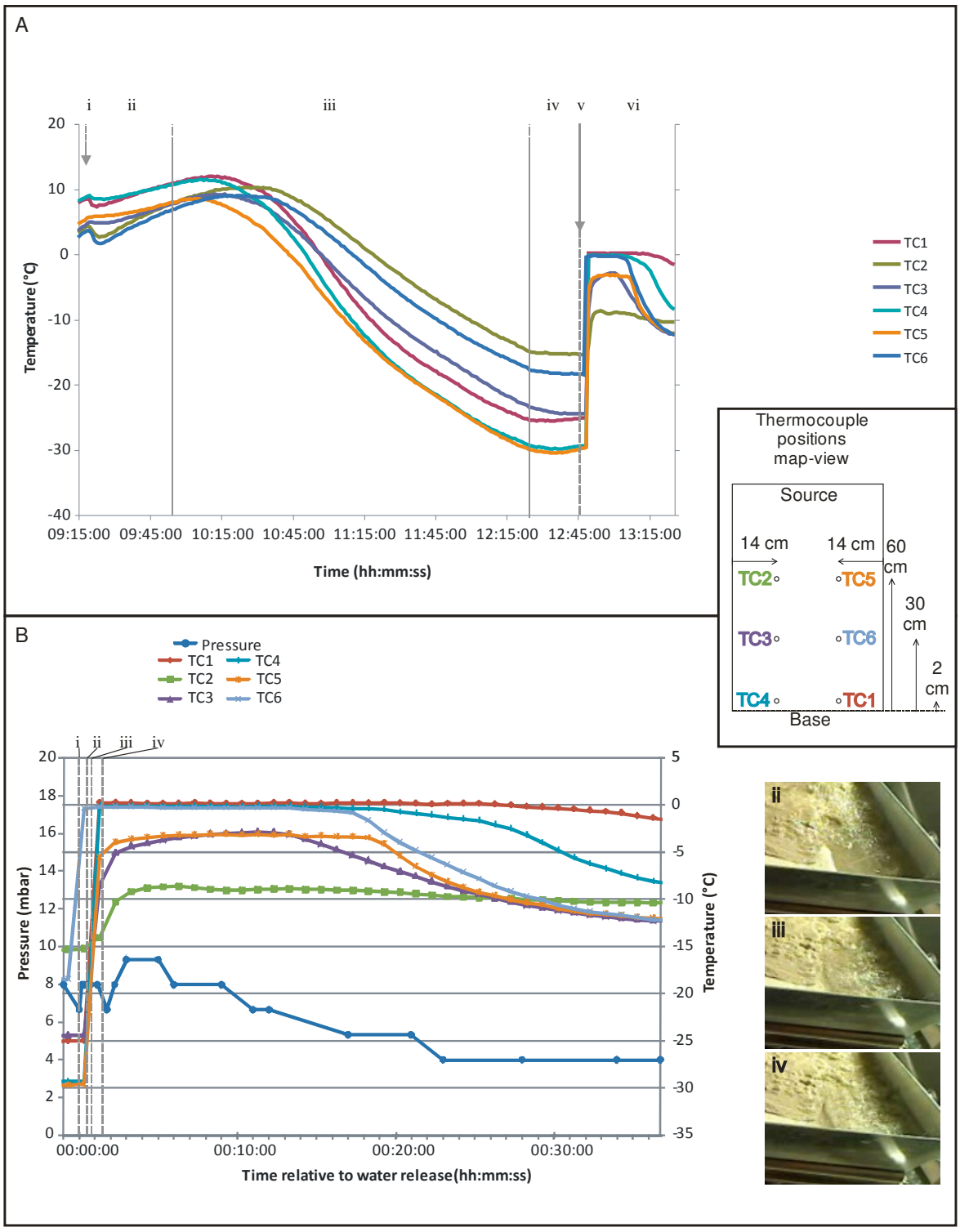

Figure 8-4. Example of the range of temperatures and pressures experienced during one simulation.
A: Plot of temperature against time for the preparation and execution of a low temperature/low pressure experiment, 090619_001, with 0.5 °C water and fine sand. The labelled time-periods are as follows: (i) vacuum pump started, (ii) period of low pressure to drive off any liquid water before freezing, (iii) cooling with liquid nitrogen, (iv) return to low pressure and extraction of any remaining gases, (v) water released and (vi) period waiting for all thermocouples to drop in temperature.
B: Plot of temperature and pressure against time for the execution of a low temperature and pressure experiment. The labelled events on the plot correspond to photo with the same label on the right. The events are as follows: (i) water starts flowing, (ii) water stops flowing, (iii) ice skin forms on surface of ponded water and, (iv) bubbles no longer forming under ice.
Inset: a map of the thermocouple positions for this experiment.

Figure 8-5. Matrix of photographs for each experiment when complete, each column vertically is a different sediment type and each row represents different ambient experiment conditions, with A being low temperature/low pressure, B ambient temperature/low pressure and C ambient temperature/ambient pressure.


A
P1040235_090619_001
B
P1040147_090615_001
C
P1030762_090520_001
D
P1030672_090519_001
E
F
P1030686_090519_001
G
P1040433_090714_001
H
P1040251_090619_001

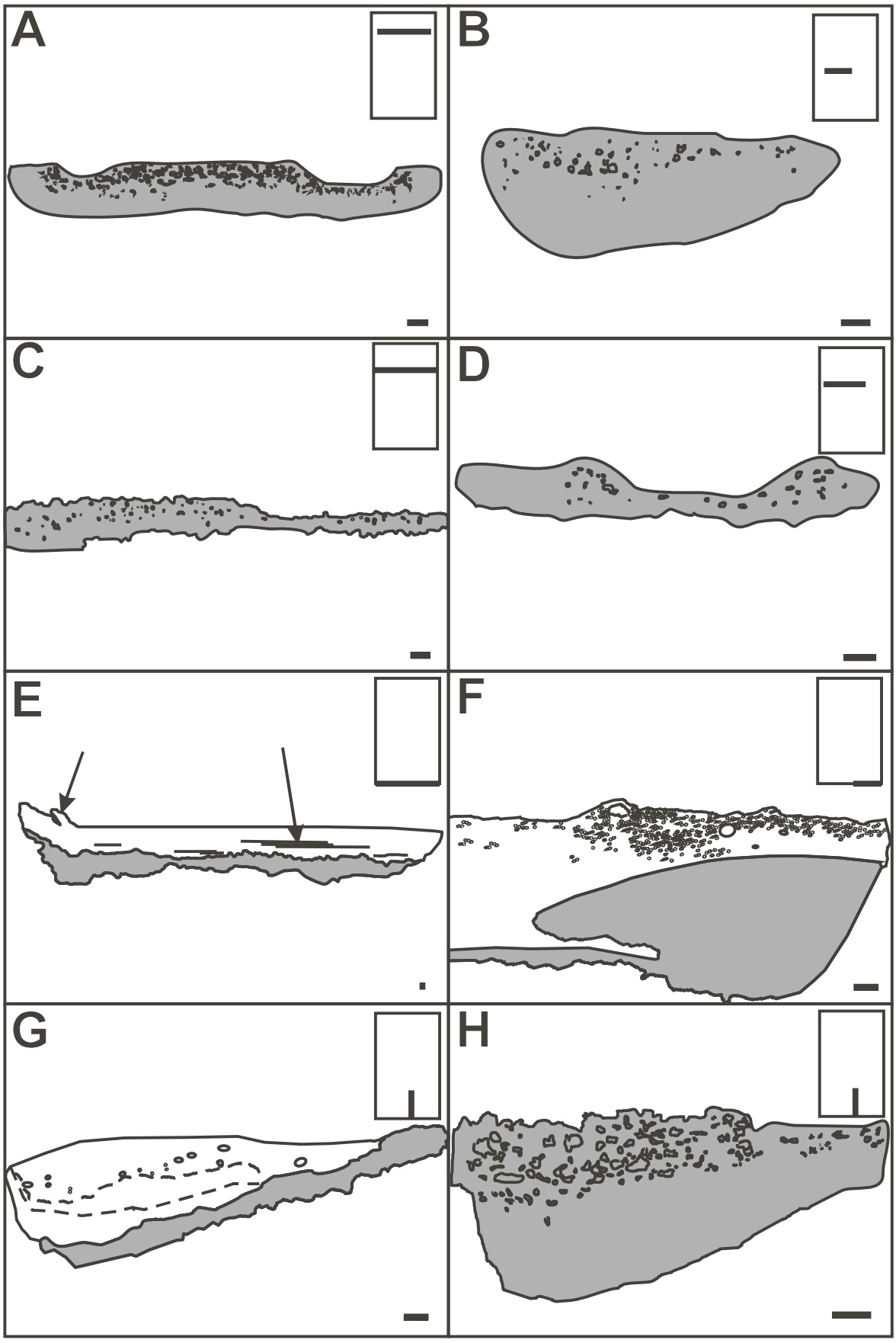

Caption over page...

Figure 8-6. Examples of frozen sediment lenses post-experiment.
Left: Photographs of observations post experiment, with the photo ID followed by the experiment ID in the bottom left of each photo. Right: Interpretive sketch from corresponding photo on left. A 1 cm scale bar is located in bottom right and the approximate plan-view position of the section is shown to the top-right of each frame. The top of the plan view insert is always the source. Grey shading represents frozen sediment-ice mix and no colour represents ice only. Some of the sketches have been rotated to more closely represent their in situ orientation.
A: Cross section through a fine sand icy-lens with two channels, where the ice is thicker for the deposits. Bubbles are concentrated at the top, but found throughout.
B: Cross section through a medium sand icy lens along a depositional lobe. Bubbles are located only in the top centimetre.
C: Cross section through a rock crush icy lens, showing weak channel in the middle, with bubbles located towards the top of the lens.
D: Cross section through a medium sand icy lens with single channel and flanking levees. The icy lens is thinner in the channel and bubbles are more frequent in the deposits.
E: Cross section of ponded water ice-wedge in rock crush, viewed end-on. Note the small amount of frozen sediment stuck to the base of the ice and the dry sediment beneath. Millimetre-scale layering can be seen in the exposed section, as indicated by the arrow on the right. The ice is extremely vesicular and almost hollow immediately behind this section. The arrow on the left shows where the section has been damaged post experiment.
F: Terminal ice-wedge deposit in medium sand, a cross section viewed end-on. The lobe of sediment within the ice corresponds in location to the end of a channel. Note the bubbles in the ice and the mm-scale laminations. The ice is extremely vesicular and almost hollow behind this section. The wedge is 8 cm thick at thickest point.
G: Ponded water ice-wedge in rock crush, longitudinal section. The right side of the frame is towards the source. Note the two distinct sections of solid ice at the base and the bubbly ice in the top centimetre, the boundaries marked with dashed lines.
H: Terminal ice-rich sediment wedge for fine sand in longitudinal section. The right side of the frame is towards the source. There is no pure ice, unlike E-G. The sediment has large bubbles in the top 1.5 cm. Watch strap is about 2 cm wide.

8.3.2. Observations: low temperature and low pressure experiments

8.3.2.1. All Sediment Types

For all sediment types the water was seen to exude gas bubbles (e.g. video 090619_001_out, Appendix E) and to form ice on introduction into the chamber, indicating simultaneous boiling and freezing. Observations of the sediment body after the experiments were completed confirm that water was able to percolate only a small depth into the bed before it froze, forming an icy-sediment lens over which the rest of the flow progressed (Figure 8-6). At the end of the experiment, the products of water flow – including any channels, levees, flow lobes and terminal deposits – could be lifted as a solid object from the tray, with the sediments underneath still being dry. Boiling resulted in the formation of bubbles within the top of the ice and the sediments, especially within material deposited by the flows. The bubbles also caused small crater-like cavities in the surface where they collapsed, or raised 'blisters' where they did not collapse. Bubbles within the sediment formed oblate cavities that were flattened horizontally. The erosional parts of the flow (for example Figure 8-6A and Figure 8-6D) had a thinner ice lens than the depositional parts of the flow. The ice lens was thickest where deposition was greatest – usually at the end of the tray. Layering defined by different ice-sediment ratios was observed in the terminal ice and sediment wedge (Figure 8-6E and Figure 8-6F). Sublimation of the ice was observed, as shown by: (i) millimetre depths of loose grains present on top of the ice lens at the end of the experiment and (ii) the extent of frost on the sides of the tray reducing over time. Where water collected at the end of the tray (e.g. video 090519_001_lhs, Appendix E), the resulting ice was extremely bubble-rich and opaque on top with an underlying translucent, bubble-free layer (Figure 8-6F and Figure 8-6G). This structure is similar to those described by Cheng and Lin (2007) and Bargery

(2008) in experiments performed with standing bodies of water at low temperature and low pressure.

Table 8-2. Summary of experimental results. Abbreviations in this table: [a] estimate, [b] weather station data, w:d – width to depth ratio, low P&T – low pressure and low temperature, low P – low pressure and ambient temperature, amb P&T – ambient pressure and temperature, amb – ambient temperature, n/a – not applicable, "-" – not measured, nc – no channel.

Experiment No.	Sediment type	Experiment Type	Flow duration (s)	Water temperature (°C)	Average pressure during experiment (mbar)	Temperature of sediment prior to experiment (°C)	Deposition volume (cm^3)	Erosion volume (cm^3)	Excess deposition (cm^3)	Excess deposition thickness over area of flow (mm)	Erosion rate ($gmin^{-1}$)	Time for flow to reach end (s)	Maximum w:d	Minimum w:d	Average w:d	Channel length (cm)	w:d at 30 cm
090515_001	fine sand	low P&T	40	5[a]	6.4	-22.3	2255	-803	1452	4.5	1863	6	12	2	5.1	80	5.6
090520_002	fine sand	low P&T	30	5[a]	7.3	-17.8	916	-558	358	1.3	1726	15	14	2.7	6.7	60	1.1
090619_001	fine sand	low P&T	30	0.5	6.8	-23.7	1616	-477	1139	4.2	1477	11	10	3.1	5.4	80	8.3
090519_001	med sand	low P&T	25	5[a]	8	-26.7	2584	-729	1855	8.6	2777	7	20	6	12	40	17
090615_001	med sand	low P&T	30	10	7.7	-23.3	1549	-895	654	2.4	2841	11	55	2.5	14	60	28
090710_001	med sand	low P&T	30	0.7	7.4	-22.5	1680	-414	1265	5.9	1315	11	10	1.4	4.1	40	3
090612_001	rock crush	low P&T	30	5	6.1	-22.7	1922	-169	1753	3.4	511	12	nc	nc	nc	nc	nc
090520_001	rock crush	low P&T	31	5[a]	8.3	-22.5	2051	-301	1749	3.6	882	18	nc	nc	nc	nc	nc
090714_001	rock crush	low P&T	30	0.5	5.6	-23	2896	-39	2858	5.9	117	20	nc	nc	nc	nc	nc
090512_001	fine sand	low P	30	amb	9.7	19.7	1242	-784	459	2.1	2424	14	20	17	18	40	-
090511_002	med sand	low P	30	amb	11.7	18.6	444	-415	29	0.2	1319	21	-	-	-	-	-
090514_001	rock crush	low P	30	amb	11.7	19.6	719	-271	447	1.1	821	30	nc	nc	nc	nc	nc
090715_001	fine sand	amb P&T	30	amb	1017[b]	25	325	-316	8	0.1	979	21	23	5	11	60	23
090716_001	med sand	amb P&T	30	amb	1017	23	356	-275	81	3	873	n/a	50	10	24	30	50
090902_002	med sand	amb P&T	30	amb	1008	19.3	271	-450	-179	-3.3	1427	n/a	6.5	6.5	6.5	10	nc
090902_001	rock crush	amb P&T	30	amb	1008	19.3	242	-295	-53	-0.1	892	n/a	33	8.3	18	30	33

8.3.2.2. Fine and Medium Sand

The icy-sediment lens formed at the base of the flow was up to 3.5 cm thick for both sand types (Figure 8-6A, Figure 8-6B, and Figure 8-6D) and there were more bubbles formed within the sediments and at the surface (Figure 8-5) than in experiments performed with the rock crush. The fine sand had the most bubbles (Figure 8-5 and Figure 8-6A) and showed abundant pitting and blisters. The bubbles ranged in size from 1 - 5 mm, although they seemed to be smaller in general in the medium sand. Both sand types formed depositional levees and terminal flow lobes, and often displayed distinct channel(s) in the erosional regime. These features caused the ice lens to range in thickness from 0.5 - 3.5 cm within the test bed. The channels and levees were linear rather than sinuous (Figure 8-5). The fine sand was observed to form more small lobes than the medium sand. The initial flow seemed to be pulsing, but once the flow settled, it concentrated in one or two paths and did not avulse for the rest of the experiment. The sands formed a depositional fan at the end of the flow, which was sometimes covered by subsequent ponded ice (Figure 8-6F). For the ~ 0.5 ºC water runs the fans were rougher and formed a cone of icy slush. In these experiments almost no water ponded at the end (Figure 8-6H). Runs that used the warmer 5 ºC water often showed ponding of water at the end of the test bed that resulted in a wedge of ice. The top 1 - 2 cm of this wedge was filled with bubbles (Figure 8-6F). Flows in both sands took 6 - 11 s to reach the end of the tray (i.e. flow speeds of ~ 0.1 - 0.2 ms^{-1};Table 8-2). The icy wedges at the end of the flow had dry sediment underneath, showing that the flow had not penetrated to the base of the tray.

8.3.2.3. Rock Crush

The icy sediment lens at the base of the flow was thinner (0.5 - 1.0 cm) and more uniform for the rock crush (Figure 8-6C) than for either of the sands. The flow began as digitate in form, but developed into sheet flow, rather than channelized flow as it did for the sand

beds (e.g. video 090612_001_out, Appendix E). On one occasion, small but detectable channels and fans did form (Figure 8-5, 090520_001), but these were within the sheet-like flow. It is notable that the depositional fan in this case was entirely composed of the finer material; coarser material was not transported. Close observation revealed that the flow front progressed by travelling around the larger clasts, before inundating them as the flow matured. In cross section, the icy sediment lens contained a concentration of coarser clasts at the top, indicating the surface had been washed free of fines. Bubbles were not observed breaking the surface in the rock crush, but were observed in the ice lens (Figure 8-6C) and ice wedge deposits at the end of the tray (Figure 8-6G). These bubbles were much smaller (≤ 1 mm) than those observed in the sands. Water was observed to pond at the end of the tray irrespective of the initial water temperature. The ice wedge which then formed at the end of the tray penetrated though the sediment to the base of the tray, except when the water was cooled to ~ 0.5 ºC, when 1 - 2 cm of dry sediment was left underneath. The time taken for the flow to reach the end of the tray was 12 - 20 s, longer than for the sands, with the lower temperature water showing the slowest speed (Table 8-2).

8.3.3. Observations: control experiments performed at 1) Earth ambient conditions and 2) Mars pressure but room temperature

8.3.3.1. All Sediment Types

The water was able to infiltrate into the sediments for all the experiments. There were therefore some obvious differences from the experiments performed at low temperature and pressure:

(i) flows were slower to progress downslope for a given sediment type (Table 8-2).

(ii) there was no ponding of water at the end of the tray.

(iii) wet haloes of sediment formed around the flows, extending downwards as well as sideways (Figure 8-7).

(iv) the flows did not cover such a large spatial area (Figure 8-5).

This suggests that wetting, infiltration and subsurface flow dominated the flow regime for each of these experiments.

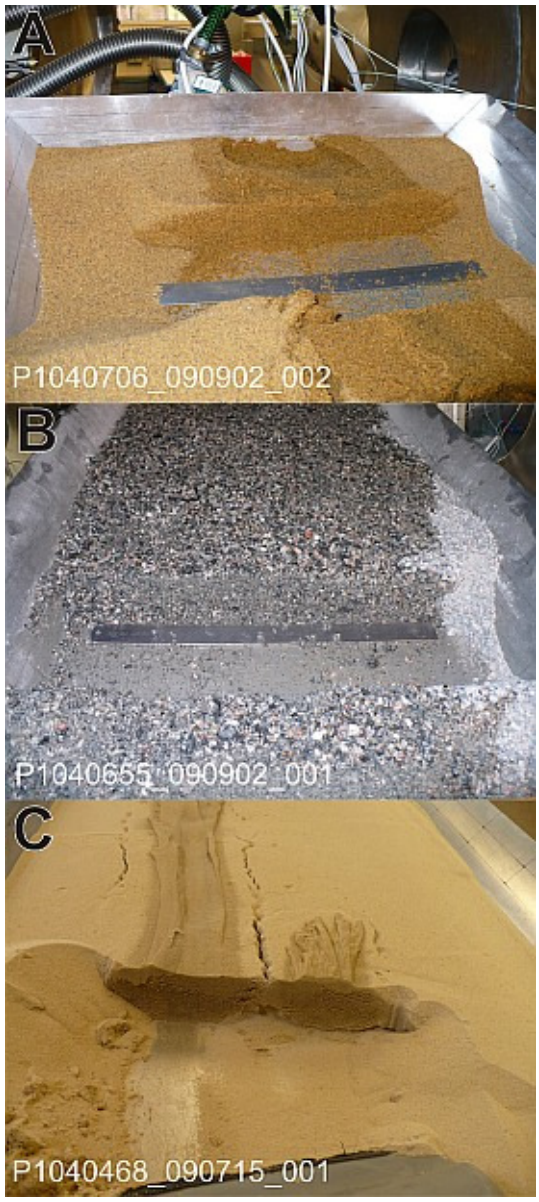

Figure 8-7. Wetted areas for the three sediment types under ambient temperature/ambient pressure with the photo ID followed by the experiment ID in the bottom left of each photo. A: medium sand showing 1-2cm infiltration halo on the surface and wider halo sub-surface, making an oval shape in cross section. Water has percolated to the end of the tray. B: rock crush showing wide wetted area from flow and vertical boundary between wet and dry. C: fine sand showing narrow percolation halo at the surface and wider percolation halo underneath, giving an oval cross section. Cracks in the surface of the sand indicate the lateral extent of the wetted area beneath the flow. Lobe to the left is ~15cm wide at widest point.

8.3.3.2. Fine and Medium Sand

The flows for both sands were notably slower to reach the end of the tray during the ambient temperature and pressure experiments than for the martian analogue experiments.

None of the flows on the medium sand substrates reached the end of the tray. During the ambient temperature/low pressure experiment both flows progressed slightly slower than for the low temperature and pressure (Table 8-2). The flows covered the narrowest planimetric area in the ambient temperature and pressure experiment and were slightly wider for the ambient temperature/low pressure experiment, but not as wide as for the low temperature and low pressure experiments (Figure 8-5). The water during and after flow percolated horizontally by ~ 5 cm for the medium sand and ~ 2 cm for the fine sand at the surface. Beneath the surface, the flows percolated horizontally ~ 10 cm for the medium sand and ~ 5 cm for the fine sand. The water percolated downwards all the way to the base of the tray beneath both flows, and the wetted area in cross-section was a flattened oblate shape (Figure 8-7A and Figure 8-7C). During the ambient temperature/low pressure experiment both sands contained bubbles and had surface blisters (e.g. see formation of blister at 63 s in video 090512_001_lhs, Appendix E). The bubbles and blisters were present in the percolation halo as well as along the flow path. There were fewer bubbles observed in both sands at room temperature/low pressure than observed for low temperature and pressure experiments, although this could have been caused by poor preservation due to the lack of freezing.

8.3.3.3. Rock Crush

The flows on the rock crush substrate progressed much more slowly for both the ambient temperature experiments than they did for the cold runs (Table 8-2). For the ambient temperature and pressure experiment the flow did not reach the end of the test bed. The flow still formed a broad sheet in both cases, but was more channelized in the uppermost portion than for the low temperature/low pressure experiments. In contrast to the low temperature/low pressure experiments, the flow spread out in a large lobe and was not initially digitate. Infiltration in both cases resulted in the water penetrating to the base of the tray under the flow lobe. The water did not percolate as far sideways as it did for the

sands (the maximum was ~ 1 cm) and the wetted area had almost vertical sides in cross section (Figure 8-7B). The sediment surface was observed to bubble during the ambient temperature/low pressure experiments (e.g. video 090514_001_lhs, Appendix E), but no bubbles were preserved within the rock crush – again, probably because there was no ice to preserve them.

8.4. Data analysis

8.4.1. Volume calculation

The x, y and z coordinates from the measured cross profiles were interpolated into a gridded surface using the Kriging method in the *Surfer 8* software. This method has provision to allow for anisotropy in data collection (a greater density of sampling was used post-experiment in some cases). A 1 cm grid size was chosen as appropriate for the wavelength of changes observed and applied to all the surfaces. To calculate the volume of erosion and deposition for each experiment the pre-experiment surface was subtracted from the post-experiment surface. The results for the overall volumes are given in Table 8-2 and the spatial results are mapped in Figure 8-8.

The deposition volumes are much larger than the erosion volumes for low temperature/low pressure experiments. Most of the additional volume can be accounted for by the ponded water at the base of the flow, and by large cavities that formed in the ice wedge as a result of boiling. Within the bounds of error (± 1 mm in height measurements) the erosion and deposition balance out for the ambient temperature/ambient pressure experiments. The data show consistent excess in deposition volume for ambient temperature/low pressure experiments, this may represent an increase in volume through incorporated gas, although I note that these values are comparable to the estimated measurement error.

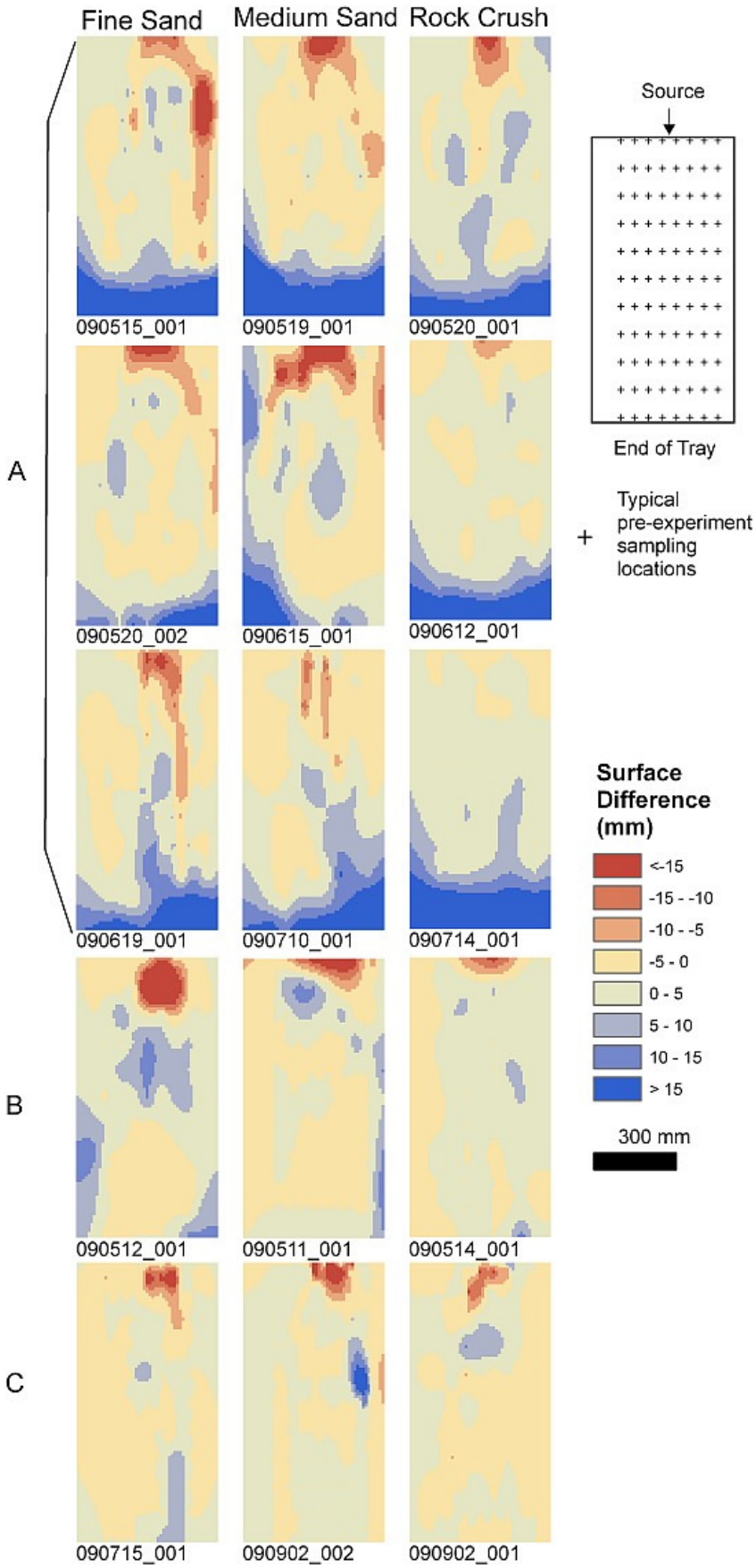

Figure 8-8. Matrix of isopach maps for each experiment , each column vertically is a different sediment type and each row represents different ambient experiment conditions, with A being low temperature/low pressure, B ambient temperature/low pressure and C ambient temperature/ambient pressure. Top-right line diagram shows typical arrangement of measured points, pre-experiment. After the experiment more measurements were taken around areas of greatest change.

Because the deposition data include additional ice, water and gas, I used the erosion volume to estimate the volume of sediment transported. From this I generated an erosion rate, based on my estimated bulk density for each material and the duration of the flow. For all the experiments this erosion rate was between 100 and 3000 $gmin^{-1}$. In general the rock crush shows much lower erosion rates than either of the sands. For the low temperature/low pressure experiments, all sediment types had higher erosion rates when using the warmer water. However, the patterns of erosion rates for the different experiments varied between each sediment type: (1) all the experiments for medium sand had similar erosion rates, apart from the low temperature/low pressure experiments with warmer water temperature, which had higher erosion rates, (2) for the fine sand, the ambient temperature/low pressure experiment had the highest erosion rate and the ambient temperature/ambient pressure the lowest erosion rate and, (3) For rock crush the erosion rate was lowest for the low temperature/low pressure with colder water, and all the other experiments have higher and very similar erosion rates.

8.4.2. Width to depth ratio of channels

The channel width to depth ratio is a function of the discharge and entrainment capacity of the flow (Chorley et al., 1984) - the lower the width to depth ratio, the more effective the channel erosion. The width to depth ratio was calculated for each cross section where a channel was present. For each experiment I measured the mean maximum and minimum width to depth ratio of all the cross sections. I also recorded the channel width to depth ratio at 30 cm from the top of the test bed for each experiment where there was a channel at this distance (Table 8-2). When more than one channel was present I summed the widths and depths and calculated an aggregate width to depth ratio for that cross section.

The width to depth ratio was generally higher for medium sand than for fine, i.e. channels in the fine sand were usually deeper for a given width. The rock crush

experiments had a much higher width to depth ratio than either of the sands (where it was measureable) although most rock crush experiments did not form channels.

8.5. Discussion

8.5.1. Transport dynamics - temperature

Erosion rates were not substantially different between the sub-freezing experiments and those performed at ambient temperature. However the formation of an ice lens at the base of the flow retarded infiltration, leading to more surface flow and therefore faster downslope flow propagation. I infer the lack of infiltration from the presence of dry sediments beneath the ice lens and from the pooling of excess water at the end of the tray. Infiltration experiments performed on soils under ambient terrestrial pressure conditions by McCauley et al. (2002) showed a similar decrease in infiltration rate for freezing soils. I infer that if my test bed had been longer, the flows under freezing conditions would have had a significantly greater runout distance than those under ambient temperatures. Freezing temperatures therefore have a fundamental affect on the behaviour of the flow, if not on the actual erosion rate. This is an important conclusion for estimates of liquid volumes and flow rates applied to martian gullies, as discussed in Section 8.5.4. I also note that solid ice particles were sometimes included in the flow for the cold water. I therefore suggest that ice formation during transport may retard flow for very cold substrates, in opposition to the reduced infiltration effect.

It would be expected that the formation of a basal icy lens would retard erosion as it turns a cohesionless substrate into one with cohesion. This was not the case in my experiments, because mechanical erosion is not the only active process. I observed that the warmer, 5 °C water onto the cold substrate caused more erosion than the colder water at ~ 0.5 °C. This observation, combined with the substantial erosion observed within a basal ice lens, leads me to infer that thermal erosion of ice within the substrate is a significant

erosion process. This finding is supported by the experimental and numerical modelling results of Costard et al. (1999) and Randriamazaoro et al. (2007), who also found decreased thermal erosion rate with colder water.

8.5.2. Transport dynamics - pressure

Our experimental data suggest that pressure is not as important as temperature for controlling the gross behaviour of the flows. However, the flow propagation speed was greater at low pressure than at ambient pressure. For example, the flows in the experiments performed with medium sand propagated to the end of the tray at ambient temperature/low pressure but only propagated to ~ 30 cm under ambient temperature/ambient pressure. The effect is less marked but still apparent for the rock crush and the fine sand. A possible explanation for enhanced flow at low pressure is that the formation of bubbles within the sediment inhibits infiltration as the water boils. This effect was noted by Prunty and Bell (2007) who found unexpectedly low infiltration rates in their low-pressure infiltration experiments. Another possible explanation might be that small bubbles in the flow caused the flow to be more buoyant, again reducing infiltration and decreasing the effective viscosity.

8.5.3. Transport dynamics – sediment type

The physical properties of the sediment affect the ability of a given flow to erode and to form channels, and therefore affect the speed of flow propagation. Two processes control these three parameters: (1) entrainment capacity, which depends on modal grainsize and flow dynamics, and (2) infiltration, which is controlled by permeability, and thus grainsize distribution.

Entrainment is controlled by the shear stress developed at the base of the flow, τ_0, defined by:

$$\tau_0 = \gamma_w R S_b \quad (8\text{-}1)$$

where γ_w is the specific weight of water (Nm^{-3}), R is the hydraulic radius, given by the ratio of channel cross sectional area to wetted perimeter and S_b is the slope of the bed (Simon and Castro, 2003). For a given particle diameter, D, the critical shear stress at the base of the flow is given by the Shields stress, τ_c, defined as:

$$\tau_c = \tau^* (\rho_s - \rho_w) g D \quad (8\text{-}2)$$

where τ^* is the critical dimensionless shear stress, ρs and ρ_w are the density of the sediment and the water respectively, and g is the acceleration due to gravity.

The sands have a lower modal grainsize, D, than the rock crush, so using Equation 8-2 they require a lower basal shear (τ_c) for optimally sized particles to be entrained. This explains why in my experiments using medium or fine sand, more erosion occurred and deeper, longer channels were developed than in experiments that used rock crush.

Sub-freezing experiments cause the flow dynamics to change, but I find the modal grainsize is still important. From Equations 8-1 and 8-2 the stress developed at the base of the flow depends on hydraulic radius, which is a standard proxy for flow depth (Simon and Castro, 2003). As described in Section 8.5.1, with the substrate at sub-freezing temperatures an ice lens formed which retarded infiltration. This meant that less water soaked into the sediment and more water was available at the surface, allowing the flow to build a greater water depth and speed. In addition channel formation confined the flow laterally which can also act to increase the flow depth. Although I cannot test this using my results, the formation of an ice lens might therefore enable larger grainsizes to be entrained. This would then create a positive feedback mechanism by which enhanced erosion leads to channel formation and thus larger particles are entrained than in flows without a freezing base. In essence, the presence of a sub-freezing substrate and water with the potential for thermal erosion leads to enhanced channel formation and therefore enhanced downcutting.

The permeability of the bed also plays a role in this process. The permeability of sediments controls the infiltration rate and is dependent on grainsize distribution. The flow propagates faster if infiltration is low, as more water is available at the surface. This is illustrated in the results from the two sand types: the fine sand has the fastest propagation speed and the lowest permeability. Interestingly, although the rock crush has even lower permeability and I would therefore expect the fastest propagation speed, this is not the case. Instead the propagation speed in the rock-crush is generally slower than for either sand. I observed that the flow removed the fines, leaving the larger grains from the rock crush material. These larger clasts could not be entrained, and instead formed roughness elements that retarded the flow and inhibited flow propagation.

I also find that the intrinsic permeability of the material becomes less important to propagation speed under sub-freezing conditions, as illustrated by the very similar flow speeds for both sand types under these conditions. However, the effect of permeability is not negligible: the rock crush has the lowest permeability and I observed that it formed the thinnest ice lens, and had the most ponding at the end of the tray (shown by large excess deposition in Table 8-2 and a thick terminal ice wedge in Figure 8-5 and Figure 8-6). A thin ice lens indicates that less water has been taken up by freezing, and the ponding implies a greater runout distance. I suggest that if it were not for the larger-sized component of the rock crush the flow propagation would be faster than for either sand.

8.5.4. Implications for martian gully formation - modelling

I now consider the two main models for gully formation: the aquifer outburst model (e.g. Malin and Edgett, 2000) in which water is sourced from either a deep or shallow underground source, and the surface melting model, (e.g. Costard et al., 2002) in which surface or ground ice melts to form runoff or debris flows.

The experiments do not attempt to simulate the processes that define the source of the water, either by releasing the water from underground, or by initiating melting of

surface ice/snow. The scale of our experiment is too small to encapsulate water sourcing processes, as well as erosion, transport and deposition in gullies. However, my experiments do provide useful information of what affect the water has (once produced) on transporting cold, dry, unconsolidated sediments. There was no intent within the design of the experiments to simulate debris flow or alluvial processes. The experiments themselves have several important similarities to debris flows, including lateral levees and depositional lobes. However, it is impossible to link these small-scale turbulent flows directly to the much larger-scale gullies on Mars and thus also impossible from these experiments to give an indication as to whether gullies on Mars are formed by alluvial or debris flow processes. It is important to note that the processes by which the gullies are formed and the process by which water is generated are not necessarily linked.

I suggest that the martian surface is likely to be colder than the freezing point of water in most cases. Even when insolation is strong, only the uppermost parts of the regolith will be warmed and just below the surface the ground will be cold. Thus any water that flows over martian ground will – at least initially as the flow front wets dry ground – probably undergo basal freezing. Water sourced from an aquifer (Malin and Edgett, 2000; Heldmann et al., 2007) is likely to have elevated temperatures compared to the surface and is therefore likely to generate flows with a high potential for thermal erosion. Thus as the flow evolves, newly formed basal ice could be remelted and erosion could be enhanced.

However, water sourced from an aquifer might also have a high dissolved salt content (Knauth and Burt, 2002). In this case the liquid might have a depressed freezing point (e.g. Chevrier and Altheide, 2008), perhaps even being a stable liquid and resisting freezing, and thus flow might be more similar to terrestrial processes, or to my low pressure, room temperature experiments. If this brine flow encountered an icy substrate, though, I would still expect my observations on thermal erosion and retarded infiltration to apply. In fact, as shown by Andersland et al. (1996) liquids (including brines and

antifreezes) with a freezing point depression temperature that is lower than that of the ice temperature can significantly increase the rate of thermal erosion of that ice.

Water formed by melt of near surface ice (e.g. Costard et al., 2002) would be close to the freezing point of that ice. Thermal erosion might in this case be less important and the effects of freezing would be enhanced. It is likely that water so close to its freezing point could transport substantial amounts of ice, as seen in my experiments, which could then form an ice-rich debris flow. This could also be the case for the aquifer model, but might occur further downslope, when sufficient thermal energy had been lost to the substrate. Possible implications of the inclusion of significant ice in the flow include: (1) dividing flow paths as the buoyant ice-clasts formed dams, (2) flow mechanics more similar to debris flow or slush flow than flow of pure water, and (3) morphological signatures of post depositional volume loss by sublimation. Kochel and Trop (2007) report debris flows containing ice blocks in Alaska which resemble classic debris flows. It is likely that significant amounts of ice would be present in the levees and other deposits in gullies on Mars. If an impact were to occur on the surface of a recent flow deposit then current technology would allow the detection of this water, e.g., the HiRISE camera has been able to detect ice at the base of impact craters in the northern lowlands (Byrne et al., 2009). Estimates of how long ice under sediment would persist under current martian climate are poorly constrained and have a large range (between 10 hours and 1300 years) and much more experimental work is needed (Chevrier et al., 2007; Bryson et al., 2008; Williams et al., 2008).

8.5.5. Implications for martian gully formation – flow rates

The flow rate I used for my simulations (0.08 ls^{-1}) is much lower than flow rates measured in gullies on Earth. Despite these low flow rates, the measured erosion rates are comparable to gullies on Earth, if they are normalised by area ($1.56x10^{-4}$ – $3.58x10^{-3}$ m/min). For example, Xiao et al. (2005) measured erosion rates from 3 x 1.5 m

experimental boxes of loess with induced rainfall on slopes of 35°. Rates of 0.1 - 2 $kgmin^{-1}$ (~ $2.2x10^{-5}$ - $4.4x10^{-4}$ m/min) were found at flow rates of 114 - 258 ls^{-1}. Piest et al. (1975) measured erosion rates in gullies ~ 200 m long and ~ 13 m wide in the loess area of Iowa. They found rates of 707 $kgmin^{-1}$ (~ $2.72x10^{-4}$ m/min) at a peak flow rate of 892 ls^{-1}. The reason my erosion rates are similar to those for higher flow rate experiments and measured values from gullies is probably due to the effects of vegetation and clay-rich cohesive soils in gullies on Earth. These effects were not taken into account in my experiments and are not applicable to Mars: there is no vegetation, and although clays have been reported on Mars (Poulet et al., 2005; Mustard et al., 2008), they are not widespread, so flows of equivalent magnitude on Mars are likely to be more erosive than those in terrestrial gullies.

Some flow rate estimates have been made for gullies on Mars, for example, Heldmann et al. (2005) estimate 30,000 ls^{-1} for a generic gully and Hart et al. (2009) estimate 750 - 83,000 ls^{-1} for bankfull discharge from gully measurements at Lyot crater. These are far in excess both of gully flow rates on Earth and the flow rate I used in my experiments. Heldmann et al. (2005) invoke these large flow rates to compensate for evaporative losses and to explain the formation of deep wide channels in single events. Hart et al. (2009) generated large discharges to fulfil their assumption of bankfull discharge. However, this is not a necessary condition, for bankfull discharge is rarely achieved in river systems on Earth, nor in mature gully systems (Torri et al., 2006). My experiments show that on short timescales evaporative losses are not important, because sufficient water remains in the system to erode, transport, deposit and freeze, without noticeable visual losses. It is apparent that the thermal enhancement of erosion and reduced infiltration with basal freezing, which increases propagation speed, is more than sufficient to compensate for evaporative losses. My experimental results thus suggest that large discharges are unnecessary to produce the runout distance and erosion needed to create gullies on Mars.

Fluid loss is an important parameter used in the modelling of gullies on Mars and has a great influence on the runout distance and morphology of the resulting flow (Pelletier et al., 2008). My work shows that under sub-freezing conditions there is some fluid loss through freezing, but it also shows that fluid loss is reduced through the inhibition of infiltration. It is likely that existing models (Heldmann et al., 2005; Pelletier et al., 2008) have greatly over-estimated this type of fluid loss. Further work is required to accurately define the quantitative limits of the fluid loss term under martian temperature and pressure for use in modelling studies.

8.5.6. Implications for martian gully formation – general predictions

Our experiments point to potential observations that could be made to test whether gullies on Mars are formed by metastable water. The inclusion of gas bubbles within the flow and especially within its deposits could be tested by measurement of the volumes of gully deposits on Mars using high resolution Digital Elevation Models (e.g. Kirk et al., 2008). If deposition volume is found to significantly exceed erosion volumes, this would suggest that ice or voids are present in the deposits. The decrease in density and increase in roughness introduced by the bubbles and sublimating ice clasts might also be detectable through thermal inertia data derived from a future high resolution thermal camera. Although I cannot apply my morphometric findings at a landscape scale, my results do suggest that the temperature and pressure environment on Mars would significantly change the morphology of any channels formed. I would therefore expect channels formed on Mars to resemble channels formed in cold arid climates on Earth, rather than those formed in more temperate locations.

8.6. Conclusions

I find that metastable liquid water under present martian conditions is able to erode similar amounts of material as stable water under above-freezing terrestrial conditions. For liquid

water at ~ 5 °C introduced into the martian environment, erosion and channel formation are higher than on Earth, and for water at ~ 0.5 °C, the erosion rate is similar to that found at Earth ambient temperature and pressure.

Sub-freezing bed temperatures cause the base of the flow to become armoured with ice, which inhibits infiltration. This promotes build-up of a greater fluid flow depth, which (i) increases the erosion rate, (ii) increases the modal grainsize which the flow is able to entrain, and (iii) increases the flow propagation speed and runout distance.

Both sub-freezing temperatures and low pressures retard infiltration into the sediment. Infiltration contributes to the "fluid loss" parameter used in modelling gullies on Mars that I suggest has previously been over-estimated. I find that intrinsic sediment permeability is less important in defining infiltration rates under sub-freezing conditions, but still acts to increase runout distance. These findings could be applied to either the commonly used aquifer or surface melting models.

Experiments revealed that flow propagation is faster under low pressure/ambient temperature than at ambient pressure/ambient temperature. I suggest that this is mainly due to gas bubbles impeding liquid infiltration. Other possible factors include promoting buoyancy in the flow, or decreasing effective viscosity. Considering my findings of faster propagation and greater erosion rate under low temperature and low pressure, I conclude that large discharges invoked by previous workers are not required to form the gullies seen on Mars.

I suggest that the low temperature and pressure martian environment will produce unique sedimentary features associated with gullies. These include: (i) an icy substrate lens, thicker in the depositional regions than the erosional regions (ii) bubbles within frozen sediment near the surface, especially in levees and deposits, and (iii) icy clasts deposited in the levees and terminal flow lobe deposits which, as the landform evolves, will result in sublimation lags or downwasting features such as pits. These deposits may be

detected by searching for low density and high roughness signatures in high resolution thermal inertia data, and by examining high resolution digital elevation models to look for deposition volumes that are greater than erosional volumes.

Chapter 9. Synthesis

9.1. Are debris flows on Earth a good analogue for gullies on Mars?

Previous studies have found that debris flows on Earth have visual similarities with gullies on Mars (e.g. Hartmann et al., 2003; Costard et al., 2007). I have found that debris flows in Iceland have a wide range of morphologies and settings, which encompass most of the variation observed in gullies on Mars. Most terrestrial debris flows are triggered by rainfall (Section 3.3), which is not a plausible mechanism for triggering on Mars (Carr and Head, 2010). However, in Iceland many debris flows are triggered by surface snowmelt (Decaulne and Sæmundsson, 2007). This mechanism is perhaps more applicable to Mars, and is similar to the surface melting model suggested by Costard et al. (2002). Debris flows triggered by snowmelt and rainfall are morphologically identical (Decaulne and Sæmundsson, 2007). This observation means that we can compare almost any debris flow on Earth to gullies on Mars without concern for exactly how the debris flow was triggered. In addition, my observations of debris flows in Iceland suggest that debris flows that are unconfined for most of their length are the most suitable analogue to gullies on Mars (Sections 4.5.1 and 4.7.6).

9.2. What are the signatures of debris flow on Earth?

On Earth, debris flows are recognised in field observations by features such as the presence of levees (Section 3.2). Although these types of observation are possible on Mars with the aid of a rover, this form of study is not currently available for any martian gully locations. Remotely sensed data has to be relied on, either in the form of images or elevation data.

The best data to date are from the HiRISE instrument and comprise images at 25 cm/pix and stereo-derived DEMS of 1 m/pix. Only rare observations of levees have been made using HiRISE images, perhaps because images of gullies are generally acquired at 15:15 (±1.15hr) local time, so incident light is unlikely to be at the best angle to highlight levees (Section 4.7.6). Elevation data do not suffer from this bias and have been used extensively on Earth to study the link between landscape form and process (Section 3.5). Landscape properties have been linked to process in a few studies on Earth (e.g. Montgomery and Foufoula-Georgiou, 1993), but usually as a by-product of another project. Using remote-sensed measurements of landforms to determine process is not often required on Earth, where *in-situ* observations and measurements are more reliable.

Using terrestrial sites with different dominant processes, but visual similarities to martian gullies, I have confirmed and added detail to these pre-existing process domains in both full-topography and long profile studies (Sections 7.7.1 and 7.7.2). I have demonstrated that elevation data can be used to morphologically discriminate between debris flow gullies, alluvial gullies and slopes dominated by dry mass wasting processes (Section 7.7).

By studying debris flows near Ísafjörður, I have found that the morphology of debris flows at a smaller scale can be used as a predictive tool (Chapter 4). At this scale (1 m/pix) debris flows are morphologically distinctive in terms of their patterns of erosion and deposition (Section 4.5.5). I have found that these patterns are intimately linked with the runout distance of unconfined debris flows (Section 4.6.2). I have also demonstrated that this link can be used to assess the hazard posed by unconfined debris flows to people and infrastructure (Section 4.7.5; Conway et al., 2010c). This is one of very few hazard assessments performed for areas affected by unconfined debris flows. The model that I have developed is both simple, because it does not require full flow dynamics modelling, and able to take into account local conditions. Use of this technique in other geographical

locations is required before my supposition that the viscosity of the debris flow is one of the principal factors controlling the patterns of erosion and deposition can be fully demonstrated. Moreover, if the necessary quality of elevation data were available on Mars, this type of analysis would be able to confirm the presence or absence of debris flows.

9.3. Are there debris flows on Mars?

I have presented the first systematic studies of long profiles and slope-area analyses for gullies on Mars (Chapters 6 and 7). The long profile analysis highlights the merits of simple methods for extracting elevation data quickly, easily and effectively over large areas. The slope-area analysis demonstrates the possibility and importance of employing tools already used in the study of terrestrial landform analysis to elevation data of Mars.

I applied the process domains, calibrated using terrestrial analogues, to gullies on Mars, and I found a substantial overlap in morphology (in long profiles and slope-area plots) between gullies on Mars and unconfined debris flows in NW Iceland and the Colorado Front Range (Sections 6.4.1 and 7.5.3). These analyses strongly indicate that debris flow is an important process in forming gullies on Mars and that gullies have a detectable and important impact on the geomorphology of slopes on Mars.

In addition, the morphology of gullies on Mars has similarities to the morphology of alluvial gully systems in arid environments on Earth (Death Valley and San Jacinto, California – Section 6.4.1). This has shown that the action of pure water flow on the surface cannot be ruled out on Mars. Comparisons to slopes without gullies, or with dry mass wasting, have shown that dry mass wasting alone cannot be responsible for all martian gullies, although it is apparently a dominant process in some cases (Sections 6.4.1 and 7.5.3).

9.4. Can gullies form on Mars today?

My experiments have confirmed that water can perform significant geomorphical work even if it is metastable, i.e. subject to boiling and freezing (Chapter 8). These are the

conditions that liquid water would experience on the surface of present-day Mars, if melted from surface ice (e.g., Hecht, 2002), or erupted from an aquifer (e.g., Heldmann and Mellon, 2004). The experiments that I performed revealed that the low temperatures on Mars would be the dominant control over flow dynamics (Sections 8.5.1 and 8.5.2). Freezing at the base of the flow results in reduced infiltration, high flow speed and hence longer runout distance than equivalent-volume flows on Earth (Section 8.5.1). This basal freezing, however, does not impede erosion (Section 8.3.2). These results suggest that additional water is not required to combat the action of freezing and boiling for short timescale events, but that similar scale landforms should require very similar quantities of water, whether formed under sub-freezing and dry, or warm and wet conditions.

9.5. Models of gully formation

Many authors have found inconsistencies that argue against the aquifer model as a plausible formation mechanism (see Section 2.5 for summary). My study highlights some additional arguments against the aquifer hypothesis. Although debris flows above Ísafjörður are triggered by undercutting of sediment by near surface groundwater (Section 4.3), these sediments need to be saturated, which is achieved by snowmelt or rainfall. Springs on their own do not cause debris flows: observations of springs on steep hill slopes in other locations in Iceland (Section 4.5.1) confirmed that they usually have only a small, negative-relief, channel-forming topographic effect. This suggests that if debris flow is indeed the dominant formation mechanism of gullies on Mars, then an aquifer formation model is not realistic. Further, as described in Section 7.7.5, study of the morphology of gullies on Mars reveals that the location of the channel heads and the form of the alcoves are more consistent with a distributed source for the gully-forming water. This is incompatible with a spring-like source. Further, because geologically-recent precipitation is very unlikely on Mars (Carr and Head, 2010), a recent distributed source of water can

only be explained by the melting of "snow", or other near-surface ice on Mars. Snowmelt in Iceland is able to trigger debris flows, as well as form pure water flows.

Although many aquifer models require the correct climatic conditions to initiate the melting of an icy plug to release the water, the patterns in gully distribution and orientation would be expected to reflect both the aquifer distribution and climatic signal. Previous studies have found only a climatic signal (see Section 2.5 for a summary) and my research supports this. Analysis of gully long profiles in Chapter 6 showed that pole-facing gullies tend to be better developed than equator-facing ones, which suggests a climatic influence. In addition, slope-area analysis in Chapter 7 confirms a difference in process with aspect, indicative of a climatic process, with gullies being found on pole-facing slopes and equator-facing slopes being dominated by mass wasting and possibly solifluction.

9.6. Implications for martian climate

My geomorphological analysis provides strong evidence that gullies on Mars are formed by wet, as opposed to dry processes. The predominance of debris flow as a process for forming martian gullies means that a small but significant, amount of water is needed to form gullies. I have demonstrated that the amount of water required is almost certainly less than already published estimates, which give discharges of 750 - 83,000 ls^{-1} (Section 8.8.5). My laboratory work has shown that once melting is achieved, small amounts of water can do significant amounts of geomorphic work, despite being only metastable (Section 8.3).

Performing some simple calculations based on my research gives an indication of how much water is likely to be required. Debris flows near Ísafjörður are small-to-medium debris flows, but are smaller than an average martian gully. The largest terrestrial debris flow that I measured in Chapter 4 had a volume of ~ 8000 m^3, coming from a source area of ~ 4500 m^2, hence the average thickness of the material that failed was ~ 1.7 m. A likely upper limit for the water content of this debris flow is ~ 50 % and the lower limit ~ 10 %

by volume (Iverson, 1997), which gives the maximum amount of water required as ~ 4000 m^3. Alcoves on Mars are generally much greater in surface area than the alcoves of the debris flows near Ísafjörður. For example, a small alcove in the crater inside Kaiser Crater (Site H) measures ~ 9000 m^2. Hence, to produce an 8000 m^3 debris flow, a sediment thickness of 0.85 m would need to fail. This would require a surface thickness of 0.09-0.45 m of ice if all the ice were located in the area of the alcove, which is unlikely. These accumulation thicknesses, especially if they extend outside the alcove, are of the same order as those predicted by radiative balance models of Williams et al. (2009) for accumulation of water ice under past high obliquity, and of Kossacki and Markiewicz (2004) for accumulation of water ice at the present day.

Observations made by other authors have made it clear that multiple events are involved in forming gullies (e.g. Dickson and Head, 2009). Gullies incised into "occupied" alcoves observed by Malin and Edgett (2000) hint that gully formation may not only be a recent geological process on Mars. My results support this interpretation, for analysis of long profiles has shown that in some cases gullies on Mars are as well developed as the examples studied from Earth (Section 6.4.2.2). In NW Iceland, for example, slope development has involved episodic debris flows eroding a volume of nearly $3x10^6$ m^3 over the last ~ 10,000 years. If we takes the flows on Mars as correspondingly seasonal, then equivalent slopes on Mars would take ~ 10,000 Mars years to form, or nearly 20,000 years. The interval between of large debris flows is approximately four years (Decaulne et al., 2005) and small to medium debris flows occur annually. It is reasonable to assume that gully-forming events on Mars would be annual, rather than a higher frequency, because the annual temperature cycle has a larger range than the diurnal cycle. Hence, it can be assumed that the minimum time required to form developed gully slopes is at least ~ 10,000 years. Reiss et al. (2004) used crater counting techniques to date surfaces underneath a gully as being 0.3 - 1.4 Ma and Schon et al. (2009) using a similar technique

dated gullies at 1.25 Ma. Hence, a reasonable timescale for full gully development is between 10^4 and 10^6 years.

Differences observed between images of Mars taken several years apart have revealed that current activity in gullies is limited to the deposition of light-toned deposits (Malin et al., 2006). These deposits have little topographic impact and it is unlikely that they are a result of gully-forming processes (Kolb et al., 2010). Support for this arises from my slope area analysis, which has revealed that the slope hosting one of these deposits is dominated by dry mass wasting. Modelling work by Pelletier et al. (2008) also presented dry mass wasting as a strong candidate mechanism for this light-toned deposit. Since (1) gully-forming processes are probably not active at the present day, (2) gullies are geologically recent (< 10^6 years) and (3) mature gully systems can take 10^4 – 10^6 years to form, this implies that there have been periods of intense gully-forming activity in the past.

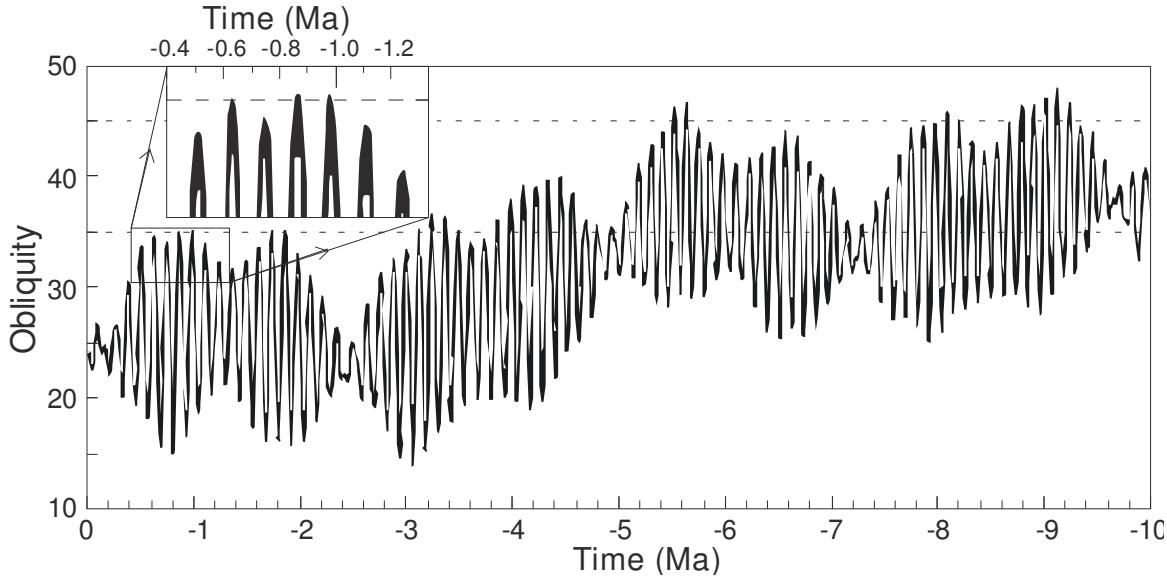

Figure 9-1. Recent martin obliquity cycles, after Laskar et al. (2004). Dotted lines indicate obliquities of 35° and 45°.

Obliquities of 35° and greater produce asymmetrical insolation between north- and south-facing slopes at mid-latitudes (Kreslavsky et al., 2008). This asymmetry is the best explanation to date for the observed global gully patterns of orientation (Section 2.5.1), in which gullies at mid latitudes face polewards and those at higher latitudes express less preference. Costard et al. (2002) argued that obliquity must be as high as 45° to produce

gullies, because this obliquity is required to: (1) produce temperatures above freezing on south facing slopes and (2) produce enough precipitable water in the atmosphere to deposit in the near surface. Since this work, it has been shown that (1) if the local slope geometry is taken into account, melting can be achieved almost anywhere, even at the present day (Hecht, 2002; Kossacki and Markiewicz, 2004) and (2) modelling past levels of precipitable water in the martian atmosphere is very sensitive to the GCM parameters (Section 2.6.1). In addition, my laboratory simulation work has confirmed that even in a metastable state, water can perform significant erosion, hence entire slopes do not need to be above freezing or have high atmospheric pressures for gullies to form, once melting has occurred. Recent work has shown that some gullies are between 0.3 - 1.4 Ma old (Reiss et al., 2004; Schon et al., 2009), but the most recent excursion to 45°obliquity was over 5 Ma ago (Figure 9-1). Hence it is more likely that gullies can form under a more moderate obliquity. The minimum value of obliquity that results in pole-facing slopes receiving more intense insolation than south-facing ones in the mid-latitudes has been found to be 35° (Kreslavsky et al., 2008). Then from Figure 9-1, it can be estimated that at least ~ 20,000 years of the last 1 Ma have been above this obliquity. The most recent excursion to this obliquity was 0.64 Ma ago (Kreslavsky et al., 2008). The duration of this window of opportunity for gully formation fits with my estimated time for gully system development, allows for gullies to have ages < 1.25 Ma and also allows for many phases of gully development in the recent past.

I have found that not only do gully numbers increase up to ~ 40° latitude (and more rapidly than the increase in availability of steep slopes, Section 6.4.2.3), but there is increased gully density here and more gullies occur in continuous slope sections, rather than as isolated patches. These are all indicators that this latitude is particularly favourable for gully formation. From published data on past insolation and water distribution it is not

clear why this would be the case. However, this new observation does allow more constraints to be placed on models of gully formation.

From my observations of slope long profiles there is some evidence that the process of gully formation is latitude dependent, with debris flow at low latitude and alluvial processes at high latitude. This latitude dependency combined with the finding that gullies always co-occur with polygons at high latitudes also implies a climatic influence. As discussed in Chapter 6, these observations could be linked. The pervasive presence of near-surface ice (as implied by the presence of polygonal ground) could significantly change the process of gully formation. As shown by my laboratory simulations cold ground inhibits infiltration (Section 8.5.1), hence this could prevent sufficient sediment becoming saturated to form a debris flow (Section 3.3).

Gullies located in the polar pits located at ~ 70°S form an anomaly – they have a high linear density, form continuously across whole slopes and occur in great numbers. I have shown that the gullies themselves are morphologically very different from the rest of the martian gullies and have greatest similarities to alluvial gullies on Earth (Chapter 6). They occur on lower slopes than gullies elsewhere, and despite there being plenty of craters at a similar latitude containing equivalent slopes to the polar pits the vast majority do not contain gullies. No model to date has found an explanation which is consistent with the observations for whole gully population and also for the location of the polar pit gullies. My work suggests that they are formed by a different process, but only detailed future work can reveal the exact nature of these enigmatic gullies.

Chapter 10. Conclusions and further work

10.1. Conclusions

This thesis has demonstrated that a better understanding of debris flows on Earth and other planets can be achieved through numerical geomorphological methods. Through in-depth study of unconfined debris flows in NW Iceland, I have developed a new simple empirical method of predicting debris flow hazard from morphology alone.

Geomorphic analysis of gullies on Mars has revealed that they are formed by wet, rather than dry processes. The signature of debris flow is clearly seen in many gully long profiles and in more detailed slope-area analysis of selected examples.

My work supports the arguments of other workers in the field that an aquifer source for the water to carve gullies is not plausible. This is because of the position of the gully heads and the form of the alcoves in slope-area analysis, and the dominant climate signal in the observed latitudinal trends.

There is an apparent change in dominant process from debris flow to alluvial at mid-latitude latitude, and a favourable latitude for gully formation at ~ 40º. Both add valuable constraints to any future climate model.

Debris flow requires a small but appreciable amount of liquid water to occur. Any volume of water condensed from the atmosphere will be relatively small, especially compared to that potentially stored underground. Despite this, I have demonstrated that atmospheric condensation would be sufficient to trigger debris flows.

By comparison with debris flow systems on Earth, I suggest that the formation of martian gullies requires annual activity for about 10^4-10^6 years. This can occur at moderate

obliquities in Mars' recent past. Laboratory simulations reveal that water is capable of significant geomorphic work at the low pressure and temperature experienced on the surface of present-day Mars. This removes the previously postulated pre-condition for entire slopes to be above freezing for long periods of time for gullies to form, and hence widens the range of obliquity values at which gullies can be formed.

Gullies on Mars provide intriguing evidence of Earth-like surface processes active on this almost airless and dry planet. Water is a potential harbour for microbial life on Mars and is necessary for human exploration of the planet. This work has shown that water has been recently active on the planet's surface, but my studies do not support the existence of a long-lived sub-surface hydrosphere that would be an ideal haven for life. However, the observations of landforms, including gullies that indicate the recent activity of liquid water on the martian surface are increasing in number and type. They show that the near-surface inventory of water is much more substantial than previously thought.

10.2. Future work

There is a lot of scope for both (1) extending the geomorphological surveys that I have completed so far and (2) applying the techniques that I have developed to other types of studies on Mars. For example, a simple and direct extension would be to verify my conclusions from the slope-area analysis. This could be done by applying the same techniques to a greater number of slopes with and without gullies and located in different settings and latitudes. These analyses could be combined with dating by impact crater counting to ascertain if differences exist between systems of different ages. The evaluation of any latitudinal trends could highlight climatic influences on slope development, not just by gully forming processes, but by solifluction, ice creep, or other processes. Similar extension could be applied to my analysis of slope long profiles. An even more robust analysis could be completed with a greater number of samples, with sampling focussed within set latitudinal bands. Long profiles could be used to investigate meandering in

gullies, which on Earth is intimately linked to channel dynamics. For example, such data could be used to determine the slope angle at which meandering occurs and the variation in channel depth downstream.

An extension of the hazard prediction for unconfined debris flows on Earth would include the collection of morphological data in different geographical locations and climatic settings to confirm that this method is applicable elsewhere. This is becoming increasingly practical as high resolution topographic data in the form of airborne laser data (LiDAR) are becoming more widely obtained and more readily available. With sufficient quality and resolution of topographic data my techniques for deriving patterns of erosion and deposition could be used for gullies on Mars. These patterns would reveal more information on the dynamics of the flow and hence the influence of the lower gravity, lower atmospheric pressure and lower temperature on the surface of Mars.

The experimental simulations that I have performed open up many interesting and useful possibilities for further work. An obvious extension is to repeat the experiments for a wider variety of materials, slopes and flow rates to ascertain if the initial results still apply. To verify that low temperature dominates over low pressure in controlling flow dynamics, comparable experiments could be performed with a cold arid atmosphere at ambient terrestrial pressure. As brines are one of the candidate fluids for forming gullies, useful data could be obtained by performing the same experiments with different brines and brine concentrations. To investigate how gully deposits would evolve on Mars, an additional experiment would be to maintain low pressure for a long period (days to months) and to measure the rate of sublimation and its effect on the surface morphology.

Useful improvements to the apparatus include: (1) locating the chamber inside a cold room, so that the air temperature and sediment temperature inside the chamber are the same; (2) using a laser scanner instead of a profiler to speed up measurements and enable

measurements without having to open the chamber, and (3) modification to allow fluid escape, so flow could be maintained for a longer period, to reach equilibrium.

References

Addison, K., 1987. Debris flow during intense rainfall in Snowdonia, North Wales: a preliminary survey. Earth Surf. Process. Landforms. **12**, 561-566.

Aharonson, O., Schorghofer, N., 2006. Subsurface ice on Mars with rough topography. J. Geophys. Res. Planets. **111**, 10.

Akca, D., 2007a. Matching of 3D surfaces and their intensities. ISPRS J. Photogramm. Remote Sens. **62**, 112-121.

Akca, D., 2007b. Least Squares 3D Surface Matching. Institut für Geodäsie und Photogrammetrie, Eidgenössische Technische Hochschule Zürich, Zürich. PhD Thesis**.**

Allison, R. J., Higgitt, D. L., 1998. Slope form and associations with ground boulder cover in arid environments, northeast Jordan. Catena. **33**, 47-74.

Ancey, C., 2007. Plasticity and geophysical flows: A review. J. Non-Newtonian Fluid Mech. **142**, 4-35.

Ancochea, E., HernÃ¡n, F., Huertas, M. J., BrÃ¤ndle, J. L., Herrera, R., 2006. A new chronostratigraphical and evolutionary model for La Gomera: Implications for the overall evolution of the Canarian Archipelago. J. Volcanol. Geotherm. Res. **157**, 271-293.

Andersen, D. T., Pollard, W. H., McKay, C. P., Heldmann, J., 2002. Cold springs in permafrost on Earth and Mars. J. Geophys. Res. Planets. **107**, 5015.

Andersland, O. B., Wiggert, D. C., Davies, S. H., 1996. Frozen soil subsurface barriers: Formation and ice erosion. J. Contam. Hydrol. **23**, 133-147.

Arfstrom, J., Hartmann, W. K., 2005. Martian flow features, moraine-like ridges, and gullies: Terrestrial analogs and interrelationships. Icarus. **174**, 321-335.

Armanini, A., Fraccarollo, L., Rosatti, G., 2009. Two-dimensional simulation of debris flows in erodible channels. Comput. Geosci. **35**, 993-1006.

Arnalds, Sauermoser, S., Jóhannesson, T., Grímsdóttir, H., 2002. Hazard zoning for Ísafjörður and Hnífsdalur, Technical report VÍ-ÚR15. Report #02020, pp. 79.

Arnalds, P., Jónasson, K., Sigurðsson, S., 2004. Avalanche hazard zoning in Iceland based on individual risk. Ann. Glaciol. **38**, 285-290.

Atkinson, K. R., 2008. Investigating the Physical Properties of Planetary Surfaces using the Huygens Penetrometer. Planetary and Space Sciences Research Institute, Open University, Milton Keynes, UK. PhD Thesis**.**

Ballantyne, C. K., Benn, D. I., 1994. Paraglacial Slope Adjustment and Resedimentation Following Recent Glacier Retreat, Fabergstolsdalen, Norway. Arct. Alp. Res. **26**, 255-269.

Balme, M., Mangold, N., Baratoux, D., Costard, F., Gosselin, M., Masson, P., Pinet, P., Neukum, G., 2006. Orientation and distribution of recent gullies in the southern hemisphere of mars: Observations from High Resolution Stereo Camera/Mars Express (HRSC/MEX) and Mars Orbiter Camera/Mars Global Surveyor (MOC/MGS) data. J. Geophys. Res. Planets. **111**, doi:10.1029/2005JE002607

Balme, M. R., Gallagher, C., 2009. An equatorial periglacial landscape on Mars. Earth. Planet. Sci. Lett. **285**, 1-15.

Balme, M. R., Gallagher, C. J., Page, D. P., Murray, J. B., Muller, J. P., 2009. Sorted stone circles in Elysium Planitia, Mars: Implications for recent martian climate. Icarus. **200**, 30-38.

Banks, M. E., McEwen, A. S., Kargel, J. S., Baker, V. R., Strom, R. G., Mellon, M. T., Gulick, V. C., Keszthelyi, L., Herkenhoff, K. E., Pelletier, J. D., et al., 2008. High Resolution Imaging Science Experiment (HiRISE) observations of glacial and periglacial morphologies in the circum-Argyre Planitia highlands, Mars. J. Geophys. Res. Planets. **113**, doi:10.1029/2007JE002994.

Bardou, E., Delaloye, R., 2004. Effects of ground freezing and snow avalanche deposits on debris flows in alpine environments. NHESS. **4**, 519-530.

Bargery, A. S., 2008. Aqueous eruption and channel flow on Mars during the Amazonian epoch. Department of Environmental Science, University of Lancaster, Lancaster, UK. PhD Thesis**.**

Barlow, N. G., Perez, C. B., 2003. Martian impact crater ejecta morphologies as indicators of the distribution of subsurface volatiles. J. Geophys. Res. Planets. **108**, doi:10.1029/2002JE002036.

Barnouin-Jha, O. S., McGovern, A., Buczkowski, D., Seelos, K., Seelos, F., Murchie, S., Ehlmann, B., Science Team, C., 2008. Martian gullies as seen by the Compact Reconnaissance Imaging Spectrometer for Mars (CRISM). AGU Fall Meeting Abstracts 32, pp. 04.

Bart, G. D., 2007. Comparison of small lunar landslides and martian gullies. Icarus. **187**, 417-421.

Benda, L., Dunne, T., 1997. Stochastic Forcing of Sediment Supply to Channel Networks from Landsliding and Debris Flow. Water Resour. Res. **33**, 2849-2863.

Benda, L., Hassan, M. A., Church, M., May, C. L., 2005. Geomorphology of Steepland Headwaters: The Transition from Hillslopes to Channels. J. Am. Water Resour. Assoc. **41**, 835-851.

Benison, K. C., LaClair, D., Walker, J., 2008. Physical sedimentology experiments with sulfuric acid solutions: Implications for Mars? Earth. Planet. Sci. Lett. **270**, 330-337.

Berman, D. C., Crown, D. A., Bleamaster Iii, L. F., 2009. Degradation of mid-latitude craters on Mars. Icarus. **200**, 77-95.

Berti, M., Genevois, R., Simoni, A., Tecca, P. R., 1999. Field observations of a debris flow event in the Dolomites. Geomorphology. **29**, 265-274.

Berti, M., Simoni, A., 2005. Experimental evidences and numerical modelling of debris flow initiated by channel runoff. Landslides. **2**, 171-182.

Berti, M., Simoni, A., 2007. Prediction of debris flow inundation areas using empirical mobility relationships. Geomorphology. **90**, 144-161.

Bibring, J.-P., Langevin, Y., Mustard, J. F., Poulet, F., Arvidson, R., Gendrin, A., Gondet, B., Mangold, N., Pinet, P., Forget, F., et al., 2006. Global Mineralogical and Aqueous Mars History Derived from OMEGA/Mars Express Data. Science. **312**, 400-404.

Bibring, J. P., Langevin, Y., Gendrin, A., Gondet, B., Poulet, F., Berthe, M., Soufflot, A., Arvidson, R., Mangold, N., Mustard, J., et al., 2005. Mars surface diversity as revealed by the OMEGA/Mars Express observations. Science. **307**, 1576-1581.

Blair, T. C., 1999. Cause of dominance by sheetflood vs. debris-flow processes on two adjoining alluvial fans, Death Valley, California. Sedimentology. **46**, 1015-1028.

Boelhouwers, J., Duiker, J. M. C., Van Duffelen, E. A., 1998. Spatial, morphological and sedimentological aspects of recent debris flows in du Toit's Kloof, Western Cape. S. Afr. J. Geol. **101**, 73-89.

Boelhouwers, J., Holness, S., Sumner, P., 2000. Geomorphological characteristics of small debris flows on junior's kop, Marion Island, maritime sub - Antarctic. Earth Surf. Process. Landforms. **25**, 341-352.

Bogaart, P. W., Tucker, G. E., de Vries, J. J., 2003. Channel network morphology and sediment dynamics under alternating periglacial and temperate regimes: A numerical simulation study. Geomorphology. **54**, 257-277.

Borga, M., Tonelli, F., Selleroni, J., 2004. A physically based model of the effects of forest roads on slope stability. Water Resour. Res. **40**, 1-9.

Bourke, M. C., 2005. Alluvial Fans on Dunes in Kaiser Crater Suggest Niveo-Aeolian and Denivation Processes on Mars. Lunar Planet. Sci. Conf. **36**, no. 2373.

Boyce, J. M., Mouginis-Mark, P., Garbeil, H., 2005. Ancient oceans in the northern lowlands of Mars: Evidence from impact crater depth/diameter relationships. J. Geophys. Res. Planets. **110**, doi:10.1029/2004JE002328.

Boyce, J. M., Garbeil, H., 2007. Geometric relationships of pristine Martian complex impact craters, and their implications to Mars geologic history. Geophys. Res. Lett. **34**, 16201.

Brardinoni, F., Hassan, M. A., 2006. Glacial erosion, evolution of river long profiles, and the organization of process domains in mountain drainage basins of coastal British Columbia. J. Geophys. Res. Earth Surface. **111**, doi:10.1029/2005JF000358.

Breien, H., De Blasio, F. V., Elverhøi, A., Høeg, K., 2008. Erosion and morphology of a debris flow caused by a glacial lake outburst flood, Western Norway. Landslides. **5**, 271-280.

Bridges, N. T., Lackner, C. N., 2006. Northern hemisphere Martian gullies and mantled terrain: Implications for near-surface water migration in Mars' recent past. J. Geophys. Res. Planets. **111**, 09014.

Brook, M. S., Kirkbride, M. P., Brock, B. W., 2008. Temporal constraints on glacial valley cross-profile evolution: Two Thumb Range, central Southern Alps, New Zealand. Geomorphology. **97**, 24-34.

Bryson, K. L., Chevrier, V., Sears, D. W. G., Ulrich, R., 2008. Stability of ice on Mars and the water vapor diurnal cycle: Experimental study of the sublimation of ice through a fine-grained basaltic regolith. Icarus. **196**, 446-458.

Burr, D. M., Carling, P. A., Beyer, R. A., Lancaster, N., 2004. Flood-formed dunes in Athabasca Valles, Mars: morphology, modeling, and implications. Icarus. **171**, 68-83.

Burr, D. M., Enga, M.-T., Williams, R. M. E., Zimbelman, J. R., Howard, A. D., Brennand, T. A., 2009. Pervasive aqueous paleoflow features in the Aeolis/Zephyria Plana region, Mars. Icarus. **200**, 52-76.

Burt, D. M., Knauth, L. P., 2003. Electrically conducting, Ca-rich brines, rather than water, expected in the Martian subsurface. J. Geophys. Res. Planets. **108**, 8026.

Byrne, S., Dundas, C. M., Kennedy, M. R., Mellon, M. T., McEwen, A. S., Cull, S. C., Daubar, I. J., Shean, D. E., Seelos, K. D., Murchie, S. L., et al., 2009. Distribution of mid-latitude ground ice on mars from new impact craters. Science. **325**, 1674-1676.

Cabrol, N. A., Grin, E. A., Herkenhoff, K., Richter, L., Science, T. A., 2007. Soil Sedimentology, Textures and Dynamics at Gusev Crater from Spirit's Microscopic Imager. Lunar Planet. Sci. Conf. **38**, no. 1784.

Carr, M. H., Crumpler, L. S., Cutts, J. A., Greeley, R., Guest, J. E., Masursky, H., 1977. Martian impact craters and emplacement of ejecta by surface flow. J. Geophys. Res. **82**, 4055-4065.

Carr, M. H., Head, J. W., 2010. Geologic history of Mars. Earth. Planet. Sci. Lett. **In Press, Corrected Proof**.

Carrara, A., Crosta, G., Frattini, P., 2008. Comparing models of debris-flow susceptibility in the alpine environment. Geomorphology. **94**, 353-378.

Carrozzo, F. G., Bellucci, G., Altieri, F., D'Aversa, E., Bibring, J. P., 2009. Mapping of water frost and ice at low latitudes on Mars. Icarus. **203**, 406-420.

Casali, J., Loizu, J., Campo, M. A., De Santisteban, L. M., Alvarez-Mozos, J., 2006. Accuracy of methods for field assessment of rill and ephemeral gully erosion. Catena. **67**, 128-138.

Catling, D. C., Claire, M. W., Quinn, R. C., Zahnle, K. J., Clark, B. C., Kounaves, S., Hecht, M. H., 2009. Possible Atmospheric Origins of Perchlorate on Mars. Lunar Planet. Sci. Conf. **40**, no. 1567.

Chandler, R. J., 1973. The Inclination of Talus, Artic Talus terraces, and Other Slopes Composed of Granular Materials. J. Geol. **81**, 1-14.

Chen, R. F., Chang, K. J., Angelier, J., Chan, Y. C., Deffontaines, B., Lee, C. T., Lin, M. L., 2006. Topographical changes revealed by high-resolution airborne LiDAR data: The 1999 Tsaoling landslide induced by the Chi-Chi earthquake. Eng. Geol. **88**, 160-172.

Cheng, H. P., Lin, C. T., 2007. The morphological visualization of the water in vacuum cooling and freezing process. J. Food Eng. **78**, 569-576.

Chevrier, V., Sears, D. W. G., Chittenden, J. D., Roe, L. A., Ulrich, R., Bryson, K., Billingsley, L., Hanley, J., 2007. Sublimation rate of ice under simulated Mars

conditions and the effect of layers of mock regolith JSC Mars-1. Geophys. Res. Lett. **34**, L02203.

Chevrier, V., Altheide, T. S., 2008. Low temperature aqueous ferric sulfate solutions on the surface of Mars. Geophys. Res. Lett. **35**, L22101

Chevrier, V. F., Hanley, J., Altheide, T. S., 2009a. Stability of perchlorate hydrates and their liquid solutions at the Phoenix landing site, Mars. Geophys. Res. Lett. **36**, 10202.

Chevrier, V. F., Ulrich, R., Altheide, T. S., 2009b. Viscosity of liquid ferric sulfate solutions and application to the formation of gullies on Mars. J. Geophys. Res. Planets. **114**, 06001.

Chittenden, J. D., Chevrier, V., Roe, L. A., Bryson, K., Pilgrim, R., Sears, D. W. G., 2008. Experimental study of the effect of wind on the stability of water ice on Mars. Icarus. **196**, 477-487.

Chorley, R. J., Schumm, S. A., Sugden, D. E., 1984. Geomorphology. Methuen & Co. Ltd, London, UK.

Christensen, P. R., 2003. Formation of recent martian gullies through melting of extensive water-rich snow deposits. Nature. **422**, 45-48.

Church, M., Stock, R. F., Ryder, J. M., 1979. Contemporary Sedimentary Environments on Baffin Island, Nwt, Canada - Debris Slope Accumulations. Arct. Alp. Res. **11**, 371-402.

Clague, J. J., Evans, S. G., Blown, I. G., 1985. A debris flow triggered by the breaching of a moraine-dammed lake, Klattasine Creek, British Columbia Can. J. Earth Sci. **22**, 1492-1502.

Clark, B. C., III, Castro, A. J., Rowe, C. D., Baird, A. K., Rose, H. J., Jr., Toulmin, P., III, Christian, R. P., Kelliher, W. C., Keil, K., Huss, G. R., 1977. The Viking X ray fluorescence experiment - Analytical methods and early results. J. Geophys. Res. **82**, 4577-4594.

Clifford, S. M., Parker, T. J., 2001. The evolution of the Martian hydrosphere: Implications for the fate of a primordial ocean and the current state of the northern plains. Icarus. **154**, 40-79.

Coe, J. A., Glancy, P. A., Whitney, J. W., 1997. Volumetric analysis and hydrologic characterization of a modern debris flow near Yucca Mountain, Nevada. Geomorphology. **20**, 11-28.

Coe, J. A., Godt, J. W., Henceroth, A. J., 2002. Debris Flows along the Interstate 70 Corridor, Floyd Hill to the Arapahoe Basin Ski Area, Central Colorado – A Field Trip Guidebook. U.S. Geological Survey Open-File Report. 02-398, pp. 38.

Coe, J. A., Godt, J. W., Wait, T. C., Kean, J. W., 2007. Field Reconnaissance of Debris Flows Triggered by a July 21, 2007, Thunderstorm in Alpine, Colorado, and Vicinity. U.S. Geological Survey Open-File Report. 2007-123, pp. 25.

Coe, J. A., Kinner, D. A., Godt, J. W., 2008. Initiation conditions for debris flows generated by runoff at Chalk Cliffs, central Colorado. Geomorphology. **96**, 270-297.

Coleman, K. A., Dixon, J. C., Howe, K. L., Roe, L. A., Chevrier, V., 2009. Experimental simulation of martian gully forms. Planet. Space Sci. **57**, 711-716.

Conway, S. J., Balme, M., Murray, J. B., Towner, M. C., Okubo, C., Grindrod, P. M., 2010a The determination of martian gully formation processes by slope-area analysis. In: M. Balme, A. S. Bargery, C. Gallagher, S. Gupta, (Eds.), Planetary Geomorphology. The Geological Society of London, in review.

Conway, S. J., Balme, M. R., Towner, M. C., Murray, J. B., 2010b. Experimental study of sediment transport by water flowing under martian conditions: application to gullies on Mars. Icarus. **in review**.

Conway, S. J., Decaulne, A., Balme, M. R., Murray, J. B., Towner, M. C., 2010c. A new Approach to Estimating Hazard posed by Debris Flows in the Westfjords of Iceland. Geomorphology. **114**, 556-572.

Corominas, J., 1996. The angle of reach as a mobility index for small and large landslides. Can. Geotech. J. **33**, 260-271.

Costa, J. E., 1984 Physical geomorphology of debris flows. In: J. E. Costa, P. J. Fleisher, (Eds.), Developments and Applications of Geomorphology. Springer-Verlag, pp. 268-317.

Costard, F., Aguirre-Puente, J., Greeley, R., Makhloufi, N., 1999. Martian fluvial-thermal erosion: Laboratory simulation. J. Geophys. Res. Planets. **104**, 14091-14098.

Costard, F., Forget, F., Mangold, N., Peulvast, J. P., 2002. Formation of recent Martian debris flows by melting of near-surface ground ice at high obliquity. Science. **295**, 110-113.

Costard, F., Forget, F., Jomelli, V., Mangold, N., 2007 Debris flows in Greenland and on Mars. In: M. Chapman, (Ed.), The Geology of Mars: Evidence from Earth-based Analogs. Cambridge University Press, Cambridge, pp. 265-278.

Crippen, J. R., 1979. Potential hazards from floodflows and debris movement in the Furnace Creek area, Death Valley National Monument, California-Nevada. U.S. Geological Survey Open-File Report. 79-991.

Curry, A. M., 1999. Paraglacial modification of slope form. Earth Surf. Process. Landforms. **24**, 1213-1228.

de Scally, F. A., Owens, I. F., 2004. Morphometric controls and geomorphic responses on fans in the Southern Alps, New Zealand. Earth Surf. Process. Landforms. **29**, 311-322.

Decaulne, A., 2001. Dynamique des Versants et Risques Naturels dans les Fjords d'Islande du Nord-Ouest l'Impact Geomorphique et Humain des Avalanches et des Debris Flows. Faculte des Lettres et Sciences Humaines, UMR 6042 – CNRS – Géodynamique des milieux naturels et anthropisés, Université Blaise Pascal, Clérmont-Ferrand. PhD Thesis**.**

Decaulne, A., Sæmundsson, Pétursson, O., 2005. Debris flow triggered by rapid snowmelt: A case study in the Gleiðarhjalli area, northwestern Iceland. Geogr. Ann. Ser. A-Phys. Geogr. **87A**, 487-500.

Decaulne, A., 2007. Snow-avalanche and debris-flow hazards in the fjords of north-western Iceland, mitigation and prevention. Nat. Hazards. **41**, 81-98.

Decaulne, A., Sæmundsson, 2007. Spatial and temporal diversity for debris-flow meteorological control in subarctic oceanic periglacial environments in Iceland. Earth Surf. Process. Landforms. **32**, 1971-1983.

Demoulin, A., 1998. Testing the tectonic significance of some parameters of longitudinal river profiles: the case of the Ardenne (Belgium, NW Europe). Geomorphology. **24**, 189-208.

Denlinger, R. P., Iverson, R. M., 2001. Flow of variably fluidized granular masses across three-dimensional terrain 2. Numerical predictions and experimental tests. J. Geophys. Res. Solid Earth. **106**, 553-566.

Dickson, J. L., Head, J. W., Kreslavsky, M., 2007. Martian gullies in the southern mid-latitudes of Mars: Evidence for climate-controlled formation of young fluvial features based upon local and global topography. Icarus. **188**, 315-323.

Dickson, J. L., Fassett, C. I., Head, J. W., 2009. Amazonian-aged fluvial valley systems in a climatic microenvironment on Mars: Melting of ice deposits on the interior of Lyot Crater. Geophys. Res. Lett. **36**, 08201.

Dickson, J. L., Head, J. W., 2009. The formation and evolution of youthful gullies on Mars: Gullies as the late-stage phase of Mars' most recent ice age. Icarus. **204**, 63-86.

Dietrich, W. E., Perron, J. T., 2006. The search for a topographic signature of life. Nature. **439**, 411-418.

Dohrenwend, J. C., Wells, S. G., Turrin, B. D., 1986. Degradation of Quaternary Cinder Cones in the Cima Volcanic Field, Mojave Desert, California. Geol. Soc. Am. Bull. **97**, 421-427.

Fan, C., Schulze-Makuch, D., Xie, H., Lu, N., 2009. Investigation of water signatures at gully-exposed sites on Mars by hyperspectral image analysis. Planet. Space Sci. **57**, 93-104.

Fannin, R. J., Wise, M. P., 2001. An empirical-statistical model for debris flow travel distance. Can. Geotech. J. **38**, 982-994.

Favalli, M., Fornaciai, A., Pareschi, M. T., 2009. LIDAR strip adjustment: Application to volcanic areas. Geomorphology. **111**, 123-135.

Félix, G., Thomas, N., 2004. Relation between dry granular flow regimes and morphology of deposits: Formation of levées in pyroclastic deposits. Earth. Planet. Sci. Lett. **221**, 197-213.

Fergason, R. L., Christensen, P. R., Kieffer, H. H., 2006. High-resolution thermal inertia derived from the Thermal Emission Imaging System (THEMIS): Thermal model and applications. J. Geophys. Res. Planets. **111**, E12004

Ferrucci, M., Pertusati, S., Sulpizio, R., Zanchetta, G., Pareschi, M. T., Santacroce, R., 2005. Volcaniclastic debris flows at La Fossa Volcano (Vulcano Island, southern Italy): Insights for erosion behaviour of loose pyroclastic material on steep slopes. J. Volcanol. Geotherm. Res. **145**, 173-191.

Fetter, C. W., 2001. Applied Hydrogeology. Prentice Hall, New Jersey.

Forget, F., Hourdin, F., Fournier, R., Hourdin, C., Talagrand, O., Collins, M., Lewis, S. R., Read, P. L., Huot, J. P., 1999. Improved general circulation models of the Martian atmosphere from the surface to above 80 km. J. Geophys. Res. Planets. **104**, 24155-24175.

Gabet, E. J., Bookter, A., 2008. A morphometric analysis of gullies scoured by post-fire progressively bulked debris flows in southwest Montana, USA. Geomorphology. **96**, 298-309.

Gaidos, E. J., 2001. Cryovolcanism and the recent flow of liquid water on Mars. Icarus. **153**, 218-223.

Gardner, J. S., 1989. High magnitude geomorphic events in the Canadian Rocky Mountains. Studia Geomorphologica Carpatho-Balcanica. **23**, 39-51.

Garvin, J. B., Sakimoto, S. E. H., Schnetzler, C., Frawley, J. J., 1999. Global Geometric Properties of Martian Impact Craters: A Preliminary Assessment Using Mars Orbiter Laser Altimeter (MOLA). The Fifth International Conference on Mars, July 19-24, 1999, Pasadena, California. abstract no.6163.

Gilmore, M. S., Phillips, E. L., 2002. Role of aquicludes in formation of Martian gullies. Geology. **30**, 1107-1110.

Glade, T., 2005. Linking debris-flow hazard assessments with geomorphology. Geomorphology. **66**, 189-213.

Godt, J. W., Coe, J. A., 2007. Alpine debris flows triggered by a 28 July 1999 thunderstorm in the central Front Range, Colorado. Geomorphology. **84**, 80-97.

Goldrick, G., Bishop, P., 2007. Regional analysis of bedrock stream long profiles: Evaluation of Hack's SL form, and formulation and assessment of an alternative (the DS form). Earth Surf. Process. Landforms. **32**, 649-671.

Griffiths, P. G., Webb, R. H., Melis, T. S., 2004. Frequency and initiation of debris flows in Grand Canyon, Arizona. Journal of Geophysical Research (Earth Surface). **109**, 04002.

Guthrie, R. H., Hockin, A., Colquhoun, L., Nagy, T., Evans, S. G., Ayles, C., 2010. An examination of controls on debris flow mobility: Evidence from coastal British Columbia. Geomorphology. **114**, 601-613.

Haberle, R. A., Murphy, J. R., Schaeffer, J., 2003. Orbital change experiments with a Mars general circulation model. Icarus. **161**, 66-89.

Haberle, R. M., McKay, C. P., Schaeffer, J., Cabrol, N. A., Grin, E. A., Zent, A. P., Quinn, R., 2001. On the possibility of liquid water on present-day Mars. J. Geophys. Res. Planets. **106**, 23317-23326.

Hack, J. T., 1957. Studies of longitudinal stream profiles in Virginia and Maryland. U.S. Geological Survey Professional Paper. **294-B**, 45-97.

Hancock, G. R., Evans, K. G., 2006. Gully position, characteristics and geomorphic thresholds in an undisturbed catchment in northern Australia. Hydrol. Processes. **20**, 2935-2951.

Hanks, T. C., Webb, R. H., 2006. Effects of tributary debris on the longitudinal profile of the Colorado River in Grand Canyon. J. Geophys. Res. Earth Surface. **111**, doi:10.1029/2004JF000257.

Hardgrove, C., Moersch, J., Whisner, S., 2009. Thermal imaging of alluvial fans: A new technique for remote classification of sedimentary features. Earth. Planet. Sci. Lett. **285**, 124-130.

Harris, C., Smith, J. S., Davies, M. C. R., Rea, B., 2008. An investigation of periglacial slope stability in relation to soil properties based on physical modelling in the geotechnical centrifuge. Geomorphology. **93**, 437-459.

Harris, K. J., Carey, A. E., Lyons, W. B., Welch, K. A., Fountain, A. G., 2007. Solute and isotope geochemistry of subsurface ice melt seeps in Taylor Valley, Antarctica. Geol. Soc. Am. Bull. **119**, 548-555.

Harris, S. A., Gustafson, C. A., 1993. Debris flow characteristics in an area of continuous permafrost, St. Elias Range, Yukon Territory. Zeitschrift fur Geomorphologie. **37**, 41-56.

Harris, S. A., McDermid, G., 1998. Frequency of debris flows on the Sheep Mountain fan, Kluane Lake, Yukon Territory. Zeitschrift fur Geomorphologie. **42**, 159-175.

Harrison, S., Whalley, B., Anderson, E., 2008. Relict rock glaciers and protalus lobes in the British Isles: Implications for Late Pleistocene mountain geomorphology and palaeoclimate. J. Quaternary Sci. **23**, 287-304.

Hart, S. D., Gulick, V. C., Parsons, R. A., Barnhart, C. J., 2009. Gully Slopes and Discharges on Lyot Crater's Central Peak. Lunar Planet. Sci. Conf. **40**, no. 2349.

Hartmann, W. K., 2001. Martian seeps and their relation to youthful geothermal activity. Space Sci. Rev. **96**, 405-410.

Hartmann, W. K., Thorsteinsson, T., Sigurdsson, F., 2003. Martian hillside gullies and Icelandic analogs. Icarus. **162**, 259-277.

Hartmann, W. K., Neukum, G., Werner, S., 2008. Confirmation and utilization of the "production function" size-frequency distributions of Martian impact craters. Geophys. Res. Lett. **35**, 02205.

Hattanji, T., Onda, Y., Matsukura, Y., 2006. Thresholds for bed load transport and channel initiation in a chert area in Ashio Mountains, Japan: An empirical approach from hydrogeomorphic observations. J. Geophys. Res. Earth Surface. **111**, doi:10.1029/2004JF000206.

Hauber, E., Gwinner, K., Kleinhans, M., Reiss, D., Di Achille, G., Ori, G. G., Scholten, F., Marinangeli, L., Jaumann, R., Neukum, G., 2009a. Sedimentary deposits in Xanthe Terra: Implications for the ancient climate on Mars. Planet. Space Sci. **57**, 944-957.

Hauber, E., Preusker, F., Trauthan, F., Reiss, D., Carlsson, A. E., Hiesinger, H., Jaumann, R., Johansson, H. A. B., Johansson, L., Johnsson, A., et al., 2009b. Morphometry of

Alluvial Fans in a Polar Desert (Svalbard, Norway): Implications for Interpreting Martian Fans. Lunar Planet. Sci. Conf. **40**, 1658.

Head, K. H., 1982 Soil classification and compaction tests. In: K. H. Head, (Ed.), Manual of Soil Laboratory Testing Vol. 1. Pentech Press, London.

Hecht, M. H., 2002. Metastability of liquid water on Mars. Icarus. **156**, 373-386.

Hecht, M. H., Catling, D. C., Clark, B. C., Deflores, L., Gospodinova, K., Kapit, J., Kounaves, S. P., Ming, D. W., Quinn, R. C., West, S. J., et al., 2009. Perchlorate in Martian Soil: Evidence and Implications. Lunar Planet. Sci. Conf. **40**, no. 2420.

Heldmann, J. L., Mellon, M. T., 2004. Observations of martian gullies and constraints on potential formation mechanisms. Icarus. **168**, 285-304.

Heldmann, J. L., Toon, O. B., Pollard, W. H., Mellon, M. T., Pitlick, J., McKay, C. P., Andersen, D. T., 2005. Formation of Martian gullies by the action of liquid water flowing under current Martian environmental conditions. J. Geophys. Res. Planets. **110**, doi:10.1029/2004JE002261.

Heldmann, J. L., Carlsson, E., Johansson, H., Mellon, M. T., Toon, O. B., 2007. Observations of martian gullies and constraints on potential formation mechanisms II. The northern hemisphere. Icarus. **188**, 324-344.

Heldmann, J. L., Conley, C., Brown, A. J., Fletcher, L., Bishop, J. L., McKay, C. P., 2009. Possible Liquid Water Origin for Atacama Desert Mudflow and Recent Gully Deposits on Mars. Icarus. **In Press, Accepted Manuscript**.

Hinchliffe, S., Ballantyne, C. K., 2009. Talus structure and evolution on sandstone mountains in NW Scotland. Holocene. **19**, 477-486.

Hoffman, N., 2000. Ideas about the surface runoff features on Mars. Science. **290**, 711-711.

Hoffman, N., 2002. Active polar gullies on Mars and the role of carbon dioxide. Astrobiology. **2**, 313-323.

Hooke, R. L., 1967. Processes on Arid-region Alluvial Fans. J. Geol. **75**, 438-460.

Hovius, N., Lea-Cox, A., Turowski, J. M., 2008. Recent volcano-ice interaction and outburst flooding in a Mars polar cap re-entrant. Icarus. **197**, 24-38.

Hübl, J., Steinwendtner, H., 2001. Two-dimensional simulation of two viscous debris flows in Austria. Phys. Chem. Earth Part C. **26**, 639-644.

Hudson, T. L., Aharonson, O., 2008. Diffusion barriers at Mars surface conditions: Salt crusts, particle size mixtures, and dust. J. Geophys. Res. Planets. **113**, doi:10.1029/2007JE003026.

Hugenholtz, C. H., Tseung, J. M. W. B., 2007. Formation of Interdigitate Patterns on Martian Alluvial Fans. Lunar Planet. Sci. Conf. **38**, no. 1011.

Hugenholtz, C. H., 2008. Frosted granular flow: A new hypothesis for mass wasting in martian gullies. Icarus. **197**, 65-72.

Hurlimann, M., Rickenmann, D., Medina, V., Bateman, A., 2008. Evaluation of approaches to calculate debris-flow parameters for hazard assessment. Eng. Geol. **102**, 152-163.

Hutter, K., Svendsen, B., Rickenmann, D., 1996. Debris flow modeling: A review. Continuum Mech. Thermodyn. **8**, 1-35.

Imaizumi, F., Hattanji, T., Hayakawa, Y. S., 2010. Channel initiation by surface and subsurface flows in a steep catchment of the Akaishi Mountains, Japan. Geomorphology. **115**, 32-42.

Innes, J. L., 1983a. Lichenometric dating of debris-flow deposits in the Scottish Highlands. Earth Surface Processes & Landforms. **8**, 579-588.

Innes, J. L., 1983b. Debris Flows. Prog. Phys. Geog. **7**, 469-501.

Innes, J. L., 1985. Magnitude- frequency relation of debris flows in northwest Europe. Geogr. Ann. Ser. A-Phys. Geogr. **67 A**, 23-32.

Iturrizaga, L., 2008. Paraglacial landform assemblages in the Hindukush and Karakoram Mountains. Geomorphology. **95**, 27-47.

Iverson, R. M., 1997. The physics of debris flows. Rev. Geophys. **35**, 245-296.

Iverson, R. M., Reid, M. E., LaHusen, R. G., 1997. Debris-flow mobilization from landslides. Annu. Rev. Earth Pl. Sc. **25**, 85-138.

Iverson, R. M., Schilling, S. P., Vallance, J. W., 1998. Objective delineation of lahar-inundation hazard zones. Geol. Soc. Am. Bull. **110**, 972-984.

Iverson, R. M., Denlinger, R. P., 2001. Flow of variably fluidized granular masses across three-dimensional terrain I. Coulomb mixture theory. J. Geophys. Res. Solid Earth. **106**, 537-552.

Iverson, R. M., Vallance, J. W., 2001. New views of granular mass flows. Geology. **29**, 115-118.

Jack, J. L., 2000. Red-shifts and red herrings in geographical ecology. Ecography. **23**, 101-113.

Jaeger, K. L., Montgomery, D. R., Bolton, S. M., 2007a. Channel and perennial flow initiation in headwater streams: Management implications of variability in source-area size. J. Environ. Manage. **40**, 775-786.

Jaeger, W. L., Keszthelyi, L. P., McEwen, A. S., Dundas, C. M., Russell, P. S., 2007b. Athabasca Valles, Mars: A lava-draped channel system. Science. **317**, 1709-1711.

Jakob, M., 2005. A size classification for debris flows. Eng. Geol. **79**, 151-161.

Jakosky, B. M., Phillips, R. J., 2001. Mars' volatile and climate history. Nature. **412**, 237-244.

Jakosky, B. M., Mellon, M. T., Varnes, E. S., Feldman, W. C., Boynton, W. V., Haberle, R. M., 2005. Mars low-latitude neutron distribution: Possible remnant near-surface water ice and a mechanism for its recent emplacement. Icarus. **175**, 58-67.

Jean, J. S., Yang, C. H., Lee, M. J., Lee, M. K., Chien, M. H., 2008. Potential antifreeze compounds in present-day Martian seepage groundwater. Terr. Atmos. Ocean. Sci. **19**, 279-289.

Jerolmack, D. J., Mohrig, D., Grotzinger, J. P., Fike, D. A., Watters, W. A., 2006. Spatial grain size sorting in eolian ripples and estimation of wind conditions on planetary surfaces: Application to Meridiani Planum, Mars. J. Geophys. Res. Planets. **111**, doi:10.1029/2005JE002544.

Johnson, A. M., Rodine, J. R., 1984 Debris flow. In: D. Brunsden, D. B. Prior, (Eds.), Slope Instability. Wiley, Chichester, pp. 257–357.

Kanji, M. A., Cruz, P. T., Massad, F., 2008. Debris flow affecting the Cubatão Oil Refinery, Brazil. Landslides. **5**, 71-82.

Keszthelyi, L. P., Jaeger, W. L., Dundas, C. M., Martínez-Alonso, S., McEwen, A. S., Milazzo, M. P., 2010. Hydrovolcanic features on Mars: Preliminary observations from the first Mars year of HiRISE imaging. Icarus. **205**, 211-229.

Kieffer, H. H., 1992. Mars. University of Arizona Press, Tucson.

Kirk, R. L., Howington-Kraus, E., Redding, B., Galuszka, D., Hare, T. M., Archinal, B. A., Soderblom, L. A., Barrett, J. M., 2003. High-resolution topomapping of candidate MER landing sites with Mars Orbiter Camera narrow-angle images. J. Geophys. Res. Planets. **108**, 8088.

Kirk, R. L., Howington-Kraus, E., Rosiek, M. R., Anderson, J. A., Archinal, B. A., Becker, K. J., Cook, D. A., Galuszka, D. M., Geissler, P. E., Hare, T. M., et al., 2008. Ultrahigh resolution topographic mapping of Mars with MRO HiRISE stereo images: Meter-scale slopes of candidate Phoenix landing sites. J. Geophys. Res. Planets. **113**, doi:10.1029/2007JE003000.

Klubertanz, G., Laloui, L., Vulliet, L., 2009. Identification of mechanisms for landslide type initiation of debris flows. Eng. Geol. **109**, 114-123.

Knauth, L. P., Burt, D. M., 2002. Eutectic brines on Mars: Origin and possible relation to young seepage features. Icarus. **158**, 267-271.

Kneisel, C., Rothenbühler, C., Keller, F., Haeberli, W., 2007. Hazard assessment of potential periglacial debris flows based on GIS-based spatial modelling and geophysical field surveys: A case study in the Swiss Alps. Permafrost Periglacial Process. **18**, 259-268.

Kneissl, T., Reiss, D., van Gasselt, S., Neukum, G., 2009. Distribution and orientation of northern-hemisphere gullies on Mars from the evaluation of HRSC and MOC-NA data. Earth. Planet. Sci. Lett. **In Press, Corrected Proof**.

Kochel, R. C., Trop, J. M., 2007. Icy Debris Fans and Flows in Alaska: Earth Analog for Recent Mars Flows. Lunar Planet. Sci. Conf. **38**, no. 1813.

Kochel, R. C., Trop, J. M., 2008. Earth analog for high-latitude landforms and recent flows on Mars: Icy debris fans in the Wrangell Volcanic Field, Alaska. Icarus. **196**, 63-77.

Kolb, K. J., McEwen, A. S., Pelletier, J. D., Science, T. H., 2009. Measuring Slopes of Gully Fan Apices Using Digital Elevation Models. Lunar Planet. Sci. Conf. **40**, no. 2268.

Kolb, K. J., Pelletier, J. D., McEwen, A. S., 2010. Modeling the formation of bright slope deposits associated with gullies in Hale Crater, Mars: Implications for recent liquid water. Icarus. **205**, 113-137.

Kossacki, K. J., Markiewicz, W. J., 2004. Seasonal melting of surface water ice condensing in martian gullies. Icarus. **171**, 272-283.

Kossacki, K. J., Markiewicz, W. J., Smith, M. D., Page, D., Murray, J., 2006. Possible remnants of a frozen mud lake in southern Elysium, Mars. Icarus. **181**, 363-374.

Kounaves, S. P., Catling, D., Clark, B. C., Deflores, L., Gospodinova, K., Hecht, M. H., Kapit, J., Ming, D. W., Quinn, R. C., Science, T. P., 2009. Aqueous Carbonate Chemistry of the Martian Soil at the Phoenix Landing Site. Lunar Planet. Sci. Conf. **40**, no. 2489.

Kreslavsky, M. A., Head, J. W., 2000. Kilometer-scale roughness of Mars: Results from MOLA data analysis. J. Geophys. Res. **105**, 26695-26712.

Kreslavsky, M. A., Head, J. W., 2003. North-south topographic slope asymmetry on Mars: Evidence for insolation-related erosion at high obliquity. Geophys. Res. Lett. **30**, doi:10.1029/2003GL017795.

Kreslavsky, M. A., 2008. Slope Steepness of Channels and Aprons: Implications for Origin of Martian Gullies. Workshop on Martian Gullies 2008, abstract no. 1303, pp. 54-55.

Kreslavsky, M. A., Head, J. W., Marchant, D. R., 2008. Periods of active permafrost layer formation during the geological history of Mars: Implications for circum-polar and mid-latitude surface processes. Planet. Space Sci. **56**, 289-302.

Kuzmin, R. O., Zabalueva, E. V., Christensen, R. R., 2009. Estimation and mapping of wintertime increase in water ice content of the martian surface soil based on seasonal thermal emission spectrometer thermal inertia variations. J. Geophys. Res. Planets. **114**, doi:10.1029/2008JE003222.

Lague, D., Davy, P., 2003. Constraints on the long-term colluvial erosion law by analyzing slope-area relationships at various uplift rates in the Siwaliks Hills (Nepal). J. Geophys. Res. Solid Earth. **108**, doi:10.1029/2002JB001893.

Lan, H., Martin, C. D., Zhou, C. H., 2008. Estimating the size and travel distance of Klapperhorn Mountain debris flows for risk analysis along railway, Canada. Int. J. Sediment Res. **23**, 275-282.

Lanza, N. L., Meyer, G. A., Okubo, C. H., Newsom, H. E., Wiens, R. C., 2010. Evidence for debris flow gully formation initiated by shallow subsurface water on Mars. Icarus. **205**, 103-112.

Larsen, I. J., Pederson, J. L., Schmidt, J. C., 2006. Geologic versus wildfire controls on hillslope processes and debris flow initiation in the Green River canyons of Dinosaur National Monument. Geomorphology. **81**, 114-127.

Larsson, S., 1982. Geomorphological Effects on the Slopes of Longyear Valley, Spitsbergen, after a Heavy Rainstorm in July 1972. Geogr. Ann. Ser. A-Phys. Geogr. **64**, 105-125.

Laskar, J., Robutel, P., 1993. The chaotic obliquity of the planets. Nature. **361**, 608-612.

Laskar, J., Correia, A. C. M., Gastineau, M., Joutel, F., Levrard, B., Robutel, P., 2004. Long term evolution and chaotic diffusion of the insolation quantities of Mars. Icarus. **170**, 343-364.

Lee, P., McKay, C. P., Matthews, J., 2002. Gullies on Mars: Clues to Their Formation Timescale from Possible Analogs from Devon Island, Nunavut, Arctic Canada. Lunar Planet. Sci. Conf. **33**, no. 2050.

Lee, P., Cockell, C. S., McKay, C. P., 2004. Gullies on Mars: Origin by Snow and Ice Melting and Potential for Life Based on Possible Analogs from Devon Island, High Arctic. Lunar Planet. Sci. Conf. **35**, no. 2122.

Lee, P., Glass, B. J., Osinski, G. R., Parnell, J., Schutt, J. W., McKay, C. P., 2006. Gullies on Mars: Fresh Gullies in Dirty Snow, Devon Island, High Arctic, as End-Member Analogs. Lunar Planet. Sci. Conf. **37**, no. 1818.

Legros, F., 2002. The mobility of long-runout landslides. Eng. Geol. **63**, 301-331.

Leverington, D. W., 2009. Reconciling channel formation processes with the nature of elevated outflow systems at Ophir and Aurorae Plana, Mars. J. Geophys. Res. Planets. **114**, 10005.

Levy, J., Head, J., Marchant, D., 2009a. Thermal contraction crack polygons on Mars: Classification, distribution, and climate implications from HiRISE observations. J. Geophys. Res. Planets. **114**, 01007.

Levy, J. S., Head, J. W., Marchant, D. R., Morgan, G. A., Dickson, J. L., 2007. Gully Surface and Shallow Subsurface Structure in the South Fork of Wright Valley, Antarctic Dry Valleys: Implications for Gully Activity on Mars. Lunar Planet. Sci. Conf. **38**, no. 1728.

Levy, J. S., Head, J. W., Marchant, D. R., Dickson, J. L., Morgan, G. A., 2009b. Geologically recent gully-polygon relationships on Mars: Insights from the Antarctic dry valleys on the roles of permafrost, microclimates, and water sources for surface flow. Icarus. **201**, 113-126.

Llanes, P., Herrera, R., Gómez, M., Muñoz, A., Acosta, J., Uchupi, E., Smith, D., 2009. Geological evolution of the volcanic island La Gomera, Canary Islands, from analysis of its geomorphology. Mar. Geol. **264**, 123-139.

Longhi, J., 2006. Phase equilibrium in the system CO_2-H_2O: Application to Mars. J. Geophys. Res. Planets. **111**, doi:10.1029/2005JE002552.

Lorente, A., Beguería, S., Bathurst, J. C., García-Ruiz, J. M., 2003. Debris flow characteristics and relationships in the Central Spanish Pyrenees. NHESS. **3**, 683-692.

Lu, X., Kieffer, S. W., 2009. Thermodynamics and mass transport in multicomponent, multiphase H_2O systems of planetary interest. Annu. Rev. Earth Pl. Sc. **37**, 449-477.

Luckman, B. H., 1992. Debris Flows and Snow Avalanche Landforms in the Lairig Ghru, Cairngorm Mountains, Scotland. Geogr. Ann. Ser. A-Phys. Geogr. **74**, 109-121.

Luo, W., Stepinski, T. F., 2009. Computer-generated global map of valley networks on Mars. J. Geophys. Res. Planets. **114**, doi:10.1029/2009JE003357.

Lyons, W. B., Welch, K. A., Carey, A. E., Doran, P. T., Wall, D. H., Virginia, R. A., Fountain, A. G., Csatho, B. M., Tremper, C. M., 2005. Groundwater seeps in

Taylor Valley Antarctica: an example of a subsurface melt event. Ann. Glaciol. **40**, 200-206.

Malin, M. C., Edgett, K. S., 2000. Evidence for recent groundwater seepage and surface runoff on Mars. Science. **288**, 2330-2335.

Malin, M. C., Edgett, K. S., Posiolova, L. V., McColley, S. M., Dobrea, E. Z. N., 2006. Present-day impact cratering rate and contemporary gully activity on Mars. Science. **314**, 1573-1577.

Mangeney, A., Bouchut, F., Thomas, N., Vilotte, J. P., Bristeau, M. O., 2007. Numerical modeling of self-channeling granular flows and of their levee-channel deposits. J. Geophys. Res. Earth Surface. **112**, doi:10.1029/2006JF000469.

Mangold, N., 2003. Geomorphic analysis of lobate debris aprons on Mars at Mars Orbiter Camera scale: Evidence for ice sublimation initiated by fractures. J. Geophys. Res. Planets. **108**, doi:10.1029/2002JE001885.

Mangold, N., 2005. High latitude patterned grounds on Mars: Classification, distribution and climatic control. Icarus. **174**, 336-359.

Mao, L., Cavalli, M., Comiti, F., Marchi, L., Lenzi, M. A., Arattano, M., 2009. Sediment transfer processes in two Alpine catchments of contrasting morphological settings. J. Hydrol. **364**, 88-98.

Marchant, D. R., Head, J. W., 2007. Antarctic dry valleys: Microclimate zonation, variable geomorphic processes, and implications for assessing climate change on Mars. Icarus. **192**, 187-222.

Marchi, L., Dalla Fontana, G., Cavalli, M., Tagliavini, F., 2008. Rocky headwaters in the Dolomites, Italy: Field observations and topographic analysis. Arct. Antarct. Alp. Res. **40**, 685-694.

Marion, G. M., Kargel, J. S., Catling, D. C., 2008. Modeling ferrous-ferric iron chemistry with application to martian surface geochemistry. Geochim. Cosmochim. Acta. **72**, 242-266.

Marquez, A., de Pablo, M. A., Oyarzun, R., Viedma, C., 2005. Evidence of gully formation by regional groundwater flow in the Gorgonum-Newton region (Mars). Icarus. **179**, 398-414.

Matthews, J. A., Shakesby, R. A., McEwen, L. J., Berrisford, M. S., Owen, G., Bevan, P., 1999. Alpine debris-flows in Leirdalen, Jotunheimen, Norway, with particular reference to distal fans, intermediate-type deposits, and flow types. Arct. Antarct. Alp. Res. **31**, 421-435.

May, C. L., Gresswell, R. E., 2004. Spatial and temporal patterns of debris-flow deposition in the Oregon Coast Range, USA. Geomorphology. **57**, 135-149.

McArdell, B. W., Bartelt, P., Kowalski, J., 2007. Field observations of basal forces and fluid pore pressure in a debris flow. Geophys. Res. Lett. **34**, doi:10.1029/2006GL029183.

McCauley, C. A., White, D. M., Lilly, M. R., Nyman, D. M., 2002. A comparison of hydraulic conductivities, permeabilities and infiltration rates in frozen and unfrozen soils. Cold Reg. Sci. Technol. **34**, 117-125.

McEwen, A. S., Hansen, C. J., Delamere, W. A., Eliason, E. M., Herkenhoff, K. E., Keszthelyi, L., Gulick, V. C., Kirk, R. L., Mellon, M. T., Grant, J. A., et al., 2007. A closer look at water-related geologic activity on Mars. Science. **317**, 1706-1709.

McLachlan, G. J., 2004. Discriminant Analysis and Statistical Pattern Recognition. John Wiley & Sons.

McNamara, J. P., Ziegler, A. D., Wood, S. H., Vogler, J. B., 2006. Channel head locations with respect to geomorphologic thresholds derived from a digital elevation model: A case study in northern Thailand. Forest Ecol. Manag. **224**, 147-156.

Medina, V., Bateman, A., Hürlimann, M., 2008a. A 2D finite volume model for debris flow and its application to events occurred in the Eastern Pyrenees. Int. J. Sediment Res. **23**, 348-360.

Medina, V., Hürlimann, M., Bateman, A., 2008b. Application of FLATModel, a 2D finite volume code, to debris flows in the northeastern part of the Iberian Peninsula. Landslides. **5**, 127-142.

Mellon, M. T., Jakosky, B. M., 1995. The distribution and behavior of Martian ground ice during past and present epochs. J. Geophys. Res. **100**, 3367.

Mellon, M. T., Phillips, R. J., 2001. Recent gullies on Mars and the source of liquid water. J. Geophys. Res. Planets. **106**, 23165-23179.

Mellon, M. T., Arvidson, R. E., Malin, M. C., Lemmon, M. T., Heet, T., Marshall, J., Sizemore, H. G., Searls, M. L., Phoenix Science Team, T., 2008. The Periglacial Landscape and Ground Ice at the Mars Phoenix Landing Site. AGU Fall Meeting Abstracts 14, pp. 08.

Miller, D. J., 1961. Geology of the Katalla district, Gulf of Alaska Tertiary province, Alaska. U.S. Geological Survey Open-File Report. 61-99.

Miller, D. J., Burnett, K. M., 2008. A probabilistic model of debris-flow delivery to stream channels, demonstrated for the Coast Range of Oregon, USA. Geomorphology. **94**, 184-205.

Mischna, M. A., Richardson, M. I., Wilson, R. J., McCleese, D. J., 2003. On the orbital forcing of Martian water and CO_2 cycles: A general circulation model study with simplified volatile schemes. J. Geophys. Res. Planets. **108**, doi:10.1029/2003JE002051.

Mischna, M. A., Richardson, M. I., 2005. A reanalysis of water abundances in the Martian atmosphere at high obliquity. Geophys. Res. Lett. **32**, 03201.

Miyamoto, H., Dohm, J. M., Baker, V. R., Beyer, R. A., Bourke, M., 2004. Dynamics of unusual debris flows on Martian sand dunes. Geophys. Res. Lett. **31**, doi:10.1029/2004GL020313.

Montgomery, D. R., Foufoula-Georgiou, E., 1993. Channel network source representation using digital elevation models. Water Resour. Res. **29**, 3925-3934.

Montgomery, D. R., Gillespie, A., 2005. Formation of Martian outflow channels by catastrophic dewatering of evaporite deposits. Geology. **33**, 625.

Moore, H. J., Jakosky, B. M., 1989. Viking landing sites, remote-sensing observations, and physical properties of Martian surface materials. Icarus. **81**, 164-184.

Moore, J. M., Howard, A. D., 2005. Large alluvial fans on Mars. J. Geophys. Res. **110**, E04005.

Morgan, G. A., Head, J. W., Marchant, D. R., Dickson, J. L., Levy, J. S., 2007. Gully Formation on Mars: Testing the Snowpack Hypothesis from Analysis of Analogs in the Antarctic Dry Valleys. Lunar Planet. Sci. Conf. **38**, no. 1656.

Moriwaki, H., Inokuchi, T., Hattanji, T., Sassa, K., Ochiai, H., Wang, G., 2004. Failure processes in a full-scale landslide experiment using a rainfall simulator. Landslides. **1**, 277-288.

Morton, D. M., Alvarez, R. M., Ruppert, K. R., Goforth, B., 2008. Contrasting rainfall generated debris flows from adjacent watersheds at Forest Falls, southern California, USA. Geomorphology. **96**, 322-338.

Moyle, W. R., 1982. Water Resources of Borrego Valley and Vicinity, California: Phase 1 - Definition of Geologic and Hydrologic Characteristics of a Basin. U.S. Geological Survey Open-File Report. 82-855, pp. 39.

Murray, J. B., Muller, J.-P., Neukum, G., Werner, S. C., van Gasselt, S., Hauber, E., Markiewicz, W. J., Head, J. W., Foing, B. H., Page, D., et al., 2005. Evidence from the Mars Express High Resolution Stereo Camera for a frozen sea close to Mars' equator. Nature. **434**, 352-356.

Musselwhite, D. S., Swindle, T. D., Lunine, J. I., 2001. Liquid CO_2 breakout and the formation of recent small gullies on Mars. Geophys. Res. Lett. **28**, 1283-1285.

Mustard, J. F., Cooper, C. D., Rifkin, M. K., 2001. Evidence for recent climate change on Mars from the identification of youthful near-surface ground ice. Nature. **412**, 411-414.

Mustard, J. F., Murchie, S. L., Pelkey, S. M., Ehlmann, B. L., Milliken, R. E., Grant, J. A., Bibring, J. P., Poulet, F., Bishop, J., Dobrea, E. N., et al., 2008. Hydrated silicate minerals on Mars observed by the Mars Reconnaissance Orbiter CRISM instrument. Nature. **454**, 305-309.

Nimmo, F., Stevenson, D. J., 2000. Influence of early plate tectonics on the thermal evolution and magnetic field of Mars. J. Geophys. Res. **105**, 11969-11980.

Norðdalh, H., 1990. Late Weichselian and early Holocene deglaciation history of Iceland. Jökull. **40**, 27-50.

O'Brien, J. S., Julien, P. Y., Fullerton, W. T., 1993. Two-dimensional water flood and mudflow simulation. J. Hydraul. Eng. **119**, 244-261.

Okuda, S., 1989. Recent studies on rapid mass movement in Japan with reference to debris hazards. Studia Geomorphologica Carpatho-Balcanica. **23**, 5-22.

Osterloo, M. M., Hamilton, V. E., Bandfield, J. L., Glotch, T. D., Baldridge, A. M., Christensen, P. R., Tornabene, L. L., Anderson, F. S., 2008. Chloride-bearing materials in the southern highlands of mars. Science. **319**, 1651-1654.

Oyarzun, R., Viedma, C., Marquez, A., Lillo, J., 2003. Freezing-resistant liquid water in porous media, a possible mechanism to account for the fluidized transport of sediments on Mars: an example from East Gorgonum crater. Terr. Nova. **15**, 238-242.

Pacifici, A., 2009. The Argentinean Patagonia and the Martian landscape. Planet. Space Sci. **57**, 571-578.

Page, D. P., 2007. Recent low-latitude freeze-thaw on Mars. Icarus. **189**, 83-117.

Page, D. P., Balme, M. R., Grady, M. M., 2009. Dating martian climate change. Icarus. **203**, 376-389.

Pankine, A. A., Tamppari, L. K., Smith, M. D., 2009. Water vapor variability in the north polar region of Mars from Viking MAWD and MGS TES datasets. Icarus. **204**, 87-102.

Parker, G., Paola, C., Whipple, K. X., Mohrig, D., 1998. Alluvial Fans Formed by Channelized Fluvial and Sheet Flow. I: Theory. J. Hydraul. Eng. **124**, 985-995.

Parsons, R. A., Nimmo, F., 2009. Fluvial Discharge Rates of Martian Gullies: Slope Measurements from Stereo HiRISE Images and Numerical Modeling of Sediment Transport. Lunar Planet. Sci. Conf. **40**, no. 1947.

Pelletier, J. D., Kolb, K. J., McEwen, A. S., Kirk, R. L., 2008. Recent bright gully deposits on Mars: Wet or dry flow? Geology. **36**, 211-214.

Perera, H., Willgoose, G., 1998. A physical explanation of the cumulative area distribution curve. Water Resour. Res. **34**, 1335-1343.

Perron, J. T., Dietrich, W. E., Howard, A. D., McKean, J. A., Pettinga, J. R., 2003. Ice-driven creep on Martian debris slopes. Geophys. Res. Lett. **30**, doi:10.1029/2003GL017603.

Perron, J. T., Kirchner, J. W., Dietrich, W. E., 2009. Formation of evenly spaced ridges and valleys. Nature. **460**, 502-505.

Peters, G. H., Abbey, W., Bearman, G. H., Mungas, G. S., Smith, J. A., Anderson, R. C., Douglas, S., Beegle, L. W., 2008. Mojave Mars simulant--Characterization of a new geologic Mars analog. Icarus. **197**, 470-479.

Phillips, J. D., Lutz, J. D., 2008. Profile convexities in bedrock and alluvial streams. Geomorphology. **102**, 554-566.

Pierson, T. C., 1980. Erosion and Deposition by Debris Flows at Mt Thomas, North Canterbury, New Zealand. Earth Surf. Process. **5**, 227-247.

Piest, M., Bradford, J. M., Wyatt, G. M., 1975. Soil Erosion and Sediment Transport from Gullies. Journal of the Hydraulics Division. **101**, 65-80.

Pirulli, M., Sorbino, G., 2008. Assessing potential debris flow runout: A comparison of two simulation models. NHESS. **8**, 961-971.

Plaut, J. J., Safaeinili, A., Holt, J. W., Phillips, R. J., Head, J. W., Seu, R., Putzig, N. E., Frigeri, A., 2009. Radar evidence for ice in lobate debris aprons in the mid-northern latitudes of Mars. Geophys. Res. Lett. **36**, 02203.

Poulet, F., Bibring, J. P., Mustard, J. F., Gendrin, A., Mangold, N., Langevin, Y., Arvidson, R. E., Gondet, B., Gomez, C., 2005. Phyllosilicates on Mars and implications for early martian climate. Nature. **438**, 623-627.

Prior, D. B., Stephens, N., Douglas, G. R., 1970. Some examples of modern debris flows in north-east Ireland. Zeitschrift für Geomorphologie,. **3**, 275-288.

Prochaska, A. B., Santi, P. M., Higgins, J. D., Cannon, S. H., 2008. Debris-flow runout predictions based on the average channel slope (ACS). Eng. Geol. **98**, 29-40.

Prunty, L., Bell, J., 2007. Infiltration Rate vs. Gas Composition and Pressure in Soil Columns. Soil Sci. Soc. Am. J. **71**, 1473-1475.

Randriamazaoro, R., Dupeyrat, L., Costard, F., Gailhardis, E. C., 2007. Fluvial thermal erosion: Heat balance integral method. Earth Surf. Process. Landforms. **32**, 1828-1840.

Rapp, A., 1960. Recent Development of Mountain Slopes in Kärkevagge and Surroundings, Northern Scandinavia. Geogr. Ann. Ser. A-Phys. Geogr. **42**, 65-200.

Rapp, A., Stromquist, L., 1976. Slope Erosion Due To Extreme Rainfall In The Scandinavian Mountains. Geografiska Annaler Series a-Physical Geography. **58**, 193-200.

Rapp, A., Nyberg, R., 1981. Alpine Debris Flows in Northern Scandinavia - Morphology and Dating by Lichenometry. Geogr. Ann. Ser. A-Phys. Geogr. **63**, 183-196.

Reiss, D., van Gasselt, S., Neukum, G., Jaumann, R., 2004. Absolute dune ages and implications for the time of formation of gullies in Nirgal Vallis, Mars. J. Geophys. Res. Planets. **109**, doi:10.1029/2004JE002251.

Reiss, D., Hiesinger, H., Hauber, E., Gwinner, K., 2009. Regional differences in gully occurrence on Mars: A comparison between the Hale and Bond craters. Planet. Space Sci. **57**, 958-974.

Rickenmann, D., 1999. Empirical relationships for debris flows. Nat. Hazards. **19**, 47-77.

Rickenmann, D., Laigle, D., McArdell, B. W., Hubl, J., 2006. Comparison of 2D debris-flow simulation models with field events. Computational Geosciences. **10**, 241-264.

Rowantree, K. M., 1991. Morphological Characteristics of Gully Networks and their Relationship to Host Materials, Baringo District, Kenya. GeoJournal. **23**, 19-27.

Salamunićcar, G., Lončarić, S., 2008. GT-57633 catalogue of Martian impact craters developed for evaluation of crater detection algorithms. Planet. Space Sci. **56**, 1992-2008.

Santi, P. M., deWolfe, V. G., Higgins, J. D., Cannon, S. H., Gartner, J. E., 2008. Sources of debris flow material in burned areas. Geomorphology. **96**, 310-321.

Scheidl, C., Rickenmann, D., Chiari, M., 2008. The use of airborne LiDAR data for the analysis of debris flow events in Switzerland. NHESS. **8**, 1113–1127.

Schon, S. C., Head, J. W., 2009. Terraced Cutbanks and Longitudinal Bars in Gully Channels on Mars: Evidence for Multiple Episodes of Fluvial Transport. Lunar Planet. Sci. Conf. **40**, no. 1691.

Schon, S. C., Head, J. W., Fassett, C. I., 2009. Unique chronostratigraphic marker in depositional fan stratigraphy on Mars: Evidence for ca. 1.25 Ma gully activity and surficial meltwater origin. Geology. **37**, 207-210.

Schorghofer, N., 2005. A physical mechanism for long-term survival of ground ice in Beacon Valley, Antarctica. Geophys. Res. Lett. **32**, doi:10.1029/2005GL023881.

Sears, D. W. G., Benoit, P. H., McKeever, S. W. S., Banerjee, D., Kral, T., Stites, W., Roe, L., Jansma, P., Mattioli, G., 2002. Investigation of biological, chemical and physical processes on and in planetary surfaces by laboratory simulation. Planet. Space Sci. **50**, 821-828.

Sears, D. W. G., Chittenden, J. D., 2005. On laboratory simulation and the temperature dependence of the evaporation rate of brine on Mars. Geophys. Res. Lett. **32**, 4.

Sears, D. W. G., Moore, S. R., 2005. On laboratory simulation and the evaporation rate of water on Mars. Geophys. Res. Lett. **32**, 4.

Selby, M. J., 1993. Hillslope Materials and Processes. Oxford University Press, Oxford.

Sharp, R. P., 1942. Mudflow Levees. Journal of Geomorphology. **5**, 90-95.

Sharp, R. P., Malin, M. C., 1975. Channels on Mars. Geol. Soc. Am. Bull. **86**, 593-609.

Shinbrot, T., Duong, N. H., Kwan, L., Alvarez, M. M., 2004. Dry granular flows can generate surface features resembling those seen in Martian gullies. Proc. Natl. Acad. Sci. U. S. A. **101**, 8542-8546.

Shinbrot, T., 2007. Delayed transitions between fluid-like and solid-like granular states. Eur. Phys. J. E. **22**, 209-217.

Simon, A., Castro, J., 2003 Measurement and Analysis of Alluvial Channel Form. In: G. M. Kondolf, H. Piégay, (Eds.), Tools in Fluvial Geomorphology. John Wiley & Sons, Chichester, pp. 291-322.

Sirkin, L., Tuthill, S. J., 1987. Late Pleistocene and Holocene deglaciation and environments of the southern Chugach Mountains, Alaska. Geol. Soc. Am. Bull. **99**, 376-384.

Sizemore, H. G., Mellon, M. T., 2008. Laboratory characterization of the structural properties controlling dynamical gas transport in Mars-analog soils. Icarus. **197**, 606-620.

Smoluchowski, R., 1968. Mars: Retention of Ice. Science. **159**, 1348-1350.

Snyder, N. P., Whipple, K. X., Tucker, G. E., Merritts, D. J., 2000. Landscape response to tectonic forcing: Digital elevation model analysis of stream profiles in the Mendocino triple junction region, Northern California. Geol. Soc. Am. Bull. **112**, 1250-1263.

Soare, R. J., Kargel, J. S., Osinski, G. R., Costard, F., 2007. Thermokarst processes and the origin of crater-rim gullies in Utopia and western Elysium Planitia. Icarus. **191**, 95-112.

Sosio, R., Crosta, G. B., Frattini, P., 2007. Field observations, rheological testing and numerical modelling of a debris-flow event. Earth Surf. Process. Landforms. **32**, 290-306.

Squyres, S. W., Carr, M. H., 1986. Geomorphic Evidence for the Distribution of Ground Ice on Mars. Science. **231**, 249-252.

Staley, D. M., Wasklewicz, T. A., Blaszczynski, J. S., 2006. Surficial patterns of debris flow deposition on alluvial fans in Death Valley, CA using airborne laser swath mapping data. Geomorphology. **74**, 152-163.

Statham, I., 1976a. A Scree Slope Rockfall Model. Earth Surf. Process. **1**, 43-62.

Statham, I., 1976b. Debris flows on vegetated screes in the Black Mountain, Carmarthenshire. Earth Surf. Process. **1**, 173-180.

Stewart, S. T., Nimmo, F., 2002. Surface runoff features on Mars: Testing the carbon dioxide formation hypothesis. J. Geophys. Res. Planets. **107**, doi:10.1029/2000JE001465.

Stock, J., Dietrich, W. E., 2003. Valley incision by debris flows: Evidence of a topographic signature. Water Resour. Res. **39**, doi:10.1029/2001WR001057.

Stock, J. D., Montgomery, D. R., Collins, B. D., Dietrich, W. E., Sklar, L., 2005. Field measurements of incision rates following bedrock exposure: Implications for process controls on the long profiles of valleys cut by rivers and debris flows. Geol. Soc. Am. Bull. **117**, 174-194.

Stock, J. D., Dietrich, W. E., 2006. Erosion of steepland valleys by debris flows. Geol. Soc. Am. Bull. **118**, 1125-1148.

Sullivan, R., Arvidson, R., Bell, J. F., Gellert, R., Golombek, M., Greeley, R., Herkenhoff, K., Johnson, J., Thompson, S., Whelley, P., et al., 2008. Wind-driven particle mobility on Mars: Insights from Mars Exploration Rover observations at ``El Dorado'' and surroundings at Gusev Crater. J. Geophys. Res. Planets. **113**, doi:10.1029/2008JE003101.

Suwa, H., Okuda, S., 1980. Dissection of valleys by debris flows. Zeitschrift fur Geomorphologie, Supplementband. **35**, 164-182.

Takahashi, T., 1981. Debris Flow. Ann. Rev. Fluid Mech. **13**, 57-77.

Tarboton, D. G., Bras, R. L., Rodriguez-Iturbe, I., 1991. On the extraction of channel networks from digital elevation data. Hydrol. Processes. **5**, 81-100.

Tarboton, D. G., 1997. A new method for the determination of flow directions and upslope areas in grid digital elevation models. Water Resour. Res. **33**, 309-319.

Tarolli, P., Fontana, G. D., 2009. Hillslope-to-valley transition morphology: New opportunities from high resolution DTMs. Geomorphology. **113**, 47-56.

Tokar, R. L., Feldman, W. C., Prettyman, T. H., Moore, K. R., Lawrence, D. J., Elphic, R. C., Kreslavsky, M. A., Head, J. W., Mustard, J. F., Boynton, W. V., 2002. Ice concentration and distribution near the south pole of Mars: Synthesis of odyssey and global surveyor analyses. Geophys. Res. Lett. **29**, 10-1.

Torri, D., Poesen, J., Borselli, L., Knapen, A., 2006. Channel width-flow discharge relationships for rills and gullies. Geomorphology. **76**, 273-279.

Treiman, A. H., 2003. Geologic settings of Martian gullies: Implications for their origins. J. Geophys. Res. Planets. **108**, doi:10.1029/2002JE001900.

Treiman, A. H., 2005. Martain Gullies and Groundwater: A Series of Unfortunate Exceptions. Lunar Planet. Sci. Conf. **36**, no. 1713.

Tucker, G. E., Bras, R. L., 1998. Hillslope processes, drainage density, and landscape morphology. Water Resour. Res. **34**, 2751-2764.

Tunusluoglu, M. C., Gokceoglu, C., Nefeslioglu, H. A., Sonmez, H., 2008. Extraction of potential debris source areas by logistic regression technique: a case study from Barla, Besparmak and Kapi mountains (NW Taurids, Turkey). Environ. Geol. **54**, 9-22.

Védie, E., Costard, F., Font, M., Lagarde, J. L., 2008. Laboratory simulations of Martian gullies on sand dunes. Geophys. Res. Lett. **35**, doi:10.1029/2008GL035638.

Warner, N., Gupta, S., Muller, J.-P., Kim, J.-R., Lin, S.-Y., 2009. A refined chronology of catastrophic outflow events in Ares Vallis, Mars. Earth. Planet. Sci. Lett. **288**, 58-69.

Warner, N. H., Farmer, J. D., 2008. Importance of aeolian processes in the origin of the north polar chasmata, Mars. Icarus. **196**, 368-384.

Whalley, W. B., Azizi, F., 2003. Rock glaciers and protalus landforms: Analogous forms and ice sources on Earth and Mars. J. Geophys. Res. Planets. **108**, doi:10.1029/2002JE001864.

Whipple, K. X., Dunne, T., 1992. The influence of debris-flow rheology on fan morphology, Owens Valley, California. Geol. Soc. Am. Bull. **104**, 887-900.

Whipple, K. X., Tucker, G. E., 1999. Dynamics of the stream-power river incision model: Implications for height limits of mountain ranges, landscape response timescales, and research needs. J. Geophys. Res. Solid Earth. **104**, 17661-17674.

Wilkerson, F. D., Schmid, G. L., 2003. Debris flows in Glacier National Park, Montana: geomorphology and hazards. Geomorphology. **55**, 317-328.

Wilkerson, F. D., Schmid, G. L., 2008. Distribution of debris flows in Glacier National Park, Montana, U.S.A. J. Mountain Sci. **5**, 318-326.

Williams, K. E., Toon, O. B., Heldmann, J., 2007. Modeling water ice lifetimes at recent Martian gully locations. Geophys. Res. Lett. **34**.

Williams, K. E., Toon, O. B., Heldmann, J. L., McKay, C., Mellon, M. T., 2008. Stability of mid-latitude snowpacks on Mars. Icarus. **196**, 565-577.

Williams, K. E., Toon, O. B., Heldmann, J. L., Mellon, M. T., 2009. Ancient melting of mid-latitude snowpacks on Mars as a water source for gullies. Icarus. **200**, 418-425.

Williams, R. M. E., Malin, M. C., 2008. Sub-kilometer fans in Mojave Crater, Mars. Icarus. **198**, 365-383.

Winder, C. G., 1965. Alluvial cone construction by alpine mudflow in a humid temperate region. Can. J. Earth Sci. **2**, 270-277.

Woods, R. A., Sivapalan, M., 1997. A connection between topographically driven runoff generation and channel network structure. Water Resour. Res. **33**, 2939-2950.

Workman, J. B., Menges, C. M., Page, W. R., Taylor, E. M., Ekren, E. B., Rowley, P. D., Dixon, G. L., Thompson, R. A., Wright, L. A., 2002. Geologic map of the Death Valley ground-water model area, Nevada and California. Miscellaneous Field Studies Map 2381-A. USGS.

Xiao, P., Zheng, F., Yao, W., 2005. Downslope erosion process under upslope runoff and sediment using a dual-box system. Int. J. Sediment Res. **20**, 136-142.

Zanuttigh, B., Lamberti, A., 2007. Instability and surge development in debris flows. Rev. Geophys. **45**, doi:10.1029/2005RG000175.

Zorzano, M. P., Mateo-Martí, E., Prieto-Ballesteros, O., Osuna, S., Renno, N., 2009. Stability of liquid saline water on present day Mars. Geophys. Res. Lett. **36**, 20201.

Appendix A. Analysis of errors

Table 4-2 summarises the main sources of error in the data collection and data processing chain. The improvement in the accuracy of the LiDAR data through matching the tracks using LS3D (Akca, 2007a, b) is clearly shown. The errors associated with data collection (with the exception of LiDAR data preprocessing) are very small compared to the errors generated in interpolating the data. This must be taken into consideration when interpreting the total volume estimates. The best volume estimate would be from a surface that had densely spaced points both before and after a debris flow occurs (both preferably from corrected LiDAR data). Given the financial costs associated with collecting LiDAR data and the unpredictable nature of debris flows, the systematic collections of such data is unlikely.

The errors from the upper and lower interpolated surfaces were combined using the standard formula:

$$\sigma_Z = \sqrt{(\sigma_A^2 + \sigma_B^2)} \quad \text{(A1)}$$

where σ_Z is the total uncertainty, and σ_A and σ_B are the uncertainties of the two surfaces. These errors vary spatially and can become large away from data points.

Appendix B. Model production

This appendix describes the method by which the curves in Figure 4-9 were generated; "*x*" refers to cumulative average slope and "*y*" refers to cumulative deposition thickness. The parameters derived from the least squares fits described in this appendix, along with their associated errors, are given in Table B-3. The equations used to generate the model curves shown in Figure 4-9 are as follows (with numbering here in the same sequence as in Figure 4-9):

$$0.03 + 1876170\ x\ e^{(-x/2.217)} \tag{B1}$$

$$(36 - x) / 8.5\ (36 - 8.5x) \tag{B2}$$

$$-0.03816 + 1.04016 / (1 + e^{((x - 36.30119) / 1.00308)}) \tag{B3}$$

$$1.012 /(1 + e^{((x - 32) / 1.00308)}) \tag{B4}$$

The shape of Eq. B1 was derived by performing least squares fit of

$$y = A + B * e^{(-x/C)} \tag{B5}$$

on the data from debris flow 2DF. The χ^2 value for the fit is 0.00547, which implies a significant *p*-value of << 0.001. The r^2 value is 0.93652.

Linear regression of the data from debris flow 5DF was used to derive Eq. B2 using the following relation:

$$y = A + Bx \tag{B6}$$

The r^2 value of this fit is 0.854663, which gives a significant p-value of << 0.0001.

The curves from Eqs. B3 and B4 were derived by performing a least squares fit of

$$y = A + (B - A) / (1 + e^{((x - C) / D)}) \qquad (B7)$$

using data from debris flow 1DF. The χ^2 value for the fit is 0.00027, which implies a significant p-value of << 0.001 and the I value of 0.99828. Equation B4 is a translation of Eq. B3 along the x-axis, an estimate of the lower limit of the data envelope.

Table B-3. Parameter values derived from least squares fits of functions given by Eqs. B5-B7 with their associated errors.

Equation	Parameter	Value	Error
B5	A	0.03267	0.01601
B5	B	1.87617×10^6	1.54541×10^6
B5	C	2.21702	0.1269
B6	A	35.04498	0.17543
B6	B	-8.52036	0.3586
B7	A	0.9834	0.00339
B7	B	-0.03816	0.00453
B7	C	36.30119	0.01725
B7	D	1.00308	0.01641

Appendix C. Measuring elevations from parallax

The following text was written by Mischa Kreslavsky as an explanation of the functioning of his stereo processing script for HiRISE (Kreslavsky, 2008) and I have added clarifications and modifications where appropriate.

In an ideal world, measurements of local elevation differences from stereo pairs work in the following way.

Here I assume that the scene is much smaller than the distance to the camera and the planetary radius, and that the image is map-projected without distortion. Rigorous photogrammetric solutions deal with finite distance to the camera and non map-projected images. With the latter assumption, pixel coordinates in the images X, Y are related to local Cartesian coordinates x, y at the surface through simple scaling:

$$x = SX$$

$$y = SY \tag{C1}$$

where S is the scale in metres per pixel.

I have two images A and B taken with different positions of the camera relative to the scene. Direction from the scene to the camera is described by two angles: camera zenith angle θ (the same as emergence angle), and camera azimuth φ. The azimuth is measured from x-axis toward y-axis. Thus, the complete description of the observation geometry for the stereo pair is given by four angles θ_A, φ_A, θ_B, φ_B.

I identify the same two points 1 and 2 in images *A* and *B* and measure their Cartesian coordinates in the images: (x_{A1}, y_{A1}), (x_{B1}, y_{B1}), (x_{A2}, y_{A2}), (x_{B2}, y_{B2}). If the surface is horizontal, the images A and B are identical, and $x_{A2} - x_{A1} = x_{B2} - x_{B1}$, $y_{A2} - y_{A1} = y_{B2} - y_{B1}$. If there is some elevation difference h between points 2 and 1, there is non-zero parallax vector l defined as:

$$l \equiv \begin{pmatrix} l_x \\ l_y \end{pmatrix} \equiv \begin{pmatrix} (x_{B2} - x_{B1}) - (x_{A2} - x_{A1}) \\ (y_{B2} - y_{B1}) - (y_{A2} - y_{A1}) \end{pmatrix} \tag{C2}$$

Cumbersome but principally simple geometry calculations give the following expression for the parallax vector from the elevation difference and observation geometry:

$$l = h \begin{pmatrix} \tan\theta_A \cos\varphi_A - \tan\theta_B \cos\varphi_B \\ \tan\theta_A \sin\varphi_A - \tan\theta_B \sin\varphi_B \end{pmatrix} \equiv hp \tag{C3}$$

I measure two components of the parallax vector, l_x and l_y, and so I need only to obtain one estimate of the elevation difference h. The best solution of this over defined problem is given by:

$$h = \frac{l \cdot p}{p^2} = \frac{l_x(\tan\theta_A \cos\varphi_A - \tan\theta_B \cos\varphi_B) + l_y(\tan\theta_A \sin\varphi_A - \tan\theta_B \sin\varphi_B)}{\tan^2\theta_A + \tan^2\theta_B - 2\tan\theta_A \tan\theta_B \cos(\varphi_B - \varphi_A)} \tag{C4}$$

Since the problem is over defined, I have also the residual:

$$\left| l - \frac{l \cdot p}{p^2} p \right|,$$

which would be zero, if the points were identified absolutely correctly and geometry were calculated absolutely correctly. It is convenient to express the residual in "vertical units", so that it characterizes an equivalent error in determination of h:

$$r \equiv \frac{1}{p} \left| l - \frac{l \cdot p}{p^2} p \right| = \frac{\left| l_y(\tan\theta_A \cos\varphi_A - \tan\theta_B \cos\varphi_B) - l_x(\tan\theta_A \sin\varphi_A - \tan\theta_B \sin\varphi_B) \right|}{\tan^2\theta_A + \tan^2\theta_B - 2\tan\theta_A \tan\theta_B \cos(\varphi_B - \varphi_A)} \tag{C5}$$

In summary, I measure (x_{A1}, y_{A1}), (x_{B1}, y_{B1}), (x_{A2}, y_{A2}), (x_{B2}, y_{B2}), then use Equations C2 and C4 to obtain the elevation difference h and Equation C5 to obtain the residual and assess the accuracy.

This approach can be generalized for the case when I have not two, but N points, and I want to have mutually consistent elevation differences between them. I measure (x_{Aj}, y_{Aj}), (x_{Bj}, y_{Bj}), j = 1, ..., N. Then I calculate coordinates (x_{A0}, y_{A0}), (x_{B0}, y_{B0}) of a "base" point:

$$x_{A0} = \frac{1}{N}\sum_{j=1}^{N} x_{Aj}\,;\, y_{A0} = \frac{1}{N}\sum_{j=1}^{N} y_{Aj}\,;\, x_{B0} = \frac{1}{N}\sum_{j=1}^{N} x_{Bj}\,;\, y_{B0} = \frac{1}{N}\sum_{j=1}^{N} y_{Bj} \qquad \text{(C6)}$$

and N parallax vectors with respect to the base point:

$$l_j = \begin{pmatrix} \left(x_{Bj} - x_{B0}\right) - \left(x_{Aj} - x_{A0}\right) \\ \left(y_{Bj} - y_{B0}\right) - \left(y_{Aj} - y_{A0}\right) \end{pmatrix}, j = 1,..., N. \qquad \text{(C7)}$$

Finally, I use Equation C4 for each l_j to obtain elevation h_j of each point and (5) to obtain a scaled residual. All elevations h_j are measured with respect to the same arbitrary datum (elevation of the "base" point).

In the real world, HiRISE map-projected images (so-called RDR, or Reduced Data Records) are formally not suitable for such parallax calculations because (1) the observation geometry varies across the image, and (2) the images are orthorectified, that is they are map-projected assuming some smoothed surface topography.

There are two ways to overcome this difficulty. The more accurate way is proposed by the HiRISE team: start with raw non-projected non-mosaiced data (EDR, or Experimental Data Records), run them through a sequence of ISIS3 programs to obtain a special image product, that can be used for parallax calculations in more or less similar way to that described above (some modification will be needed, as the result is not actually map-projected).

This method uses a different approach, which is less accurate, but much quicker. It uses the RDR data set and ignores difficulty (1) above. Mischa Kreslavsky reports up to 1.5 deg varying bias in slopes as a result of this assumption. However, the method accurately accounts for difficulty (2) by compensating distortion introduced by the orthorectification procedure.

Appendix D. Stream power on Mars

The derivation of the shear stress erosion model relies on the assumption that erosion rate (E) is a power law of bed shear stress (τ_b):

$$E = k\,\tau_b^{\,a} \tag{D1}$$

where k and a are positive constants. Following Snyder (2000), Whipple & Tucker (1999) I use the assumptions of conservation of mass (water) and steady uniform flow to obtain the following expression of basal shear stress:

$$\tau_b = \rho C_f^{1/3}\left(\frac{gSQ}{W}\right)^{2/3} \tag{D2}$$

where ρ is the density of water, C_f is a dimensionless friction factor, g is the acceleration due to gravity, S is the local channel slope, Q is the stream discharge and W is the stream width. I then include a relationship for basin hydrology and hydraulic geometry given by:

$$Q = k_q A^c \tag{D3}$$

$$W = k_w Q^b \tag{D4}$$

where k_q and k_w are constants, A is the drainage area and b and c are positive dimensionless constants. Combining 2-5, leads to:

$$E = k_e A^m S^n \tag{D5}$$

where:

$$k_e = k_b k_w^{\,-2a/3} k_q^{\,2a(1-b)/3} \rho^a\, g^{2a/3} \tag{D6}$$

$$m = (2ac/3)(1-b) \tag{D7}$$

$$n = 2a/3 \tag{D8}$$

Given this, if I now define a constant k_m for Mars, based on the approximation that gravitation acceleration is approximately one third that on Earth:

$$k_m = (1/3)^{2a/3} k_e = (1/3)^n k_e \tag{D9}$$

To derive Equation 7-1, in the main text, I have to include the expectation that over long timescales, uplift rate (U) and erosion rate compete to change the landscape elevation (z):

$$\frac{\partial z}{\partial t} = U - E = U - k_e A^m S^n \tag{D10}$$

where t is a given time-step. Now if I assume that the system is in equilibrium in which erosion is balanced by uplift rate, $\partial z / \partial t = 0$, then:

$$S = (U/k_e)^{1/n} A^{-m/n} \tag{D11}$$

Comparing this to Equation (7-1), in the main text, I have:

$$k = (U/k_e)^{1/n} \tag{D12}$$

$$\theta = -m/n \tag{D13}$$

If I then include my k_m constant for Mars defined in Equation D9 in Equation D11 I get:

$$S = (U/k_m)^{1/n} A^{-m/n} \tag{D14}$$

$$S = 3(U/k_e)^{1/n} A^{-m/n} \tag{D15}$$

Thus for a given drainage area I would expect the slope on Mars to be three times greater than for the same drainage area on Earth. Or, in log-log terms:

$$Log\ S = log3 + 1/n\ log(U/ke) - m/n\ logA \tag{D16}$$

Hence, in theory, pixels located within an alluvial channel on Mars, for a given material, would need to be three times steeper for a given drainage area to achieve the stream power necessary to form channels.

Appendix E. Videos of experiments

The videos are saved on the accompanying DVD. Over the page is Table E-1 showing the file structure of the data. You need a media player that can play .wmv (e.g. windows media player) and .mov (e.g. quicktime) formats. The filenames are formed from the experiment identifier numbers shown in Table 8-2 followed by a three letter code, which indicates the position of the camera. “lhs” was a side-viewing camera, which was positioned on the left hand side of the tray as viewed from above with the water outlet at the top. “inc” was a front viewing camera, facing towards the water outlet, inside the chamber, with a low resolution. “out” was a front viewing camera positioned outside the chamber, facing towards the water outlet, with a high resolution. Not all camera angles were available for every experiment because of one or more of the following reasons: interference from exterior equipment disrupted the image, camera was not available and operator error.

The folder name gives information on the experiment type, formed firstly by a code representing the pressure/temperature condidiotns of the experiment and secondly a code representing the material type. “amb” stands for ambient terrestrial temperature and pressure, “lowPT” for low pressure and low temperature and “press” for low pressure and ambient temperature. “fine” stands for fine sand, “med” for medium sand and “rc” for rock crush.

Table E-1. File structure of DVD containing videos of experiments in Chapter 8.

Folder	Subfolder	File
● amb_fine	• 090715_001	090715_001_lhs.wmv
		090715_001_out.MOV
● amb_med	• 090716_001	090716_001_lhs.wmv
		090716_001_out.MOV
	• 090902_002	090902_001_lhs.wmv
		090902_002_out.MOV
● amb_rc	• 090902_001	090902_001_lhs.wmv
		090902_001_out.MOV
● lowPT_fine	• 090515_001	090515_001_inc.wmv
		090515_001_lhs.wmv
		090515_001_out.MOV
	• 090520_002	090520_002_inc.wmv
		090520_002_lhs.wmv
		090520_002_out.MOV
	• 090619_001	090619_001_inc.wmv
		090619_001_lhs.wmv
		090619_001_out.MOV
● lowPT_med	• 090519_001	090519_001_inc.wmv
		090519_001_lhs.wmv
		090519_001_out.MOV
	• 090615_001	090615_001_inc.wmv
		090615_001_lhs.wmv
		090615_001_out.MOV
	• 090710_001	090710_001_inc.wmv
		090710_001_lhs.wmv
		090710_001_out.MOV
● lowPT_rc	• 090520_001	090520_001_inc.wmv
		090520_001_lhs.wmv
		090520_001_out.MOV
	• 090612_001	090612_001_inc.wmv
		090612_001_lhs.wmv
		090612_001_out.MOV
	• 090714_001	090714_001_lhs.wmv
		090714_001_out.MOV
● press_fine	• 090512_001	090512_001_inc.wmv
		090512_001_lhs.wmv
● press_med	• 090511_002	090511_002_inc.wmv
		090511_002_lhs.wmv
● press_rc	• 090514_001	090514_001_inc.wmv
		090514_001_lhs.wmv